Therapeutic Gene Delivery into Retinal Cells by MEA-based Electroporation

Von der Fakultät für Mathematik und Naturwissenschaften der RWTH Aachen University zur Erlangung des akademischen Grades eines Doktors der Naturwissenschaften genehmigte Dissertation

vorgelegt von

Saishreyas Iyer
Master of Science Molecular Biology and Biotechnology
aus
Chennai, Indien

Berichter: Univ.-Prof. Dr. rer. nat. Björn Kampa
Priv.-Doz. Dr. rer. nat. Sandra Johnen
Univ.-Prof. Dr. rer. nat. Frank Müller

Tag der mündlichen Prüfung: *9. Februar 2026*

Diese Dissertation ist auf den Internetseiten der Universitätsbibliothek online verfügbar.

Table of contents

Table of contents ..... **i**

Zusammenfassung ..... **vi**

Abstract ..... **vii**

Abbreviations and acronyms ..... **ix**

1. Introduction **1**

1.1. Mammalian retina 1

1.1.1. Structure of the retina 1

1.1.2. Müller cells 2

1.2. Disorders of the retina 3

1.2.1. Age-related macular degeneration (AMD) 3

1.2.2. Retinopathia pigmentosa (RP) 4

1.2.2.1. Retinal remodeling 4

1.3. Treatment options for retinal dystrophies 6

1.3.1. Visual rehabilitation and treatment of associated ocular anomalies 6

1.3.2. Mutation independent approaches 7

1.3.2.1. Dietary supplements 7

1.3.2.2. Cell replacement using stem cells 7

1.3.2.3. Retinal prostheses 7

1.3.2.4. Optogenetics 9

1.4. Gene therapy 9

1.4.1. Curative approaches 9

1.4.2. Additive approaches....10
1.4.2.1. PEDF in the eye....10
1.4.2.2. BDNF in the eye....11
1.5. Techniques used for gene therapy....11
1.5.1. Transduction....11
1.5.2. Non-viral transfection....12
1.5.2.1. *Sleeping Beauty* Transposon System....13
1.5.2.2. Electroporation of cells in suspension....14
1.5.2.3. Electroporation of cells on a surface with the NEPA-21 device....16
1.5.2.4. Electroporation of cells on a surface with the MEA device....17
2. Aim and approach....20
3. Materials and methods....21
3.1. Materials....21
3.1.1. Devices....21
3.1.2. Consumables....22
3.1.3. Chemicals....24
3.1.4. Kits....26
3.1.5. Antibodies....27
3.1.6. Software....28
3.2. Methods....29
3.2.1. Cell lines....29
3.2.2. Primary Müller cells....29
3.2.2.1. Animals....29
3.2.2.2. Retinal isolation....29
3.2.2.3. Primary Müller cell isolation and cultivation.....30
3.2.3. Plasmids....32
3.2.3.1. Constructs....32

3.2.3.2. Transformation 33
3.2.3.3. Plasmid isolation 34
3.2.4. Electroporation 34
3.2.4.1. Electroporation of cells in suspension 34
3.2.4.2. Electroporation of cells on a surface 35
3.2.4.3. Electroporation of cells with the MEA device 36
3.2.5. Methods to analyse transfection efficiency 38
3.2.5.1. Fluorescence microscopy 38
3.2.5.2. Flow cytometry analysis 38
3.2.5.3. ELISA-based protein quantification 39
3.2.5.4. SDS-PAGE 39
3.2.5.6. Quantitative real-time PCR 41
3.2.6. Methods to analyse transfected cells 42
3.2.6.1. Cell viability assay 42
3.2.6.2. Immunocytochemical analysis 43
3.2.6.3. Cell size/shape comparison 43
3.2.7. Statistical analysis 44
4. Results 46
4.1. Transfection of A-172 cells in suspension 46
4.1.1. Transfections with the fluorescent reporter *Venus* 46
4.1.1.1. Long term analysis of transfection efficiency 49
4.1.2. Transfections with *PEDF* 52
4.1.3. Transfections with *BDNF* 54
4.1.3.1. Cell viability comparison for *PEDF*/*BDNF*-transfected cells 57
4.2. Transfection of A-172 cells cultured on a surface 58
4.2.1. Transfections with the fluorescent reporter *Venus* 58
4.2.2. Transfections of cells on a surface with *PEDF* 60

4.2.3. Transfections of cells on a surface with *BDNF* 62
4.3. Electroporation with the MEA device 64
4.3.1. Transfections with the A-172 cell line 64
4.3.2. Transfections with the R28 cell line 65
4.3.2.1. Genetic modifiability of the R28 cell line 65
4.3.2.2. MEA transfections with the R28 cell line 67
4.4. Relation between cell size/shape and transfection parameters 69
4.5. Experiments with primary Müller cells 75
4.5.1. Isolation and characterization of Müller cells 75
4.5.2. Transfection of Müller cells in suspension 78
4.5.3. Transfection of Müller cells cultured on a surface 80
5. Discussion 82
5.1. *PEDF* and *BDNF* as candidates for additive gene therapy 83
5.2. Transfections of cells in suspension 84
5.3. Transfections of cells cultured on a surface 87
5.4. Transfections with the MEA device 89
5.5. Role of cell size, shape and orientation in transfection 92
5.6. Cultivation and transfection of primary Müller cells 94
5.7. Conclusion and outlook 97
6. References 99
7. Appendix and Raw Data 123
8. List of Figures 165
9. List of tables 168
10. List of pipelines 171
11. Data availability 172
12. Publications 173
13. Curriculum vitae 174

14. Eidesstattliche Erklärung 175

15. Hilfestellungen 176

16. Danksagung.....178

Zusammenfassung

Retinopathia pigmentosa (*RP*) ist eine Gruppe von erblichen Netzhautdystrophien, die zur Erblindung führen. Die mit der *RP* einhergehende Umgestaltung der Netzhaut verringert die Effizienz der Stimulation der retinalen Ganglienzellen (RGCs). Derzeit gilt die Gentherapie mit viralen Vektoren als vielversprechender Ansatz für die Behandlung genetisch bedingter Augenerkrankungen. Trotz ihres Erfolgs hat diese Technik auch Nachteile. In der vorliegenden Arbeit wurde das nicht-virale *Sleeping Beauty* (*SB*) Transposon System verwendet, das eine stabile Integration von Transgenen in das Genom der Zielzellen gewährleistet. Da die Müller-Gliazellen ein geeignetes und gut zugängliches Ziel innerhalb der RP-Netzhaut darstellen, wurde in der aktuellen Studie die genetische Modifizierbarkeit der Glioblastom-Zelllinie A-172 sowie der retinalen Vorläuferzelllinie R28 mittels Elektroporation analysiert. Die Elektroporation der Zellen erfolgte in Suspension oder im adhärenten Zustand. Hierzu wurde entweder eine Elektrode über den Zellen platziert oder die Zellen wurden auf speziell angefertigten Mikroelektrodenarrays (MEAs), die als vielversprechende Kandidaten für eine lokalisierte Niederspannungs-Elektroporation gelten, kultiviert. Zusätzlich zu den Genen, die für das *Yellow Fluorescent Protein* (*YFP*, *Venus*) und *Green Fluorescent Protein* (*GFP*) kodieren, wurden die Gene für die protektiv wirkenden *Pigment Epithelium-Derived Factor* (*PEDF*) und *Brain-Derived Neurotrophic Factor* (*BDNF*) zur Transfektion verwendet. Die höchste Transfektionseffizienz für A-172 Zellen in Suspension betrug 37,2 ± 22,5%, die für R28-Zellen 16,1 ± 8,50%. Die Transfektion mit *PEDF* und *BDNF* ergab Sekretionsraten von 1.090 ± 1.640 pg PEDF/h/10^4 Zellen und 71,0 ± 65,0 pg BDNF/h/10^4 Zellen. Bei der Elektroporation von adhärenten A-172 Zellen wurde eine maximale Transfektionseffizienz von 2,75 ± 0,87% erreicht; Transfektionen mit *PEDF* ergaben Sekretionsraten von 68,9 ± 32,5 pg/h/10^4 Zellen. Im Gegensatz zu den R28 Zellen war die MEA- basierte Transfektion der A-172 Zellen nicht erfolgreich. Die Transfektion von in Suspension befindlichen primären Müller-Zellen, die aus vier Wochen alten C57BL/6J Mäusen isoliert wurden, lieferte erste positive Ergebnisse. Die Ergebnisse dieser Arbeit zeigen, dass die Transfektion von gliaartigen Zellen auf einem MEA möglich, jedoch im Vergleich zur Transfektion von Zellen in Suspension weit weniger effizient ist. Die Transfektion primärer Gliazellen ist ebenfalls durchführbar. Diese Ergebnisse bilden eine wichtige Grundlage für die Entwicklung von Netzhautimplantaten mit integrierten MEAs, die sowohl die Stimulation von RGCs als auch die Transfektion von Müller-Zellen ermöglichen.

Abstract

Retinopathia pigmentosa (*RP*) is a group of hereditary retinal dystrophies that lead to blindness. Retinal remodeling that occurs during RP reduces the efficiency of retinal ganglion cell (RGC) stimulation. Currently, gene therapy using viral vectors is considered a promising approach for the treatment of genetic eye diseases. Despite its success, this technique also has disadvantages. In the present study, the non-viral *Sleeping Beauty* (*SB*) transposon system was used, which ensures stable integration of transgenes into the genome of the target cells. Since Müller glial cells are an appropriate and accessible target within the RP retina, the genetic modifiability of the glioblastoma cell line A-172 and the retinal progenitor cell line R28 were analyzed by electroporation. Electroporation of the cells was performed in suspension or in the adherent state. For this purpose, either an electrode was placed above the cells or the cells were cultivated on custom-made microelectrode arrays (MEAs), which are considered promising candidates for localized low voltage electroporation. In addition to the genes coding for the yellow fluorescent protein (*YFP*, *Venus*) and green fluorescent protein (*GFP*), the genes coding for the protective pigment epithelium-derived factor (*PEDF*) and brain-derived neurotrophic factor (*BDNF*) were used for transfection. The highest transfection efficiency for A-172 cells in suspension was 37.2 ± 22.5% and for R28 cells 16.1 ± 8.50%. Transfection with *PEDF* and *BDNF* yielded secretion rates of 1,090 ± 1,640 pg PEDF/h/10^4 cells and 71.0 ± 65.0 pg BDNF/h/10^4 cells, respectively. For the electroporation of adherent A-172 cells, a maximum transfection efficiency of 2.75 ± 0.87% was achieved; transfections with *PEDF* resulted in secretion rates of 68.9 ± 32.5 pg/h/10^4 cells. Unlike R28 cells, the MEA-based transfection of A-172 cells was not successful. The transfection of primary Müller cells in suspension, isolated from four week old C57BL/6J mice, provided first positive results. The results of this work show that transfection of glial-like cells on a MEA is possible, but far less efficient compared to the transfection of cells in suspension. The transfection of primary glial cells is also feasible. These results form an important basis for the development of retinal implants with integrated MEAs that enable both the stimulation of RGCs and the transfection of Müller cells.

This project was funded by the RTG 2610 InnoRetVision of the DFG Deutsche Forschungsgemeinschaft

Abbreviations and acronyms

ºC	celcius
µ	micro
AAV	adeno-associated virus
AMD	age-related macular degeneration
ANOVA	analysis of variance
APS	ammonium persulphate
ARVO	association for research in vision and ophthalmology
BDNF	brain-derived neurotrophic factor
bp	base pair
BSA	bovine serum albumin
cDNA	complementary DNA
CHO	Chinese Hamster Ovary
CLSM	confocal laser scanning microscope
CMOS	complementary metal oxide semiconductor
CMV	cytomegalovirus
CV	coefficient of variation
DAPI	4′,6-diamidino-2-phenylindole
DMEM	Dulbecco's modified Eagle medium
DMSO	dimethyl sulfoxide
DNA	deoxyribonucleic acid
dNTP	deoxynucleotide triphosphate
DPBS	Dulbecco's phosphate buffered saline
e	eccentricity
E.coli	*Escherichia coli*
EBSS	Earle's balanced salt solution

ECIS	electric cell-substrate impedance sensing
EDTA	ethylenediaminetetraacetic acid
ELISA	enzyme-linked immunosorbent assay
EMT	eye movement training
ERG	electroretinogram
FACS	fluorescence-assisted cell sorting
FBS	fetal bovine serum
FDA	food and drug administration
fMRI	functional magnetic resonance imaging
g	gram
G	gauge
GAPDH	glyceraldehyde 3-phosphate dehydrogenase
GCL	ganglion cell layer
GFAP	glial fibrillary acidic protein
GFP (EGFP)	green fluorescent protein (Enhanced GFP)
GOI	gene of interest
GS	glutamine synthetase
h	hour
H_2O_2	hydrogen peroxide
hBMCs	human bone-marrow derived mesenchymal stem cells
HCL	hydrochloric acid
hMSCs	human mesenchymal stem cells
IgG	immunoglobulin G
ILM	inner limiting membrane
IMI	intelligent medical implant
INL	inner nuclear layer
IPL	inner plexiform layer
IR/DR	inverted repeats/direct repeats
IRIS	intelligent retinal implant systems
l	litre
LANUV	Landesamt für Natur, Umwelt und Verbraucherschutz

LCA	leber congenital amaurosis
LEO	low-vision enhancement optoelectronic
LRP-1	low-density lipoprotein
LVV	lentiviral vectors
M	molar
m	milli
MEA	microelectrode array
MG	Müller glia
MLMT	multi-luminescence mobility testing
Na_2HPO_4	di-sodium hydrogen phosphate
NaCl	sodium chloride
NaOH	sodium hydroxide
NGF	nerve growth factor
OLM	outer limiting membrane
ONL	outer nuclear layer
OPL	outer plexiform layer
PBS	phosphate buffered saline
PCB	printed circuit board
PCR	polymerase chain reaction
PEDF	pigment epithelium-derived factor
PFA	paraformaldehyde
pH	potential of hydrogen
PI	propidium iodide
PP	poring pulse
PRIMA	photovoltaic retinal implant
rcf	relative centrifugal force
RLU	relative light units
RNA	ribonucleic acid
RP	*retinopathia pigmentosa*
RPE	retinal pigment epithelium
rpm	revolutions per minute

RT	room temperature
s	second
SB	*Sleeping Beauty*
SDS	sodium dodecyl sulphate
siRNA	small interfering RNA
SOC	super optimal broth with catabolite repression
SYBR	iTaq Universal SYBR Green Supermix
TAE	tris/acetic acid/EDTA
TBS	tris-buffered saline
TEMED	N,N,N′,N′-tetramethylethylenediamine
TP	transfer pulse
Tris	tris(hydroxymethyl)aminomethane
V	volt
VEGF	vascular endothelial growth factor
VGIC	voltage-gated ion channel
VPA	valproic acid
V_{pp}	voltage peak to peak
WT	wild type
YFP	yellow fluorescent protein

1. Introduction

1.1. Mammalian retina

1.1.1. Structure of the retina

The retina is part of the central nervous system and plays an important role in the detection and initial processing of images by the eye. The mature mammalian retina consists of five basic types of neuronal cells - photoreceptors, horizontal cells, bipolar cells, amacrine cells and retinal ganglion cells (RGCs) - and an accompanying glial cell type, the Müller glia (MG). It has a laminar organization, with the cell somata being arranged in three nuclear layers, separated by two plexiform layers (Figure 1). Processing of visual information flows in a defined direction, from the outer to the inner layers. The outermost of the five layers, called the outer nuclear layer (ONL) consists of the cell bodies of specialized sensory neurons that detect light, the rod and cone photoreceptors. Rods are extremely sensitive to light and are responsible for dim-light vision. Cones are less sensitive but have a faster response during phototransduction. Each cone is sensitive to a specific wavelength of light and is responsible for color vision (1). Both rods and cones transmit the visually evoked signals to the interneurons in the inner nuclear layer (INL), which comprises the cell bodies of horizontal, bipolar and amacrine cells. Photoreceptors and interneurons form synapses in the outer plexiform layer (OPL): rods and cones synapse onto specific types of bipolar cells and the synaptic transmissions are modulated by the horizontal cells. The interneurons process the visual information and transmit it to the RGCs, whose cell bodies are present in the ganglion cell layer (GCL), with their axons making up the nerve fibre layer (NFL). The synapses between interneurons and RGCs occur in the inner plexiform layer (IPL). The RGCs are the output neurons of the retina and connect to the higher visual centres in the brain via the optic nerve. The excitation of the RGCs can be either by a feedforward inhibition from amacrine cell

synapses onto RGC dendrites or a feedback inhibition of the amacrine cells contacting the axon terminals of bipolar cells (1). These different cell types, comprising of 60 different types of neurons, together form an elaborate network to perform the tasks of image detection and processing, creation of contrast and transmission of these signals to the brain (2). The outermost and innermost layers of the retina are the outer limiting membrane (OLM) and inner limiting membrane (ILM) respectively. MG extend throughout the retina and contribute to the formation of the OLM and ILM (Figure 1). The retinal pigment epithelium (RPE) is a densely packed monolayer of pigmented cells that lies on the outside of the retina and serves many important functions like absorption of light and maintenance of the blood retinal barrier (2).

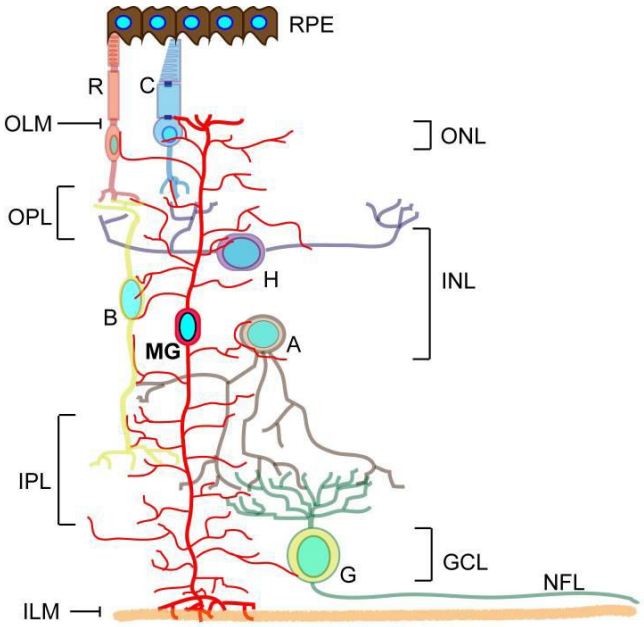


Figure 1: Schematic illustration of the mammalian retina different retinal layers and the arrangement of the different cell types in these layers are shown (2).

1.1.2. Müller cells

Müller cells are radial glial cells in the inner vertebrate retina. They originate from multipotent progenitor cells (3), span the entire thickness of the retina and have a cylindrical fibre-like shape (4, 5). They fulfill a wide range of functions to ensure the functionality and survival of the retinal neurons (6, 7), such as monitoring retinal homeostasis, supporting neurons by releasing trophic factors like brain-derived neurotrophic factor (BDNF) and antiangiogenic factors like pigment epithelium-derived factor (PEDF) and thrombospondin-1, recycling neurotransmitters, controlling ionic balance in the extracellular space (8-11) and serving as

barriers and conduits for the transfer of molecules like glutamine and pyruvate between different retinal cells and compartments (12-14). They are also crucial to retinal structure and function, for example, by playing a role in the formation and maintenance of the blood-retinal barrier, where the constituent endothelial cells depend on the surrounding glial cells for regulation of the microenvironment (15-17).

Finally, Müller cells play an important role in ensuring that light reaches the photoreceptors. Most structures within the retina, especially those in the NFL and both OPL and IPL, are phase objects that cause scattering of light that passes through the retina (18-20). Müller cells have several special optical properties, including low light scattering, which allows them to funnel light through the retina with minimal light loss (7). Every mammalian Müller cell is coupled, on an average, to one cone photoreceptor cell (21). This suggests that the Müller cells form an array of biological optical fibres designed to maximize light collection and minimize light scattering (7).

1.2. Disorders of the retina

Globally, at least 2.2 billion people are affected by some form of vision impairment (22). In at least one billion, or almost half of these cases, the visual impairment could have been prevented or still needs to be addressed. The main causes of visual impairment are refractive errors, cataract, diabetic retinopathy, glaucoma, *retinopathia pigmentosa* (*RP*) and age-related macular degeneration (AMD), which are responsible for almost one billion cases (23, 24).

1.2.1. Age-related macular degeneration (AMD)

Many of the common causes of blindness like AMD, glaucoma, myopathy and diabetic retinopathy are multifactorial and caused by a combination of several factors. AMD is the largest cause of blindness in patients 60 years and older (24). Although age is the biggest risk factor for AMD, several other environmental factors also contribute to the condition. These include smoking (25), hypertension (26), lifestyle (27, 28) and gender. In a healthy retina, the RPE manages the elimination of photoreceptor waste. As the retina ages, reactive oxygen species accumulate in the RPE, leading to cell degeneration and the pathology of the disease (29). AMD can occur in two forms - dry and wet AMD. In the dry form, drusen deposits form between the RPE and Bruch’s membrane, caused by several factors such as inflammation,

oxidative stress and several genetic components (30, 31). The wet form is less common, yet responsible for most cases of blindness. It is characterized by pathological neovascularization originating from the choroid and growing under and into the retina, causing blood and serum to leak into the subretinal space.

1.2.2. Retinopathia pigmentosa (RP)

Retinal dystrophies are characterized by various genetic conditions that impact the function of the retina. They include rod-cone dystrophies, cone-rod dystrophies, chorioretinal degenerations and macular degenerations. One of these monogenetic diseases is *RP*, a group of genetic disorders that leads to a gradual loss of vision. It affects around one in 5000 people worldwide, making it the most common inherited retinal disease (32, 33). It is known to be caused by mutations in one of at least 100 genes (34). Mutations in more than 25 genes have been reported to cause autosomal dominant *RP* (34), with mutation in over 45 genes being reported as the cause for autosomal recessive *RP* (35) and six genes being linked with X-linked *RP*. The disease pathology can also be limited to the eye (non-syndromic) or syndromic, where mutations in certain genes leads to combined retinal and non-retinal conditions, like in Usher syndrome and Bardet–Biedl syndrome (36)

The first symptom of *RP* is the loss of night vision (nyctalopia). This is followed by a narrowing of the visual field. Depending on the severity of the disease, many patients have tunnel vision and some even suffer from complete vision loss. Patients with late effects of *RP* can develop perceived flashes of light (photopsia), which can even progress to hallucinations (37).

1.2.2.1. Retinal remodeling

A retina affected by *RP* undergoes a series of changes, collectively referred to as retinal remodeling (Figure 2). Remodeling occurs in three distinct phases. Phase 1 shows early signs of photoreceptor stress. This phase is characterized by rod degeneration. The rod cells pass through stressed, deconstructed, irreversibly stressed, and apoptotic stages (38). In phase 2, photoreceptor loss occurs, followed by glial remodeling of the ONL. With the loss of the rod outer segments, the rhodopsin level of the plasma membrane in the rod inner segments rises, increasing the rate of rod death. The collapse of the subretinal space parallels the ablation of the cone outer segments and the remodeling of the inner segment. Cone deconstruction involves the rearrangement of cone opsins into the inner segments, changes in the expression levels of some essential proteins, and a transient extension of the axons into the neural retina.

At this stage, the cones start to die, and this process can be accelerated by the migration of activated microglia into the sensory retina (38). Müller cells are also affected by the remodelling. The MG undergo gliosis as part of a larger series of changes in the retinal structure (39). Gliosis involves increased expression of glial fibrillary acidic protein (GFAP) in the MG and hypertrophy, a process in which the cells increase in size (40, 41). Expansion of this fibrotic distal seal by MG seals the remaining cones from the outside of the retina. The initial remodeling of the neural retina starts with the rod and cone bipolar cells retracting their dendrites and revising their expression of receptor proteins for synaptic signaling. The rod-directed axon terminal fields of the horizontal cells retract, while the cone-targeted somas of the horizontal cells hypertrophy and extend new neurites into the IPL. All bipolar and horizontal cell undergo remodelling (38).

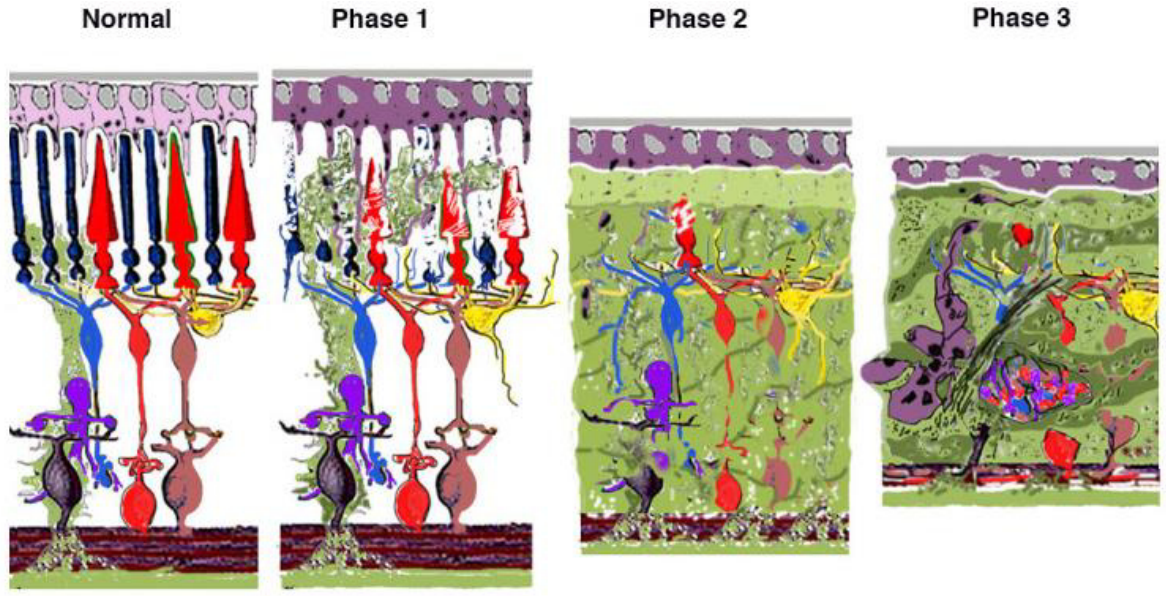


Figure 2: Remodelling of the mammalian retina in retinal degeneration, Normal - healthy retina; **Phase 1 -** rod degeneration: rod cell death, rod neurite extension and cone outer segment truncation; **Phase 2 -** Cone degeneration: massive rod death, cone neurite extension, progressive cone cell death, Müller cell somatic translocation to the ONL and the early stages of the glia seal; **Phase 3 -** neurite remodeling, MG hypertrophy, inversion of amacrine and bipolar cells into the inner plexiform and ganglion cell layers, progressive neuronal cell death, RPE cell loss; dark blue - rods, red - cones, ON cone bipolar cell and ON ganglion cell, brown - OFF cone bipolar cells , OFF ganglion cells, yellow - horizontal cells, purple - amacrine cells, light green - Müller cell seal, dark green - reactive Müller cells, dark brown - GCL, pink - RPE (image adapted from review, Jones et al, 2016 (42)).

Phase 3 involves an prolonged period of neural, glial and vascular remodeling of the surviving retina (43). In early phase 3, deafferentation of the neural retina is complete and Müller cell sealing becomes denser. The MG hypertrophies and forms large columns that segment the retina. Neurons of the IPL begin to remodel and global neuronal death becomes detectable (38). *RP* also appears to progress differently depending on the degree of cone survival. In cone decimating *RP* (44, 45), aggressive retinal remodeling occurs in phase 2 and 3. In contrast, in cone sparing *RP*, remodeling and cell death are delayed by isolated areas of survivor cones (43, 46).

1.3. Treatment options for retinal dystrophies

As there are a large number of genes that can cause retinal dystrophy such as *RP*, there is no single cure. However, several gene therapy approaches are being researched, each of which addresses a single possible cause of *RP* (47, 48). In addition, there are several treatment options for the symptoms of the disease.

1.3.1. Visual rehabilitation and treatment of associated ocular anomalies

Visual training and rehabilitation can maximize the remaining vision of *RP* patients and thus enhance their ability to deal with normal tasks. *RP* patients have been shown to need a longer reaction time and more mental effort (49, 50) along with an increased risk of colliding with other pedestrians (51). New devices, software and artificial intelligence-based tools are being researched to provide *RP* patients with more degree of independence while performing daily tasks. One example is the Low-vision Enhancement Optoelectronic (LEO) belt, which has increased the accuracy of mobility and self-confidence of patients (52).

RP treatment options could be combined with treatment of associated ocular anomalies to improve visual performance. In a study involving six patients with progressive *RP*, conducted over 8 - 10 months, the patients were given eye movement training (EMT) daily for 5 - 10 minutes (53). The reading performance following EMT increased in five out of the six patients, which was confirmed with a functional magnetic resonance imaging (fMRI) before and after EMT.

1.3.2. Mutation independent approaches

1.3.2.1. Dietary supplements

Research into limiting *RP* pathology by the implementation of dietary supplements is ongoing. One example is the treatment with oral valproic acid (VPA), which inhibits the inflammatory response by inducing apoptosis in microglial cells (54) and has been shown to improve visual acuity in *RP* patients (55).

Treating children with vitamin A resulted in a slower decrease in the amplitude of the cone electroretinogram (ERG). However, due to the small size of the study sample, no definite conclusions could be drawn (56).

1.3.2.2. Cell replacement using stem cells

Stem cells are also being investigated as a potential treatment option for *RP*. When transplanted, stem cells have the potential to differentiate into retinal cells and integrate into the patient's retinae (as reviewed in (57)). In one study, the noggin gene was transduced into adult human bone marrow-derived mesenchymal stem cells (hBMSCs), and the resulting stem cells had an increased ability to differentiate into neural and photoreceptor cells (58). In another study, mesenchymal stem cells (MSCs) were differentiated into photoreceptor cells (59).

Despite the progress made, some studies have shown a chronic immune response to the transplanted cells (60). Another major challenge is the low integration rate of transplanted photoreceptor precursors into the host retina (61). Further research needs to be conducted before more stem cell therapies become commercially available.

1.3.2.3. Retinal prostheses

Retinal prostheses are another area of vision preservation that has been intensively researched. There are three different types of visual prostheses (Figure 3). Epiretinal prosthesis systems are placed next to the nerve and ganglion cell layers on the retinal surface (62, 63). They usually consist of an external, glass-mounted camera that communicates wirelessly with an epiretinal microelectrode array. Some examples include Argus II (64), Intelligent Medical Implant/Intelligent Retinal Implant Systems II (IMI/IRIS II) (65, 66) and EPI-RET III (67). The advantage of epiretinal implants is that surgeons are more familiar with the surgical techniques used. Placing an implant close to the vitreous cavity could also contribute to heat dissipation (62). The second type of retinal prostheses, subretinal implants, are placed at the

level of the degenerated photoreceptors. In this way, the intrinsic signal processing capacity of the retinal interneurons can be effectively used. However, this is only possible if the retina retains its remaining physical morphology after photoreceptor degeneration (38, 68). Some examples of subretinal implants include the Boston Retinal Implant (similar to the Argus II but inserted in the subretinal space (69)), Alpha IMS and AMS (70) and the Photovoltaic Retinal Implant (PRIMA) (71). The last type of retinal prostheses are suprachoroidal. This system is less invasive and more accessible for replacement, but also carries a significant risk of hemorrhage as the suprachoroidal space is highly vascularized (62).

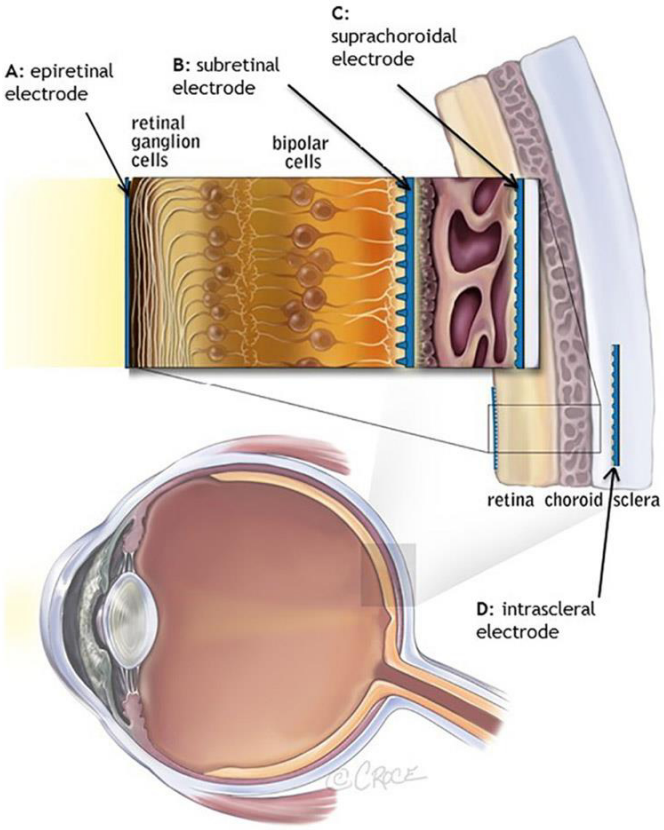


Figure 3: Anatomical locations for the different types of retinal prostheses. (A) epiretinal position; **(B)** subretinal space; **(C)** suprachoroidal implant (72).

Despite the advantages of using retinal prostheses, they also have disadvantages. The highest estimated visual acuity achieved with a retinal prosthesis is that of the Alpha IMS, with a vision of 6/150 Snellen, although this is far inferior to natural vision (62, 73, 74). The resolution of prosthetic systems is limited by several factors, including electrode density, size, number and spacing of the electrodes, electrode contact and image persistence (75).

The theoretical maximum resolution of existing electrode arrays is at least 12 times lower compared to the normal retina (62, 76). All these disadvantages of current retinal prostheses highlight the need for a deeper understanding of the structure and functioning of the degenerated retina, not to mention improved implants, the use of better materials and techniques for the construction of the intraocular chips.

1.3.2.4. Optogenetics

The aim of optogenetics is to deliver opsins to surviving cells in a degenerated retina in order to make them sensitive to light. Recent preclinical studies have used human opsins, such as rhodopsin, cone opsins and melanopsin. However, other studies have used microbial-derived opsins (77). In one study, a channel rhodopsin with enhanced light-sensitivity was delivered using the CAG promoter, which required a device for opsin stimulation. To date, no safety concerns have been reported (78).

All of the above examples demonstrate the extensive research on the use of mutation-independent approaches in the treatment of *RP*. However, there are no absolute treatment options and the results are inconclusive, making further research necessary.

1.4. Gene therapy

Gene therapy involves the treatment of a genetic disease by introduction of gene/cellular function altering genetic material. For inherited retina disorders such as *RP*, gene therapy represents an important therapeutic strategy due to its ability to address the underlying genetic defects. Despite extensive research, no standardized therapies currently exist for patients with *RP*, primarily due to its marked genetic heterogeneity involving mutations in over 100 different genes, each affecting distinct molecular pathways implicated in photoreceptor function and survival.

1.4.1. Curative approaches

Genetic defects caused by a mutation in a specific gene can be treated by supplying the correct copy of the gene. Gene therapy has been shown to rescue photoreceptor cells and restore vision in *RP* animal models (79, 80). The eye is an accessible target organ and immunologically isolated, which makes it an ideal candidate for gene therapy (32).

An example of a Food and Drug Administration (FDA)-approved gene therapy is Luxturna (Voretigene neparvovec-rzyl) for treating *RP* caused due to a bi-allelic mutation in the *RPE65* gene (81, 82). The correct copy of the gene is delivered using an adeno-associated virus (AAV) vector. Treatment resulted in significant improvement with no adverse side effects and a multi-luminance mobility testing (MLMT) score of 1.8 in the intervention group, one year after treatment (83). A sustained improvement was also observed at the follow-up after three years, with an MLMT score of 2.4 for direct-intervention patients (84). However, a subset of patients developed progressive perifoveal chorioretinal atrophy after surgery in addition to chorioretinal atrophy around the retinotomy site (85).

1.4.2. Additive approaches

Additive gene therapy is a type of gene therapy where a functional copy of a gene is introduced into a patient to supplement normal function without altering or removing the existing mutant gene. In the case of multifactorial diseases like AMD, it is difficult to come up with one specific gene therapy approach to treat the disease. Additive approaches Neuroprotective approaches involving treatment with growth factors or antioxidants (86), aimed at slowing the progression of the disease, are more useful in such cases. A study by Pinto *et al.*, involving the treatment of rd10 and wild type (WT) mice retinae with human recombinant and synthetic PEDF fragments, resulted in an increased ONL thickness in rd10 mice *in vivo* (87). In the current study, the neuroprotective agents PEDF and BDNF (88) were analyzed.

1.4.2.1. PEDF in the eye

PEDF, a neurotrophic glycoprotein, belongs to the family of non-inhibitory serpins (88) and has anti-angiogenic, neurotrophic and anti-oxidative properties (89). It is a 418 amino acid protein that has a mass of 50 kDa (90) and is highly conserved in mammals (91). It was originally isolated at the University of Southern California by Tombran Tink. J and Johnson L.V, from a conditioned medium of cultured human fetal RPE cells (92). PEDF is naturally occurring and is primarily secreted by the RPE, although it also secreted by the MG during retinal hypoxia (93). PEDF-deficient mice were shown to have a faster vascular expansion rate (94, 95) and mice with genetic over-expression of PEDF showed significantly suppressed retinal neovascularization (96). PEDF and PEDF-derived peptides strongly inhibit choroidal (97-100) and corneal neovascularization (44, 45, 101, 102). PEDF also aids the survival of

retina neurons (103, 104), RPE cells (105), retinal progenitor cells (106) and photoreceptors (103, 105, 107-109).

1.4.2.2. BDNF in the eye

BDNF, a neurotrophic glycoprotein, which belongs to the neurotrophin family and the Nerve Growth Factor (NGF) superfamily, exhibits neuroprotective, angiogenic, and anti-oxidative properties (110). It is synthesized in the endoplasmic reticulum as a 32 - 35 kDa precursor protein. The terminal domain of the precursor is then cleaved to yield the 119 amino acid long 13 kDa mature BDNF (111-113). BDNF was first isolated from the pig brain by Yves-Alain Barde and Hans Thoenen (114). While high levels of BDNF have been detected in the hippocampus, amygdala, cerebellum and cerebral cortex in both rodents and humans, the highest levels were found in hippocampal neurons (115, 116). Additionally, BDNF expression was also detected in the RGCs, amacrine cells and Müller cells (11, 117). BDNF is important for neurogenesis, synaptogenesis and synaptic plasticity (118) and was shown to be a potent neuroprotective agent, following optic nerve injury in the mammalian retina (119-125). It also plays a role in maintaining the structural integrity and visual responsiveness of the neurons (126, 127). BDNF gene delivery into eye by intravitreal injection demonstrated stable long-term expression, long-term upregulation of cell survival pathways downstream of BDNF, and RGC neuroprotection (128). In addition, *BDNF* gene delivery to MG has been shown to increase RGC survival in rats (129, 130).

1.5. Techniques used for gene therapy

Transfection is a technique employed in gene therapy to introduce exogenous nucleic acids into cells in order to genetically modify them. The efficient delivery of genetic material is carried out by gene delivery vehicles called vectors. Transfection methods can be broadly classified into transduction, which involves the use of viral vectors, and non-viral transfection methods.

1.5.1. Transduction

Viruses are the most highly evolved vectors available in nature and so a lot of research involves the use of viruses to introduce genetic material into a target cell. There are different types of viral vectors, of which retroviruses (131), AAVs and lentiviruses are frequently used.

Retroviruses are generally used to transfect dividing cells while adenoviruses, AAVs and herpes viruses can be used to transfect non-dividing cells as well (132). The *Retroviridae* family, with a genome of two single stranded RNA copies, can be used to stably integrate genetic information into the host (133, 134). Nevertheless, retroviral transduction is associated with a high risk of insertional mutagenesis and gene disruption (135). This was demonstrated in the study where a retroviral vector encoding the γc protein was used for *ex vivo* transduction of autologous CD34+ bone marrow stem cells, which were then returned to the patient. T-cell leukemias were reported in four out of nine successfully treated patients, which correlated with integration of the gene therapy vector near proto-oncogenes (136). Lentiviral vectors are also part of the *Retroviridae* family and are more suited to transgene delivery due to a higher packaging capacity of up to 9 kb (137). An example of a lentiviral gene therapy is the recently terminated clinical trial involving the delivery of *ABCA4* gene to treat Stargardt's disease (138). The study used a subretinal injection to target photoreceptor cells in 27 patients. Three patients showed serious adverse events, including increased intraocular pressure, uveitis and chorioretinopathy. Additionally, lentiviral vectors suffer from insufficient methods for the production of high titre value stocks and the safety concerns due to the their HIV-origin (reviewed in (139, 140)).

In contrast, AAVs are a safer virus for gene therapy due to their lower immunogenicity and pathogenicity in humans (141). The relative safety of AAVs is due to their lack of the genes necessary for the expression and replication of their own genome (reviewed in (134)). The small packaging capacity (<5 kb) of AAVs, however, limits their ability to deliver large-sized therapeutic genes (132) (142). Viral vectors also carry other disadvantages, including spread of viruses into adjacent organs (143), and inflammatory reaction to the virus (144). Finally, gene therapies involving viral vectors are extremely expensive due to production costs (145). Consequently, there is a growing need to develop alternative strategies for genetic engineering.

1.5.2. Non-viral transfection

Non-viral transfection approaches are an emerging area of research and can be classified as either chemical or physical methods. Chemical transfection often uses lipids which trap the naked genetic material within liposomes. The liposomes then fuse with the cell membrane and facilitate entry of the genetic material into the cell via endocytosis (146). Physical/mechanical transfection methods include the use of physical forces like electricity (electroporation),

ultrasound (sonoporation), laser (laser irradiation) or magnetism (magnetofection) as a means of transfection. Following delivery into the cell by physical or chemical means, genetic material may either persist episomally or integrate into the host genome. While several studies involve the use of plasmids that persist within the cells, this technique has its disadvantage. A study by Ehrhardt *et al.* demonstrated that when non-viral, episomally persisting plasmid DNA was used, transgene expression levels and DNA copy numbers decreased by 95 and 99%, respectively (147). Recent research have focussed on implementing non-viral transfections systems that can ensure integration of the transgene into the host genome. A prominent example of a non-viral integrating system is the non-viral *Sleeping Beauty* transposon system.

1.5.2.1. *Sleeping Beauty* Transposon System

The *Sleeping Beauty (SB)* transposon system is a non-viral DNA transposon system developed from the Tc1/mariner family (148) that overcomes the disadvantages of viral transduction by using transposons, which are discrete genetic fragments that can jump between distinct genomic loci within a single cell. They display a reduced immunogenicity compared to viral vectors, an improved safety profile (149), an increased cargo capacity (150), high gene expression rates and long term expression of the transgene (143). In addition, the transgene is integrated into the host cells' genome randomly into TA motifs, minimising the risk of insertional mutagenesis without triggering an immune response (151-154).

The *SB* system used in the current study comprises two plasmid vectors: one containing a synthetic gene encoding *SB100X* transposase gene and the other plasmid containing a cloned non-autonomous gene of interest (GOI) flanked by transposase binding sites contained within inverted repeat/direct repeat (IR/DR) regions (Figure 4A). When delivered to cells, the *SB100X* transposase binds, after it has been expressed and translated, to the transposase binding sites. It then catalyzes the excision and integration of the GOI from the plasmid DNA into the cell's genome (Figure 4B). *SB*-mediated gene transfer was shown to be successful in different and primary cell types including human hematopoietic progenitors, mesenchymal stem cells, muscle stem/progenitor cells (155) It was also reported to have positive results in the treatment of disease models like colorectal cancer and glioblastoma (156, 157). The plasmids are usually introduced into the cells by means of electroporation.

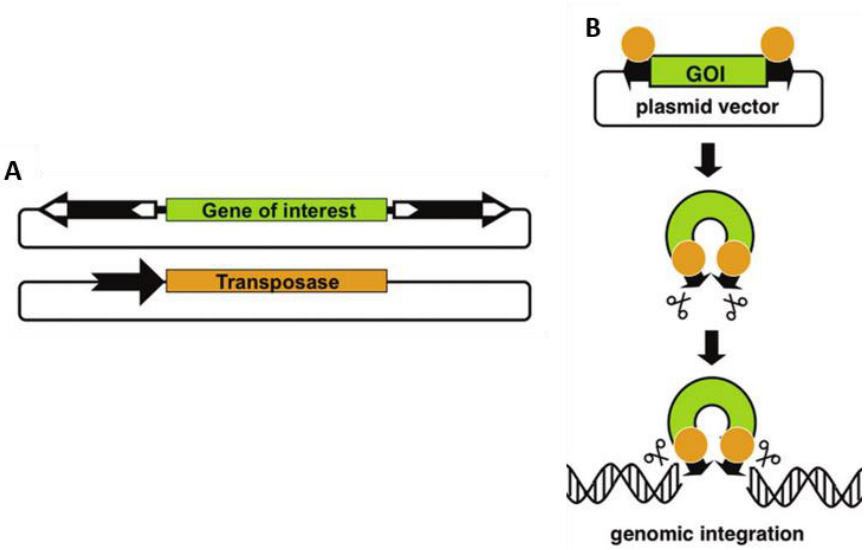


Figure 4: The *Sleeping Beauty* transposon system. (A) bi-component, trans-arrangement transposon vector system for delivering transgenes that are maintained in plasmids. One component contains a gene of interest (green) between the transposon TIRs carried by a plasmid vector, whereas the other component is a transposase expression plasmid, in which the black arrow represents the promoter driving expression of the transposase; **(B)** the transposon carrying GOI is excised from the donor plasmid and integrated at a chromosomal site by the transposase. This image was derived from (158)

1.5.2.2. Electroporation of cells in suspension

Electroporation is a physical transfection technique in which cells or tissues placed between two electrodes, are exposed to pulsed electric fields (100 - 1000 V/cm) (159, 160). This results in a potential difference across the cell membrane due to redistribution of local ions (161). Once the transmembrane potential exceeds the dielectric strength of the membrane, transient hydrophilic pores are formed across the membrane that allow the entry of foreign genetic material such as plasmids or mRNA into the cell (Figure 5).

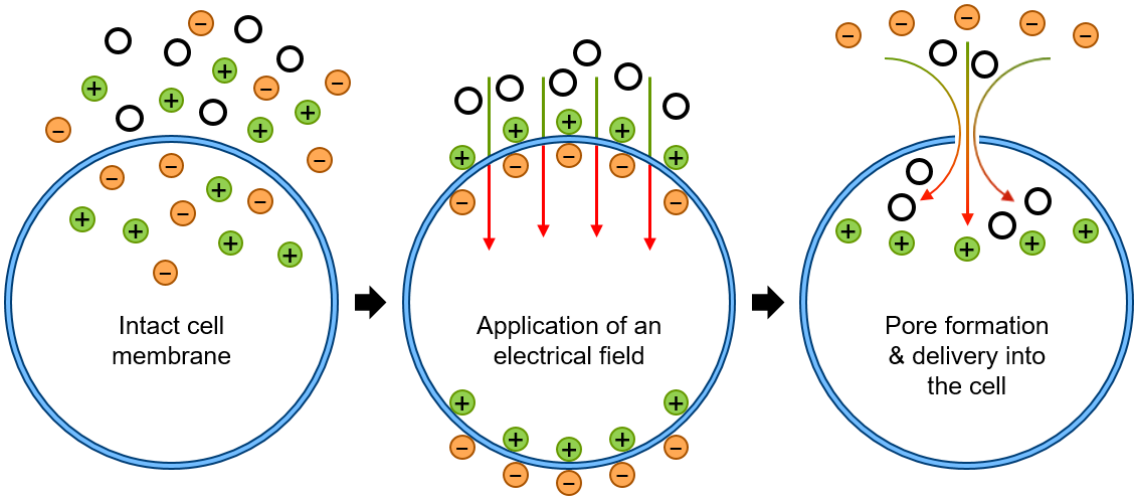


Figure 5: Mechanism of electropermeabilization and electroporation. left panel: intact state of the phospholipid membrane when no electric field is applied; central panel: reorientation of phospholipids and redistribution of charges when an electric field is applied; right panel: formation of hydrophilic pores and the entry of genetic material into the cell in a sustained electric field.

Cells in suspension are electroporated in a specific buffer mixed with plasmid DNA. The mixture is usually placed in a cuvette with a parallel plate electrode arrangement (162) (Figure 6 A). High voltages are usually required to achieve the electric field strength of 1 kV/cm necessary for membrane pore formation as a result of the large distance between the electrodes (162, 163).

The Neon Transfection System is a variation of the cuvette electroporation system that uses a special pipette instead of the traditional cuvette. The tip of the pipette, where the biological sample is contained, delivers a high electric field (Figure 6 B). The tip is designed to maximize the gap distance between the two electrodes while simultaneously minimizing the surface area of the electrodes (164). This results in a higher transfection efficiency compared to the cuvette system due to a more uniform electric field. minimal pH change, lesser ion formation and negligible heat generation (143).

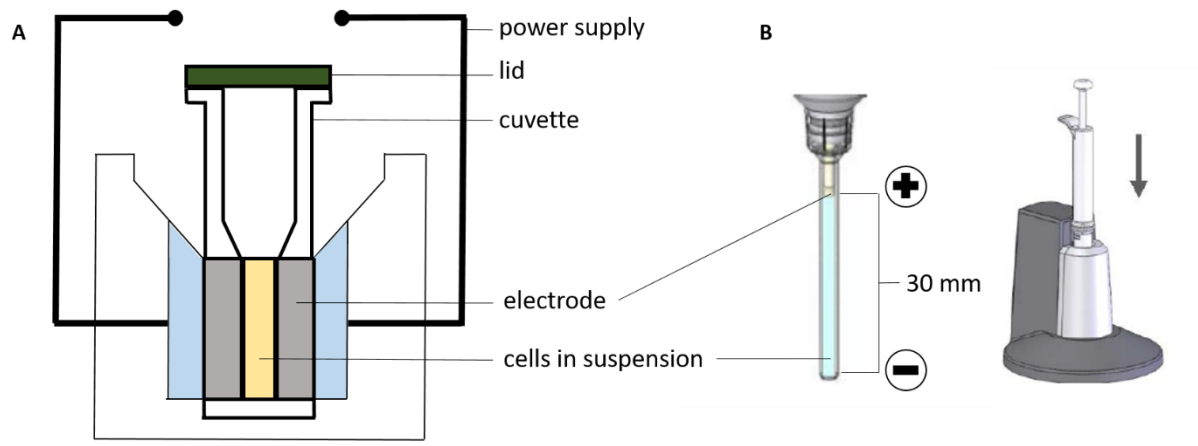


Figure 6: Cuvette-based and pipette tip-based electroporation. (A) schematic of the standard cuvette electroporation system; (adapted from (165)); **(B)** left panel: schematic of the Neon pipette tip; right panel: the Neon pipette placed into the docking port before electroporation (right) (164)

1.5.2.3. Electroporation of cells on a surface with the NEPA-21 device

Electroporation of cells in suspension is very efficient. However, since most mammalian cell types in their natural state are attached to a substrate or organized in a tissue structure, electroporation in suspension is artificial in comparison. A different method of electroporation is required that allows a more natural arrangement of the cells during transfection.

The NEPA-21 Electroporator Type II is a novel customizable device that allows electroporation *in situ, ex vitro* and *in vitro*. The electroporation, which uses square pulses, happens in a four-step pulsing with voltage decay and results in higher transfection efficiency and higher viability compared to transfection in suspension using the commonly used cuvette-based Amaxa Nucleofector, without the use of special buffers (166). The four steps involved are: (1) a poring pulse (PP) mode using multiple pulses with a higher voltage of shorter duration, designed to form pores in the cell membrane, (2) a polarity exchanged PP step, (3) a transfer pulse (TP) mode using multiple pulses of lower voltage and a longer duration, designed to deliver the target molecules into the cells with minimum damage, and (4) a polarity exchanged TP step.

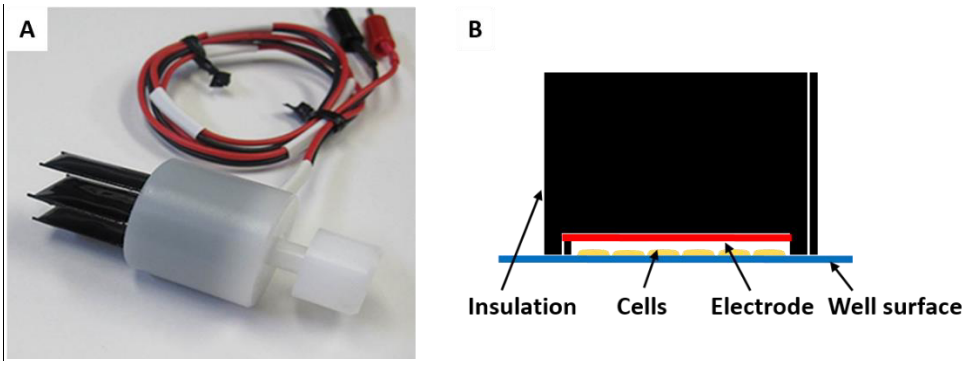


Figure 7: The CUY900-13-3-5 cell culture plate electrode used for transfection with the NEPA-21 device. **(A)** a picture of the electrode. The red and black wires were connected to the NEPA-21 device and the black plates were inserted into the well; (**B)** a cross section of the electrode as it appears when placed in a well. (image adapted from (167)).

In the present research, the NEPA-21 device was employed because it offered the possibility of using an electrode configuration for transfection of cells cultivated on a surface like a cell culture dish. Specifically, the CUY900-13-3-5 cell culture plate electrode was used with the NEPA device. This electrode had three parallel metal plates which were completely insulated except for the bottom edge (Figure 7 A). The electrode was used over cells cultivated on the surface of wells in a 24-well plate (Figure 7 B).

1.5.2.4. Electroporation of cells on a surface with the MEA device

In conventional electroporation, high voltages between the opposing electrodes are required to achieve an electric field strength necessary for membrane pore formation (162, 163). A MEA consists of a single integrated device which contains independent and electrically isolated microelectrodes. Each of these electrodes are capable of recording electrical signals from one or a group of neurons. MEAs can consist of 10 - 1,000 electrodes and provide higher spatiotemporal specificity and good signal-to-noise ratio compared to other methods like electroencephalography and electrocorticography (reviewed in (168)). Compared to conventional approaches, MEA-based electroporation allows operation with low voltages and provides localized transfection (163). In recent years, these advantages of MEAs has seen their use in electroporation studies. Successful *in vitro* electroporation, where the cells were cultured and transfected directly on the electrodes, has been demonstrated in combination with electric cell-substrate impedance sensing (ECIS) (169, 170). In one study, Duckert *et al.* reported a successful electroporation and gene electrotransfer on a high-definition complementary metal oxide semiconductor (CMOS) MEA with over 16,000 individual addressable subcellular-

dimension electrodes (171). Another study by Zeck. G and Herrmann. T demonstrated electrostimulation and electroporation in rd1 mice retinae. The electroporation in this case was successfully carried out in close vicinity to the stimulation electrodes (172). Finally, Zhang *et al.* developed a flexible microelectrode array for retinal electroporation with which they achieved a uniform distribution of the electric field over the retina, combined with a significantly reduced voltage requirement (173). Their study also allowed a precise gene delivery due to a controlled local application of the electric field.

The current study involved the use of MEAs consisting of 60 gold electrodes evaporated onto borosilicate glass wafers with titanium deposited as an adhesion layer in-between and a Parylene-C coating for feedline insulation (Figure 8 A) (174). The MEAs were developed and analyzed in a previous study by Kauth *et al.*. They reported that initial transfection experiments using these MEAs, performed on HEK293T cells with pmaxGFP was successful (Figure 8 B). Additionally, they reported that the ideal electrode shape was semicircular-triangular (174, 175). The current research involved the study of the genetic modifiability of the glial A-172 cell line and the retinal progenitor R28 cell line with the MEA device. Three different electrode shapes were analyzed - triangle, circular and semicircular-triangular (Figure 8 C).

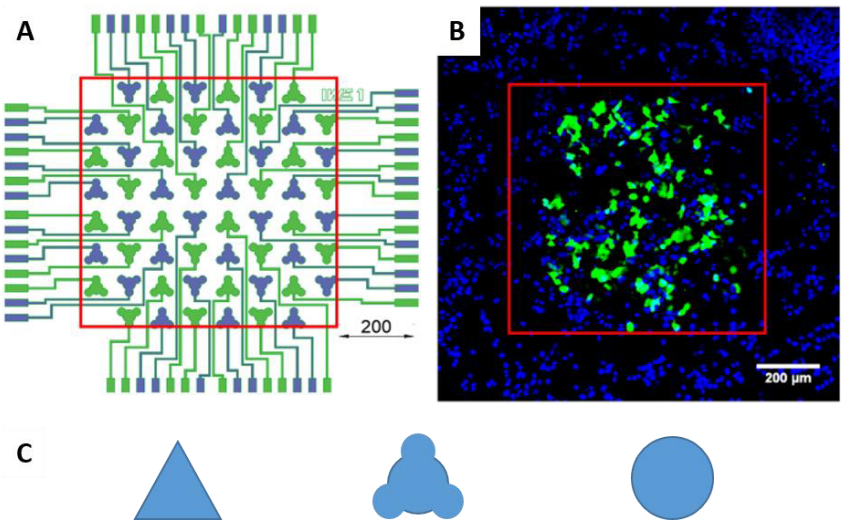


Figure 8: The MEA design used for transfection experiments; (A) electrode arrangement used in the current study. During pulses, all purple electrodes were at the same time-dependent sinus potential and all green electrodes were grounded. Dimension is depicted in µm; **(B)** preliminary transfection experiments of HEK-293 cell line with pmaxGFP. Image captured at (100×, CLSM). The green areas are GFP-expressing cells, 24 hours after electroporation. DAPI staining is shown in blue (174), **(C)** different electrode shapes used in the present study (adapted from (175)).

1.6. Role of geometric properties of cell on transfection

Over the years, several attempts have been made to explain the differences in transfection efficiency between different cell lines and transfection conditions. One theory, proposed by Rosazza *et al.* (160), explained the dependence of efficient electroporation on cell size and shape. When an electric field is applied to the cell, the potential difference induced in the cell membrane is added to the resting potential difference of the cell. When the total value of the resulting potential difference reaches or exceeds the critical potential of the cell (corresponding to the critical electric field value of the cell), permeabilization of the cell membrane begins (160). Although the critical potential difference depends on the cell type and ranges between 200 mV and 500 mV for animal, plant or bacterial cells (176-180), this value is generally the same for most biological membranes (approximately 300 mV). This could mean that the critical value of the electric field usually depends on the size and other geometric properties of the cell (160). The theory that cell shape, size and orientation play an essential role in transfection efficiency has been tested and confirmed in previous research. Agarwal *et al.* showed by single-cell electroporation of fluorescence-labelled A-549 cells that transfection efficiency increased with increasing cell size and sphericity (181). Zu *et al.* showed that transfection efficiency is directly proportional to the size of the cell by transfecting mammalian cell lines with *GFP* using micropillar array electroporation (182). In addition, Towhidi *et al.* demonstrated that cells aligned in the direction of the electric field were transfected more efficiently than cells that are not (183).

In the current study, the effect of the geometric properties of the cell on transfection efficiency was investigated . Three cell lines, A-172, R28 and ARPE-19 were analysed prior to and post-transfection, using the Cell-Profiler software to measure cell area and eccentricity. In order to accurately represent the variation in sizes within a population of cells, the coefficient of variation (CV) of the 2D cell area was used for analysis.

$$CVa = \sigma/\mu$$

where CVa is the CV of the 2D cell area, μ is the mean area and σ is the standard deviation.

Whether the cells are more circular or elliptical was measured using the eccentricity (*e*) value. Eccentricity is a measure of the distance between one node on a graph and all other nodes (184). It gives the shape of a system. A circle has an *e* value of 0, while an ellipse has a value between 0 and 1.

2. Aim and approach

The aim of the study was to explore and evaluate the feasibility of non-viral gene transfer using the *SB* transposon system. The potential of different electroporation-based techniques for the stable transfection of reporter genes and protective genes was investigated. The techniques included transfection of cells in suspension and during cultivation of the cells on a surface. Particular attention was paid to the use of a customized microelectrode array (MEA) device for transfection. A further aim was to establish primary Müller glial cell cultures and to investigate the feasibility of electroporation-based transfection of primary Müller glial cells.

To achieve this aim, the study employed electroporation-based delivery of reporter genes *Venus* and *GFP*, and therapeutic genes *PEDF* and *BDNF*, using the non-viral *SB* transposon system. The glioblastoma cell line A-172 and the retinal progenitor cell line R28 were used in *in vitro* studies to assess transfection efficiency achieved with these cell lines, when employing different electroporation devices, including transfection in suspension with the Neon Transfection System and transfection on a surface with the NEPA-21 device. A custom MEA-based electroporation device was tested to determine its feasibility as a platform for localized, low-voltage electroporation. Quantitative assessment of transfection efficiency was performed with a flow cytometry analysis. PEDF/BDNF protein secretion was analyzed qualitatively with an SDS PAGE, followed by a western blot and quantitatively with an enzyme-linked immunosorbent assay (ELISA). An analysis of *PEDF/BDNF* gene expression was conducted with a quantitative real-time PCR (RT qPCR). Additionally, primary Müller glial cells isolated from C57BL/6J WT mice retinae using a papain-based dissociation protocol, were transfected in suspension to evaluate the feasibility of transfection. The presence of Müller cells was confirmed with an immunocytochemical analysis performed with antibodies against Müller cell markers. A final comparison of images of the different cell lines used, prior to and post-transfection, allowed a study of the dependence of transfection efficiency on cell shape, size and orientation. These findings provide a foundational understanding for integrating gene delivery into MEA-based retinal implants.

3. Materials and methods

3.1. Materials

3.1.1. Devices

The devices used in this study are listed in tables 1 and 2. The corresponding companies and location of their headquarters are indicated.

Table 1: Overview of general devices and the corresponding companies.

General devices	Company
CFX Opus 96 real-time PCR system	Bio-Rad Laboratories, Hercules, CA, US
ChemiDoc imaging system	Bio-Rad Laboratories, Hercules, CA, US
Confocal microscope LSM 710	Carl Zeiss Microscopy GmBH, Jena, Germany
Eppendorf research pipette (100 µl, 200 µl, 1000 µl)	Eppendorf, Hamburg, Germany
Eppendorf research plus pipette (10 µl)	Eppendorf, Hamburg, Germany
Flow cytometer BD FACS Canto II	BD Biosciences, Franklin Lakes, NJ, US
Haemocytometer Neubauer BlueBrand	Merck, Darmstadt, Germany
Leica DMi8 microscope	Leica Camera, Wetzlar, Germany
Leica DMI4000 B microscope	Leica Camera, Wetzlar, Germany
Mastercycler Nexus thermal cycler	Eppendorf, Hamburg, Germany
Mini-PROTEAN tetra cell	Bio-Rad Laboratories, Hercules, CA, US
Nanodrop ND-1000 spectrophotometer	Avantor, Randor, PA, US
Pipetboy acu 2	Integra Biosciences Corp., Hudson, NH, US
PowerPac basic	Bio-Rad Laboratories, Hercules, CA, US

SpectraMax iD3 microplate reader	Molecular Devices LLC, San Hose, CA, US
Stereo microscope M80	Leica Camera, Wetzlar, Germany
Sub-Cell GT - electrophoresis chamber	Bio-Rad Laboratories, Hercules, CA, US
Sub-Cell GT gel runner	Bio-Rad Laboratories, Hercules, CA, US
ThermoMixer C	Eppendorf, Hamburg, Germany
Trans-Blot turbo transfer system	Bio-Rad Laboratories, Hercules, CA, US

Table 2: Overview of electroporation devices and the corresponding companies.

Electroporation devices		**Company**
Neon device	Microporator MP-100 PeqLab digi bio	Avantor, Randor, PA, US
	Neon pipette	ThermoFischer Scientific, Waltham, MA, US
NEPA device	NEPA electrode CUY900-13-3-5	Nepa gene, Ichikawa, Chiba prefecture, Japan
	Plug, cover cable - C115CB-2	Nepa gene, Ichikawa, Chiba prefecture, Japan
	Super electroporator NEPA21-II	Nepa gene, Ichikawa, Chiba prefecture, Japan
MEA device	192256A-1 USB A/B 2.0 cable	Artisan Technology Group, Champaign, IL, US
	Function generator MFG-2230M	GW Instek, Taiwan
	Microeletrode arrays	Developed at IWE-1, RWTH Aachen
	Motherboard	Developed at IWE-1, RWTH Aachen
	Oscilloscope Picoscope 2208B	Pico, Cambridgeshire, UK
	SYV-50-2-41 coaxial cable	Jiangsu Elesun Cable Co. Ltd., Nanjing, China
	TA375 cable (100MHz voltage divider scope probe 1:1/10:1)	PSE- Priggen Special Electronic GmbH, Pico, Cambridgeshire, UK

3.1.2. Consumables

Consumables used in this study are listed in table 3. The corresponding companies and location of their headquarters are indicated.

Table 3: Overview of consumables and the corresponding companies

Consumables	Company
Agarose gel casting stand	Bio-Rad Laboratories, Hercules, CA, US
Amersham Protean supported 0.2 µm nitrocellulose blotting membrane	Cytiva, Marlborough, MA, US
Bacterial cell spreader Drigalski glass	Carl Roth GmBH, Karlsruhe, Germany
Cannula 27 G Sterican	Braun, Melsungen, Germany
Cell culture plates (24-well)	Jet Biofil, Guangzhou, China
Cell culture plates (48-well)	Eppendorf, Hamburg, Germany
Centrifuge tubes (15 ml, 50 ml)	Starlab International GmBH, Hamburg, Germany
Cover Slips # 1.5	ThermoFischer Scientific, Waltham, MA, US
Cryotubes	Nalge Nunc Int. Corp., Rochester, NY, US
Feather disposable scalpel No 21	Feather, Servoprax, Wesel, Germany
FisherScientific plastic pipettes (5 ml, 10 ml, 25 ml)	ThermoFischer Scientific, Waltham, MA, US
Greiner 12 ml culture tubes with vent plug	Merck, Darmstadt, Germany
Hard-shell 96-well PCR plates	Bio-Rad Laboratories, Hercules, CA, US
Immu-mount	Epredia, Breda, Netherlands
Microcentrifuge tubes (1.5 ml, 2 ml)	Sarstedt AG & Co.KG, Nümbrecht, Germany
Microscope cover glass (superior, 24 x 50 mm)	Paul Marienfeld GmbH & Co.KG, Lauda-Königshofen, Germany
Microseal ‘B’ seal	Bio-Rad Laboratories, Hercules, CA, US
Mini-PROTEAN TGX stain-free gels	Bio-Rad Laboratories, Hercules, CA, US
Nunc Lab-Tek II chamber slide (4 well)	ThermoFischer Scientific, Waltham, MA, US
PCR tubes (0.2 ml, 0.5 ml)	Starlab International GmBH, Hamburg, Germany
Petri dish	Corning Inc., Corning, NY, US
Polystyrene round-bottom tube with cell-strainer cap 12 x 75 mm style (5 ml)	Corning Inc., Corning, NY, US
Surgical microscissors PD040-41	Precisemed GmBH, Tuttlingen, Germany

T-75 cell culture flask	ThermoFischer Scientific, Waltham, MA, US
TipOne pipette tips with filter (10 µl, 200 µl, 1000 µl)	Starlab International GmBH, Hamburg, Germany
TipOne pipette tips without filter (10 µl, 200 µl, 1000 µl)	Starlab International GmBH, Hamburg, Germany
Tweezers Inox 08 style 5	Dumont, Montignes, Switzerland
Tweezers style 5	Hermle Labortechnik GmBH, Wehingen, Germany
White opaque tissue culture plate (96-well)	Corning Inc., Corning, NY, US

3.1.3. Chemicals

Chemicals used in this study are listed in table 4. The corresponding companies and location of their headquarters are indicated.

Table 4: Overview of chemicals and the corresponding companies.

Chemicals	Company
Trypsin EDTA 1x (0.05%, 0.25%)	ThermoFischer Scientific, Waltham, MA, US
2-mercaptoethanol	Merck KGaA, Darmstadt, Germany
6-aminohexanoic acid	AppliChem GmBH, Darmstadt, Germany
Acrylamide 4K-solution (30%)	AppliChem GmBH, Darmstadt, Germany
Agar	Carl Roth GmBH, Karlsruhe, Germany
Agarose LE	Biozym Scientific GmBH, Hessisch Olendorf, Germany
Albumin, fraction V biotin-free	Carl Roth GmBH, Karlsruhe, Germany
Ammonium persulphate	Serva Electrophoresis GmBH, Heidelberg, Germany
Amphotericin B	Merck KGaA, Darmstadt, Germany
Ampicillin sodium salt	Carl Roth GmBH, Karlsruhe, Germany
Betaine	Sigma-Aldrich, Burlington, MA, US
Bromophenol blue sodium salt	Merck KGaA, Darmstadt, Germany
Carbogen gas	Linde PLC, Dublin, Ireland

Chloramphenicol	Sigma-Aldrich, Burlington, MA, US
Dimethylsulfoxide (DMSO)	Merck KGaA, Darmstadt, Germany
Disodium hydrogen phosphate (Na_2HPO_4)	RdH Laborchemikalien GmbH, Seelze, Germany
DMEM/F-12 (1:1)	PAN Biotech GmbH, Aidenbach, Germany
DNA stain clear G	Serva Electrophoresis GmbH, Heidelberg, Germany
DPBS (w/o calcium & magnesium)	PAN Biotech GmbH, Aidenbach, Germany
Dulbecco's Modified Eagle Medium (DMEM)	PAN Biotech GmbH, Aidenbach, Germany
Competent Novablue *E.coli* (K-12)	Sigma-Aldrich, Burlington, MA, US
Ethylenediaminetetraacetic acid (EDTA)	Serva Electrophoresis GmbH, Heidelberg, Germany
Ethanol 70% (v/v)	Otto Fischar GmbH, Saarbrucken, Germany
Ethanol absolute	Otto Fischar GmbH, Saarbrucken, Germany
Foetal bovine serum (FBS) good	PAN Biotech GmbH, Aidenbach, Germany
Gel loading dye purple (6x)	New England Biolabs Inc., Ipswich, MA, US
Gelatine gold	Carl Roth GmbH, Karlsruhe, Germany
Glacial acetic acid	Morphisto GmbH, Offenbach,Germany
Glucose solution (100 g/l)	PAN Biotech GmbH, Aidenbach, Germany
Glutaraldehyde solution (25%)	Merck KGaA, Darmstadt, Germany
Glycerin (water free)	Carl Roth GmbH, Karlsruhe, Germany
Glycine	Merck KGaA, Darmstadt, Germany
Hydrochloric acid (HCl, 37%)	VWR BDH Chemicals, Darmstadt, Germany
Hydrogen peroxide (H_2O_2, 30%)	AppliChem GmbH, Darmstadt, Germany
Imidazol buffer grade	AppliChem GmbH, Darmstadt, Germany
Isofluorane	Piramal Critical Care B.V. Hallbergmoos, Netherlands
iTaq universal SYBR green supermix	Bio-Rad Laboratories, Hercules, CA, US
Luminol	Honeywell International Inc., Charlotte, NC, US
MEM vitamin solution	Gibco, Paisley, UK
Ni-NTA superflow	Qiagen GmbH, Hilden, Germany

Non-essential amino acids (100x)	PAN Biotech GmBH, Aidenbach, Germany
Non-fat dried milk powder	AppliChem GmBH, Darmstadt, Germany
Paraformaldehyde (PFA)	Sigma-Aldrich, Burlington, MA, US
p-coumaric acid	Honeywell International Inc., Charlotte, NC, US
Penicillin and streptomycin	Merck KGaA, Darmstadt, Germany
Peptone	Carl Roth GmBH, Karlsruhe, Germany
Quick load 2-log DNA ladder	New England Biolabs Inc., Ipswich, MA, US
RNase-ExitusPlus	AppliChem GmBH, Darmstadt, Germany
Sodium dodecyl sulphate (SDS)	AppliChem GmBH, Darmstadt, Germany
SOC medium	Novagen, Merck, Darmstadt, Germany
Sodium chloride (NaCl)	VWR BDH Chemicals, Darmstadt, Germany
Sodium hydroxide (NaOH) flakes pure	Merck KGaA, Darmstadt, Germany
TEMED (99%) for electrophoresis	Carl Roth GmBH, Karlsruhe, Germany
Tergazyme	Sigma-Aldrich, Burlington, MA, US
Tricine	AppliChem GmBH, Darmstadt, Germany
Tris(hydroxymethyl)aminomethane	Serva Electrophoresis GmBH, Heidelberg, Germany
Triton X-100 (for molecular biology)	Sigma-Aldrich, Burlington, MA, US
Trypan blue solution	Merck KGaA, Darmstadt, Germany
Tween 20 (for molecular biology)	AppliChem GmBH, Darmstadt, Germany
Yeast extract	Carl Roth GmBH, Karlsruhe, Germany

3.1.4. Kits

Kits used in this study are listed in table 5. The corresponding companies and location of their headquarters are indicated.

Table 5: Overview of kits and the corresponding companies.

Kits	Company
Human PEDF ELISA kit	Xpress Biotech International, Frederick, MD, US

Neon transfection kit - 10 µl	ThermoFischer Scientific, Waltham, MA, US
Papain dissociation system	Worthington Biochem Corp., Lakewood, NJ, US
Quantikine human free BDNF ELISA kit	R and D Systems Inc., Minneapolis, MA, US
Reverse transcription system	Promega Corporation, Fitchburg, WI, US
RNase-free DNase set	Qiagen GmBH, Hilden, Germany
RNeasy micro kit	Qiagen GmBH, Hilden, Germany
Cell Titer-Glo cell viability assay	Promega Corporation, Fitchburg, WI, US
Plasmid maxi kit	Qiagen GmBH, Hilden, Germany

3.1.5. Antibodies

Antibodies used in this study are listed in tables 6 and 7. The corresponding companies and location of their headquarters are indicated.

Table 6: Overview of primary antibodies and the corresponding companies.

Primary antibody	Company
Anti-human BDNF antibody (polyclonal, rabbit)	Abcam Inc. Cambridge, UK
Anti-human GFAP antibody (polyclonal, chicken)	Novus, Bio-Techne GmBH, Wiesbaden, Germany
Anti-human GS antibody (monoclonal, mouse)	Becton Dickinson & Co., Franklin Lakes, NJ, US
Anti-human PEDF antibody (polyclonal, rabbit)	Xpress Biotech International, Frederick, MD, US
Recombinant anti-vimentin antibody (monoclonal, rabbit)	Abcam Inc. Cambridge, UK

Table 7: Overview of secondary antibodies and the corresponding companies

Secondary antibody	Company
Anti-chicken IgY Fc fragment - Alexa Fluor 647 (polyclonal, goat)	Dianova, Biozol GmBH. Hamburg, Germany

Anti-mouse IgG H+L - Cy3 (polyclonal, donkey)	Dianova, Biozol GmBH. Hamburg, Germany
Anti-rabbit IgG H+L (HRP) (polyclonal, goat)	Abcam Inc. Cambridge, UK
Anti-rabbit IgG H+L - Alexa Fluor 488 (polyclonal, goat)	Abcam Inc. Cambridge, UK

3.1.6. Software

Software used in this study is listed in table 8. The corresponding companies and location of their headquarters are indicated.

Table 8: Overview of software and the corresponding companies.

Software	Company
BD FACS Diva	Becton Dickinson & Co., Franklin Lakes, NJ, US
Cell Profiler 4.2.6	Broad Institute, MIT, Cambridge, MA, US
CFX Maestro vr 2.2	Bio-Rad Laboratories, Hercules, CA, US
Fiji	Open source
LAS X life science microscope	Leica Microsystems, Wetzlar, Germany
NanoDrop 1000	Informer Technologies Inc, Los Angeles, CA, US
PicoScope 7 T&M early access	Pico, Cambridgeshire, UK
Prism 10.3.0	GraphPad Software Inc, Boston, MA
SoftMax Pro 7	Molecular Devices LLC, San Jose, CA, US
Zen Blue	Carl Zeiss Microscopy GmBH, Jena, Germany

3.2. Methods

3.2.1. Cell lines

Human A-172 glioblastoma cells (ATCC CRL-1620) were maintained in DMEM, supplemented with 10% FBS, 4 mg/ml glucose (added if DMEM F-12 was used), 80 U/ml penicillin, 80 µg/ml streptomycin and 2.5 µg/ml amphotericin B. Medium was changed once a week. Cells were passaged weekly using 0.05% trypsin EDTA at a ratio of 1:5.

Rat R28 retinal precursor cells (185, 186) were maintained in DMEM supplemented with 10% FBS, 89.54 µg/ml non-essential amino acids, 102.41 µg/ml (8.91 µg/ml vitamins and 93.5 µg/ml inorganic salts) MEM vitamin solution, 110 U/ml penicillin and 110 µg/ml streptomycin. Cells were passaged twice a week using 0.05% trypsin EDTA at a ratio of 1:50.

Human ARPE-19 retinal pigment epithelial cells (ATCC CRL-2302) were maintained in DMEM /F-12, supplemented with 10% FBS, 80 U/ml penicillin, 80 µg/ml streptomycin and 2.5 µg/ml amphotericin B. Medium was changed once a week and the cells were passaged weekly using 0.05% trypsin EDTA at a ratio of 1:10.

All cell lines were maintained at 37°C in a humidified atmosphere of 95% air and 5% CO_2.

3.2.2. Primary Müller cells

3.2.2.1. Animals

Male and female C57BL/6J WT mice aged four weeks (Janvier, Le Genest-Saint-Isle, France) were used for isolation of the retinas. Mice were kept under controlled light conditions (12:12 hour light/dark cycle) at room temperature (RT) of 21-23°C and humidity of 35-65% with water and food available *ad libitum* at the Institute of Laboratory Animal Science, Faculty of Medicine, RWTH Aachen University. Mice were deeply anesthetized and sacrificed with an overdose of isoflurane and then decapitated. The experiments were performed in accordance with the ARVO Statement for the Use of Animals in Ophthalmic and Vision Research and the German Animal Welfare Act after approval by the regulatory authorities (reference number: 90003A4) and in accordance with the ARRIVE guidelines (187).

3.2.2.2. Retinal isolation

Retinal isolation was performed under a clean bench using a stereo microscope. After sacrifice, the eyes were enucleated by spreading the eyelids, placing bent forceps (no. 7) under the

eyeball to expose the optic nerve and cutting it with scissors underneath the forceps. The eyes were immediately transferred to a petri dish filled with warm phosphate-buffered saline (PBS) supplemented with 100 U/ml penicillin and 100 µg/ml streptomycin. The first eye was pierced at the limbus with a 27 G cannula. The pierced hole served as the entry point for the precision spring scissors, which were used to cut the eye in half radially (Figure 9 A and B). The lens was removed by gently pulling with forceps (no. 5) to allow better access for the PBS to reach the retina (Figure 9 C). Two fine forceps (no. 5) were inserted between retina and eye cup, moving them around to detach the retina almost completely (Figure 9 D).

The eye cup was turned inside out and the retina was completely removed by cutting through the optic nerve (Figure 9 E). The vitreous body was detached from the rim of the eye cup using two fine forceps and dragged to the centre of the retina. The complete vitreous body was collected at the papilla and removed in one piece by pulling gently (Figure 9 F). The isolated retinae were checked for possible residues and maintained in fresh, warm PBS until the start of the Müller cell isolation.

3.2.2.3. Primary Müller cell isolation and cultivation.

Prior to isolation, 4-well LabTek chamber glass slides were coated with 0.2% gelatin for one hour at 37ºC and stored in PBS until further use. Primary Müller cell isolation was performed using the Worthington Papain Dissociation kit according to the manufacturer's protocol. Earle's Balanced Salt Solution (EBSS) was adjusted to a pH range of 7.2-7.4 before use by bubbling with carbogen gas (5% CO_2 and 95% O_2) and used to dissolve the kit components. Isolated retinae were transferred to a petri dish containing a mixed enzymatic solution of 20 U/ml papain and 200 U/ml DNase (Figure 9 G). The tissue was dissected into smaller fragments using a No. 21 Feather disposable scalpel. The resulting retinal suspension was transferred to a centrifuge tube and incubated at 37°C with 5.5% CO_2 on a shaker set to 70 rpm for 40 minutes. Following enzymatic digestion, the mixture was gently triturated six times to facilitate the dissociation of any remaining intact tissue fragments (Figure 9 H) and left to rest for up to five minutes to allow undigested tissue to settle at the bottom. The supernatant was collected in a fresh 15 ml centrifuge tube and centrifuged at 280 rcf for five minutes at RT. The pellet was reconstituted in EBSS supplemented with 3 mg/ml ovomucoid inhibitor, 3 mg/ml albumin and 200 U/ml DNase This cell mixture was carefully laid on top of a solution of 10 mg/ml ovomucoid inhibitor and 10 mg/ml albumin such that the two liquids did not mix (Figure 9 I). Müller cells were visible as a ring between the two liquid layers. This setup was centrifuged at 70 rcf for six minutes at RT and the resulting pellet was reconstituted in warm

DMEM supplemented with 20% FBS, 80 U/ml penicillin and 80 µg/ml streptomycin. The cells were plated on gelatin-coated chamber glass slides and incubated at 37°C with 5.5% CO_2. The medium was changed 24 hours after isolation, ensuring that most of the remaining cells were glial cells (188), followed by a medium change every fourth subsequent day. This was done for four weeks or until the isolated cells reached confluence of at least 50%. Before transfection, the cells were passaged using 0.25% trypsin EDTA for two minutes. The suspension was centrifuged at 500 rcf for 10 minutes to collect the cells for further use.

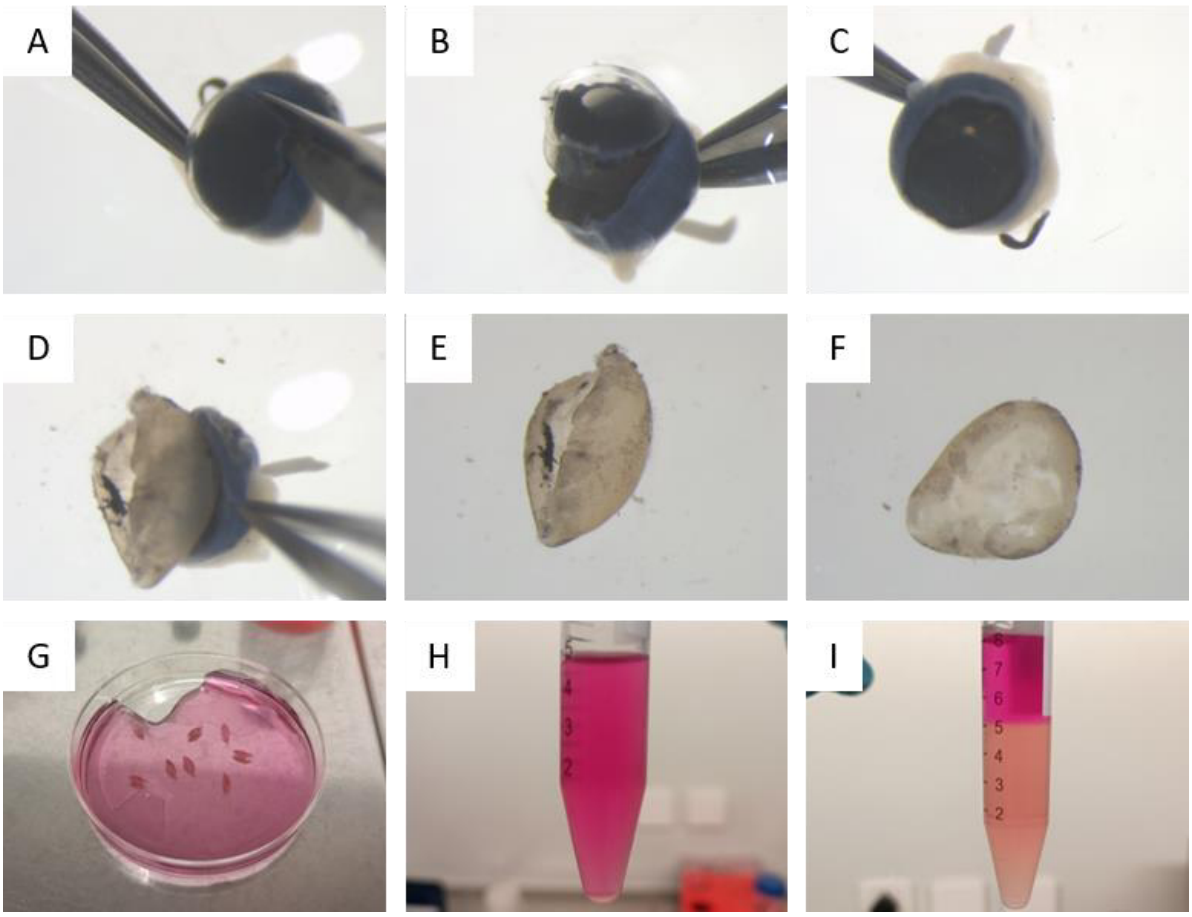


Figure 9: Individual steps of the Müller cell isolation from WT mouse retinas. (A, B) the isolated eye was held in place with tweezers and cut open with spring scissors; **(C)** the cornea and the lens were been removed from the eye cup; **(D)** the retina was detached from the eye cup, only remaining attached at the optic nerve; **(E)** the retina was completely detached from the eye cup by cutting the optic nerve, but the vitreous still remained in the retina; **(F)** the vitreous was removed from the retina; **(G)** the isolated retinae were collected in a Petri dish filled with papain solution; **(H)** the retinae were digested in the papain solution; **(I)** the digested retina mixture was layered on top of an ovomucoid inhibitor solution.

3.2.3. Plasmids

3.2.3.1. Constructs

The *SB* transposon system, consisting of the *SB100X* transposase plasmid, pCMV(CAT)T7-SB100 (4755 bp), and the transposon plasmids pT2-CAGGS-Venus (5888 bp) (189), pT2-CMV-PEDF/EGFP (7205 bp) (143) or pT2-CMV-BDNF/EGFP (6745 bp) (88), was used for transfection with the Neon and the NEPA-21 devices (Figure 10). All transposon plasmids were based on pT2/BH (Addgene plasmid #26556), while the transposase plasmid was from Addgene #34879.

The eukaryotic expression cassettes were flanked by inverted terminal repeats (ITRs). The *SB* transposase plasmid (Figure 10 A) consisted of the *SB100x* gene expressed under the control of the CMV promoter. Concerning pT2-CAGGS-Venus transposon plasmid (Figure 10 B), the CAGGS promoter drove the expression of *yellow fluorescent protein (YFP)*. The PEDF and BDNF transposon plasmids (Figure 10 C and D) contained the cDNA of the *PEDF* (*Serpinf1*) gene (Ensembl Gene ID: ENSMUSG00000000753) or the human *BDNF* gene (Ensembl Gene ID: ENSG00000176697) respectively. The two genes were expressed under control of the cytomegalovirus (CMV) promoter and fused to a C-terminal 6× histidine-tag. Co-translation of the *enhanced green fluorescent protein (EGFP)* was enabled by the pIRES-EGFP-vector-derived synthetic intron (IVS) and an internal ribosomal entry site (IRES) (190). The *SB100X* transposase plasmid and the respective transposon plasmid were used at a ratio of 1:16. Additionally, the pmaxGFP plasmid was used for transfections with the MEA device (Addgene #177825).

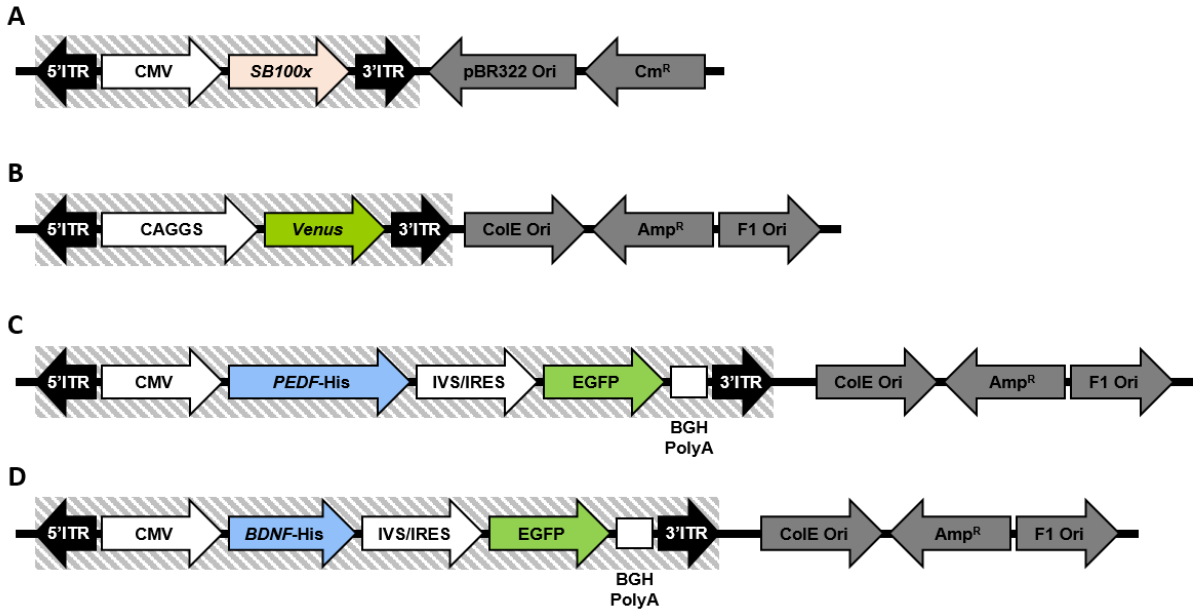


Figure 10: Illustration of the *SB* transposase and transposon plasmids used in this study. (A) plasmid sequence for the **pCMV(CAT)T7-SB100** transposase plasmid; **(B)** plasmid sequence for the **pT2-CAGGS-*Venus*** transposon plasmid (adapted from (189)); **(C)** plasmid sequence for the **pT2-CMV-PEDF/EGFP** transposon plasmid (Adapted from Johnen *et al.*, 2012 (143)); **(D)** plasmid sequence for the **pT2-CMV-BDNF/EGFP** transposon plasmid (88).

3.2.3.2. Transformation

Plasmids were amplified by transforming *Escherichia coli* (*E.coli)* K-12 according to the manufacturer's instructions. Bacteria were transformed with plasmid at a ratio of 1:10 (v/v) with a 30 second heat shock at 42ºC. Following this, the cells were plated on LB agar plates containing the antibiotic specific to the plasmid used. Transformation with *Venus*, *PEDF* or *BDNF* plasmids required 0.1 µg/ml ampicillin, while *SB100X* required 0.034 µg/ml chloramphenicol and pmaxGFP required 50 µg/ml kanamycin. The plates were checked for positive transformed colonies after an overnight incubation at 37ºC.

LB agar	NaCl	0.171 M
	Peptone	10 g/l
	Yeast extract	5 g/l
	Agar	20 g/l

3.2.3.3. Plasmid isolation

The selected plasmid colonies were individually seeded into 5 ml LB medium containing the required antibiotics (0.1 µg/ml ampicillin/ 0.034 µg/ml chloramphenicol) and incubated at 37ºC overnight on a bacterial shaker at 200 rpm. 1 ml of this pre-culture was transferred into 100 ml of fresh LB medium, which was then incubated overnight at 37ºC and 200 rpm. Plasmid isolation was performed with the plasmid maxi kit according to the manufacturer's protocol. For the elution of the plasmid, 125 - 250 µl TE buffer, which contains the chelating agent EDTA, was used to reduce DNase activity and allow long term storage of the plasmid. The concentration of the eluted plasmid was measured using a Nanodrop spectrophotometer. The plasmids were verified with a restriction analysis followed by an agarose gel electrophoresis, at 80ºC for one hour. After verification, the plasmids required for transfection of cells in suspension were diluted to 350 ng/µl in Tris-CL buffer as this allowed the maintenance of a more consistent pH, while also minimizing the effect of EDTA on cell culture. The composition of the LB medium and the buffers are given below.

LB medium	NaCl	0.171 M
	Peptone	20 g/l
	Yeast extract	10 g/l
TE buffer	Tris	10 mM
	EDTA	1 mM
	Dissolved in distilled water (pH 8)	
Tris CL buffer	Tris	10 mM
	Dissolved in distilled water (pH 8.5)	

3.2.4. Electroporation

3.2.4.1. Electroporation of cells in suspension

Cells in suspension were electroporated with the Neon Transfection System using the Neon 10 µl kit according to the manufacturer's protocol. 5 x 10^4 A-172/R28 cells were suspended in 11 µl buffer R and combined with 1 µl of purified plasmid mixture which contained the *SB100X* transposase plasmid and the respective transposon plasmid at a ratio of 1:16 and a concentration of 350 ng/µl. Transfected cells were transferred into 24-well tissue culture plates containing 1 ml fresh medium without antibiotics and antimycotic. Penicillin, streptomycin and

ampicillin were added with the first medium exchange three days after electroporation. Cell morphology and fluorescence were assessed at regular intervals by phase contrast and fluorescence microscopy.

For the transfection of the primary Müller cells, four-week-old primary cells were used. The passaged cells were used in their entirety for each transfection. A mixture of the transposase and transposon plasmids with a total concentration of 500 ng per transfection was used. The transfected cells were plated on 4-well chamber slides coated with 0.2% gelatin and maintained for one to two weeks before performing immunocytochemical analyses. Medium without antibiotics was used immediately following transfection and was replaced with medium containing antibiotics, three days post-transfection.

3.2.4.2. Electroporation of cells on a surface

Electroporation of cultivated cells was carried out with the NEPA-21 electroporator. 5 x 10^4 A-172 cells were seeded per well in a 24-well plate, 24 hours before the transfection. Before electroporation, the cells were washed twice with PBS and once with DMEM/Ham's F-12 medium without FBS. 500 µl *SB100X* and pT2 Venus plasmid mixture (1:16) in DMEM/Ham's F-12 medium without FBS was prepared with a concentration of 420 ng/µl. For electroporation of cells cultivated in a 24-well plate, the CUY900-13-3-5 electrode was used (Figure 11). Two different pulses, a PP of high voltage and short duration (voltage: 125 - 275 V, pulse length: 1 - 5 ms, pulse interval: 50 ms, number of pulses: 2, decay rate: 10%, with or without polarity exchange) and a TP of low voltage and longer duration (voltage: 30 V, pulse length: 50 ms, pulse interval: 50 ms, number of pulses: 5, decay rate: 40%, with or without polarity exchange) were used and the current limit was switched off, as recommended by the manufacturer for electroporation of adherent cells *in vitro*.

The pulse was applied with the electrode once or twice, with the electrode rotated by 90° during the second pulse application. The two possible placements of the electrode were tried together with different combinations of PP and TP voltages, pulse widths and polarity exchange settings, leading to four possible setups of the device. The electrode was cleaned periodically with a sandpaper to remove build-up of protein and cell debris on the electrode surface. The plasmid solution was reused for 12 wells after which, a new plasmid solution was prepared. Following electroporation, the cells were incubated for three days in DMEM/F12 supplemented with 10% FBS, but without antibiotics and antimycotic. Downstream analysis of the transfected cultures was performed seven days post-transfection.

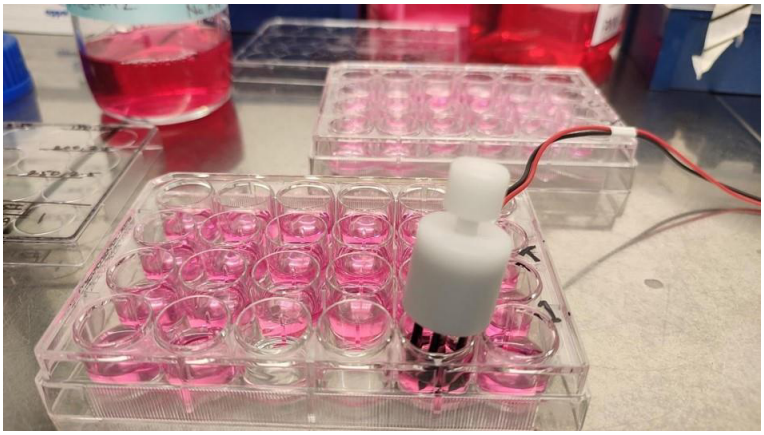


Figure 11: The CUY900-13-3-5 electrode placed inside a 24 well, ready for electroporation

3.2.4.3. Electroporation of cells with the MEA device

MEA-based electroporation was performed using a custom-made device (Figure 13 A) which was designed at the Institut für Werkstoffe und Electrotechnik I (IWE-1), RWTH Aachen University (174). Each MEA had two compartments/wells, an inner well which housed the electrode array and an outer well formed by fitting a glass ring on to the printed circuit board (PCB) (Figure 12 B). The inner well of each MEA was treated with 0.1% gelatine for one and a half hours at RT to prevent cell lift off during electroporation (174). This was followed by 5 mg/ml glutaraldehyde treatment for 20 minutes to crosslink the gelatine (191). The MEAs were washed at least 10 times with PBS to completely remove any trace of glutaraldehyde since it is toxic to the cells. The cells were seeded 24 hours before transfection. 1.98 x 10^4 A-172/R28 cells were seeded onto the inner well of each MEA, followed by an incubation under the bench for 30 minutes and then a 30 minute incubation at 37ºC before adding more medium to the outer well. Electroporation was performed using 750 ng pmaxGFP per MEA. The desired pulses were delivered using a Gwinstek MFG-2230 M multi-channel function generator and the output was read by a Picoscope 2000 series oscilloscope (Figure 12 A). 40 kHz sine wave pulses were used and the applied voltage (10 - 16 V) and pulse duration (100 - 200 ms) were varied to find the optimal settings. The applied voltage refers to the total voltage delivered (voltage peak to peak, V_{pp}), so the voltage for one peak of the sine wave was in the range of 5 - 8 V. Different arrangements of active and ground electrodes were set by turning the switches on the MEA motherboard on or off (Figure 12 A and 13). After transfection, the MEAs were left under the bench for 10 minutes to allow the cells to rest, following which, fresh

medium was slowly added to the outer well. The cells were analysed by fluorescence microscopy, 24 hours after electroporation.

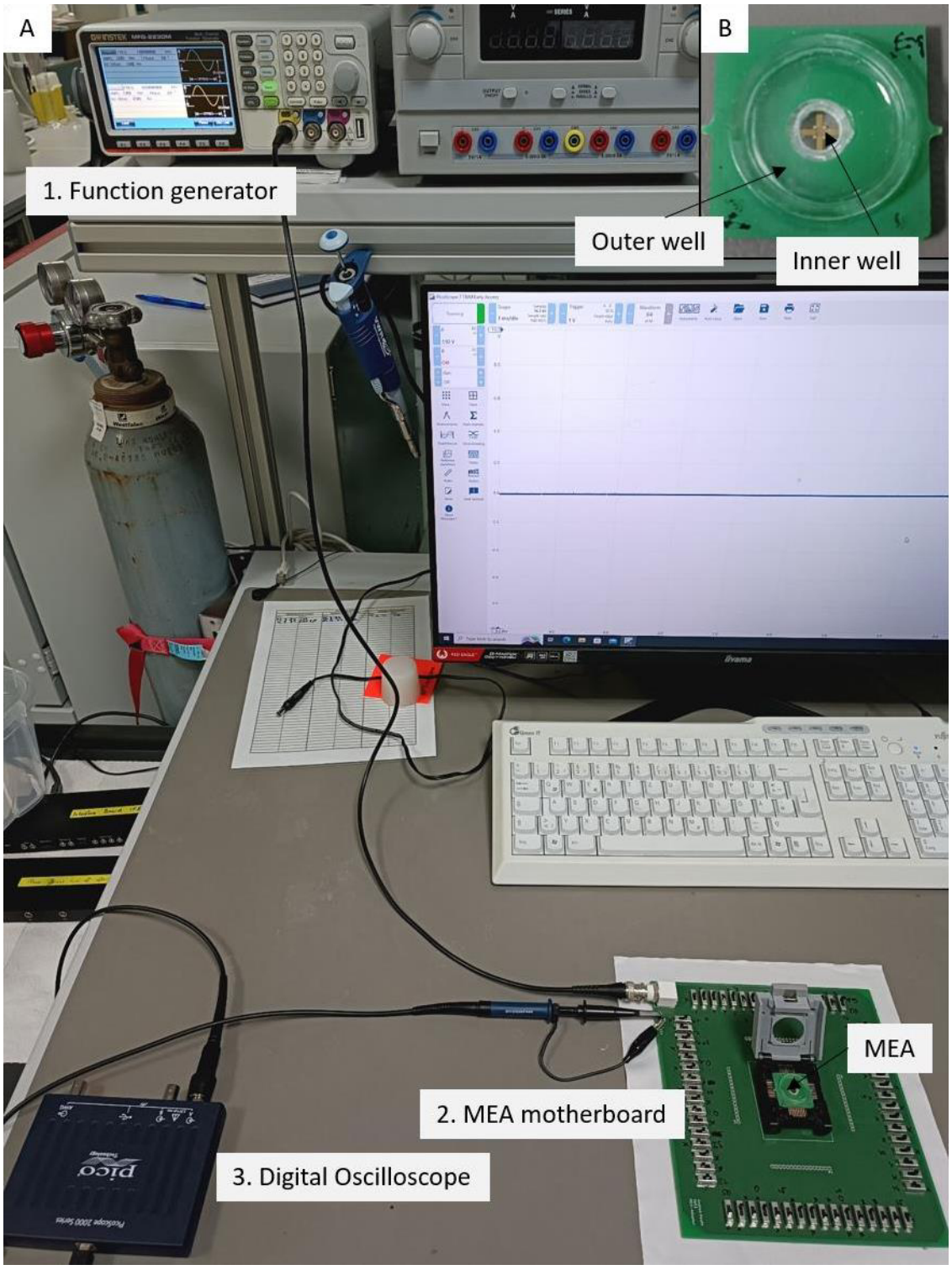


Figure 12: Installation of the MEA setup used for electroporation. (A) the multichannel function generator (1) was connected to the MEA motherboard (2) using the SYV-50-2-41 coaxial cable and was used to create the

necessary pulse. The MEA motherboard was connected to the oscilloscope (PicoScope 2208B) (3) with the TA375 cable (passive 100MHz voltage divider scope probe 1:1/10:1) and the oscilloscope was connected to the PC using the 192256A-1 USB A/B 2.0 cable (image above). The output from the oscilloscope was read using the PicoScope 7 T&M early access software using channel A on the oscilloscope and the software; **(B)** the MEA where the electroporation occurred. Transfection was performed in the inner well and fresh medium was added to the outer well after the procedure.

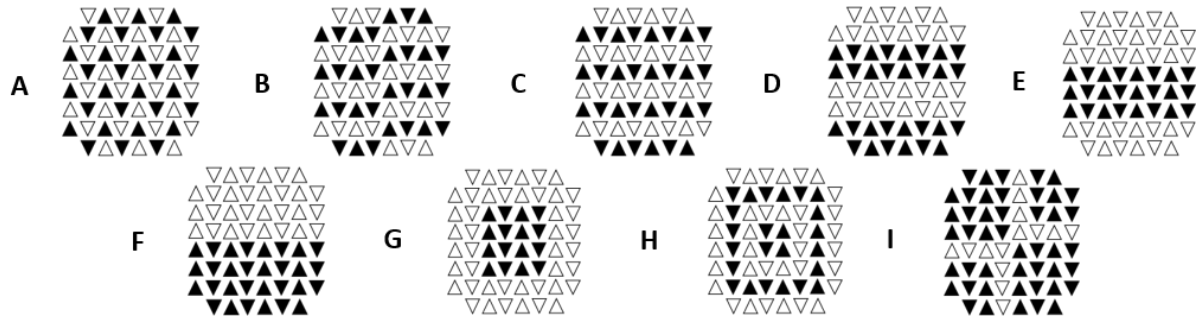


Figure 13: The different arrangements of active electrodes (white) and ground electrodes (black); (A) checkerboard arrangement; **(B)** long checkerboard arrangement; **(C)** single alternating rows; **(D)** double alternating row; **(E)** multiple alternating rows; **(F)** half arrangement; **(G)** concentric arrangement; **(H)** repeated concentric arrangement; **(I)** butterfly arrangement

3.2.5. Methods to analyse transfection efficiency

3.2.5.1. Fluorescence microscopy

The cell cultures were initially analysed for Venus-positive cells, 24 hours post-transfection, by capturing fluorescence and phase contrast images using Leica DMi8 microscope. Long term analysis of Venus-transfection was analysed by performing fluorescence microscopy a week post-transfection, followed by once every month for up to four months.

3.2.5.2. Flow cytometry analysis

The percentage of Venus-transfected cells, a week up to four months post-transfection, was analysed by flow cytometry. The wells were washed once with warm PBS after which the cells were detached with 0.05% trypsin and centrifuged at 106 rcf for 10 minutes. The pellet was washed again with PBS, reconstituted in 100 µl PBS and filtered through the cap of a 5 ml polystyrene round-bottom tube. Flow cytometry was performed using the BD FACS Canto II device.

3.2.5.3. ELISA-based protein quantification

An enzyme-linked immunosorbent assay (ELISA) was performed to analyse PEDF and BDNF secretions in culture supernatants of control and *PEDF/BDNF*-transfected A-172 cells, a week post-transfection. Cells were incubated for 24 hours in 1 ml of culture medium, from which PEDF and BDNF were quantified using the Human PEDF ELISA kit and Human Free BDNF Quantikine ELISA kit respectively according to the manufacturer's protocol (88, 143). The optical density (OD) was measured at an emission wavelength of 450 nm for both PEDF and BDNF using the SpectraMax iD3 ELISA plate reader and the results were correlated with cell number. Cells were counted manually using a haemocytometer after being trypsinized with 0.05% trypsin.

3.2.5.4. SDS-PAGE

Positive transfection in *PEDF/BDNF*-transfected samples was confirmed with an SDS PAGE and western blot, which were performed as previously described (143, 192). The stain-free analyses were performed on Mini-Protean TGX Stain-free gels. The cell culture supernatants were heated with an equal volume of 2x SDS sample buffer and separated at 80 V for two hours on a 10% acrylamide gel (PEDF) or one and a half hours on a 15% acrylamide gel (BDNF). A protein ladder served as a marker to confirm the correct molecular weights. The components required for the preparation of the gels and buffers necessary for SDS PAGE are listed below.

Separating gel buffer	Tris	0.75 M
	SDS	0.007 M
	HCL	until pH 8.8
Stacking gel buffer	Tris	0.25 M
	SDS	0.007 M
	HCL	until pH 6.8
	Dissolved in distilled water	
2x SDS sample buffer	Stacking gel buffer	25%
	Glycerine (water free)	2.17 M
	SDS	0.138 M
	2-mercaptoethanol	0.25 M
	Bromophenol blue	on spatula tip
	Dissolved in distilled water	
SDS PAGE running buffer	Tris	0.25 M

glycine	1.92 M
SDS	0.034 M
Dissolved in distilled water	

		10% Separating gel	**15% Separating gel**	**Stacking gel**
SDS gel	Separating gel buffer	2.5 ml	2.5 ml	-
	Stacking gel buffer	-	-	1.25 ml
	Acrylamide 30%	3.3 ml	5 ml	0.75 ml
	APS 10%	50 µl	50 µl	50 µl
	Temed	8 µl	8 µl	10 µl
	Water	4.2 ml	2.5 ml	3 ml

3.2.5.5. Western blot

Following SDS PAGE, the proteins from the gels were transferred to nitrocellulose membranes with a pore size of 0.45 µm, using a semi-dry electroblotting technique. The blots were first washed for 10 minutes in 1x tris-buffered saline (TBS) buffer and were then blocked with 3% BSA/1x TBS for one hour at RT. The blocked blots were washed twice in 1x TBS-Tween/Triton buffer for 10 minutes and once in 1x TBS buffer for 10 minutes. This was followed by the incubation of the blots in the respective primary antibodies overnight. For PEDF analysis, a rabbit polyclonal anti-PEDF antibody (1:4000 in 3% BSA/TBS) was used and for BDNF, a rabbit polyclonal anti-BDNF antibody (1:500 in 3% BSA/TBS) was used. After incubation, the blots were again washed twice in 1x TBS-Tween/Triton buffer for 10 minutes and once in 1x TBS for 10 minutes. This was followed by the treatment with the secondary antibody for one hour at RT (goat polyclonal anti-rabbit IgG H+L (HRP), 1:2000, in 10% milk powder/1x TBS buffer). The blots were then washed four times in 1x TBS-Tween/Triton buffer. The membranes were transferred to an electrochemiluminescent solution. Immediately before protein band detection, 6 µl 30% H_2O_2 was added to the membranes. The components required for the preparation of buffers and solutions are listed below. The bands were visualized by chemiluminescence using the ChemiDoc MP Imaging System.

TBS buffer	Tris	0.2 M
	NaCl	1.37 M
	Dissolved in distilled water (pH 7.6)	
TBS Tween/Triton buffer	Tween-20	0.001 M
	Triton X-100	0.0008 M
	dissolved in 1x TBS	
Anode buffer	Tris	0.299 M
	Tricine	0.099 M
	Dissolved in distilled water	
Cathode buffer	Tris	0.029 M
	6-aminohexanoic acid	0.299 M
	Dissolved in distilled water	
Luminol solution	Luminol	0.248 M
	Dissolved in DMSO	
p-coumaric acid solution	p-coumaric acid	0.09 M
	Dissolved in DMSO	
Electrochemiluminescent	Tris	0.1 M, 20 ml
solution	Luminol solution	100 µl
	p-coumaric acid solution	100 µl

3.2.5.6. Quantitative real-time PCR

Using quantitative real-time polymerase chain reaction (RT qPCR), expression levels of *PEDF* and *BDNF* were analysed. Total RNA was isolated using the RNeasy mini kit together with the RNase-free DNase set according to the protocol of the manufacturer. Reverse transcription was carried out on 1 µg total RNA using the reverse transcription system. All real-time PCR reactions were performed on CFX Opus 96 using the iTaq Universal SYBR Green Supermix according to the manufacturer's instructions.

For quantification of mRNA expression levels, cDNA samples of transfected and non-transfected A-172 cells were run twice alongside the internal control gene *GAPDH*. Reactions were performed with diluted cDNA, corresponding to 2 ng of initially used total RNA, and a primer concentration of 0.25 µM, with the primers listed in table 9.

Table 9: Primers utilized in RT qPCR

Primer	Sequence
GAPDH forward	5'-ATC CCA TCA CCA TCT TCC AG-3'
GAPDH reverse	5'-ATG AGT CCT TCC ACG ATA CC-3'
PEDFcod4 forward	5'-TAG ACC GAG AAC TGA AGA CCG-3'
PEDFcod4 reverse	5'-TGT GTC TGT GTC CCT CAG TAC-3'
endBDNF forward	5′-CTT CTT GTG TAT GTA CAT TGA CC-3′
endBDNF reverse	5′-CTT AAC TGA ATA ATT TAC CCT GTT ATG-3′

Thermal cycler conditions were used as given in table 10. The PCR was run for 50 cycles (*PEDF*) or 45 cycles (*BDNF*). Data were processed using the CFX Maestro software and analyzed using the comparative CT ($2^{-\Delta\Delta CT}$) method, which described relative gene expression.

Table 10: Thermal cycler conditions applied for RT qPCR

Step	Temperature	Time	Cycles
Denaturation	95 ºC	30 s	-
Denaturation	95 ºC	10 s	
Annealing	61 ºC	20 s	x 45/ 50 cycles
Elongation	72 ºC	30 s	
Elongation	72 ºC	60 s	-
Cooling	4 ºC	-	-

3.2.6. Methods to analyse transfected cells

3.2.6.1. Cell viability assay

Cell viability was measured with the CellTitreGlo kit according to the manufacturer's recommendations. Following transfection in suspension, the A-172 cells were seeded onto a 48-well plate and the cells were washed with PBS, 24 hours later. The contents of the kit were mixed and 100 µl of this mixture was added to each well, along with an equal volume of fresh medium. The plate was shaken at 1000 rpm for a couple of minutes to rupture the cells, following which the plate was kept at rest for 10 minutes. The contents of the plate were then

transferred to a 96-well plate and the OD was analysed with an emission wavelength of 560 nm, using the SpectraMax iD3 ELISA plate reader.

3.2.6.2. Immunocytochemical analysis

Purity of primary Müller cell cultures was verified by performing an immunocytochemical analysis on cells maintained in culture for one to two weeks. The cells were gently washed thrice with warm PBS. Samples were incubated for 10 minutes in 4% PFA, followed by three washes with PBS and a 10 minute incubation in 0.1% Triton X-100. Primary antibody solution for non-transfected test samples was prepared with 1:200 mouse monoclonal anti-human glutamine synthetase (GS) antibody, 1:200 chicken polyclonal anti-human GFAP antibody and 1:200 rabbit monoclonal recombinant anti-vimentin antibody dissolved in 5% BSA/PBS, while the primary antibody solution for transfected test samples lacked anti-vimentin antibody. The cells were washed thrice with PBS and the test samples were incubated with the primary antibody solution in the dark at RT (overnight), while the control samples were incubated in 5% BSA/PBS without primary antibodies. The next day the samples were washed thrice in PBS, followed by a one hour incubation of both control and test samples in the secondary antibody solution which was prepared for the non-transfected test samples with 1:200 donkey polyclonal anti-mouse IgG H+L - Cy3, 1:200 goat polyclonal anti-chicken IgY Fc fragment - Alexa Fluor 647, 1:200 goat polyclonal anti-rabbit IgG H+L Alexa Fluor 488 and 1:500 DAPI dissolved in 5% BSA/PBS, and for the transfected test samples, without anti-rabbit IgG. Finally, the samples were washed thrice with PBS. Since Neon transfection experiments were carried out with primary cells cultured on chamber glass slides, the walls of the chamber were removed following immunological staining. The fixed samples were protected with a rectangular coverslip using a drop of Immu-Mount mounting medium and analysed with the Leica DMi8 inverted microscope. Immunocytochemistry for NEPA-transfected samples was performed directly on the 24-well plates where the cells were transfected and a circular 13 mm coverslip was used instead. The samples were analysed in this case, with the Leica DMI4000 B microscope.

3.2.6.3. Cell size/shape comparison

The effects of cell size, shape and geometry on transfection were studied by analysing images of transfected and non-transfected cells in suspension and on a surface from the cell lines ARPE-19, A-172 and R28 using the Cell Profiler 4.2.6 software, which allowed for comparison of area and eccentricity of cells. The appearance of cells in suspension was emulated as closely

as possible by imaging ARPE-19 and A-172 cells following passaging, immediately after the cells had settled at the bottom of the flask, ensuring that most of the cells were spherical but also on the same plane. Imaging was performed 24 hours post-transfection in the case of ARPE-19 and R28 cells and also a week post-transfection in the case of A-172 cells. Images of cells immediately after seeding were analysed with a simpler software pipeline compared to cells cultured on a surface, which additionally required manual editing of the cells (Figure 14).

Regarding editing, the raw image was first inverted and a $\log_2$ transformation was applied to the inverted image using the Invert Math function. The borders of the log transformed image were enhanced using Enhance Edges function. This image was then used to identify primary objects. Since the identified objects did not correspond to cells accurately, manual editing was used wherever necessary. The mean cell areas were compared using the corresponding CV values, while the eccentricity was measured directly using the mean *e* for each image.

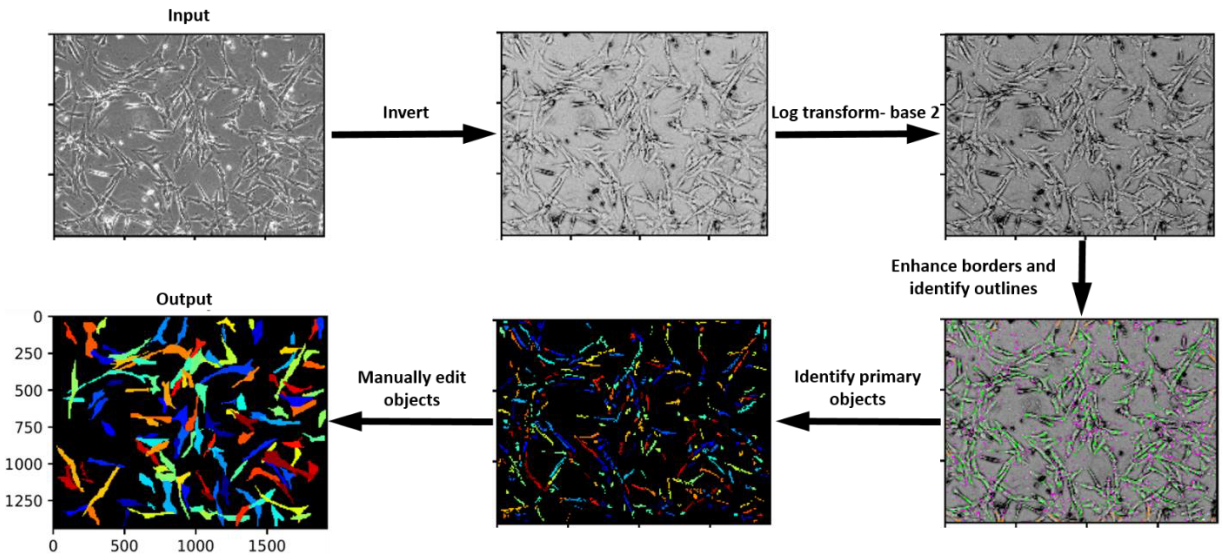


Figure 14: The basic pipeline for measuring cell properties from images of cells cultured on a surface with the aid of the Cell Profiler 4.2.6 software.

3.2.7. Statistical analysis

The results were displayed as a box and whisker plot, where the central line in the box indicates the median and the spot indicates the mean, while the magnitude of standard deviation is indicated by the width of the plot. First, the homoscedasticity of the data was tested with the Brown-Forsythe test and the normality of the data was confirmed with the Shapiro-Wilk normality test. For statistical analysis and graphical visualization of data, a one-way analysis

of variance (ANOVA), followed by a Dunnet's post hoc test (when comparing all the test samples against the control) or a Tukay's post-hoc test (when comparing every test sample against every other sample), was performed using GrpahPad Prism 10. When the data was confirmed to be non-normally distributed, the Kruskal-Wallis non-parametric test was performed paired with Dunn's multiple comparison. Unless otherwise specified, values are indicated as mean ± standard deviation to indicate the precision of the compared means and to allow an easy estimation of the confidence intervals and thus the significance of the collected data. The symbols and significance levels for all statistical tests are as follows: $*p \leq 0.05$, $**p \leq 0.01$, $***p \leq 0.001$ and $**** p \leq 0.0001$. The exact conditions of the analyses performed and the dependent variables used are specified in the legend of each relevant figure.

4. Results

4.1. Transfection of A-172 cells in suspension

4.1.1. Transfections with the fluorescent reporter *Venus*

The Neon Transfection System, which allows the transfection of cells in suspension, had already been well established within our working group, making it an ideal device to measure the genetic modifiability of a cell line. The glioblastoma cell line A-172 was chosen for initial experiments because of its glial origin. The cells were transfected with the gene encoding *YFP* (*Venus*) using the *SB* transposon system. Sixteen different arrangements of voltage, pulse number and pulse width were tested, ranging from 1000 - 1350 V for the voltage, 20 - 30 ms for the pulse width and 1 - 3 for the pulse number. Fluorescence microscopy images of transfected cells captured 24 hours post-transfection (Figure 15) indicated that four of the tested conditions - 1000 V, 30 ms, 3 pulses; 1100 V, 30 ms, 2 pulses; 1150 V, 30 ms, 2 pulses and 1200 V, 25 ms, 2 pulses, demonstrated the most promising outcomes. In order to confirm these observations, a flow cytometry analysis was performed six days post-transfection (Figure 16). The highest possible transfection efficiency, 62.4%, was observed at 1100 V, 30 ms, 2 pulses, with a mean efficiency of 33.0 ± 15.2% (Figure 16, setting 5), while the highest mean transfection efficiency of 37.2 ± 22.5% was observed with 1100 V, 30 ms, 3 pulses (setting 6). On the other hand, the lowest mean transfection efficiency, 5.67 ± 3.77%, was observed with 1100 V, 20 ms, 2 pulses (setting 3), a setting which was then compared against every other setting with an ordinary one-way ANOVA. The highest difference in significance was observed with settings 5, 6, 8 and 2, followed by settings 9, 11 and 13. Increasing the pulse number or width led to an increase in the transfection efficiency combined with a decrease in cell viability, as long as the voltage was kept constant (Figure 16, 17). The transfection efficiency increase was observed across different voltages as well, as long as the pulse width and number were kept constant. Nevertheless, the latter case was only true until 1150 V (Figure 17), beyond which, no such pattern could be observed.

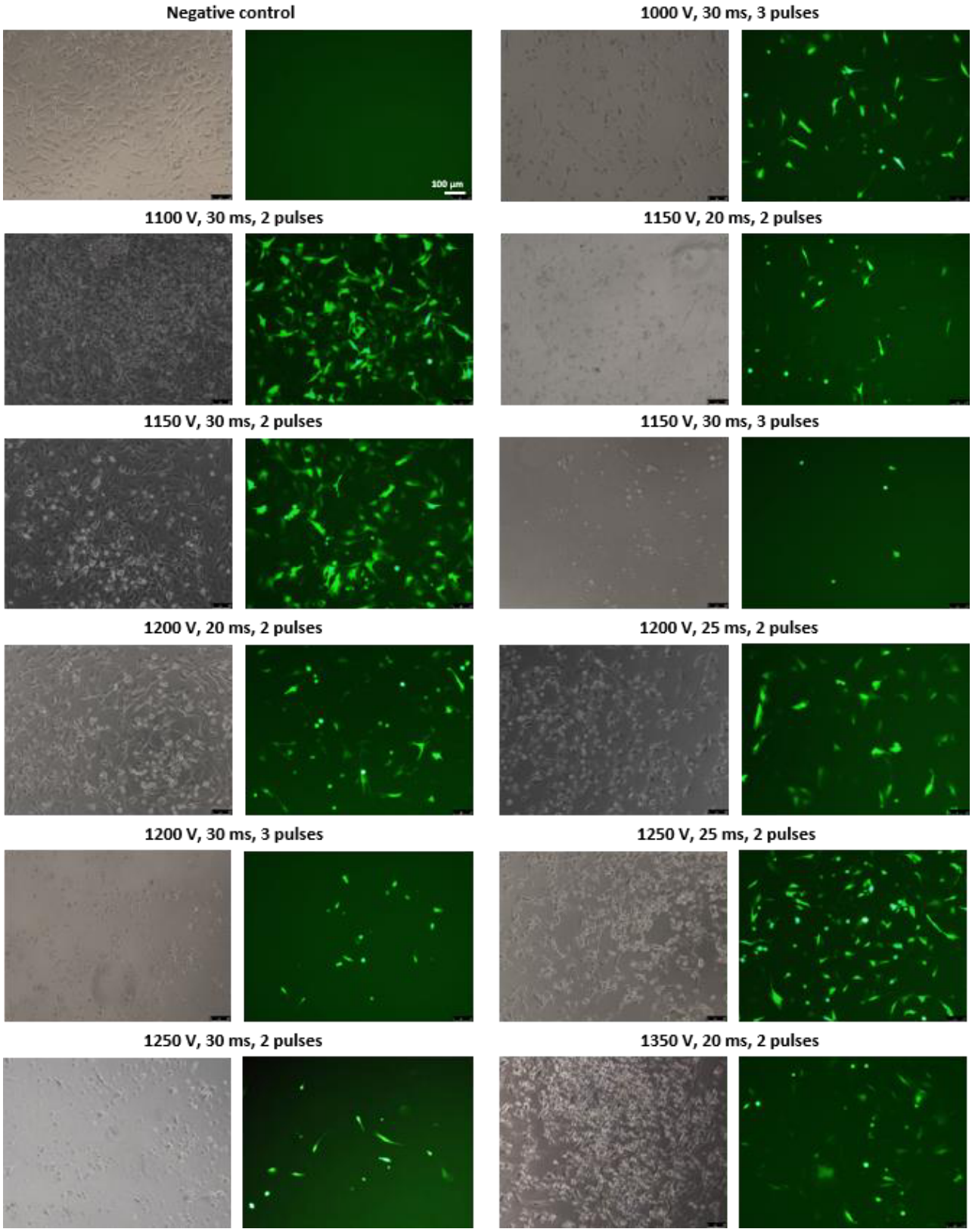


Figure 15: The *Venus*-positive A-172 cells, transfected in suspension using the Neon Transfection System, as observed 24 hours post-transfection. The panels on the left show the phase contrast images and the panels on the right show the fluorescence images of the respective setting used for transfection.

Cell viability achieved post-transfection was measured with a luminescence assay, performed 24 hours post-transfection (Figure 17). Luminescence (cell viability) for most settings was under 1 x 10^6 Relative Light Units (RLU), half the viability observed with the non-transfected control. The highest cell viability post-transfection was observed with setting 3 (1.87 ± 0.2 x 10^6 RLU), which also displayed the lowest transfection efficiency, while the lowest viability (5.6 ± 3.25 x 10^4 RLU) was observed with 1200 V, 30 ms, 3 pulses. When compared to setting 3, settings 5, 8 and 11 were chosen due to their significant transfection efficiencies (Figure 16), while setting 6 was dropped since it displayed a low cell viability (Figure 17). In conclusion, a high mean efficiency of 35.5 ± 13.9%, coupled with a good cell viability of 5.86 ± 1.63 x 10^5 RLU was detected with 1150 V, 30 ms, 2 pulses (setting 8), making it the ideal option from amongst the four chosen settings.

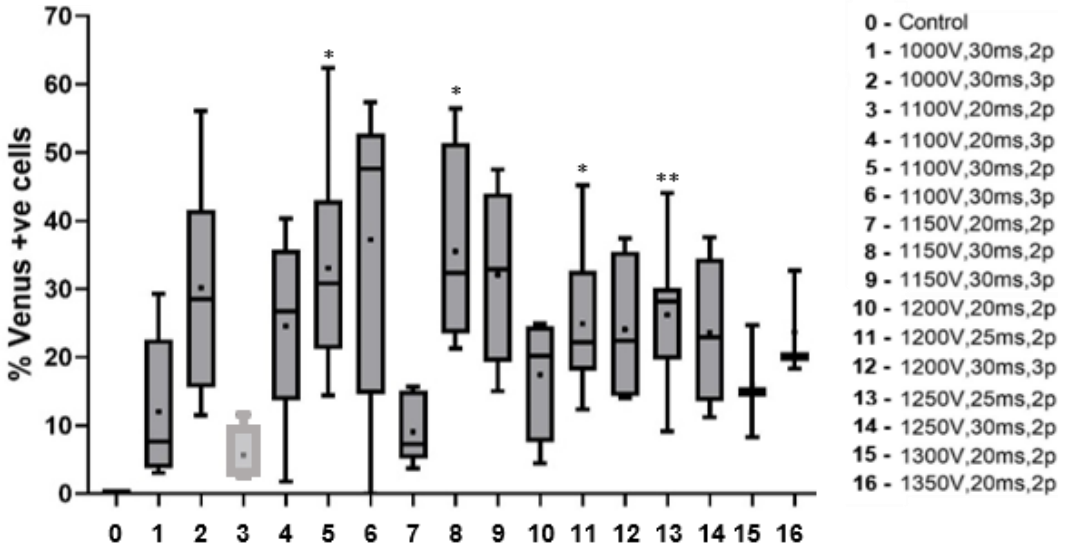


Figure 16: Flow cytometry analysis of *Venus*-transfected A-172 cell cultures, six days post-transfection. The graph shows the transfection efficiency (measured by flow cytometry) of the different settings, six days post-transfection; statistical analysis: all settings have been compared against 1100 V, 20 ms, 2 pulses setting (light grey), using the Kruskal-Wallis non parametric test with the Dunn's multiple comparison, n = 2-13; $p \geq 0.05$ (ns), $p < 0.05$ (*), p = 0.0076 (**).

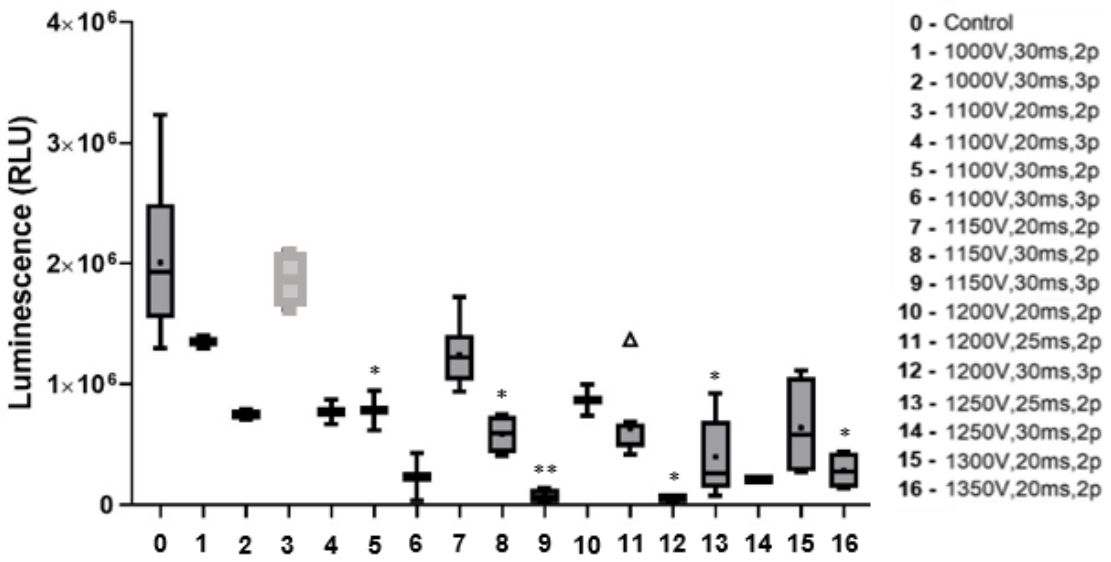


Figure 17: Luciferase-based cell viability analysis of *Venus*-transfected A-172 cell culture, 24 hours post-transfection. The graph shows cell viability measured 24 hours post-transfection using a luciferase assay. The triangle symbol over the bar for 1200 V, 25 ms, 2 pulses represents an outlier; statistical analysis: all settings have been compared against 1100 V, 20 ms, 2 pulses setting (light grey), using the Kruskal-Wallis non parametric test with the Dunn's multiple comparison, n = 2-13; $p \geq 0.05$ (ns), $p < 0.05$ (*), $p = 0.0020$ (**).

4.1.1.1. Long term analysis of transfection efficiency

Stability of transfection achieved with A-172 cells in suspension was studied with a long term analysis conducted over a period of four months. Transfections with *Venus* were performed using the four settings chosen from the initial study. The transfected cells were maintained in culture and analyzed with a flow cytometry analysis initially conducted six days post-transfection and then on every fourth subsequent week. Fluorescent images, recorded during each analysis, showed that the population of transfected cells reduced over time. The transfected cell population, which initially showed a high degree of variability in its fluorescence intensity, gradually became uniform in fluorescence (Figure 18, yellow and orange arrows). Over time, most of the transfected cells localized into densely populated clumps, with non-transfected cells being focused in the areas outside the cell-clumps (Figure 18, white arrows). Additionally, the cells looked progressively thin with an increased rate of blebbing.

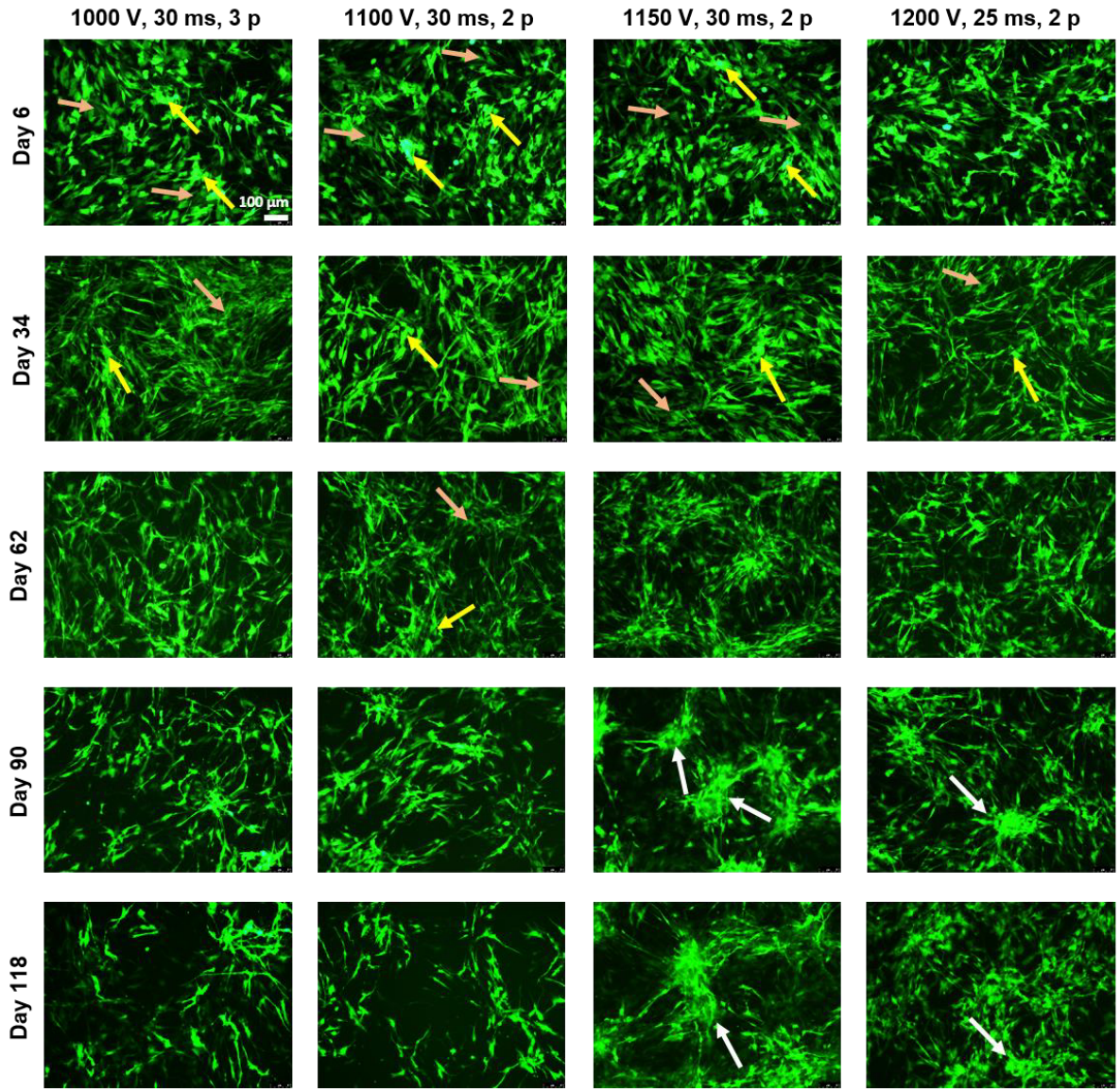


Figure 18: Fluorescence images of *Venus*-expressing A-172 cells, transfected with the four optimal settings and recorded over four months (10x). The yellow arrows indicate the cells with the highest fluorescence while the orange arrows indicate the cells displaying moderate to low fluorescence. Clumps of transfected cells are indicated with white arrows.

The fluorescence microscopy images were compared with the results from the flow cytometry analysis. It was confirmed that the transfection efficiency decreases with time (Figure 19). The mean transfection efficiency achieved using 1150 V, 30 ms, 2 pulses, was 44.2 ± 10% on day six and 14.1 ± 17.3% on day 118. In comparison, the remaining settings had consistently lower mean efficiencies of 32.02 ± 11.9% and 8.60 ± 6.88% for 1000 V, 33.9 ± 8.87% and 2.03 ± 1.01% for 1100 V and 32.2 ± 9.2% and 6.60 ± 7.79% for 1200 V on day six and 118 respectively. A Shapiro-Wilk test indicated that the data was normally distributed. An ordinary one-way ANOVA, performed in between efficiencies measured on different days of every

setting, indicated 1100 V to have a significant drop in efficiency from day 90 onwards, when compared to the efficiency observed on day six. In contrast, the first significant drop in efficiency in the case of both 1150 V and 1200 V was observed at day 62. Nevertheless, 1100 V displayed the lowest mean efficiency on day 118 compared to all the other settings. In conclusion, 1150 V was selected as the optimal approach to *Venus* transfection of A-172 cells in suspension, based on both the initial and final transfection efficiencies achieved.

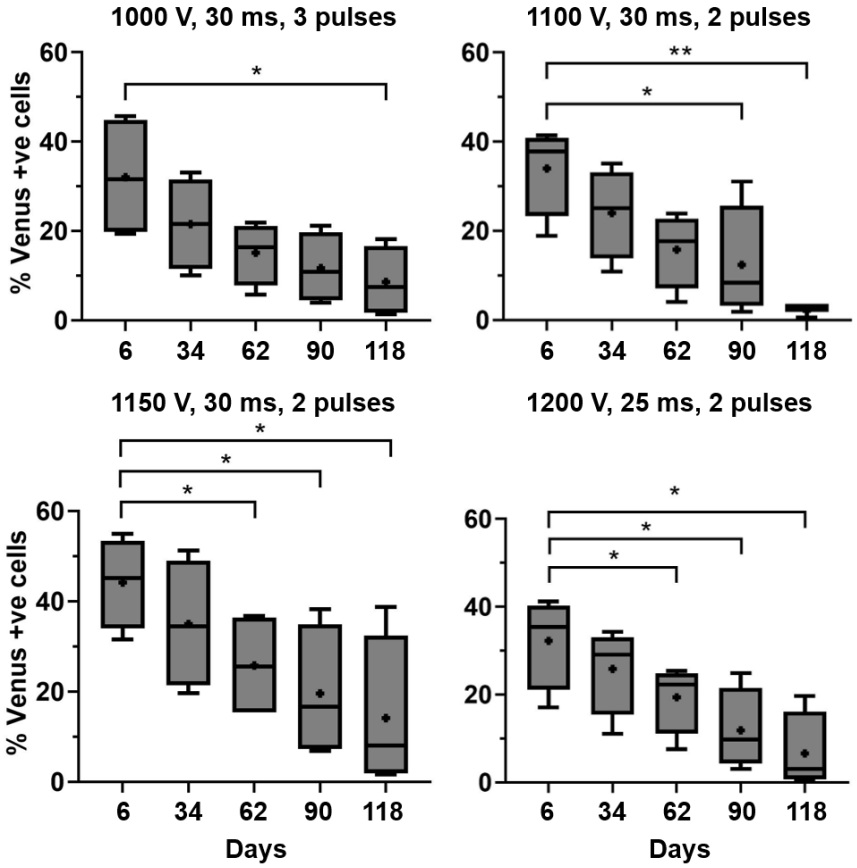


Figure 19: Long term analysis of *Venus* transfected A-172 cells, studied over a period of four months. Plot of long-term transfection efficiencies observed post-transfection of cells with the four settings chosen from the initial experiments; statistical analysis: data passed the Brown-Forsythe test for homoscedasticity ($p \geq 0.05$ (ns)) and the Shapiro-Wilk normality test ($p \geq 0.05$ (ns), except 1150 V, 62 days where $p = 0.0495$ (*)). The % Venus +ve cells, achieved on days 34, 62, 90 and 118 have been compared against day 6 using an ordinary one-way ANOVA with the Dunnet's post-hoc test, $n = 4$ for all samples, except 1200 V, day 118 ($n = 3$); $p \geq 0.05$ (ns), $p < 0.05$ (*), $p = 0.0057$ (**).

4.1.2. Transfections with *PEDF*

PEDF has antiangiogenic and neurotrophic properties that make it an attractive candidate protein for additive gene therapy. The A-172 cell line was transfected with *PEDF* and analysed further to determine the protein yield and overall transfection efficiency. An initial western blot, six days post-transfection and 24 hours after medium change, allowed a qualitative observation of a successful transfection (Figure 20 A). A more quantitative analysis of the western blot gels was achieved by measuring the mean band areas of the different setups used over multiple experiments (Figure 20 B) and correlating them directly with rate of protein production. The highest mean band area of 1.58 ± 0.24 pixel^2 was observed with 1200 V while 1150 V and 1100 V showed the next best results of 1.51 ± 0.35 pixel^2 and 1.50 ± 0.22 pixel^2 respectively. When compared to the control with an ordinary one-way ANOVA, 1150 and 1200 V displayed a significant increase in band area.

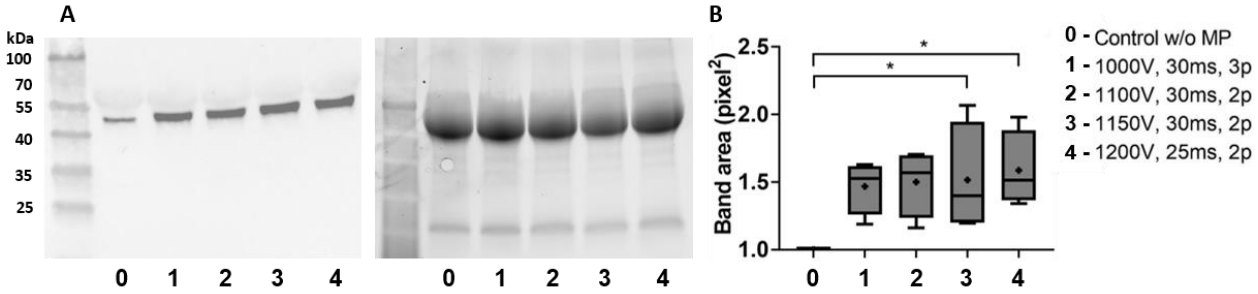


Figure 20: SDS PAGE and western blot of supernatant from A-172 cells transfected with *PEDF* using the Neon Transfection System six days post-transfection. **(A)** left panel: western blot analysis of the transfected samples with anti-PEDF antibodies, compared to the non-transfected control; right panel: detection of uniform sample application using a stain-free gel; **(B)** analysis of the intensity of the western blot bands. The experimental values were normalized to the corresponding control group to account for baseline variability; statistical analysis: data passed the Brown-Forsythe test for homoscedasticity ($p = 0.1549$ (ns)) and the Shapiro-Wilk normality test ($p \geq 0.05$ (ns)). All settings have been compared against the control using an ordinary one-way ANOVA with the Dunnet's post-hoc test, $n = 4$; $p \geq 0.05$ (ns), $p < 0.05$ (*).

An ELISA was performed to allow a quantitative determination of the PEDF yield (Figure 21). Transfection led to an increase in protein yield of 20.52 (1000 V), 14.38 (1100 V), 3.23 (1150 V) and 7.00 (1200 V) times the mean control PEDF yield. As voltage was increased from 1000 to 1150 V, the mean protein yield decreased from 1.09 ± 1.42 x 10^3 pg/h/10^4 cells to one sixth the yield, at 0.17 ± 0.05 x 10^3 pg/h/10^4 cells. The second highest protein yield of 0.76 ± 0.8 x 10^3 pg/h/10^4 cells was achieved with 1100 V These results were in contradiction

to what was observed with the western blot, where 1000 V yielded the lowest band intensity. However, none of the observed increases in protein yield were statistically significant compared to the control.

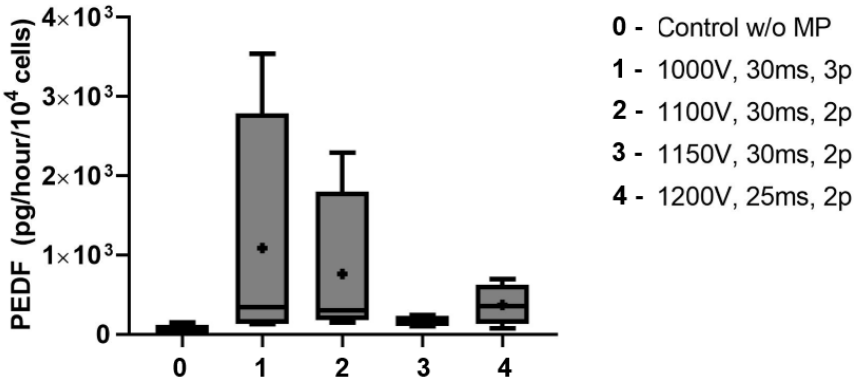


Figure 21: ELISA based analysis of PEDF protein secretion from A-172 cells transfected using the Neon Transfection System, six days post-transfection. The protein concentration is displayed in pg/h/10^4 cells; statistical analysis: data passed the Brown-Forsythe test for homoscedasticity ($p = 0.4628$ (ns)) and the Shapiro-Wilk normality test ($p \geq 0.05$ (ns), except 1000 and 1100 V where $p < 0.05$ (*)). All settings have been compared against the control using an ordinary one-way ANOVA with the Dunnet's post-hoc test, $n = 4$; $p \geq 0.05$ (ns)

An RT qPCR was performed to quantify the gene expression rates of *PEDF* (Figure 22) and the 2ΔCt method was used for analysis. The highest 2ΔCt ratio of $3.90 \pm 1.79 \times 10^3$, was observed with 1150 V, indicating the highest *PEDF* expression with this setting. This was followed closely by 1200 V, with a ratio of $3.46 \pm 3.2 \times 10^3$. The results with the two remaining settings were in agreement with the western blot analysis, with 1000 V showing the lowest ratio ($2.12 \pm 0.57 \times 10^3$). However, as seen from an ordinary one-way ANOVA, none of the observed increases in gene expression were statistically significant compared to the control. A comparison of western blot and RT qPCR results demonstrated the best voltage range for *PEDF* transfection to be 1150 - 1200 V.

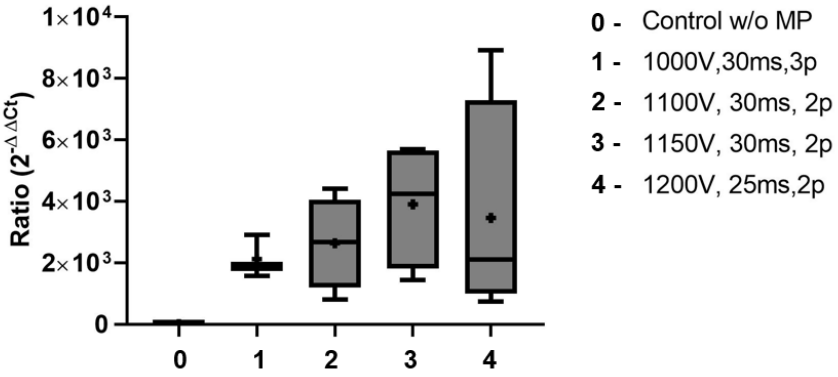


Figure 22: Expression analysis of *PEDF* gene measured by real-time quantitative PCR, six days post transfection of the A-172 cells with the Neon Transfection System. A high ratio indicates a high gene expression. The experimental values were normalized to the corresponding control group to account for baseline variability; statistical analysis: data passed the Brown-Forsythe test for homoscedasticity ($p = 0.3206$ (ns)) and the Shapiro-Wilk normality test ($p \geq 0.05$ (ns)). All settings have been compared against the control using an ordinary one-way ANOVA with the Dunnet's post-hoc test; $n = 4$ for all samples except 1000 V ($n = 3$); $p \geq 0.05$ (ns).

4.1.3. Transfections with *BDNF*

BDNF is a potent neuroprotective agent and is important for synaptic plasticity. This makes it another excellent candidate for additive gene therapy. The A-172 cell line was transfected with *BDNF* and analysed to determine the protein yield and overall transfection efficiency. The initial western blot gel image (Figure 23 A), indicated 1000 V to be the setting with the most BDNF expression. However, band-area analysis conducted over multiple blots, showed a similar mean band area for all settings, with a minimum mean band area of 80.9 ± 60.9 pixel^2 with 1000 V and a maximum mean area of 89.6 ± 83.1 pixel^2 observed with 1100 V (Figure 23 B). The second highest mean area was observed with 1150 V (89.3 ± 74.1 pixel^2). As seen from an ordinary one-way ANOVA, none of the observed increases in band area were statistically significant compared to the control.

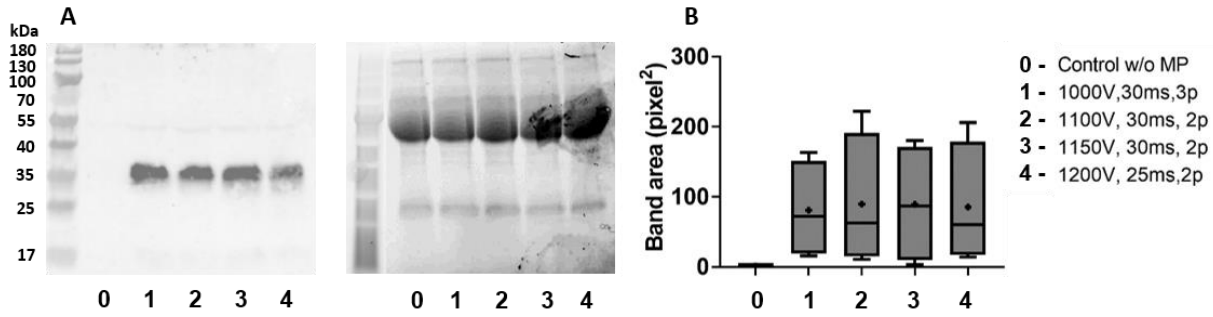


Figure 23: SDS PAGE and western blot of supernatant from A-172 cells transfected with *BDNF* using the Neon Transfection System, six days post-transfection. **(A)** left panel: western blot analysis of the transfected samples with anti-BDNF antibodies, compared to the non-transfected control; right panel: detection of uniform sample application using a stain-free gel **(B)** quantitative analysis of western blot band areas. The experimental values were normalized to the corresponding control group to account for baseline variability; statistical analysis: data passed the Brown-Forsythe test for homoscedasticity ($p = 0.0866$ (ns)) and the Shapiro-Wilk normality test ($p \geq 0.05$ (ns)). All settings have been compared against the control using an ordinary one-way ANOVA with the Dunnet's post-hoc test, $n = 4$; $p \geq 0.05$ (ns).

Quantitative BDNF expression was analysed with an ELISA (Figure 24). Transfection led to an increase in protein yield of 142.9 (1000 V), 199.2 (1100 V), 156.4 (1150 V) and 100.9 (1200 V) times the mean control BDNF yield. The highest mean BDNF yield (71.7 ± 56.4 pg/h/10^4 cells) was observed with 1100 V. An ordinary one-way ANOVA showed that the increase in protein yield achieved with 1100 V was statistically significant compared to the control. The second highest yield of 56.3 ± 19.7 pg/h/10^4 cells was observed with 1150 V. In general, the BDNF ELISA results were consistent with the western blot gel analysis, with the only exception being 1200 V, which yielded the lowest BDNF concentration (36.3 ± 15.5 pg/h/10^4 cells). Nevertheless, total BDNF yields were low compared to PEDF yields. A comparison of ELISA results for the two proteins showed that the highest BDNF yield of 71.7 ± 56.4 pg/h/10^4 cells was 15 times lower than the highest PEDF yield of $1.09 \pm 1.42 \times 10^3$ pg/h/10^4 cells (Figure 21 and 24) .

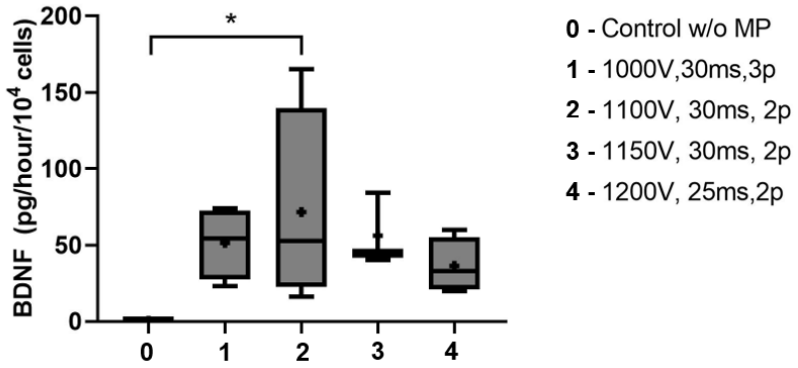


Figure 24: ELISA based analysis of BDNF protein secretion from A-172 cells transfected using the Neon Transfection System, six days post-transfection. The protein concentration is displayed in pg/h/10^4 cells; statistical analysis: data passed the Brown-Forsythe test for homoscedasticity ($p = 0.2375$ (ns)) and the Shapiro-Wilk normality test ($p \geq 0.05$ (ns)). All settings have been compared against the control using an ordinary one-way ANOVA with the Dunnet's post-hoc test, $n = 4$ for all samples except 1150 V ($n = 3$); $p \geq 0.05$ (ns), $p = 0.0356$ (*).

Finally, an RT qPCR was performed to quantify the gene expression rates of *BDNF*-transfected cells (Figure 25). Contrary to what was observed with the ELISA results, 1200 V displayed the highest mean *BDNF* expression rate, with a 2ΔCt ratio of 216.2 ± 260.5. Nevertheless, the other settings (Figure 25, settings 1, 2 and 3) followed a similar trend as the BDNF ELISA results. 1100 V yielded the second highest mean gene expression, with a 2ΔCt ratio of 187.8 ± 196.8, although as seen from an ordinary one-way ANOVA, none of the observed increases in gene expression were statistically significant compared to the control. Overall, 1100 V yielded consistently good results regarding *BDNF* transfection.

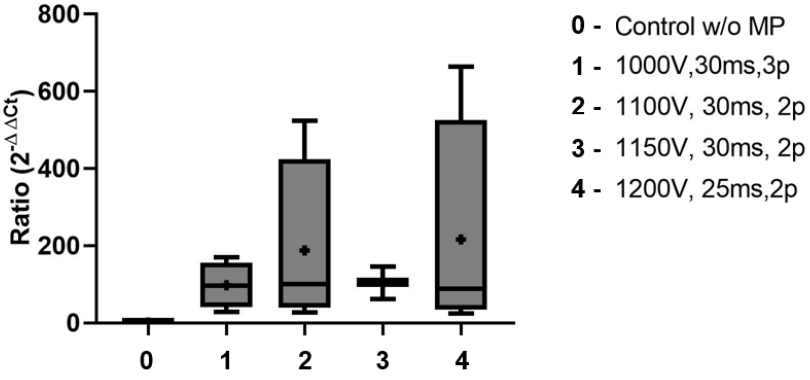


Figure 25: Expression analysis of *BDNF* gene measured by real-time quantitative PCR, six days post-transfection of the A-172 cells with the Neon Transfection System. A higher ratio indicates a higher gene expression. The experimental values were normalized to the corresponding control group to account for baseline variability; statistical analysis: data passed the Brown-Forsythe test for homoscedasticity ($p = 0.4992$ (ns)) and the Shapiro-Wilk normality test ($p \geq 0.05$ (ns), except 1200 V, where $p = 0.0288$ (*)). All settings have been

compared against the control using an ordinary one-way ANOVA with the Dunnet's post-hoc test, n = 4 for all samples, except 1200 V, where n = 3; $p \geq 0.05$ (ns).

4.1.3.1. Cell viability comparison for *PEDF*/*BDNF*-transfected cells

A preliminary cell viability assay was performed, 24 hours post-transfection, in order to gain an understanding of cell survival in response to PEDF/BDNF secretion (Figure 26). Both *PEDF* and *BDNF* transfections were performed on the same plate and so the control was the same for both samples. As expected, the luminescence value (cell viability) was maximum for the control in the case of both *PEDF* and *BDNF* transfections. Additionally, both PEDF and BDNF samples displayed a decrease in the mean luminescence with an increase in voltage until 1150 V, along with a slight increase in mean luminescence at 1200 V. The highest mean luminescence values, observed at 1000 V for *PEDF* ($1.07 \pm 0.39 \times 10^6$ RLU) and *BDNF* ($0.85 \pm 0.37 \times 10^6$ RLU) transfected samples, were, respectively, 0.567 and 0.453 times the mean control luminescence. In addition, mean luminescence values for *PEDF*-transfected samples were 1.25 (1000 V), 1.58 (1100 V), 1.20 (1150 V) and 1.15 (1200 V) times the mean luminescence values for *BDNF*-transfected samples. In conclusion, the mean PEDF luminescence value for each voltage attempted was slightly higher than the corresponding BDNF luminescence value, although an ordinary one-way ANOVA showed that this difference was not significant.

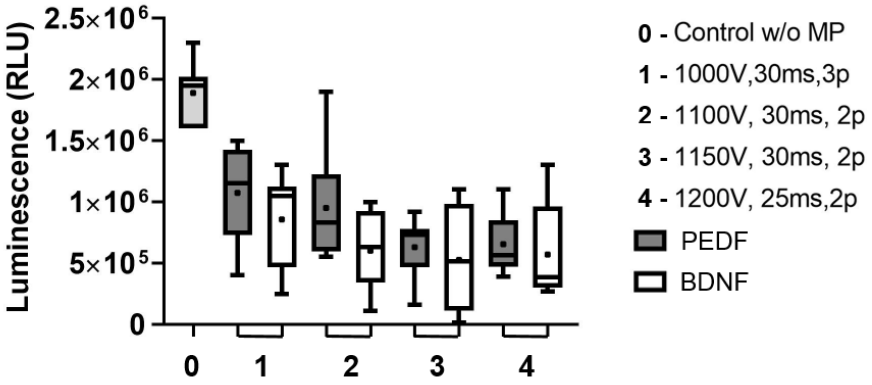


Figure 26: Comparison of cell viability of cells transfected with *PEDF* and *BDNF*, 24 hours post-transfection of the A-172 cells with the Neon Transfection System. The bars show the luminescence level of *PEDF* (dark grey) and *BDNF* (white)-transfected cells, measured with a luminescence assay. Since the control was the same in the case of both PEDF and BDNF, it is depicted in light grey; statistical analysis : data passed the Brown-Forsythe test for homoscedasticity (p = 0.6416 (ns)) and the Shapiro-Wilk normality test ($p \geq 0.05$ (ns)).

The *PEDF*-transfected sample for each voltage attempted has been compared against the corresponding *BDNF*-transfected sample using an ordinary one-way ANOVA with the Tukay's post-hoc test, n = 10; $p \geq 0.05$ (ns)

4.2. Transfection of A-172 cells cultured on a surface

4.2.1. Transfections with the fluorescent reporter *Venus*

Following transfection in suspension, the genetic modifiability of the A-172 cells cultivated on a surface was established with the NEPA-21 device. Cells, cultivated on the surface of 24-well plates for 24 hours, were transfected with the gene encoding *YFP* (*Venus*) using the *SB* transposon system. The combination of two possible electrode orientations (0º/0 + 90º) accompanied by PP and TP pulses with (±) or without polarity exchange (+), resulted in four setups: (A) PP: ±, TP ±, electrode: 0º, (B) PP: ±, TP: ±, electrode: 0 + 90º, (C) PP: ±, TP: +, electrode: 0 + 90º, and (D) PP: +, TP: ±, electrode: 0 + 90º (Figure 27 A-D). Nine different combinations of voltage and pulse width were attempted for the PP in each setup, while the TP was kept constant. Initial fluorescence microscopy, conducted 24 hours post-transfection, indicated a higher transfection rate in setups A and D (Figure 27 E), when the PP was maintained at 200 V, 5 ms. A flow cytometry analysis was conducted to quantify transfection efficiency, a week post-transfection.

Setups A, C and D displayed a similar trend, where the mean transfection efficiency rose steadily across settings 1 - 3 and then again across settings 4 - 6 (Figure 27). Among the first six settings, the highest meant transfection efficiencies of 1.30 ± 0.43% for setup A, 1.50 ± 0.5% for setup C and 2.57 ± 0.75% for setup D were observed consistently with a PP of 200 V, 5 ms (setting 6). Setup B displayed the lowest transfection efficiency across all setups. Sample collection was challenging due to the very low cell viability achieved with this setup and was not possible beyond a PP of 200 V, 5 ms.

Regarding the maximum mean transfection efficiencies achieved, setups A, C and D displayed a maximum at a PP of 200 V, 5 ms, while with setup B, a maximum efficiency of 0.6% was possible with a PP of 150 V, 2.5 ms. Additionally, the maximum efficiency of 2.57 ± 0.75% observed with setup D was the also the maximum across all four setups. A one-way ANOVA comparing every setting against every other setting in each setup, indicated no significant increase in transfection efficiency post-transfection for setups A and B. In contrast, most of the voltages higher than 200 V, 5 ms, delivered with setup D, displayed a significant difference

compared to the mean efficiency achieved with a PP of 125 V, 2.5 ms. Especially, a PP of 200 V, 5 ms delivered with setup D had a significant increase in efficiency when compared against most settings involving lower voltages. As a result, setup D was chosen for further experiments with the NEPA device. Although a high efficiency was achieved once with 275 V, 2.5 ms for both setups C and D, it was not considered due to extremely low cell viability which limited the collection of sufficient samples for flow cytometry.

The mean transfection efficiencies achieved with the NEPA device were compared with those achieved with the Neon device. The highest mean efficiency of 37.2 ± 22.5% observed with 1100 V, 30 ms, 3 pulses for the Neon device, was 14.5 times higher than the maximum observed with the NEPA device, which suggested that transfections with cells in suspension had an increased success compared to cells cultivated on a surface.

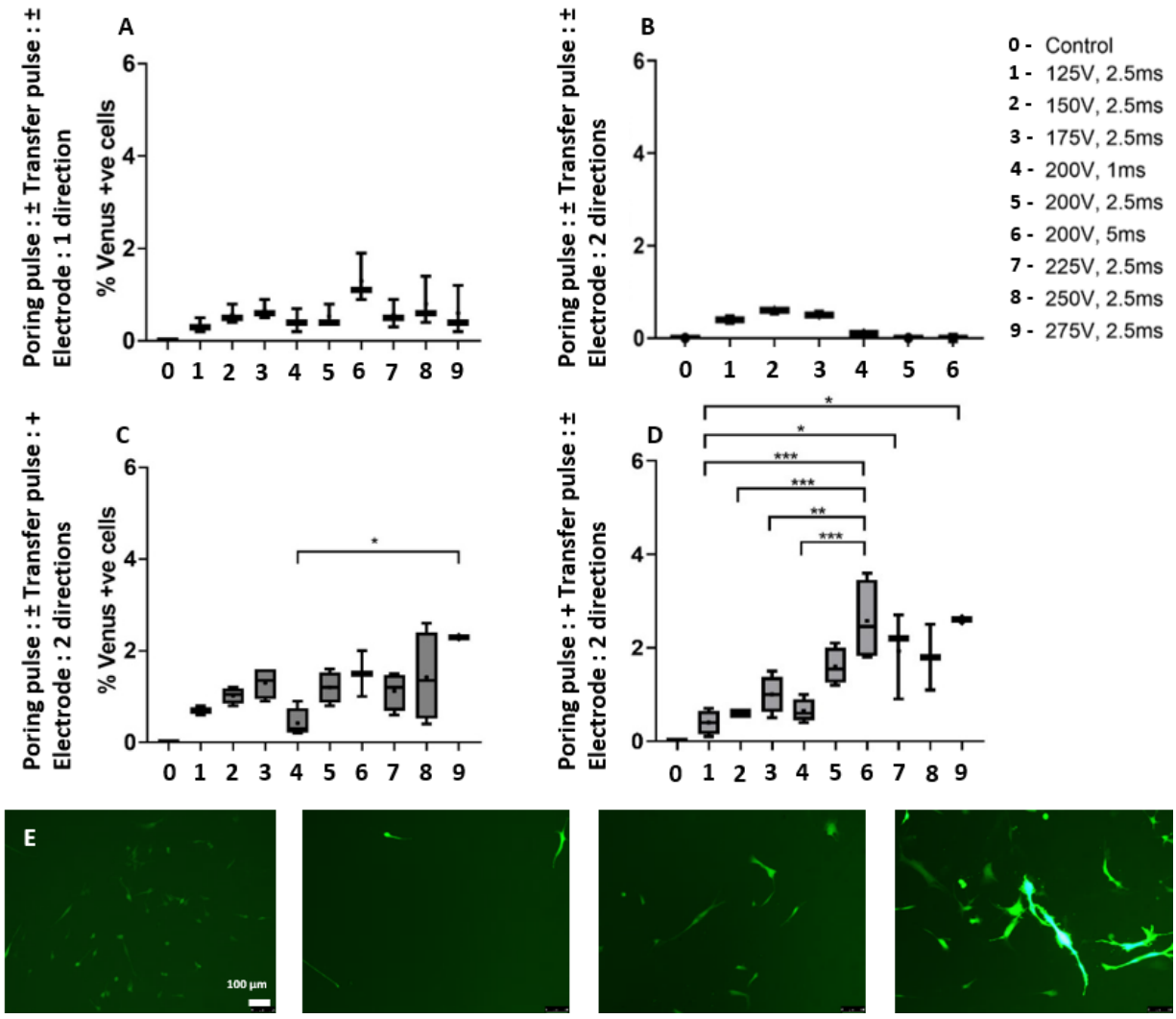


Figure 27: Flow cytometry analysis of A-172 cells transfected on a surface with *Venus* using the NEPA-21 electroporation device, seven days post-transfection. The voltages shown here refer to the PP while the TP was

maintained as constant, at 30 V, 50 ms; **(A)** transfection efficiency when both PP and TP were applied with polarity exchange, but the electrode was placed in one direction only; **(B)** transfection efficiency when PP and TP were applied with polarity exchange and the electrode was placed in both directions; **(C)** transfection efficiency when the PP was polarity exchanged and the TP was not while the electrode was placed in both directions; **(D)** transfection efficiency when the PP was not polarity exchanged, while the TP was, with the electrode being placed in both directions; statistical analysis: data could not be tested for homoscedasticity due to low sample size in some data sets, but passed the Shapiro-Wilk normality test ($p \geq 0.05$ (ns), except 200 V, 1 ms in C ($p = 0.0409$ (*)) and 150 V, 2.5 ms in D ($p = 0.0239$ (*))). All settings have been compared amongst each other using an ordinary one-way ANOVA with the Tukay's post-hoc test, n = 1-4; $p \geq 0.05$ (ns), $p < 0.05$ (*), $p = 0.0073$ (**), $p < 0.001$ (***); **(E)** fluorescence images of cells transfected with a PP of 200 V, 5 ms using the different setups, 24 hours post-transfection - far left (A), middle left (B), middle right (C) and far right (D).

4.2.2. Transfections of cells on a surface with *PEDF*

The next step in the NEPA-21 experiments was the electroporation of A-172 cells with genes for neuroprotective proteins, PEDF and BDNF. The A-172 cell line was transfected with *PEDF* using the setup chosen in the *Venus* experiments with the NEPA device (Figure 27, setup D), and analysed a week post-transfection. The initial western blot (Figure 28 A, top panel), displayed similar protein bands for all settings. Multiple gel images were analysed to measure the average band areas to gain a quantitative understanding of the settings with the highest PEDF expression (Figure 28 B). Contrary to what was observed with the *Venus* experiments, the highest transfection efficiency was no longer achieved when the PP was set to 200 V, 5 ms but rather with 125 V, 2.5 ms, which displayed a band area of 0.98 ± 0.11 pixel^2. Interestingly, the mean band areas of every setting was lesser than the corresponding control, although as seen from an ordinary one-way ANOVA, none of the settings displayed a statistically significant difference compared to the control.

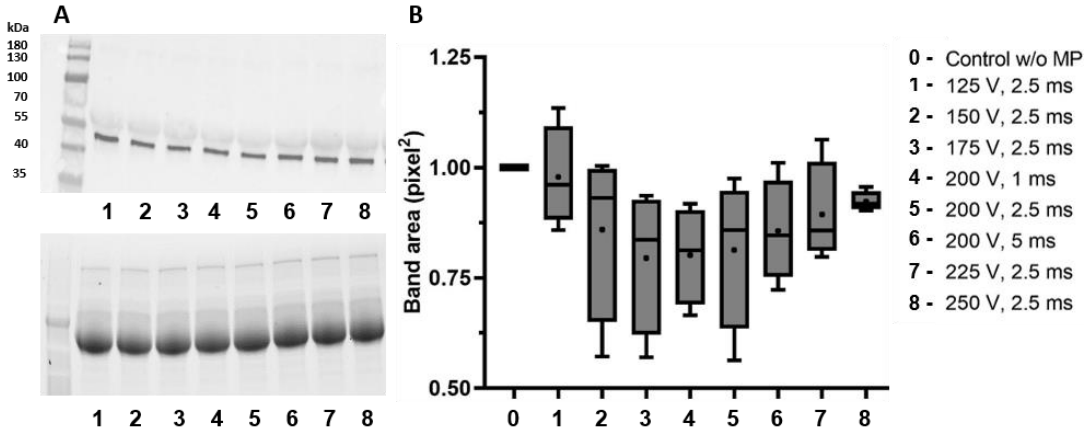


Figure 28: SDS PAGE and western blot of supernatants from A-172 cells transfected with *PEDF* using the NEPA-21 electroporation device, seven days post-transfection. The voltages shown here refer to the PP while the TP was maintained as constant, at 30 V, 50 ms; **(A)** top panel: western blot analysis of the transfected samples with anti-PEDF antibodies, compared to the non-transfected control; bottom panel: detection of uniform sample application using a stain-free gel. (negative control is not shown); **(B)** quantitative analysis of western blot band areas. The experimental values were normalized to the corresponding control group to account for baseline variability; statistical analysis: data passed the Brown-Forsythe test for homoscedasticity ($p = 0.5712$ (ns)) and the Shapiro-Wilk normality test ($p \geq 0.05$ (ns)). All settings have been compared against the control using an ordinary one-way ANOVA with the Dunnet's post-hoc test, $n = 4$; $p \geq 0.05$ (ns).

An ELISA was performed to gain a quantitative insight into the low expression levels of *PEDF*-transfected cells (Figure 29). When compared to the control, an increase in protein yield was observed post-transfection, of 12.08 (125 V, 2.5 ms), 14.87 (150 V, 2.5 ms), 20.04 (175 V, 2.5 ms), 14.16 (200 V, 1 ms), 4.76 (200 V, 2.5 ms), 10.90 (200 V, 5 ms), 13.79 (225 V, 2.5 ms) and 21.01 (250 V, 2.5 ms) times the mean control PEDF yield. The highest mean protein levels were achieved when the PP was set to 250 V, 2.5 ms with 68.9 ± 26.6 pg/h/10^4 cells and at 175 V, 2.5 ms with 65.7 ± 44.8 pg/h/10^4 cells. When the cells were transfected with *PEDF* using the setting (200 V, 5 ms) that gave the best results with the *Venus* transfections, the resulting mean PEDF yield was an average 35.76 ± 35.09 pg/h/10^4 cells. The lowest mean PEDF yield was achieved at 200 V, 2.5 ms, with 15.6 ± 14.6 pg/h/10^4 cells. Overall, 175 and 250 V showed the highest significance in protein yield when compared to the control with the Kruskal-Wallis test.

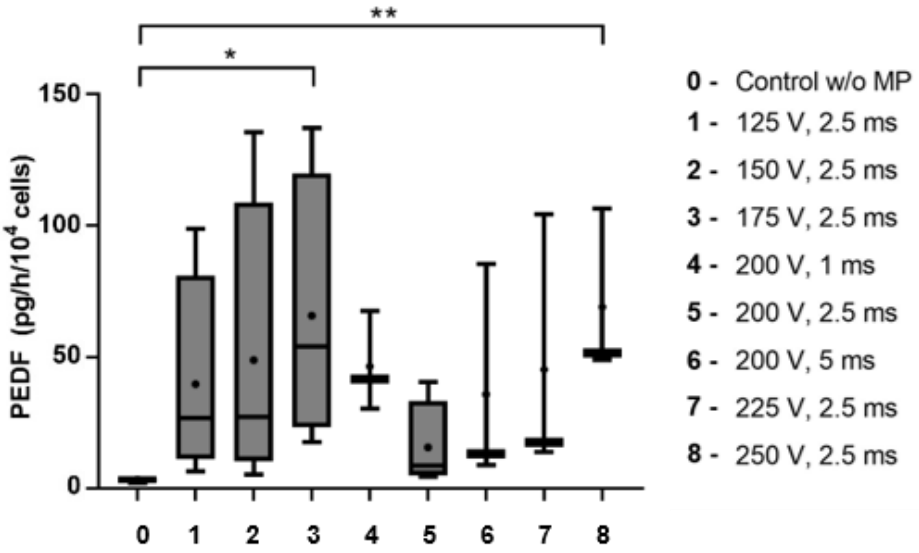


Figure 29: ELISA-based analysis of PEDF protein secretion by A-172 cells transfected with *PEDF* using the NEPA-21 electroporation device, seven days post-transfection. The voltages shown here refer to the PP while the TP was maintained as constant, at 30 V, 50 ms; statistical analysis: all settings have been compared

against the control using the Kruskal-Wallis non parametric test with the Dunn's multiple comparison, n = 4; $p \geq 0.05$ (ns), $p = 0.0160$ (*) and $p = 0.0098$ (**).

Finally, an RT qPCR was performed to quantify the gene expression rates of *PEDF* for the different settings (Figure 30). Setting the PP higher than 200 V, resulted in insufficient cell numbers for further analysis because of which these results were not considered in the final comparison. A significant increase in mean gene expressions was observed at a PP of 200 V, 5 ms, with a $2\Delta Ct$ ratio of 10.53 ± 8.58, closely followed by a ratio of 9.76 ± 12.34, observed at a PP of 175 V, 2.5 ms. The mean gene expression until 200 V, 2.5 ms followed a similar trend as the mean protein production (Figure 29). Based on a relatively higher mean observed in both the ELISA and qPCR results, a PP of 175 V, 2.5 ms was concluded to be ideal for *PEDF* transfections with the NEPA device.

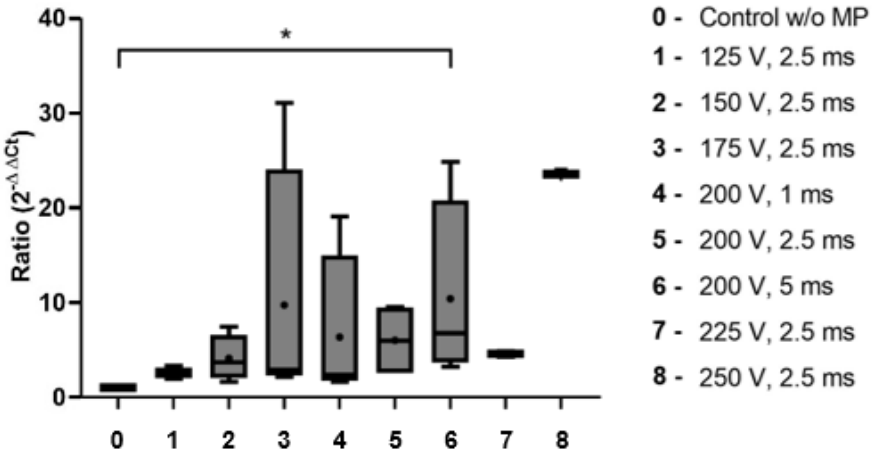


Figure 30: Expression analysis of the *PEDF* gene measured by quantitative real-time PCR performed for A-172 cells transfected with *PEDF* using the NEPA-21 electroporation device, seven days post-transfection. The voltages shown here refer to the PP while the TP was maintained as constant, at 30 V, 50 ms. The experimental values were normalized to the corresponding control group to account for baseline variability; statistical analysis: all settings have been compared against the control using the Kruskal-Wallis non parametric test with the Dunn's multiple comparison, n = 4 for all samples except 225 V (n = 2) and 250 V (n = 1); $p \geq 0.05$ (ns), $p = 0.0107$ (*).

4.2.3. Transfections of cells on a surface with *BDNF*

A-172 cells were transfected with *BDNF* using the NEPA device and analysed a week post-transfection. However, PP settings of 150 - 200 V, 2.5 ms were exclusively used due to low cell viability with the other settings in initial experiments. A western blot, performed to visualize the protein expression, displayed no characteristic bands, suggesting little protein

expression (Figure 31). A quantitative analysis of the protein bands could not be performed as a result.

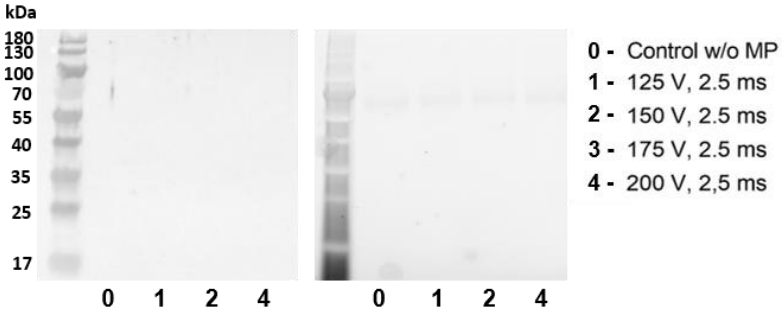


Figure 31: SDS PAGE and western blot supernatants from A-172 cells transfected with *BDNF* using the NEPA-21 electroporation device, seven days post-transfection (n=3). left panel: western blot analysis of the transfected samples with anti-BDNF antibodies compared to the non-transfected control; right panel: detection of uniform sample application using a stain-free gel.

Following western blot, an ELISA was performed to quantify the BDNF protein expression (Figure 32). The negative control displayed a mean BDNF secretion of 81.64 ± 49.66 pg/h/10^4 cells. Compared to the control, transfection led to a mean increase in protein yield of 25.30 times (2.06 ± 1.43 x 10^3 pg/h/10^4 cells) with 125 V, 2.5 ms, 23.55 times (1.92 ± 1.1 x 10^3 pg/h/10^4 cells) with 150 V, 155.8 times (12.7 ± 8.07 x 10^3 pg/h/10^4 cells) with 175 V and 31.13 times (2.54 ± 0.13 x 10^3 pg/h/10^4 cells) with 200 V. Nevertheless, there was a high variation in the protein secretion rates obtained over multiple duplicate experiments. Despite the statistically significant increase in BDNF protein production obtained with one setting (175 V) when compared with the control, *BDNF*-transfection with the NEPA device and the subsequent analyses were complicated by very low cell viability post-transfection.

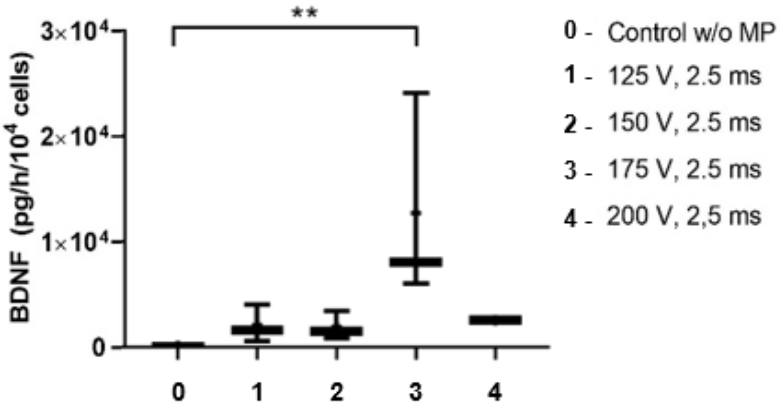


Figure 32: ELISA-based analysis of BDNF protein secretion by A-172 cells transfected with *BDNF* using the NEPA-21 electroporation device, seven days post-transfection. statistical analysis: all settings have been

compared against the control using the Kruskal-Wallis non parametric test with the Dunn's multiple comparison, n = 3 for all samples except 200 V (n = 2); $p \geq 0.05$ (ns), $p = 0.0051$ (**).

Finally, a real time quantitative PCR was performed to quantify the gene expression rates of *BDNF* for the different settings (Figure 33). The highest mean gene expression rate was observed when using a PP of 150 V, 2.5 ms, with a 2ΔCt ratio of 1.67 ± 1.17, followed by a ratio of 1.53 ± 0.53 at 175 V, 2.5 ms. However, as seen from a Kruskal-Wallis non parametric test, none of the test samples were statistically different compared to the control. A comparison of ELISA and qPCR results for PEDF (Figure 29 and 30) and BDNF (Figure 32 and 33), indicated that a PP of 175 V, 2.5 ms was the most ideal for transfection.

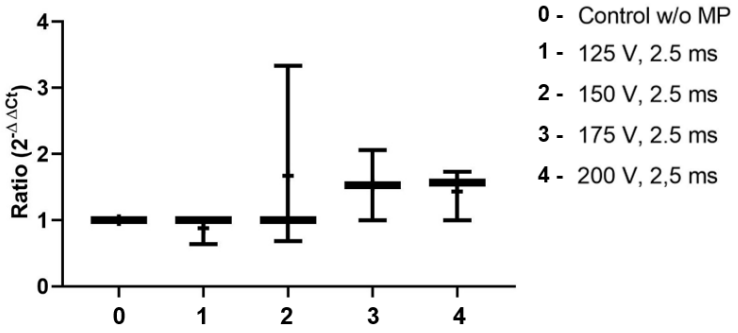


Figure 33: Expression analysis of the *BDNF* gene measured by real-time quantitative PCR performed for A-172 cells transfected with *BDNF* using the NEPA-21 electroporation device, seven days post-transfection. The experimental values were normalized to the corresponding control group to account for baseline variability; statistical analysis: all settings have been compared against the control using the Kruskal-Wallis non parametric test with the Dunn's multiple comparison, n = 3 for all samples except 175 V (n = 2); $p \geq 0.05$ (ns).

4.3. Electroporation with the MEA device

4.3.1. Transfections with the A-172 cell line

A MEA device, housing a MEA consisting of 60 gold electrodes capable of electroporation, was developed by the IWE-1, RWTH Aachen University. A-172 cells were chosen for transfection because of their glial origin. The cells were seeded on the MEA surface, 24 hours prior to transfection, which was performed with 750 ng pmaxGFP per MEA. No gelatine coating was utilized initially which led to the loss of a significant proportion of cells following transfection. As a result, all later experiments employed 0.1% gelatine coating on the MEA surfaces. Three different electrode shapes were attempted - circular, triangular and semi-

circular triangular. A sine pulse of 40 kHz, V_{pp} 8 - 14 V and 100 - 200 ms was used, coupled with different arrangement of active and ground electrodes. Nevertheless, the transfection efficiency was low (Figure 34). The florescent cells were often circular, displaying a drastic change in morphology following transfection.

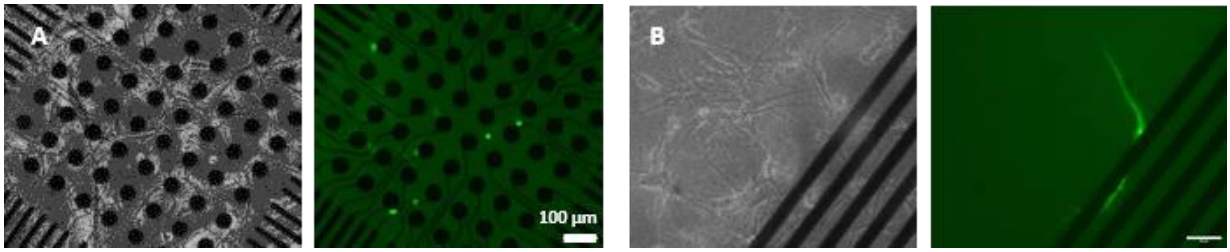


Figure 34: Results of MEA-based transfection of A-172 cells with pmaxGFP, 24 hours post-transfection (10x). left panel: phase contrast image; right panel: fluorescence image. **(A)** cells transfected with circular electrodes, multiple alternating rows arrangement of active electrodes and a sine wave pulse of 12 V, 150 ms; **(B)** cells transfected with triangular electrodes, repeated concentric arrangement of active electrodes and a sine wave pulse of 14 V, 100 ms.

4.3.2. Transfections with the R28 cell line

4.3.2.1. Genetic modifiability of the R28 cell line

Following the A-172 transfection experiments with the MEA device, another cell line was sought as an alternative. The R28 cell line was chosen for this purpose. The genetic modifiability of this cell line was studied with 350 ng *Venus* and 5 x 10^4 cells per transfection, by employing the Neon device. The non-transfected cells displayed a significantly higher growth rate compared to transfected cells (Figure 35) and 72 hours post-transfection, a majority of the cell population was non-transfected. A flow cytometry analysis was performed as early as 48 hours post-transfection (Figure 36).

The maximum mean transfection efficiency of 16.1 ± 7.36% was observed at 1200 V, although 1300 V and 1150 V had similar mean efficiencies of 14.1 ± 5.97% and 13.2 ± 4.64% respectively. An ordinary one-way ANOVA comparing the control to the transfected samples displayed the highest significance at 1200 V. The maximum transfection efficiency that could be achieved using the Neon device, with the R28 cell line (27.5%), was approximately 2.3 times lower compared to the maximum efficiency that could be achieved with the A-172 cell line. Nevertheless, since the R28 cells were relatively easy to transfect (not shown) and

initial experiments with the MEA device displayed positive results, they were used for transfection experiments with the MEA device.

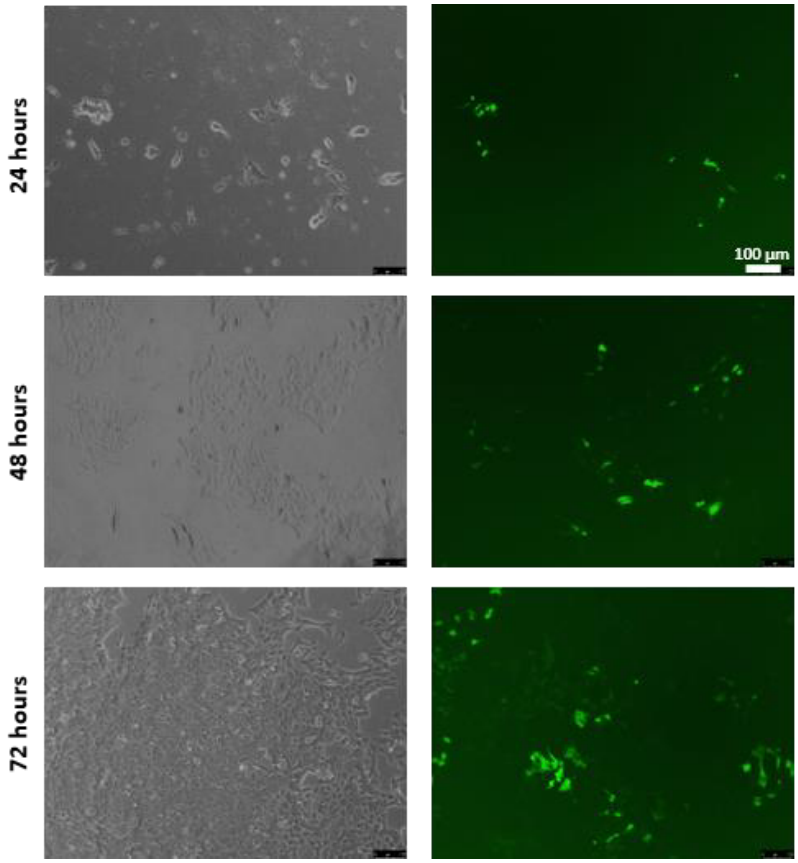


Figure 35: Fluorescence images of *Venus*-transfected R28 cell line at different time points (10x). Non-transfected cells rapidly outgrow the transfected cells (top to bottom). left panel: phase contrast image; right panel: fluorescence image.

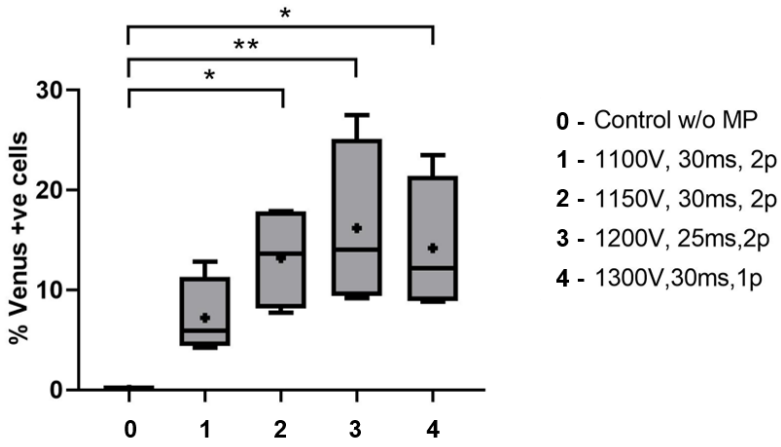


Figure 36: Flow cytometry analysis of R28 cells transfected with *Venus* using the Neon Transfection System, 48 hours post-transfection; statistical analysis: data passed the Brown-Forsythe test for homoscedasticity ($p = 0.0679$ (ns)) and the Shapiro-Wilk normality test ($p \geq 0.05$ (ns)). All settings have been compared against the

control using an ordinary one-way ANOVA with the Dunnet's post-hoc test, n = 4; $p \geq 0.05$ (ns), $p < 0.05$ (*), $p = 0.0087$ (**).

4.3.2.2. MEA transfections with the R28 cell line

Following the initial transfection experiments, the R28 cell line was transfected with the MEA device (Figure 37). Two types of controls, a negative control with no plasmid or applied voltage and a positive control with 750 ng pmaxGFP but no applied voltage, were implemented (Figure 37 A-C). Different electrode shapes and arrangement of active to ground electrodes were attempted for the transfection. A sine wave pulse of 40 kHz, V_{pp} 8 - 14 V and a pulse width of either 150 or 162.5 ms was employed for transfection of cells. No fluorescent cells were observed in either control, 24 hours post-transfection. Negligible transfection was observed when 8 V was applied even with a higher pulse width. Initial positive transfection (Figure 37 D) was observed with triangle electrodes and a 14 V 150 ms pulse when the repeated concentric setting (Figure 14 H) was adopted. An identical setting was also adopted with circular electrodes. However, few transfected cells were observed (Figure 37 E).

The pulse width was raised to 162.5 ms and transfection was attempted with different electrode shapes and settings. Initially, the half arrangement of active electrodes (Figure 14 F) was implemented using triangular electrodes. The positive transfection observed (Figure 37 F) was similar in efficiency to Figure 37 D. The results for circular and semi-circular triangular electrodes employing the increased pulse width has been shown in Figure 37 H-K. Additionally, in Figure 37 H, all the transfected cells belonged to the same colony, which was identified at a significant distance from the electrodes. Several setups, including repeated concentric, half and checkerboard arrangement of electrodes, were attempted. Although transfection was possible, a high efficiency could not be achieved. In many cases, the transfected cells were situated outside the electrode array area. The highest transfection efficiency was achieved when the repeated concentric setting was adopted, alongside triangular electrodes, to deliver a 14 V, 162.5 ms sine wave pulse (Figure 37 G). A significant proportion of the transfected cell population was located in the electrode array area in this case, but a few transfections also yielded transfected cells outside this area.

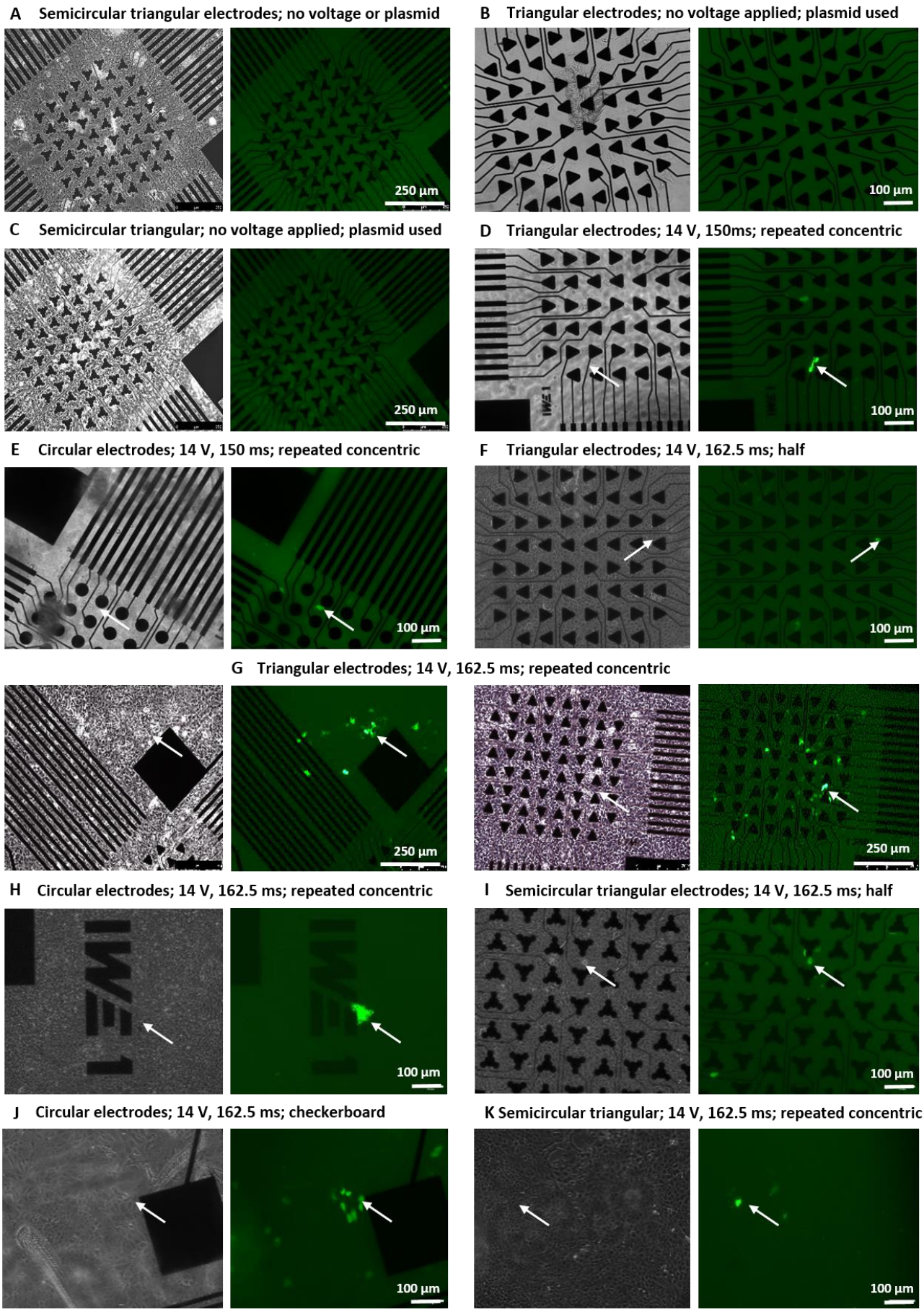

A Semicircular triangular electrodes; no voltage or plasmid
250 µm
B Triangular electrodes; no voltage applied; plasmid used
100 µm
C Semicircular triangular; no voltage applied; plasmid used
250 µm
D Triangular electrodes; 14 V, 150ms; repeated concentric
100 µm
E Circular electrodes; 14 V, 150 ms; repeated concentric
100 µm
F Triangular electrodes; 14 V, 162.5 ms; half
100 µm
G Triangular electrodes; 14 V, 162.5 ms; repeated concentric
250 µm
250 µm
H Circular electrodes; 14 V, 162.5 ms; repeated concentric
100 µm
I Semicircular triangular electrodes; 14 V, 162.5 ms; half
100 µm
J Circular electrodes; 14 V, 162.5 ms; checkerboard
100 µm
K Semicircular triangular; 14 V, 162.5 ms; repeated concentric
100 µm

Figure 37: Results of MEA-based electroporation of R28 cells, transfected with pmaxGFP, 24 hours post-transfection (10x); left panel: phase contrast image; right panel: fluorescence image; **(A)** negative control with no plasmid or voltage applied; **(B,C)** positive controls, with plasmid used, but no voltage applied; **(D-K)** R28 cells transfected using the MEA device, with different combinations of electrode shape, voltage, pulse width and arrangement of active to ground electrodes. Sample transfected cells have been indicated in each image with white arrows.

A preliminary measurement of the transfection efficiency was made by manually measuring the cells in each MEA post-transfection. Contrary to what was observed with the fluorescence microscopy, there was no significant difference in efficiency amongst the different electrode shapes when the repeated concentric arrangement of active electrodes were used (Figure 38A). A conclusion could not be drawn regarding the other electrode setups due to the low overall success in transfection. The available results are shown in Figure 38 (B and C).

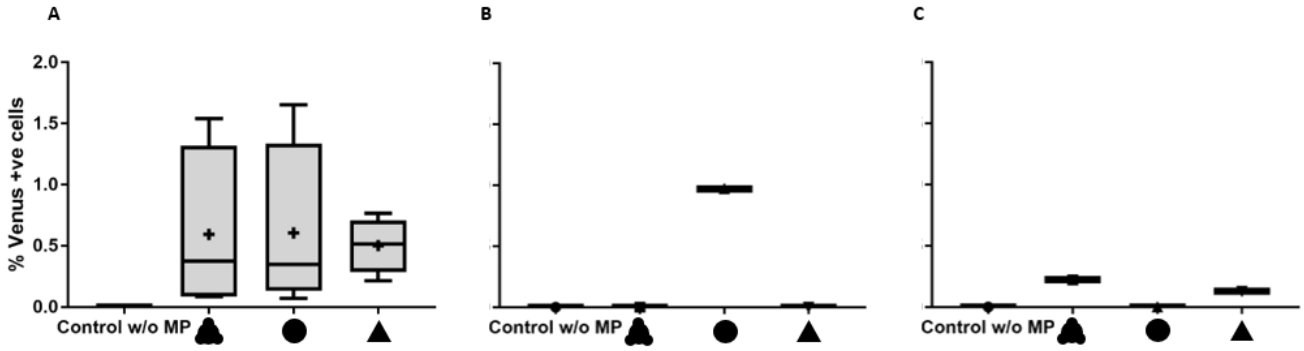


Figure 38: **Results of MEA-based electroporation of R28 cells, transfected with pmaxGFP, 24 hours post-transfection (10x); (A)** transfections performed with the repeated concentric arrangement of active electrodes **s**tatistical analysis: data passed the Brown-Forsythe test for homoscedasticity ($p = 0.2657$ (ns)) and the Shapiro-Wilk normality test ($p \geq 0.05$ (ns)). All settings have been compared against the control using an ordinary one-way ANOVA with the Dunnet's post-hoc test, $n = 4$; $p \geq 0.05$ (ns); **(B)** transfections performed with the checkerboard arrangement of active electrodes ($n = 1$); **(C)** transfections performed with the half arrangement of active electrodes ($n = 1$).

4.4. Relation between cell size/shape and transfection parameters

The correlation between cell size, geometry and transfection efficiency was studied with the aid of the Cell Profiler 4.2.6 software. Pictures of three different cell lines - A-172, R28 and ARPE-19, captured before and post-transfection, were examined. The average cell area of each cell line was analysed in the initial study. For this purpose, the cells were studied on a surface, prior to transfection. In the case of A-172 and ARPE-19 cell lines, the necessary images could

be captured with cell cultures that had been maintained in culture for a week. However, the R28 cell line displayed a high growth rate, due to which the image had to captured 24 hours post-passaging. Nevertheless, due to the differences in average cell shapes between the three cell lines, a single standard software pipeline, which was capable of accurately measuring the properties of cells from all three cell lines could not be arranged and the cells shapes had to be manually traced over the microscopy images (Figure 39 A-C). The mean cell area was calculated separately for each image, taking into account all the cell areas in that image, following which, multiple images for each cell line were condensed into a single data set (Figure 39 D). Although the number of cells varied between each image, the effect of this variation was considered to be negligible for ease of understanding. A-172 cell line, with a total mean 2D cell area of $9.87 \pm 2.35 \times 10^4$ μm^2 (Figure 39 D), displayed the largest mean cell size compared to the other two cell lines, with 1.3 times the mean cell area of ARPE-19 cells ($7.65 \pm 6.13 \times 10^4$ μm^2) and 2.5 times the mean cell area of R28 cells ($3.95 \pm 2.28 \times 10^4$ μm^2). An ordinary one-way ANOVA displayed a statistically significant difference between the mean cell areas of A-172 and R28 cell lines.

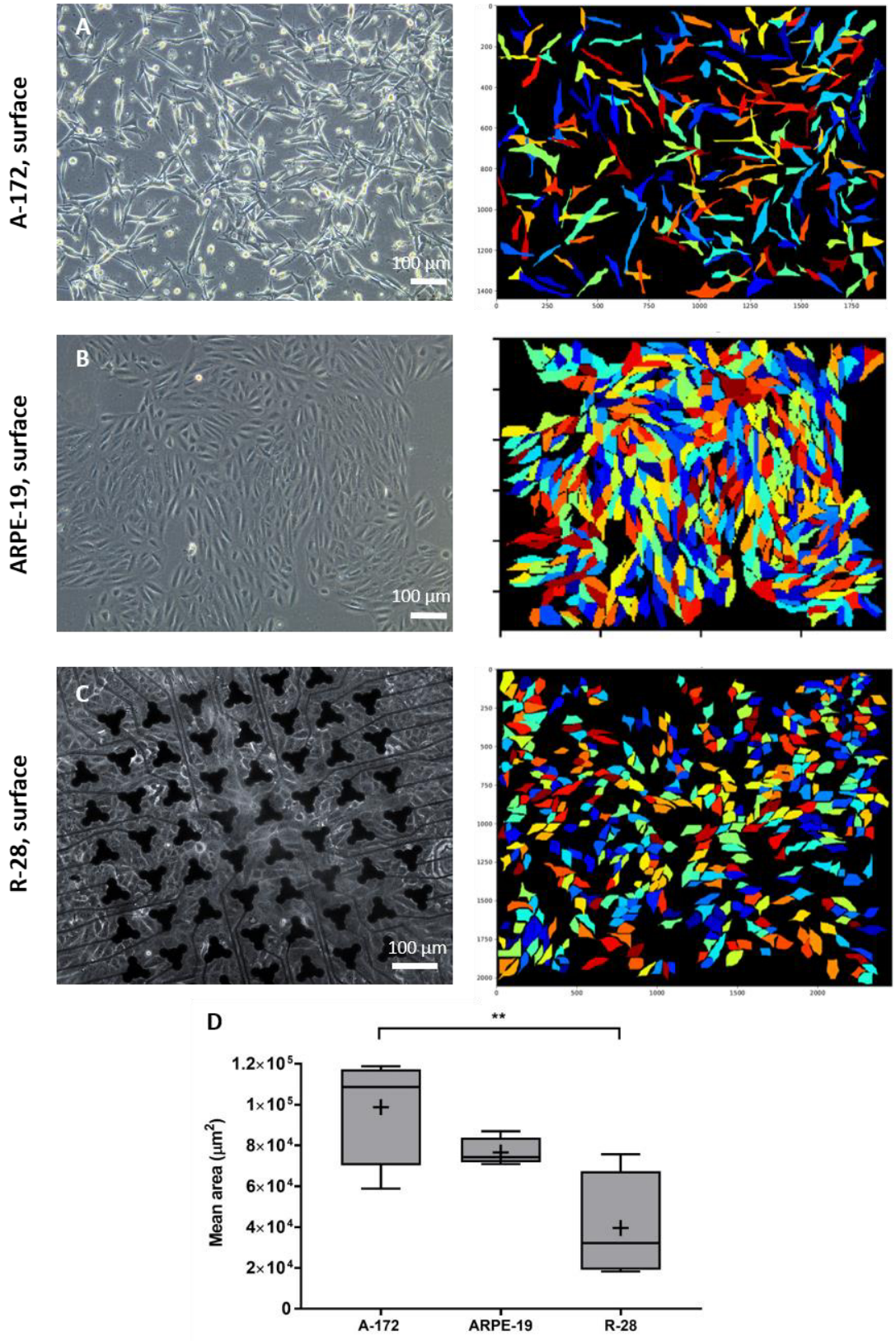


Figure 39: Cell mean area measurement using Cell Profiler 4.2.6 software; left panel: phase contrast image, right panel: manually edited cell outlines used for further measurement; **(A)** A-172 cells on a surface, prior to the passage directly preceding transfection; **(B)** ARPE-19 cells on a surface, prior to the passage directly preceding transfection; **(C)** R28 cells on a surface, before transfection, 24 hours after seeding; **(D)** comparison of mean 2D

area of cells on a surface for different cell lines before transfection. A-172 and ARPE-19 were imaged using Leica DFC 7000T (1 pixel = 4.54 µm) and R28 was imaged using Zeiss Axiocam 705 mono (1 pixel = 3.45 µm); statistical analysis: data passed the Brown-Forsythe test for homoscedasticity ($p = 0.3759$ (ns)) and the Shapiro-Wilk normality test ($p \geq 0.05$ (ns)). both R28 and ARPE-19 mean areas have been compared against A-172 with an ordinary one-way ANOVA with the Dunnet's post-hoc test, $n = 4$; $p = 0.3152$ (ns), $p = 0.0082$ (**).

CV is a dimensionless quantity, calculated by dividing the standard deviation by the mean (193). It gives a measure of the variability in a system and in this case, the area. In Figure 40 (left panel), the CV has been calculated for the 2D areas of the cells (CVa) from the different cell lines used in this study in order to draw a comparison between the variability in cell size and the voltage requirements for transfection. Prior to transfection, CVa was calculated with phase contrast images, while, post-transfection, it was calculated with fluorescent images. When observed immediately after seeding, CVa of A-172 and ARPE-19 cells did not exceed 0.3 (Figure 40, A1 and B1) but increased two fold after the cells attached properly to a surface with a mean CVa of 0.56 ± 0.07 and 0.4 ± 0.07 for the two cell lines respectively (Figure 40, A2 and B2). The CVa of R28 cells on a surface, however, was 0.47 ± 0.02 (Figure 40, D1), suggesting that the variability in area among R28 cells was not as low as ARPE-19 cells, although also not as high as A-172 cells.

When studying A-172 cells on a surface, prior to and post-transfection, it was observed that the CVa decreased from 0.56 ± 0.07 before transfection to 0.54 ± 0.13, 24 hours post-transfection (Figure 40, A2 and A3). This decrease in CVa was notable six days post-transfection, with a mean of 0.43 ± 0.04 (Figure 40, A4). In the case of ARPE-19 cells, CVa increased from 0.4 ± 0.08 before transfection to 0.46 ± 0.07, 24 hours post-transfection (Figure 40, B2 and B3). For experiments involving transfection of the A-172 cell line with the NEPA-21 device, CVa was measured prior to and post-transfection with two different setups (Figure 27, A and D). The CVa one week post-transfection, with the ideal setup chosen from the NEPA experiments (Figure 27 D), was 1.24 times the value observed prior to transfection (Figure 40 C1 and C2). The CVa with the second setup (Figure 27 A), one week post-transfection, decreased by 1.24 times the value prior to transfection (Figure 40 C1 and C3). Concerning MEA transfections with the R28 cell line, the CVa decreased from 0.47 ± 0.02 before transfection, to 0.36 ± 0.02, 24 hours post-transfection (Figure 40, D2 and D3). Comparing these trends with the known voltage requirements for transfection of ARPE-19

(143) and A-172 cells and their respective transfection efficiencies, it was observed that, as CVa increased, the mean transfection efficiency decreased.

Following the CVa measurements, *e* values were measured to determine the sphericity of different cell lines, prior to and post-transfection (Figure 40, right panel). When comparing cells immediately after seeding and on a surface, mean *e* increased from 0.55 ± 0.02 to 0.92 ± 0.02 respectively in the case of A-172 cells (Figure 40, A1 and A2) and from 0.43 ± 0.07 to 0.84 ± 0.55 respectively in the case of ARPE-19 cells (Figure 40, B1 and B2). In conclusion the cells for both cell lines showed an elliptical morphology on a surface with twice the *e* value compared to when the cells were in suspension. On an average, among the three cell lines studied on a surface, the R28 cell line had the most spherical cells, with an *e* of 0.79 ± 0.08 (Figure 40 D2), while A-172 had the most elliptical cells.

The elliptical nature of A-172 cells increased the longer they were maintained in culture, as was observed when comparing mean *e* for the non-transfected A-172 cells maintained in culture for 24 hours and for a week (Figure 40 A2 and C1).

A-172 cells, 24 hours post-transfection with the Neon Transfection System, displayed a drop in mean *e* (0.85 ± 0.02), compared to when the cells were cultivated on a surface prior to transfection (Figure 40, A3 and A2). However, when observed a week post-transfection (Figure 40 A4), mean *e* had increased to pre-transfection levels. In the case of the ARPE-19 cell line, a similar trend was observed; a decrease in *e* from 0.84 ± 0.05 before transfection to 0.74 ± 0.05, 24 hours post-transfection.

Next, the eccentricity of A-172 cells was studied in the context of transfection with the NEPA-21 device. Little change was observed in this case, with cells on a surface before and one week post-transfection, displaying similar *e* values (Figure 40, C1 - 3). A similar result was observed in the case of MEA transfections with the R28 cell line, with negligible variation in *e* when comparing cells prior to and post-transfection (Figure 40, D2 and D3).

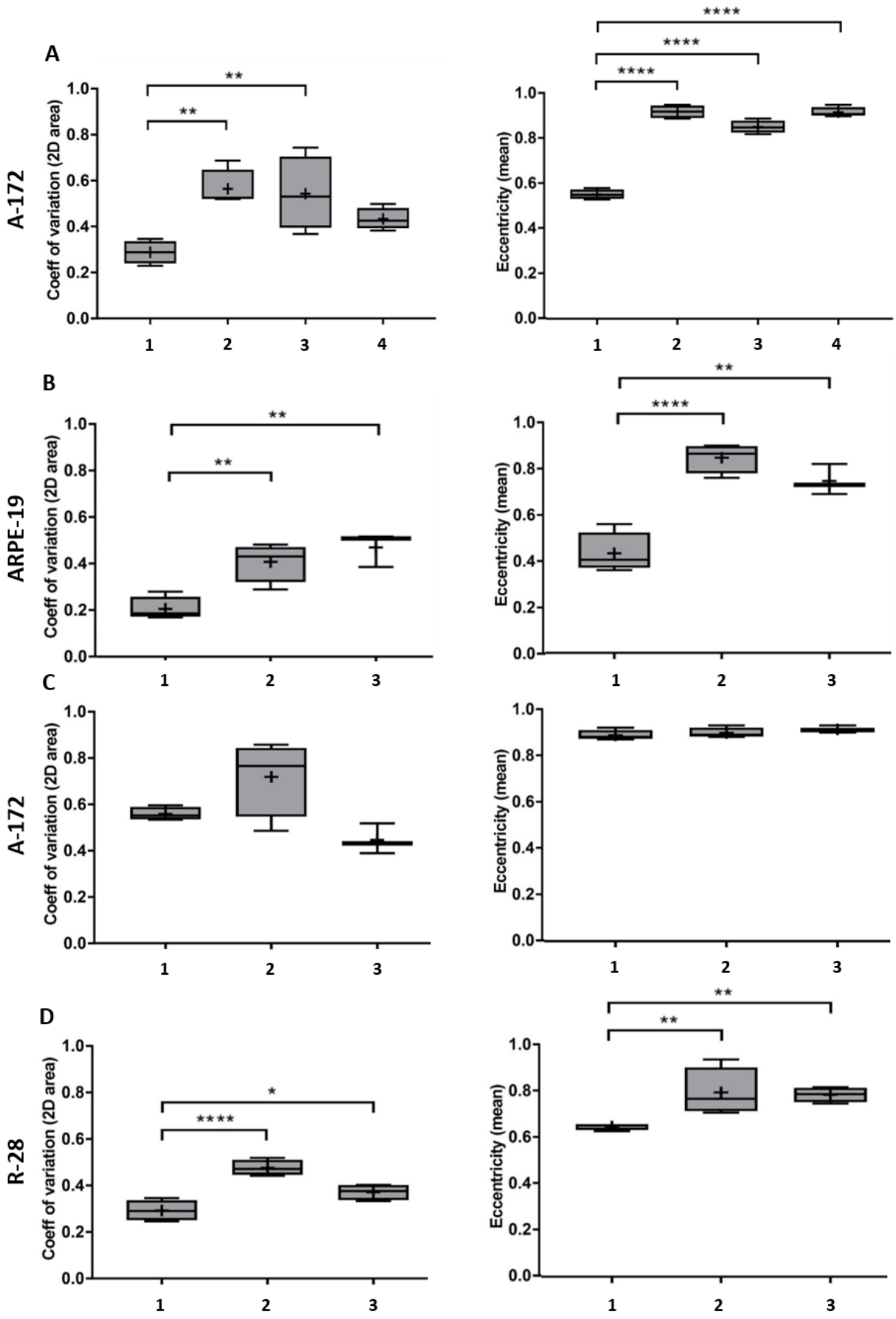

A
A-172
Coeff of variation (2D area)
Eccentricity (mean)
B
ARPE-19
Coeff of variation (2D area)
Eccentricity (mean)
C
A-172
Coeff of variation (2D area)
Eccentricity (mean)
D
R-28
Coeff of variation (2D area)
Eccentricity (mean)

Figure 40: Comparison of different cell properties, before and post-transfection. left panel: CV of 2D cell area, right panel: mean *e* values; **(A)** A-172 cells transfected with the Neon device (1200 V, 25 ms, 2 pulses); **1:** cells immediately post-seeding to emulate cells in suspension; **2:** cells on a surface, prior to the passage directly preceding transfection; **3:** cells on a surface, 24 hours following transfection; **4:** cells on a surface, one week following transfection; **(B)** ARPE-19 cells transfected with the Neon device; **1:** cells immediately post-seeding to emulate cells in suspension; **2:** cells on a surface, prior to the passage directly preceding transfection; **3:** cells on a surface, 24 hours following transfection; **(C)** A-172 cells transfected with the NEPA device (PP of 200 V, 5 ms); **1:** cells on a surface, 24 hours after seeding, and directly preceding transfection; **2:** cells on a surface, one week post-transfection (electrode: 0 + 90º, PP + TP±); **3:** cells on a surface, one week post-transfection (electrode: 0º, PP± TP±); **(D)** R28 cells transfected with the MEA device (sine wave pulse of 40 kHz, 14 V, 162.5 ms); **1:** cells immediately post-seeding to emulate cells in suspension; **2:** cells on a surface, 24 hours after seeding, and directly preceding transfection; **3:** cells on a surface, 24 hours post-transfection (triangular electrodes); statistical analysis: data passed the Brown-Forsythe test for homoscedasticity ($p \geq 0.05$ (ns)) and the Shapiro-Wilk normality test ($p \geq 0.05$ (ns)), except cells on a surface, prior to passage, directly preceding transfection (A2 (left)); $p = 0.0051$ (**). All data sets (2, 3 and 4) have been compared against cells immediately post seeding (1) in A, B and D or against cells on a surface, 24 hours after seeding, directly preceding transfection (1) in C, with an ordinary one-way ANOVA with the Dunnet's post-hoc test, $n = 4$; $p \geq 0.05$ (ns), $p < 0.01$ (**), $p < 0.0001$ (****).

4.5. Experiments with primary Müller cells

4.5.1. Isolation and characterization of Müller cells

Following successful transfection experiments with A-172 and R28 cell line, Müller cells were isolated from four week old C57BL/6J WT mice. Primary Müller cells which had been maintained in culture for four days or more, displayed a spindle shaped morphology, typically observed in glial cells (Figure 41 and 42). The medium was exchanged with fresh medium, 24 hours post-isolation to ensure most of the remaining cells were Müller cells. The first two weeks of the primary Müller cells in culture did not yield sufficient confluence for transfection (Figure 41). By the third - fifth week in culture, confluence was sufficient for further experiments (Figure 42). Nevertheless, 100% Müller cell purity could not be achieved.

Presence of Müller cells was confirmed with an immunocytochemical analysis where the cells were fixed with 4% PFA/ 0.1% Triton X-100 in 5% BSA and treated with antibodies against GS, vimentin and GFAP, accompanied by a nuclear counterstaining with DAPI. Müller cell were confirmed with positive fluorescence for both GS and vimentin antibodies (Müller cell markers). The vimentin fluorescence was consistently much brighter than the observed GS

fluorescence (Figure 43). Additionally, a few Müller cells displayed positive fluorescence for GFAP.

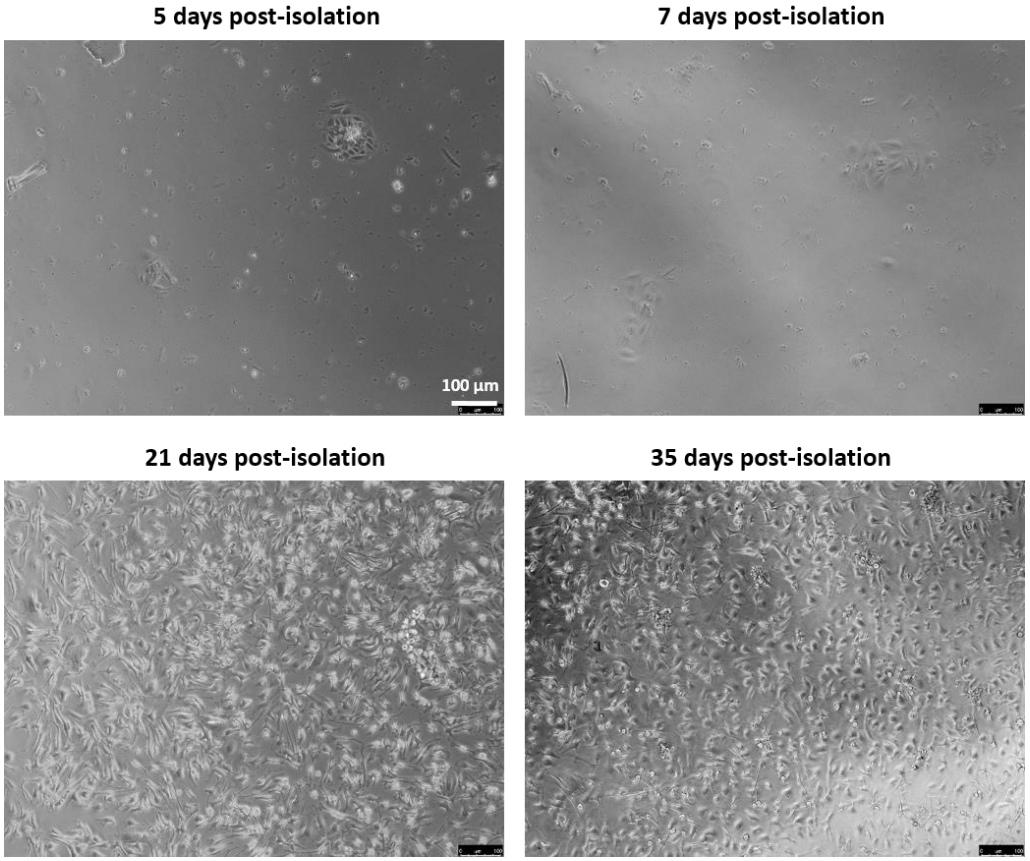


Figure 41: Primary Müller cells, as observed at different time points after isolation (10x).

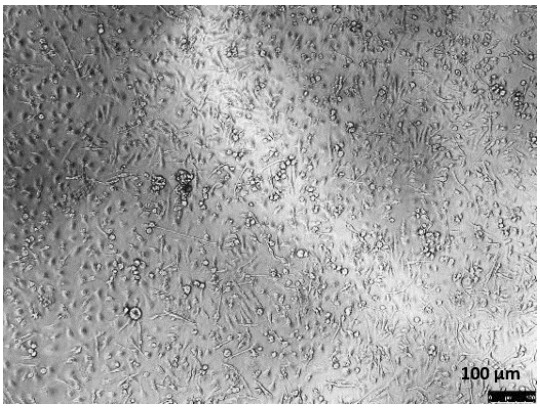


Figure 42: Primary Müller cell culture 21 days post-isolation (P0) as observed immediately prior to electroporation and subsequent immunocytochemical analysis (10x).

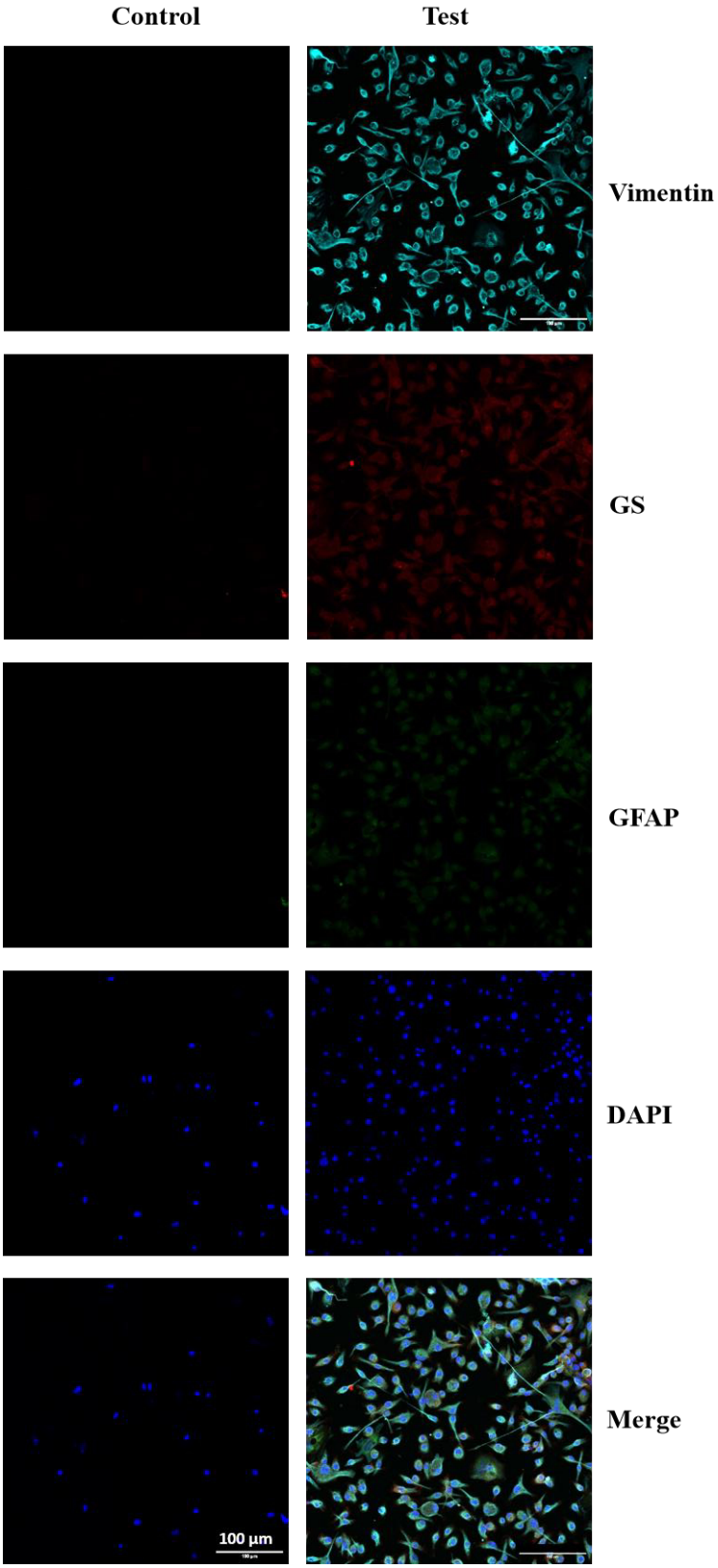


Figure 43: Immunocytochemical analysis of primary Müller cell cultures isolated from four-week-old C57BL/6J WT mice (20x), four weeks post-isolation. (A) Immunocytochemical control samples which were not treated with primary antibodies; **(B)** Immunocytochemical test samples where fixed cells were analyzed with antibodies against vimentin (teal), GS(red) and GFAP (green); cell nuclei were counterstained with DAPI (blue).

4.5.2. Transfection of Müller cells in suspension

The genetic modifiability of the isolated primary Müller cells was established with initial experiments using the Neon device. Primary Müller cell cultures, at least three weeks old, were transfected with *Venus* (350 ng mixture of transposon and transposase plasmids), using the ideal settings chosen from the A-172 transfection experiments (Figure 19). The cell viability and transfection efficiency achieved were determined by phase contrast and fluorescence microscopy to be significantly low (Figure 44). Additionally, the surviving cells displayed a change in morphology, along with blebbing .The identity of the surviving cells post-transfection could not be determined due to the change in morphology and reduced cell viability.

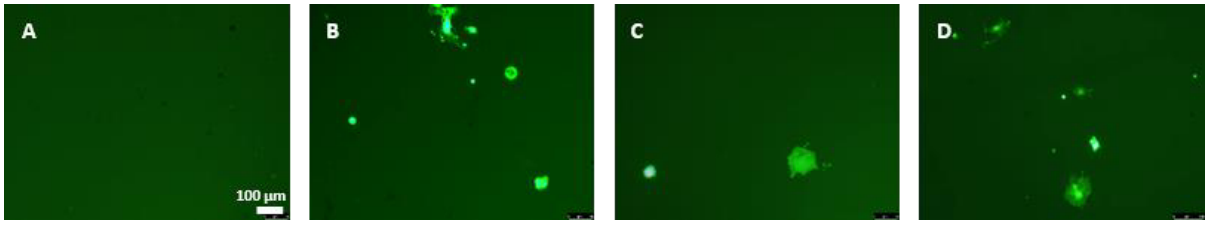


Figure 44: Fluorescent images of the primary Müller cells transfected with *Venus*, using the Neon Transfection System (10x). Transfected cells do not show typical Müller cell morphology; **(A)** negative control; **(B)** cells transfected with 1100 V, 30 ms, 2 pulses, as observed 24 hours post-transfection; **(C)** cells transfected with 1150 V, 30 ms, 2 pulses, as observed 24 hours post-transfection; **(D)** cells transfected with 1150 V, 30 ms, 2 pulses, as observed 96 hours post-transfection.

In order to increase the survival of the cells post-transfection, only primary cell cultures with 50% cell confluence or higher, were utilized (Figure 42). The voltage limit was increased (1200 - 1300 V), along with plasmid quantity (500 - 550 ng), in an attempt to improve the transfection efficiency. At higher voltages, automatic delivery of two pulses was not possible and as a result, the second pulse had to be delivered manually (Figure 45 A and B). Among all the settings attempted, the highest transfection efficiency was achieved with two separate pulses of 1200 V, 25 ms (Figure 45 A). Increasing the voltage to 1240 V (550 ng plasmid) drastically reduced the number of transfected Müller cells (Figure 45 B), although increasing the voltage further to 1300 V (500 ng plasmid), slightly improved the efficiency (Figure 45 C). An immunocytochemistry, performed on the transfected cells, confirmed the presence of transfected Müller cells (Figure 45), although the transfection efficiency was quite low in general. Vimentin antibody was not used for treating the transfected samples.

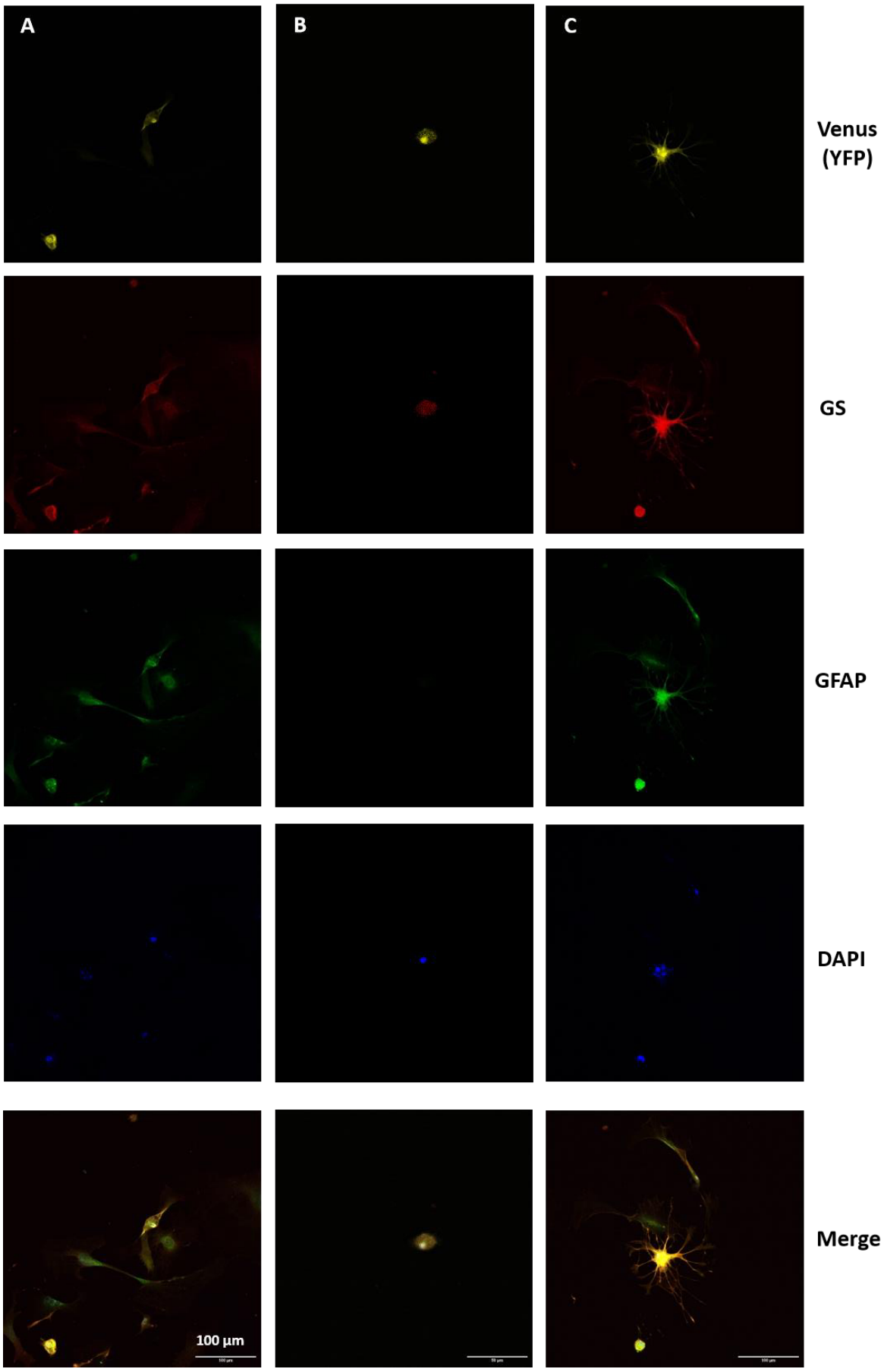

A
B
C
Venus (YFP)
GS
GFAP
DAPI
Merge
100 µm

Figure 45: Immunocytochemical analysis of transfected primary Müller cell cultures, seven days post-transfection with *Venus*, using the Neon Transfection System (20x). (A) 1200 V, 25 ms applied as two separate pulses with 500 ng plasmid. Transfection was performed four weeks post-isolation; **(B)** 1240 V, 25 ms applied as two separate pulses with 550 ng plasmid. Transfection was performed five weeks post-isolation; **(C)** 1300 V, 30 ms, 1 pulse with 500 ng plasmid. Transfection was performed four weeks post-isolation. Venus fluorescence was depicted in yellow and the fixed cells were analyzed with antibodies against GS (red) and GFAP (green) while cell nuclei were counterstained with DAPI (blue). Transfected samples were not stained with the anti-vimentin antibody.

4.5.3. Transfection of Müller cells cultured on a surface

Following Neon transfection experiments, the primary Müller cells in culture were transfected with the NEPA-21 device. The plasmid concentration, PP and TP polarities, TP settings and electrode direction were maintained identical to the NEPA-21 A-172 experiments, Two different PP settings were attempted - 175 V, 2.5 ms and 200 V, 2.5 ms.

The cell viability was extremely low post-transfection and Venus fluorescence was not significant. The cells were stained against GS and GFAP and the nuclei were counterstained with DAPI to confirm the presence of transfected Müller cells. The samples were imaged with the Leica DMI4000 B inverted microscope. However, visualization of GFAP immunostaining alongside the DAPI counterstain was not noticeable (Figure 46). Although positive GS immunoreactivity was detected at 175 V, the signal was relatively weak, and the labelled cells appeared small and circular. At 200 V, a clearly transfected cell was observed; however, GS staining remained faint at this voltage as well. Overall, primary Müller cells displayed a lower transfection rate when transfected on a surface compared to transfection in suspension, an observation which was similar to the one made with the transfection of the A-172 cell line.

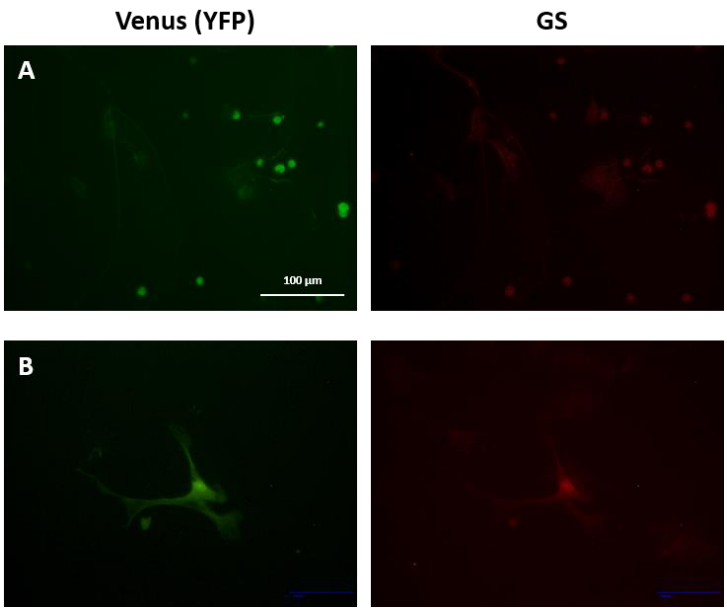


Figure 46: Immunocytochemical analysis of primary Müller cell cultures transfected with *Venus*, 14 days post-transfection with the NEPA-21 device (20x). **(A)** cells transfected with 420 ng/µl plasmid, employing a PP of 175 V, 2.5 ms applied as two separate pulses; **(B)** cells transfected with 420 ng/µl plasmid, employing a PP of 200 V, 2.5 ms applied as two separate pulses. The cells were transfected three weeks post-isolation. Fixed cells were analyzed with an antibody against GS(red). Venus expression is depicted in green.

5. Discussion

RP is the most common inherited retinal disease (32, 33). Multiple therapeutic strategies have been explored for its management, among which viral vector–mediated gene therapy has emerged as a prominent and widely adopted approach. However, viral gene therapy approaches have their disadvantages, including, but not limited to, immune reaction to the viral vector which reduces its effectiveness, reduced target cell specificity, cytotoxicity of the vectors used, insertional mutagenesis and a high manufacturing cost (194, 195). As an example, in one study, administration of a gene therapy using human adenovirus as the vector, resulted in the death of an 18 year old patient (196). Another study showed that over 98% of viral vector DNA interacts with host's red blood cells (RBCs) instead of their intended target, the lung carcinoma cells (197). Additionally, Cattoglio *et al.* determined that HIV based retroviral vectors integrate within or around protein coding regions or microRNAs of the host, leading to a high risk of insertional mutagenesis (198). Even lentiviral vectors (LVVs), created specifically for a lower risk to the host, resulted in the development of leukemia in one fourth of the patients being treated (199). The currently popular and FDA-approved gene therapy for *RP*, Vortigene neparvovec-rzyl (Luxturna), involves a subretinal injection of a AAV2 viral vector carrying the natural gene sequence of the human *RPE65* gene (200, 201). The AAVs used in this therapy also have their disadvantages. The AAV genome does not integrate into the host genome, which leads to the loss of the corrected gene when the cell replicates. Moreover, AAVs have a limited load capacity, limiting the size of the gene they can carry (reviewed in (195)).

The *SB* transposon system has been suggested as a non-viral alternative to viral gene therapy. *SB*, a DNA transposon belonging to the Tc1/mariner superfamily (148) (202), combines the advantages of viral and non-viral delivery methods, while minimising the disadvantages of the viral techniques. This system has a high cargo capacity, high gene transfer, high expression rates, long-term expression of the transgene and a reduced risk of insertional mutagenesis (151-154). Zayed *et al.* developed a hyperactive variant of the *SB* transposase with almost eight times the transpositional activity of the wild *SB* transposase (150), while Mates *et al*. reported

on a hyperactive *SB* variant, with which over a 100 times the efficiency of the normal *SB* system was achieved (189). *SB100X* was applied in previous research by our group. Johnen *et al.* achieved gene delivery to RPE cells (bovine and human origin) with the Neon Transfection System using the *SB* transposon system, resulting in 100% transfection efficiency with *Venus* and 30% with *PEDF* (143). A study by Harmening *et al.,* involving the transfection of ARPE-19 cells and primary human RPE cells with *Venus* resulted in transfection efficiencies of 100 % and 80 % respectively (200). In this case, the *SB100x* transposase mRNA was used.

The current study focused on optimizing parameters for the transfection of the glioblastoma cell line A-172 with the *SB* transposon system using different electroporation devices, allowing us to study the potential of glial cells as a target for non-viral gene therapy. Müller cells were chosen as the cell-type of interest, since the hypertrophy of MG in an *RP* retina (42) would make these cells a bigger target for transfection *in vivo*. However, the initial *in vitro* studies were performed with the A-172 cell line due to its glial origin and ease of handling. A previous study comparing the glioblastoma cell lines A-172 and T-98G showed that these two cell lines accurately represent a glioblastoma and its mesenchymal origin (203). Both cell lines expressed the mesenchymal marker vimentin and showed no expression of GFAP (203), features which are also exhibited in WT Müller cells (204). Nevertheless, Müller cells also express GFAP under stress conditions (204). The retinal progenitor cell line R28, which has a very strong glial component (185), was also used for the transfection experiments. This cell line expresses both vimentin and GFAP (185), similar to stressed Müller cells, and is robust and readily cultured. However, the R28 cell line is multi-phenotypic, i.e. it is able to develop different morphologies when exposed to sufficiently different medium conditions (185). It was only used when transfection with the A-172 cells was unsuccessful. Nevertheless, following the transfection experiments with the A-172 and R28 cell lines, primary Müller cells were used in order to gain accurate information regarding the possibility of their transfection.

5.1. *PEDF* and *BDNF* as candidates for additive gene therapy

PEDF and BDNF have been widely recognized for their neuroprotective properties in previous research. One study explored the neuroprotective effect of PEDF by treating rat retinal cultures and crushed rat optic nerves. PEDF enhanced both RGC survival and axon regeneration *in vitro* and *in vivo* (205). The neuroprotective activity of PEDF has been attributed to defined peptide

regions, and the functional significance of these small peptide fragments has been extensively characterized over many years (206-208). As an example, a study conducted by Bernardo-Colon *et al.* determined the efficacy of neuroprotective effect of small peptides derived from PEDF (209). These peptides, delivered to the eyes of *rd10* and $Rho^{P23H/+}$ mice as eye drops, successfully reached the retina and improved both photoreceptor survival and retinal function. Zhang *et al.* demonstrated that PEDF downregulated vascular endothelial growth factor (VEGF) expression levels in a dose dependent manner after 48 hours of treatment in both A-172 and U-87 cell glioblastoma cell lines (210). Previous research has demonstrated the neuroprotective properties of BDNF. One study utilized a double-transgenic mouse model of primary rod photoreceptor degeneration coupled with inducible expression of *BDNF* in photoreceptors to demonstrate that increased *BDNF* expression in provides strong protection against oxidative injury-induced photoreceptor cell death along with protection from death caused by mutant rhodopsin (211). In another study, rat iris pigment epithelium cells transfected with *BDNF* via lipofection, demonstrated a neuronal rescue effect against induced neuroretinal cell death and phototoxic damage in both *in vitro* and *in vivo* experiments (212). Zhou *et al*. generated neural stem cells overexpressing BDNF, via retroviral transduction and then transplanted these cells into normal rat retinae. Stem cells overexpressing BDNF differentiated into neuron more efficiently compared with the cells without BDNF overexpression. Finally, a study demonstrated that BDNF protected retinal neurons from hyperglycemia *in vitro* in a dose dependent manner (213). The neuroprotective effect of BDNF has also been demonstrated indirectly. Lower BDNF levels were associated with a glioblastoma phenotype, an observation that was also made by Wójtowicz *et al.*, who measured BDNF levels in the cerebrospinal fluid and plasma of patients (214). In conclusion, PEDF and BDNF are excellent candidates for additive gene therapy study in an *RP* retina. In the current study, transfections with the *PEDF*/*BDNF* plasmids were performed in A-172 cells, both in suspension and when the cells were cultured on a surface, following the initial transfections with the *Venus* reporter gene.

5.2. Transfections of cells in suspension

The Neon Transfection System is a small-scale bench-top device used to transfect cells in suspension. The device had been extensively used within our research group and was chosen as the primary device to analyse transfection of the A-172 cell line with *Venus*, *PEDF* and

BDNF. Initial transfections of the A-172 cell line with the *Venus* reporter transposon using the *SB100X* transposase showed positive results, which are summarized in Figures 15-17. Figure 16 illustrated that transfection efficiency increased continuously with increasing pulse width or pulse number at any given voltage. Additionally, a stronger dependence of the results on pulse width and number of pulses was observed, with 30 ms, 3-pulse settings consistently showing lower viabilities compared to 30 ms, 2-pulse settings (Figure 16). While this result can be explained by electroporation-induced necrosis, which shows a dependence on pulse amplitude and number of pulses (215, 216), it is contrary to what was shown in another study (217), in which transfection of primary bovine fibroblasts with rectangular pulses showed a negligible dependence on pulse number. Nevertheless, the significance of voltage should not be underestimated since in the current study, since the setting 1150 V, 30 ms, 2 pulses yielded good and reliable results with regards to both transfection efficiency and cell viability compared to other settings with the same pulse width and number (Figure 16 and 17).

A marked fluctuation in the fluorescence intensity within the transfected cell populations was observed (Figure 18). This was also reported by Cao *et al.* when they transfected HeLa cells in suspension and on a surface using a nano-electroporation platform (218, 219).They observed that the cells closest to the plasmid source showed the highest fluorescence intensity. This indicated that the fluorescence intensity of the cells is directly proportional to the number of introduced plasmid copies. In this context, it was demonstrated in a previous study that variation in the amount of plasmid uptake by cells can be reduced by increasing the membrane tension of the cells (220).

Another observation made in the current was that the proportion of transfected cells decreased the longer the cells were maintained in culture (Figure 18 and 19). There could be several reasons for this. The first reason could be the faster growth rate of non-transfected cells compared to transfected cells. Over time, the non-transfected cells outgrow the transfected cells. The difference in growth rate was demonstrated by Matsuyama *et al.*(221). This effect was also reported by a previous study conducted in our working group, involving transfection of ARPE-19 cells with *Venus* using the *SB* transposon system (200). A second reason could be a side effect of the *SB* transposon system, as demonstrated in a study by Walisko *et al.* The reduction in transfected cell growth rate in this case, was reported to be specifically due to the downregulation of cyclin-D1 expression by the *SB* transposase due to its interaction with the transcription factor Miz-1 (222). Another study reported a cytotoxic effect of the *SB* transposase that was dose dependent, while being independent of the presence of the transgene-

carrying plasmid (223). A third reason could be a suppression of transgene expression that occurs in transfected cells. One study demonstrated by transfecting a pre-B cell line with *GFP*, that retroviral transcription of a transgene was suppressed in a heritable and irreversible manner (224). Additionally, they demonstrated that this suppression occurred over several months and was independent of the previous conditions. Finally, it was reported by Batard *et al.* that cells with a maximum DNA load are negatively affected in terms of cell growth and survival while expressing the highest level of the transgene (225). In another study, the size of the plasmids used were demonstrated to affect the cell survival immediately post-transfection, with large plasmids (> 6 kb) resulting in low cell viabilities (226). In the current study, the smallest plasmid, pT2-CAGGS-Venus (5888 bp), and the largest plasmid, pT2-CMV-PEDF/EGFP (7205 bp), resulted in comparable cell viabilities at 1150 and 1200 V when analysed with a luciferase assay performed 24 hours post-transfection (Figure 17 and 26). On the other hand, pT2-CMV-BDNF/EGFP (6745 bp) resulted in a lower cell viability by comparison (Figure 26). Nevertheless, the difference in the survival rates across the different plasmids used in the current study was not significant overall and no definite conclusion could be drawn regarding the effect of plasmid size.

A previous study by Peng *et al.* using Chinese Hamster Ovary (CHO) mouse melanoma and rat heart myoblast cells with nano-, micro- and millisecond pulses showed that the rate of decrease in cell survival after transfection depends on the cell type (227). The current study included transfections of the A-172 cell line and the R28 cell line with the *Venus* reporter plasmid using the Neon device, which allowed comparison of differences in transfection efficiency and cell viability by cell type. The typical doubling time for A-172 cells is 40 - 48 hours (203, 228), and these cells required at least six days to reach sufficient cell density for downstream analyses (Figure 1). In contrast, the R28 cell line, due to its faster doubling time (24 hours) (229), only required culturing for two days post-transfection before downstream analyses (Figure 36). The maximum achievable mean transfection efficiency for A-172 cells (37.2 ± 22.5 %) was 2.3-fold higher than that for R28 cells. This is in contrast to a study by Neuhaus *et al.* who compared *EGFP* transfection in nine cell lines and observed that the cell lines with the shortest doubling times had the highest transfection efficiency (230).

As a final observation, as time progressed, most of the transfected cells were detected in clumps, with non-transfected cells being concentrated in the areas outside the clumps (Figure 18). This could be due to the gradual change in the viscosity of the medium. When cells die, the intracellular contents are spilled into the medium, including free DNA, proteins and

cytokines. The free DNA increases the viscosity of the solution in the immediate environment. This was demonstrated by Newton *et al.* who observed an increase in the viscosity of *E.coli* cultures together with an increase in the ratio of sheared cells and concluded that this was due to interactions between living cells and leaked cell contents such as DNA (231). The released proteins can also trigger inflammatory responses in the surrounding healthy cells (232), causing these cells to undergo programmed cell death. Together, these factors would lead to clumping of the damaged cells and cells in the vicinity (Figure 18).

Following the *Venus* transfections, A-172 cells were transfected with *PEDF* and *BDNF*. *PEDF* transfection led to a 3 - 20 fold increase in protein yield, compared to the control (Figure 21). In this case, 1000 V was the setting with the highest yield, although, in contrast, a western blot showed a significant increase in band area compared to the control, when 1150 and 1200 V were applied (Figure 20). The latter result was supported by an RT qPCR (Figure 22). An ELISA, performed with *BDNF*-transfected samples demonstrated a drastic increase in protein production (100 - 200 fold) compared to the control (Figure 23). In this case, 1100 V was consistently the setting with the best results. When studying the increase in protein productions achieved with *PEDF* and *BDNF* transfections, the latter consistently provided a higher increase in protein production as opposed to the larger transposon plasmid *PEDF*, when comparing the yield against their respective controls. However, when comparing the protein yields directly, PEDF-transfections resulted in much better outcomes (170 - 1090 pg/h/10^4 cells) compared to BDNF-transfections (36 - 71 pg/h/10^4 cells).

Regarding the possible effect of plasmid size on the differences in protein yield observed, a study by Ribeiro *et al*. explores the idea of the effect of plasmid size on transfection efficiency (233). They demonstrated that when human MSCs and mouse NSCs were transfected with smaller plasmids, the intracellular plasmid copy number achieved was higher than larger plasmids. Nevertheless in the current study, further experiments need to be conducted to confirm the role of plasmid size.

5.3. Transfections of cells cultured on a surface

The NEPA-21 Electroporator II is a customizable electroporation device with a wide variety of electrodes setups that can be used to transfect cells or tissue *in vitro*, *in vivo* or *ex vivo*. The NEPA-21 device performs electroporation by delivering two separate pulses - a high energy

pulse of short duration (PP), meant to create a large number of transient pores with a post-pulse life of a few milliseconds, and a low energy pulse of longer duration (TP), meant to create a smaller number of larger pores which facilitate transfer of genetic material into the cell (234). This device has been extensively used for transfection experiments. One example is the study conducted by Hayashi *et al.*, in which they knocked down low-density lipoprotein receptor-related protein 1 (LRP1) in Müller cells using LRP1-specific small interfering RNA (siRNA) (235). One of the objectives of the current study was to analyse the transfection of A-172 cells cultivated on a surface. The NEPA-21 device, in combination with the CUY900-13-3-5 electrode, was well suited for this purpose. The CUY900 series of electrodes is specifically meant for cells cultured on surfaces. The electrode is placed onto the cells from above. Previous research utilizing these electrodes has shown promising results in C2C12-derived myotubes (236), primary mouse neurons (237) and rat Müller cells (235).

In the current research, it was evident that *Venus* transfection of A-172 cells cultivated on a surface resulted in a much lower efficiencies compared to transfection in suspension (Figure 16 and 27). Further transfections with *PEDF*/*BDNF* led to similar results, with much lower protein yields (Figure 29 and 32) compared to transfections with the Neon device. This is consistent with the results of Porosk *et al.*, who compared transfection of CHO cells in suspension and on a surface and reported a reduction in efficiency in the latter case (238). *PEDF* transfection led to a 4 - 20 fold increase in protein yield compared to the control while *BDNF* transfection led to a 23 - 155 fold increase. Contrary to the observation made when comparing with transections with the Neon device, the direct PEDF protein yield achieved (15 - 70 pg/h/10^4 cells) was also lower compared to the BDNF protein yield (2.06 - 12.7 x 10^3 pg/h/10^4 cells). However, the cell viability post-transfection on a surface, was much lower with *BDNF* transfections (2.5 - 102.5 x 10^3 cells/ml) compared to *PEDF* transfections (5 - 340 x 10^3 cells/ml), which made the downstream analysis of *BDNF*-transfected samples challenging.

Previous research by Yoshimitsu *et al.* demonstrated the importance of PP and TP parameters on the transfection frequency (239). They observed that transfection efficiency increased only up to a certain limit of PP and TP and decreased after reaching this limit. The importance of separating the two pulses was demonstrated in another study, where TP in combination with PP significantly increased luciferase activity in transfected murine muscle samples compared to PP alone (240). Finally, André *et al.* demonstrated the importance of a time interval between PP and TP (234). They reported that separating PP and TP allowed them greater flexibility and

independent control of the parameters involved, resulting in efficient gene electrotransfer in the tissues explored.

According to the manufacturer's instructions for the NEPA-21 device, the electrode had to be rotated 90º and the transfection had to be performed twice for each well, using both PP and TP with polarity exchange (±) to achieve a uniform distribution of the electric field. However, this led to excessive stress on the cells, significantly reducing their viability, as evident from the negligible cell survival rate in Figure 27 B. Placing the electrode in only one direction led to a slight improvement in cell viability when both PP and TP were applied with polarity exchange (±) (Figure 27 A). However, the maximum transfection efficiency was observed when TP was applied with polarity exchange (±) and PP without (+) (Figure 27 D). As a result, the setup used in Figure 27 D (PP: +, TP: ±, electrode: 0 + 90º) was chosen for all further transfections with cells on surfaces.

5.4. Transfections with the MEA device

Retinal implants are a treatment option for *RP* patients. The first implants were based on the structure of a healthy retina, but did not take into account the degenerative changes, which explains why these implant structures were less successful than expected. Genetic engineering of retinal cells *in vivo* using MEAs to produce protective proteins could potentially have a positive effect on retinal remodelling, thereby increasing the efficacy of retinal prostheses. Previous studies have already shown that it is possible to transfect cells using MEAs. Guo and Zhu used a microarray chip to successfully transfect HeLa cells with plasmid encoding *EGFP* (241). In another study, the authors established a single-cell individualized electroporation method using MEAs via real-time impedance monitoring, to transfect cells from different cell lines with *EGFP*, and were able to achieve transfection efficiencies over 95% (242). Further, Duckert *et al*. successfully transfected HeLa cells with mCherry-mRNA via MEA-based electroporation (171). Finally, a study demonstrated the use of MEAs for site-specific transfection of HeLa cells with Alexa 488-tagged scrambled sequence of siRNA (243).

Recently, Kauth *et al.* successfully transfected adherent HEK-293T cells with pmaxGFP using a specialized MEA (174). The current work focused on transfection of A-172 and R28 cell lines with pmaxGFP using the MEAs designed by Ms. Andrea Kauth (IWE-1, RWTH Aachen)

to determine whether glial cells and retinal progenitor cells are potential candidates for electroporation using this technology.

Previous research has shown that electrode shape in a MEA is a crucial factor in ensuring a uniform electric field distribution to all cells. Ms. Aracelys Garcia Moreno, who performed the seminal work on MEA-based electroporation devices at the IWE-1, reported that the electrode shape with the best electric field distribution combined semicircular shapes in a triangular arrangement (175). These new electrodes, described as semicircular-triangular, were also used by Kauth *et al.* in their research (174). Another important aspect of MEA-based electroporation is the arrangement of active and ground electrodes within the array. Kauth *et al.* determined that the best option in this context was a checkerboard arrangement. Nevertheless, not all MEA-based research has found the checkerboard arrangement to be the best option. Browne *et al.*, who used an electrode array to transfect HEK-293 cell monolayers with *GFP* (244), found that the best option in this case was a tandem configuration of active to ground electrodes. In another study, Kung *et al.* used needle electrodes in a concentric active-ground electrode arrangement, to perform successful transfection in the brain of zebrafish, with minimized scarring and tissue damage (245). In the present work, different arrangements of active and ground electrodes were attempted (Figure 13) to determine the ideal setup. It was observed that, contrary to the observation by Ms. Moreno and Kauth *et al*., triangle electrodes were the best for transfection, coupled with the repeated concentric arrangement of active-ground electrodes shown in Figure 13. In a previous study, triangle electrodes in an interdigitated electrode setup, were reported to have strong induced electric fields to at the corners of the triangles, which could contribute to an increased rate of electroporation at these sites (246).

The shape of the delivered pulses also plays a critical role in the process of transfection (247). Sánchez *et al.* studied the effects of electroporation using sinusoidal pulses and compared them with those of bipolar square pulses (248). They concluded that there was equivalence in terms of the average power applied to the cell membrane. The authors suggested using sine waves with well-defined narrow frequency band to enable better uncoupling of the different effects of the electric field during transfection. Kauth *et al.* also used sine wave pulses in their study with the MEA device (174).

When comparing the frequency with the strongest cell distribution against the total impedance, a peak occurred at approximately 40 kHz. At this point, the voltage drop across the adherent cells is the largest, so that the electric field strength at the cell membrane is at its maximum

(174). Based on this data, the present study was conducted using sine wave pulses of 40 kHz in all experiments. Initially, A-172 cells were used, but MEA transfections did not work well with this cell line, so we switched to the R28 retinal progenitor cell line, which displayed successful transfection during preliminary experiments. This difference in transfection efficiency, specifically between the R28 and A-172 cell lines could be due to the presence/absence of voltage-gated ion channels (VGICs). The application of an electric field to cells can disrupt VGICs, leading to the formation of stable and complex pores in the voltage sensor domains of the VGICs, which in turn would reduce the stability of the cell membrane (249). When comparing the two cell lines in question, the R28 cell line was found to lack VGICs (250), while the A-172 cell line was found to express high levels of voltage-gated sodium channels on the cell surface (251). Nevertheless, other cell properties like average cell area and geometry could also play a vital role in the transfection efficiency (160).

In the present study, it was observed that the transfected cells were sometimes located outside the electrode area (Figure 37, G, H, J and K). This could be due to electroporation-induced cell detachment, an effect that has been documented previously. One example is the study where it was reported that electroporation of MCF-7 cells led to an alteration in cell adhesiveness and phenotype, which in turn led to decreased cell-substrate contacts and increased cell-cell contacts (252). In this case, the cells were cultured on a fibronectin-coated 24-well plate before transfection with propidium iodide (PI) using a custom electrode. Nevertheless, in the same study, the authors concluded that the overall decrease in adhesion observed in the MCF-7 cell line due to electroporation was not significant. An alternative explanation for the cells found outside the electrode area is cell migration and division that occurs in the 24 hours between electroporation and analysis of transfection, an effect that was also reported by other research groups (253, 254). In Figure 37 (D, E, G and I), a few transfected cells were observed in the non-conducting space between two electrodes. This could be due to fringing of the electric field into the inter-electrode space, as observed in dye loading studies for HEK-293 and Hep G2 cells (169). When the two opposing electrodes are close to each other and the field does not penetrate deeply into the bulk electrolyte, the resulting fringing of the electric field may result in sufficient field strength in the gap between electrodes to transfect cells in these areas (169).

5.5. Role of cell size, shape and orientation in transfection

Different cell lines show different transfection efficiencies. Transfection of the ARPE-19 cell line with *Venus* and the *SB* transposon system resulted in 100% efficiency (143). However, transfections of the A-172 and R28 cell lines resulted in much lower efficiencies (Figure 17 and 37). It was also observed that transfection efficiency decreased when transfecting A-172 cells on a surface compared to transfecting them in suspension (Figure 28 and 17). Moreover, electroporation of R28 cells with the MEA device resulted in transfected cells (Figure 37), whereas it was hardly possible to transfect A-172 cells with the parameters tested (Figure 34).

In this study, the dependence of transfection efficiency on the geometric properties of the cells was investigated. The two-dimensional (2D) cell areas and geometric properties of cells in images of the cell lines A-172, ARPE-19 and R28 were measured individually for each cell and compared. For the comparison of mean 2D cell areas directly (Figure 39), images of cells cultured on surfaces were used. However, for subsequent CVa and *e* comparisons (Figure 40), images of both cells in suspension and on a surface were used. For better understanding, a larger 2D cell area was also interpreted as a larger cell surface area and vice versa. In order to obtain an accurate image of the cells in suspension, it was important that as many cells as possible were on the same plane during imaging acquisition. For this purpose, the cells were passaged and the image was taken immediately after the cells first settled on the surface. At this point, most of the cells were still spherical and on the same plane. When plated on a surface, there was a significant difference in the mean 2D area between cells from the different cell lines, with A-172 cells having the largest mean cell size and R28 having the smallest (Figure 39). While this effect could explain the different ideal voltages required for the transfection of different cell lines, it could not be proven conclusively in the current study. Additionally, it had been observed that cells immediately after seeding or in suspension have a smaller 2D area than cells attached on a surface (Appendix, table 24), since cells in suspension adopt a spherical shape (255-257). When they attach to a surface, the cells spread out, thereby increasing their surface area (258). The larger surface area of adherent cells could explain why they require a lower voltage transfection compared to cells in suspension (Figure 28 and 17). This effect was demonstrated in a previous study on the transfection of CHO cells (259).

In the current study, it was observed that the more uniform cells in a particular cell line were in terms of cell size, the higher the transfection efficiency. This conclusion was drawn by comparing the known transfection efficiencies of the ARPE-19 (143) and A-172 cell lines

(Figure 17) in suspension with the corresponding variation in the average 2D cell area of these cell lines (Figure 40, A2 and B2). The variation in cell area was measured using the coefficient of variation of the 2D cell area (CVa), which was determined from microscopy images and it was observed that an increase in CVa was accompanied with a decrease in transfection efficiency. However, further experiments need to conducted to determine the exact role of CVa on transfection efficiency. The measure of CVa may also explain the difference in transfection efficiency observed between cells transfected in suspension and on a surface, for any given cell line. In Figure 39 A, A-172 cells show a significant increase in their respective CVa when the cells attach to the surface, compared to in suspension.

The slight decrease in CVa of A-172 cells, as observed 24 hours post-transfection using the Neon device, followed by a further decrease in CVa when observed one week post-transfection (Figure 40, A 2-4), can be explained by changes that occur in the cell population as a result of electroporation. Transfection alters the morphology of cells, an observation made by Zhurbitskaya *et al.* during transfection of immortalized rat embryonic fibroblasts (260). This effect was also observed by Graybill *et al.* during transfection of the glioblastoma cell line U-251. The cells became round immediately post-transfection and regained their original morphology a few hours later (261). In the present study, the initial change in the morphology of the transfected cells led to an increase in the CVa of the cell population, followed by a decrease in CVa as the living cells recovered their old morphology. Overall, a slight decrease in CVa 24 hours post-transfection, was expected, as observed in Figure 40 (A2 and A3). The more cells recovered from transfection, the further CVa decreased, which was observed one week after electroporation in A-172 cells (Figure 40, A2 and A4). When comparing these observations with R28 cells transfected with the MEA device, a significant increase in CVa was observed when the cells attached to the MEA surface, followed by a drastic decrease, 48 hours post-transfection (Figure 40 D). Additionally, the inverse relation observed between the transfection efficiency and CVa in the A-172 cell line, was not clearly visible with the R28 cell line. The short doubling and recovery time of R28 cells could be the reason for these observations.

Analysis of A-172 cells one week post-transfection on a surface using the NEPA device showed mixed results (Figure 40, C 1-3). The expected decrease in CVa after transfection was observed, but only when the electrode was placed in one direction, with both PP and TP applied with polarity exchange (±) (Figure 40 C3). On the other hand, Figure 40 C2, where PP was applied without (+) and TP with polarity exchange (±), showed a significant increase in CVa,

which could be due to the greater dependence of transfection on TP compared to PP, as shown by Satkauskas *et al.* in their work (240). A higher TP would cause greater changes in the morphology (261), but would also lead to higher transfection efficiency (Figure 28).

The investigation of the cell shape and its orientation within the electric field may also explain the observed differences in transfection efficiency between transfection in suspension and on a surface. The polarization of the cell membrane during electroporation is not uniform across its entire surface. The membrane is hyperpolarized where it faces the anode and depolarized where it faces the cathode. This effect was observed by Gross *et al.* when they applied an electric field to A-431 human carcinoma cells (262). The fluorescent probe used in this study was detected most strongly on the side of the cell facing the anode. Another study investigating the electroporation of sea urchin eggs showed that the increase in membrane conductivity occurred more rapidly on the side of the cell facing the anode (263, 264). The orientation of the cell within the electric field determines the cell surface area affected by the electric field. This was demonstrated by Valič *et al.* in their study on the transfection of CHO cells (265). Rosazza *et al.* theorized that, given a certain electric field strength and a non-spherical cell, the permeabilization area is largest when the longest axis of the cell is parallel to the electric field lines, and *vice versa* (160). Since A-172 cells are spindle-shaped on a surface, the influence of cell orientation on transfection efficiency would be much greater compared to A-172 cells in suspension. This would result in a decrease in the transfection efficiency of A-172 cells on a surface compared to electroporation in suspension (Figure 17 and 28). To prove that A-172 cells in suspension are more spherical than cells on a surface, the eccentricity (*e*) of the cell population was examined. When a cell attaches to a surface, it becomes more elliptical, leading to an increase in *e*. This was observed in both the A-172 cell line (Figure 40, A1 and A2) and the ARPE-19 cell line (Figure 40, B1 and B2). In this case, the mean values of *e* were used. The *e* value also reflected the change in cell morphology post-transfection (261). Both A-172 and ARPE-19 cells transfected with the Neon device showed a decrease in *e,* 24 hours after transfection (Figure 40, A3 and B3). Interestingly, cells transfected on a surface showed no significant change in *e* in either the A-172 and R28 cell lines (Figure 40, C and D), even one week post-transfection. This suggested a lack of flexibility in the morphology of cells transfected on surfaces.

5.6. Cultivation and transfection of primary Müller cells

Müller cells play an important supporting role in the retina. For this purpose, they have a unique structure that allows them to span the entire thickness of the retina (266). Müller cells are so important for retinal function that they are the only cell type that comes into contact with and envelops the cell bodies and processes of every class of retinal neuron (reviewed in (267)). The fovea of primates has Müller cells and photoreceptors in a 1:1 ratio, while these cells occur in a 1:11 ratio in the periphery of the retina (268). The gliosis that occurs during retinal remodelling causes the MG to expand and form a seal across the entire retina (39, 41, 42). All these reasons make the MG a possible candidate for gene therapy. Previous research has investigated the advantage of using Müller cells as a target. One study focused on the potential of Müller cells as a target in CRB1 *RP* mouse models and concluded that the combined targeting of both Müller cells and photoreceptors yielded the most ideal results (269). Peynshaert *et al.* transfected Müller cells with *GFP* mRNA using lipofection and found that the transfected cells were able to maintain high protein expression even under lipoplex-induced stress conditions such as hypoxia, hyperglycemia, and oxidative stress (270). In another study, rat Müller cells were transfected with *hPEDF*. They reported that secreted PEDF was able to protect the transfected cells against H_2O_2-mediated cell death (271). Eichler *et al.* investigated the survival of RGCs in co-culture with Müller cells and reported that co-culture had a similar protective effect as direct treatment of RGCs with PEDF (272). They concluded that enhancing the PEDF secretion function of Müller cells could be beneficial for promoting RGC survival in neurodegenerative diseases of the retina. In this context, BDNF was also investigated as a GOI. In a study by Gauthier *et al.*, rat Müller cells were transduced with BDNF. As a result, the ERG recordings of the treated eyes were preserved (273). These findings provide initial insight into the advantages of using MG as a target for gene therapy.

The present research also explored the idea of using Müller cells as a target for gene therapy. The isolation and cultivation of primary Müller cells was established within our group as a part of the current study. The protocol was based on the work of Xiao *et al*. (274), with several modifications to optimize cell survival and primary cell yield. Specifically, since the previous protocol suggested using at least two mice, the current work used four mice per isolation in order to obtain a higher cell yield per batch. The enzymatic dissociation time was reduced from 60 minutes to 40 minutes to improve cell viability. For coating the culture surfaces, a 0.2% gelatine solution was used in place of 0.1%, as this was observed to result in a slight improvement in cell adherence. Unlike the original protocol, which included 2 - 3 passages, cells were maintained without passaging until transfection to prevent cell loss during passaging

and to reduce additional cell stress. Pereiro *et al.* also established the isolation of Müller cells from mammalian retinas and reported that 24 hours after plating the isolated cell mixture, Müller cells constituted the majority of cells attaching to the surface. By replacing the medium at this time point, they were able to obtain a relatively pure culture of Müller cells (188). This technique was adapted in our work, instead of the initial medium change five days after isolation, as suggested by Xiao *et al*. The protocol was initially altered to use the same amount of FBS in the medium as the A-172 cell line (10%), although the concentration was increased to 20% since better cell survival was observed in the latter case.

The isolated Müller cells were cultivated on Lab-Tek II chamber slides (RS glass) with a cell culture area of 1.7 cm^2. This was done to enable direct immunocytochemistry without passaging the cells. Immunocytochemistry of the isolated cells demonstrated that the cells were positive not only for MG markers such as GS and vimentin, but also for GFAP. GFAP expression is typically detected in MG in response to retinal detachment (275) or damage (276, 277). Therefore, the GFAP observed in Figure 43 could be a result of the retinal isolation process. GFAP expression in isolated primary Müller cells has been detected in previous studies on human and rat retinas (278, 279).

The Müller cells were first transfected with the Neon device (Figure 44) using identical settings and plasmid concentration as for the A-172 experiments (Figure 19), as both are of glial origin. After the first passage, half of the cells were used for transfection, while the other half was used to propagate the culture. However, a significant proportion of cells died after the passaging and transfection process. Additionally, it was observed that the morphology of the transfected cells differed drastically from normal MG morphology (Figures 42, 44 and 45). Since it was crucial to improve the viability of the cells, the Müller cell cultures were used in their entirety in further experiments.

Electroporation-induced bubble formation near the electrode has been demonstrated in previous research (280, 281). Microbubbles have also been recognized as a challenge in Neon device-based electroporation, potentially leading to sparking and reduction in transfection efficiency (282). In the current study too, bubble formation had been observed with the transfection of the A-172 cells with higher voltages (1300 V and above). In the context of Müller cell transfection, bubble formation was observed near the electrode during the first pulse application, when voltages higher than 1150 V were attempted. This prevented the second pulse from being delivered properly due to little contact of the electrode with the transfection buffer.

The first pulse was therefore initially delivered to one portion of the cells, after which the second portion of the cells was combined with the transfected cells in order to be exposed to a second pulse. This was done in order to ensure transfection of all the isolated Müller cells while also reducing electroporation-induced stress on the cells. Immunocytochemistry results show positive transfection in Müller cells, although the transfection efficiency was low (Figure 45). No anti-vimentin antibody was used for the immunocytochemistry of the transfected samples, as the emission wavelength of the secondary antibody was similar to that of Venus, with which the cells were transfected.

Additional Müller cells cultures were used for NEPA transfections. Since the cells were stressed after isolation and transfection, immunocytochemistry was performed directly on the 24-well plates in which the cells were maintained. These preliminary results show us that transfection of Müller cells with the *SB* transposon system is possible. However, further optimisation of the transfection parameters is necessary and must be investigated in further research.

5.7. Conclusion and outlook

The current study sought to establish the transfection of glial cell lines and primary cells in suspension and on a surface. Glial cells were chosen based on the fact that the gliosis that happens with the retina during RP might make the Müller glial cells a better target for gene therapy. The results observed led to the conclusion that these transfections using the *SB* transposon system are possible, not only for the Venus reporter, but also with the neuroprotective genes *PEDF* and *BDNF*. Further studies have to be performed regarding the long term transfections with *PEDF* and *BDNF*. The effect that the expressed proteins have on transfected and non-transfected cells when in a co-culture also has to be studied in the future.

MEA transfection was successfully demonstrated in the current study. Several other combinations of active and ground electrodes, exist, which, if tested, could provide us more information regarding the ideal set of parameters for transfection with the MEA device. The MEA electrode array covers a very small area and specific techniques need to be developed to optimally harvest the transfected cells for further analyses.

When elucidating the possible correlation between cell size, geometry and the transfection efficiency, the next step would be to test if other cell parameters like cell axes length and lipid content of the cell membrane, have an effect on the overall transfection efficiency.

The isolation of primary Müller cells from four week old WT mice was established in the current study. Fine tuning of this protocol is possible to increase the yield. Additionally, the *PEDF*/*BDNF* transfection of Müller cells is yet to be established. Of particular interest would be the transfection of Müller cells using the MEA device.

In conclusion, in the current work, further insights were gained into the transfection of glial and retinal progenitor cell lines in suspension and on a surface. These studies were expanded upon, with transfection using a custom MEA device. It was also reported that transfection of primary Müller cells in suspension is possible. Further studies could expand on this research and lead to the merging of the functionalities of GCL stimulation and transfection of Müller cells on a MEA chip.

6. References

1. Hoon M, Okawa H, Della Santina L, Wong RO. Functional architecture of the retina: development and disease. Progress in retinal and eye research. 2014;42:44-84.
2. Goldman D. Müller glial cell reprogramming and retina regeneration. Nature reviews Neuroscience. 2014;15(7):431-42.
3. Turner DL, Cepko CL. A common progenitor for neurons and glia persists in rat retina late in development. Nature. 1987;328(6126):131-6.
4. Reichenbach A, Reichelt W. Postnatal development of radial glial (Müller) cells of the rabbit retina. Neuroscience letters. 1986;71(2):125-30.
5. Magalhães MM, Coimbra A. The rabbit retina Müller cell. A fine structural and cytochemical study. Journal of Ultrastructure Research. 1972;39(3):310-26.
6. Bringmann A, Pannicke T, Grosche J, Francke M, Wiedemann P, Skatchkov SN, *et al*. Müller cells in the healthy and diseased retina. Progress in Retinal and Eye Research. 2006;25(4):397-424.
7. Franze K, Grosche J, Skatchkov SN, Schinkinger S, Foja C, Schild D, *et al*. Müller cells are living optical fibers in the vertebrate retina. Proceedings of the National Academy of Sciences of the United States of America. 2007;104(20):8287-92.
8. Bringmann A, Pannicke T, Biedermann B, Francke M, Iandiev I, Grosche J, *et al*. Role of retinal glial cells in neurotransmitter uptake and metabolism. Neurochemistry International. 2009;54(3-4):143-60.
9. Pow DV, Crook DK. Direct immunocytochemical evidence for the transfer of glutamine from glial cells to neurons: use of specific antibodies directed against the d-stereoisomers of glutamate and glutamine. Neuroscience. 1996;70(1):295-302.
10. Schütte M, Werner P. Redistribution of glutathione in the ischemic rat retina. Neuroscience letters. 1998;246(1):53-6.

11. Seki M, Nawa H, Fukuchi T, Abe H, Takei N. BDNF is upregulated by postnatal development and visual experience: quantitative and immunohistochemical analyses of BDNF in the rat retina. Investigative Ophthalmology and Visual Science. 2003;44(7):3211-8.

12. Tout S, Chan-Ling T, Holländer H, Stone J. The role of Müller cells in the formation of the blood-retinal barrier. Neuroscience. 1993;55(1):291-301.

13. Shen W, Fruttiger M, Zhu L, Chung SH, Barnett NL, Kirk JK, *et al*. Conditional Müller cell ablation causes independent neuronal and vascular pathologies in a novel transgenic model. The Journal of Neuroscience. 2012;32(45):15715-27.

14. Nagelhus EA, Horio Y, Inanobe A, Fujita A, Haug FM, Nielsen S, *et al*. Immunogold evidence suggests that coupling of K+ siphoning and water transport in rat retinal Müller cells is mediated by a coenrichment of Kir4.1 and AQP4 in specific membrane domains. Glia. 1999;26(1):47-54.

15. Reichenbach A, Bringmann A. New functions of Müller cells. Glia. 2013;61(5):651-78.

16. Bringmann A, Iandiev I, Pannicke T, Wurm A, Hollborn M, Wiedemann P, *et al*. Cellular signaling and factors involved in Müller cell gliosis: neuroprotective and detrimental effects. Progress in Retinal and Eye Research. 2009;28(6):423-51.

17. Erickson KK, Sundstrom JM, Antonetti DA. Vascular permeability in ocular disease and the role of tight junctions. Angiogenesis. 2007;10(2):103-17.

18. Knighton RW, Jacobson SG, Kemp CM. The spectral reflectance of the nerve fiber layer of the macaque retina. Investigative Opthalmology and Visual Science. 1989;30(11):2392-402.

19. Martins-Ferreira H, de Castro GO. Light-scattering changes accompanying spreading depression in isolated retina. Journal of Neurophysiology. 1966;29(4):715-26.

20. Toth CA, Narayan DG, Boppart SA, Hee MR, Fujimoto JG, Birngruber R, *et al*. A comparison of retinal morphology viewed by optical coherence tomography and by light microscopy. Archives of Ophthalmology (Chicago, Ill : 1960). 1997;115(11):1425-8.

21. Reichenbach A, Robinson SR. Phylogenetic constraints on retinal organisation and development. Progress in Retinal and Eye Research. 1995;15(1):139-71.

22. Report: World Health Organization world report on vision. 2019.

23. GBD blindness and vision impairment collaborators. Causes of blindness and vision impairment in 2020 and trends over 30 years, and prevalence of avoidable blindness in relation to VISION 2020: the Right to Sight: an analysis for the Global Burden of Disease Study. The Lancet Global health. 2021;9(2):e144-e60.

24. Wong WL, Su X, Li X, Cheung CM, Klein R, Cheng CY, *et al*. Global prevalence of age-related macular degeneration and disease burden projection for 2020 and 2040: a systematic review and meta-analysis. The Lancet Global health. 2014;2(2):e106-16.

25. Smith W, Mitchell P, Leeder SR. Smoking and age-related maculopathy. The Blue Mountains eye study. Archives of Ophthalmology (Chicago, Ill : 1960). 1996;114(12):1518-23.

26. Katsi VK, Marketou ME, Vrachatis DA, Manolis AJ, Nihoyannopoulos P, Tousoulis D, *et al*. Essential hypertension in the pathogenesis of age-related macular degeneration: a review of the current evidence. Journal of Hypertension. 2015;33(12):2382-8.

27. Chapman NA, Jacobs RJ, Braakhuis AJ. Role of diet and food intake in age-related macular degeneration: a systematic review. Clinical & Experimental Ophthalmology. 2019;47(1):106-27.

28. Shaw PX, Stiles T, Douglas C, Ho D, Fan W, Du H, *et al*. Oxidative stress, innate immunity, and age-related macular degeneration. AIMS Molecular Science. 2016;3(2):196-221.

29. Moreno-García A, Kun A, Calero O, Medina M, Calero M. An overview of the role of lipofuscin in age-related neurodegeneration. Frontiers in Neuroscience. 2018;12:464.

30. Coleman HR, Chan CC, Ferris FL, 3rd, Chew EY. Age-related macular degeneration. Lancet (London, England). 2008;372(9652):1835-45.

31. Carleton M, Oesch NW. Bridging the gap of vision restoration. Fronteirs in Cellular Neuroscience. 2024;18.

32. Boughman JA, Conneally PM, Nance WE. Population genetic studies of *retinitis pigmentosa*. American Journal of Human Genetics. 1980;32(2):223-35.

33. O'Neal TB, Luther EE. *Retinitis Pigmentosa*. StatPearls. Treasure Island (FL) ineligible companies. StatPearls Publishing LLC.; 2024.

34. Daiger SP, Bowne SJ, Sullivan LS. Genes and mutations causing autosomal dominant *retinitis pigmentosa*. Cold Spring Harbor Perspectives in Medicine. 2014;5(10).

35. Rivolta C, Sharon D, DeAngelis MM, Dryja TP. *Retinitis pigmentosa* and allied diseases: numerous diseases, genes, and inheritance patterns. Human Molecular Genetics. 2002;11(10):1219-27.

36. Daiger SP, Sullivan LS, Bowne SJ. Genes and mutations causing *retinitis pigmentosa*. Clinical Genetics. 2013;84(2):132-41.

37. O'Hare F, Bentley SA, Wu Z, Guymer RH, Luu CD, Ayton LN. Charles Bonnet Syndrome in advanced *retinitis pigmentosa*. Ophthalmology. 2015;122(9):1951-3.

38. Marc RE, Jones BW, Watt CB, Strettoi E. Neural remodeling in retinal degeneration. Progress in Retinal and Eye Research. 2003;22(5):607-55.

39. Jones BW, Pfeiffer RL, Ferrell WD, Watt CB, Marmor M, Marc RE. Retinal remodeling in human *retinitis pigmentosa*. Experimental Eye Research. 2016;150:149-65.

40. Milam AH, Li ZY, Fariss RN. Histopathology of the human retina in *retinitis pigmentosa*. Progress in Retinal and Eye Research. 1998;17(2):175-205.

41. Zhao TT, Tian CY, Yin ZQ. Activation of Müller cells occurs during retinal degeneration in RCS rats. Advances in experimental medicine and biology. 2010;664:575-83.

42. Jones BW, Marc RE, Pfeiffer RL. Retinal degeneration, remodeling and plasticity. Webvision: The Organization of the Retina and Visual System. Salt Lake City (UT): University of Utah Health Sciences Center. 1995.

43. Marc RE, Jones BW. Retinal remodeling in inherited photoreceptor degenerations. Molecular Neurobiology. 2003;28(2):139-47.

44. Kuo CN, Chen CY, Chen SN, Yang LC, Lai LJ, Lai CH, *et al*. Inhibition of corneal neovascularization with the combination of bevacizumab and plasmid pigment epithelium-derived factor-synthetic amphiphile INTeraction-18 (p-PEDF-SAINT-18) vector in a rat corneal experimental angiogenesis model. International Journal of Molecular Sciences. 2013;14(4):8291-305.

45. Matsui T, Nishino Y, Maeda S, Yamagishi S. PEDF-derived peptide inhibits corneal angiogenesis by suppressing VEGF expression. Microvascular research. 2012;84(1):105-8.

46. Jones BW, Watt CB, Frederick JM, Baehr W, Chen CK, Levine EM, *et al*. Retinal remodeling triggered by photoreceptor degenerations. The Journal of Comparative Neurology. 2003;464(1):1-16.

47. McClements ME, Elsayed MEAA, Major L, de la Camara CM-F, MacLaren RE. Gene therapies in clinical development to treat retinal disorders. Molecular Diagnosis & Therapy. 2024;28(5):575-91.

48. Amato A, Arrigo A, Aragona E, Manitto MP, Saladino A, Bandello F, *et al*. Gene therapy in inherited retinal diseases: An update on current state of the art. Frontiers in Medicine. 2021;8:750586.

49. Turano KA, Geruschat DR, Stahl JW. Mental effort required for walking: effects of *retinitis pigmentosa*. Optometry and Vision Science. 1998;75(12).

50. Geruschat DR, Turano KA, Stahl JW. Traditional measures of mobility performance and *retinitis pigmentosa*. Optometry and Vision Science. 1998;75(7):525-37.

51. Peli E, Apfelbaum H, Berson EL, Goldstein RB. The risk of pedestrian collisions with peripheral visual field loss. Journal of Vision. 2016;16(15):5-.

52. Brown FE, Sutton J, Yuen HM, Green D, Van Dorn S, Braun T, *et al*. A novel, wearable, electronic visual aid to assist those with reduced peripheral vision. PLOS ONE. 2019;14(10):e0223755.

53. Yoshida M, Origuchi M, Urayama S, Takatsuki A, Kan S, Aso T, *et al*. fMRI evidence of improved visual function in patients with progressive *retinitis pigmentosa* by eye-movement training. NeuroImage Clinical. 2014;5:161-8.

54. Chen PS, Wang CC, Bortner CD, Peng GS, Wu X, Pang H, *et al*. Valproic acid and other histone deacetylase inhibitors induce microglial apoptosis and attenuate lipopolysaccharide-induced dopaminergic neurotoxicity. Neuroscience. 2007;149(1):203-12.

55. Kumar A, Midha N, Gogia V, Gupta S, Sehra S, Chohan A. Efficacy of oral valproic acid in patients with *retinitis pigmentosa*. Journal of ocular pharmacology and therapeutics : the official journal of the Association for Ocular Pharmacology and Therapeutics. 2014;30(7):580-6.

56. Berson EL, Weigel-DiFranco C, Rosner B, Gaudio AR, Sandberg MA. Association of vitamin A supplementation with disease course in children with *retinitis pigmentosa*. JAMA Ophthalmology. 2018;136(5):490-5.

57. Singh MS, MacLaren RE. Stem cells as a therapeutic tool for the blind: biology and future prospects. Proceedings Biological Sciences. 2011;278(1721):3009-16.

58. Tao YX, Xu HW, Zheng QY, FitzGibbon T. Noggin induces human bone marrow-derived mesenchymal stem cells to differentiate into neural and photoreceptor cells. Indian Journal of Experimental Biology. 2010;48(5):444-52.

59. Nadri S, Yazdani S, Arefian E, Gohari Z, Eslaminejad MB, Kazemi B, *et al*. Mesenchymal stem cells from trabecular meshwork become photoreceptor-like cells on amniotic membrane. Neuroscience letters. 2013;541:43-8.

60. Zhang X, Bok D. Transplantation of retinal pigment epithelial cells and immune response in the subretinal space. Investigative Opthalmology and Visual Science. 1998;39(6):1021-7.

61. Hambright D, Park KY, Brooks M, McKay R, Swaroop A, Nasonkin IO. Long-term survival and differentiation of retinal neurons derived from human embryonic stem cell lines in un-immunosuppressed mouse retina. Molecular Vision. 2012;18:920-36.

62. Bloch E, Luo Y, da Cruz L. Advances in retinal prosthesis systems. Therapeutic Advances in Ophthalmology. 2019;11:2515841418817501.

63. Marc R, Pfeiffer R, Jones B. Retinal prosthetics, optogenetics, and chemical photoswitches. ACS Chemical Neuroscience. 2014;5(10):895-901.

64. Luo YH, da Cruz L. The Argus II retinal prosthesis system. Progress in Retinal and Eye Research. 2016;50:89-107.

65. Keserue M, Post N, Hornig R, Zeitz O, Richard G. Long term tolerability of the first wireless implant for electrical epiretinal stimulation. Investigative Ophthalmology & Visual Science. 2009;50(13):4226-.

66. Richard G, Keserue M, Feucht M, Post N, Hornig R. Visual perception after long-term implantation of a retinal implant. Investigative Ophthalmology & Visual Science. 2008;49(13):1786-.

67. Walter P. A Fully intraocular approach for a bi-directional retinal prosthesis. In: Gabel VP, editor. Artificial Vision: A clinical guide. 2017; p. 151-61.

68. Jones BW, Marc RE. Retinal remodeling during retinal degeneration. Experimental Eye Research. 2005;81(2):123-37.

69. Rizzo JF, Shire DB, Kelly SK, Troyk P, Gingerich M, McKee B, *et al*., editors. Development of the boston retinal prosthesis. 2011 Annual international conference of the IEEE engineering in medicine and biology society. 2011.

70. Zrenner E, Bartz-Schmidt KU, Besch D, Gekeler F, Koitschev A, Sachs HG, *et al*. The subretinal implant ALPHA: implantation and functional results. In: Gabel VP, editor. Artificial Vision: A Clinical Guide. 2017; p. 65-83.

71. Lee DY, Lorach H, Huie P, Palanker D. Implantation of modular photovoltaic Subretinal Prosthesis. Ophthalmic Surgery, Lasers & Imaging Retina. 2016;47(2):171-4.

72. Ayton LN, Blamey PJ, Guymer RH, Luu CD, Nayagam DA, Sinclair NC, *et al*. First-in-human trial of a novel suprachoroidal retinal prosthesis. PLOS One. 2014;9(12):e115239.

73. Stingl K, Schippert R, Bartz-Schmidt KU, Besch D, Cottriall CL, Edwards TL, *et al*. Interim results of a multicenter trial with the new electronic subretinal implant Alpha AMS in 15 patients blind from inherited retinal degenerations. Frontiers in Neuroscience. 2017;11:445.

74. Humayun MS, Dorn JD, da Cruz L, Dagnelie G, Sahel JA, Stanga PE, *et al*. Interim results from the international trial of Second Sight's visual prosthesis. Ophthalmology. 2012;119(4):779-88.

75. Pérez Fornos A, Sommerhalder J, da Cruz L, Sahel JA, Mohand-Said S, Hafezi F, *et al*. Temporal properties of visual perception on electrical stimulation of the retina. Investigative Ophthalmology & Visual Science. 2012;53(6):2720-31.

76. Zrenner E. Fighting blindness with microelectronics. Science Translational Medicine. 2013;5(210):210ps16.

77. McClements ME, Staurenghi F, MacLaren RE, Cehajic-Kapetanovic J. Optogenetic gene therapy for the degenerate retina: Recent Advances. 2020;14.

78. Yan B, Viswanathan S, Brodie SE, Deng WT, Coleman KE, Hauswirth WW, *et al*. A clinically viable approach to restoring visual function using optogenetic gene therapy. Molecular therapy Methods & Clinical Development. 2023;29:406-17.

79. Piri N, Grodsky JD, Kaplan HJ. Gene therapy for *retinitis pigmentosa*. Taiwan Journal of Ophthalmology. 2021;11(4):348-51.

80. Xi Z, Vats A, Sahel JA, Chen Y, Byrne LC. Gene augmentation prevents retinal degeneration in a CRISPR/Cas9-based mouse model of PRPF31 *retinitis pigmentosa*. Nature Communications. 2022;13(1):7695.

81. Maguire AM, Simonelli F, Pierce EA, Pugh EN, Jr., Mingozzi F, Bennicelli J, *et al*. Safety and efficacy of gene transfer for Leber's congenital amaurosis. The New England Journal of Medicine. 2008;358(21):2240-8.

82. Dias MF, Joo K, Kemp JA, Fialho SL, da Silva Cunha A, Jr., Woo SJ, *et al*. Molecular genetics and emerging therapies for *retinitis pigmentosa*: Basic research and clinical perspectives. Progress in Retinal and Eye Research. 2018;63:107-31.

83. Russell S, Bennett J, Wellman JA, Chung DC, Yu Z-F, Tillman A, *et al*. Efficacy and safety of voretigene neparvovec (AAV2-hRPE65v2) in patients with *RPE65*-mediated inherited retinal dystrophy: a randomised, controlled, open-label, phase 3 trial. The Lancet. 2017;390(10097):849-60.

84. Maguire AM, Russell S, Chung DC, Yu Z-F, Tillman A, Drack AV, *et al*. Durability of Voretigene Neparvovec for biallelic *RPE65*-mediated inherited retinal disease: Phase 3 Results at 3 and 4 Years. Ophthalmology. 2021;128(10):1460-8.

85. Gange WS, Sisk RA, Besirli CG, Lee TC, Havunjian M, Schwartz H, *et al*. Perifoveal chorioretinal atrophy after subretinal Voretigene Neparvovec-rzyl for *RPE65*-mediated Leber Congenital Amaurosis. Ophthalmology Retina. 2022;6(1):58-64.

86. Hill D, Compagnoni C, Cordeiro MF. Investigational neuroprotective compounds in clinical trials for retinal disease. Expert opinion on investigational drugs. 2021;30(5):571-7.

87. Hernández-Pinto A, Polato F, Subramanian P, Rocha-Muñoz A, Vitale S, de la Rosa EJ, *et al*. PEDF peptides promote photoreceptor survival in rd10 retina models. Experimental Eye Research. 2019;184:24-9.

88. Mattern L, Otten K, Miskey C, Fuest M, Izsvak Z, Ivics Z, *et al*. Molecular and functional characterization of BDNF-overexpressing human retinal pigment epithelial cells established by *Sleeping Beauty* transposon-mediated gene transfer. International Journal of Molecular Sciences. 2022;23(21).

89. Becerra SP, Dass CR, Yabe T, Crawford SE. Pigment epithelium-derived factor: chemistry, structure, biology, and applications. Journal of Biomedicine & Biotechnology. 2012;2012:830975.

90. Minkevich NI, Lipkin VM, Kostanyan IA. PEDF - A noninhibitory Serpin with neurotrophic activity. Acta naturae. 2010;2(3):62-71.

91. Tombran-Tink J, Aparicio S, Xu X, Tink AR, Lara N, Sawant S, *et al*. PEDF and the serpins: phylogeny, sequence conservation, and functional domains. Journal of Structural Biology. 2005;151(2):130-50.

92. Tombran-Tink J, Johnson LV. Neuronal differentiation of retinoblastoma cells induced by medium conditioned by human RPE cells. Investigative Opthalmology and Visual Science. 1989;30(8):1700-7.

93. Eichler W, Yafai Y, Keller T, Wiedemann P, Reichenbach A. PEDF derived from glial Müller cells: a possible regulator of retinal angiogenesis. Experimental Cell Research. 2004;299(1):68-78.

94. Huang Q, Wang S, Sorenson CM, Sheibani N. PEDF-deficient mice exhibit an enhanced rate of retinal vascular expansion and are more sensitive to hyperoxia-mediated vessel obliteration. Experimental Eye Research. 2008;87(3):226-41.

95. He X, Cheng R, Benyajati S, Ma JX. PEDF and its roles in physiological and pathological conditions: implication in diabetic and hypoxia-induced angiogenic diseases. Clinical Science (London, England : 1979). 2015;128(11):805-23.

96. Haurigot V, Villacampa P, Ribera A, Bosch A, Ramos D, Ruberte J, *et al*. Long-term retinal PEDF overexpression prevents neovascularization in a murine adult model of retinopathy. PLOS One. 2012;7(7):e41511.

97. Park K, Jin J, Hu Y, Zhou K, Ma JX. Overexpression of pigment epithelium-derived factor inhibits retinal inflammation and neovascularization. The American Journal of Pathology. 2011;178(2):688-98.

98. Mori K, Duh E, Gehlbach P, Ando A, Takahashi K, Pearlman J, *et al*. Pigment epithelium-derived factor inhibits retinal and choroidal neovascularization. Journal of Cellular Physiology. 2001;188(2):253-63.

99. Saishin Y, Silva RL, Saishin Y, Kachi S, Aslam S, Gong YY, *et al*. Periocular gene transfer of pigment epithelium-derived factor inhibits choroidal neovascularization in a human-sized eye. Human Gene Therapy. 2005;16(4):473-8.

100. Amaral J, Becerra SP. Effects of human recombinant PEDF protein and PEDF-derived peptide 34-mer on choroidal neovascularization. Investigative Opthalmology and Visual Science. 2010;51(3):1318-26.

101. Dawson DW, Volpert OV, Gillis P, Crawford SE, Xu H, Benedict W, *et al*. Pigment epithelium-derived factor: a potent inhibitor of angiogenesis. Science (New York, NY). 1999;285(5425):245-8.

102. Kuo CN, Yang LC, Yang CT, Lai CH, Chen MF, Chen CY, *et al*. Inhibition of corneal neovascularization with plasmid pigment epithelium-derived factor (p-PEDF) delivered by synthetic amphiphile INTeraction-18 (SAINT-18) vector in an experimental model of rat corneal angiogenesis. Experimental Eye Research. 2009;89(5):678-85.

103. Cayouette M, Smith SB, Becerra SP, Gravel C. Pigment epithelium-derived factor delays the death of photoreceptors in mouse models of inherited retinal degenerations. Neurobiology of Disease. 1999;6(6):523-32.

104. Cao W, Tombran-Tink J, Chen W, Mrazek D, Elias R, McGinnis JF. Pigment epithelium-derived factor protects cultured retinal neurons against hydrogen peroxide-induced cell death. Journal of Neuroscience Research. 1999;57(6):789-800.

105. Wang Y, Subramanian P, Shen D, Tuo J, Becerra SP, Chan CC. Pigment epithelium-derived factor reduces apoptosis and pro-inflammatory cytokine gene expression in a murine model of focal retinal degeneration. ASN neuro. 2013;5(5):e00126.

106. Zhu D, Deng X, Spee C, Sonoda S, Hsieh CL, Barron E, *et al*. Polarized secretion of PEDF from human embryonic stem cell-derived RPE promotes retinal progenitor cell survival. Investigative Ophthalmology and Visual Science. 2011;52(3):1573-85.

107. Cao W, Tombran-Tink J, Elias R, Sezate S, Mrazek D, McGinnis JF. *In vivo* protection of photoreceptors from light damage by pigment epithelium-derived factor. Investigative Ophthalmology and Visual Science. 2001;42(7):1646-52.

108. Imai D, Yoneya S, Gehlbach PL, Wei LL, Mori K. Intraocular gene transfer of pigment epithelium-derived factor rescues photoreceptors from light-induced cell death. Journal of Cellular Physiology. 2005;202(2):570-8.

109. Jablonski MM, Tombran-Tink J, Mrazek DA, Iannaccone A. Pigment epithelium-derived factor supports normal development of photoreceptor neurons and opsin expression

after retinal pigment epithelium removal. The Journal of Neuroscience : the official journal of the Society for Neuroscience. 2000;20(19):7149-57.

110. Ernfors P, Wetmore C, Olson L, Persson H. Identification of cells in rat brain and peripheral tissues expressing mRNA for members of the nerve growth factor family. Neuron. 1990;5(4):511-26.

111. Bothwell M. Functional interactions of neurotrophins and neurotrophin receptors. Annual Review of Neuroscience. 1995;18:223-53.

112. Klein R, Conway D, Parada LF, Barbacid M. The trkB tyrosine protein kinase gene codes for a second neurogenic receptor that lacks the catalytic kinase domain. Cell. 1990;61(4):647-56.

113. Klein R, Nanduri V, Jing SA, Lamballe F, Tapley P, Bryant S, *et al*. The trkB tyrosine protein kinase is a receptor for brain-derived neurotrophic factor and neurotrophin-3. Cell. 1991;66(2):395-403.

114. Barde YA, Edgar D, Thoenen H. Purification of a new neurotrophic factor from mammalian brain. The EMBO Journal. 1982;1(5):549-53.

115. Hofer M, Pagliusi SR, Hohn A, Leibrock J, Barde YA. Regional distribution of brain-derived neurotrophic factor mRNA in the adult mouse brain. The EMBO Journal. 1990;9(8):2459-64.

116. Timmusk T, Palm K, Metsis M, Reintam T, Paalme V, Saarma M, *et al*. Multiple promoters direct tissue-specific expression of the rat BDNF gene. Neuron. 1993;10(3):475-89.

117. Telegina DV, Kolosova NG, Kozhevnikova OS. Immunohistochemical localization of NGF, BDNF, and their receptors in a normal and AMD-like rat retina. BMC Medical Genomics. 2019;12(2):48.

118. Kowiański P, Lietzau G, Czuba E, Waśkow M, Steliga A, Moryś J. BDNF: A key factor with multipotent impact on brain signaling and synaptic plasticity. Cellular and Molecular Neurobiology. 2018;38(3):579-93.

119. Chen H, Weber AJ. BDNF enhances retinal ganglion cell survival in cats with optic nerve damage. Investigative Ophthalmology and Visual Science. 2001;42(5):966-74.

120. Cheng L, Sapieha P, Kittlerova P, Hauswirth WW, Di Polo A. TrkB gene transfer protects retinal ganglion cells from axotomy-induced death *in vivo*. The Journal of Neuroscience : the official journal of the Society for Neuroscience. 2002;22(10):3977-86.

121. Di Polo A, Aigner LJ, Dunn RJ, Bray GM, Aguayo AJ. Prolonged delivery of brain-derived neurotrophic factor by adenovirus-infected Müller cells temporarily rescues injured

retinal ganglion cells. Proceedings of the National Academy of Sciences of the United States of America. 1998;95(7):3978-83.

122. Mansour-Robaey S, Clarke DB, Wang YC, Bray GM, Aguayo AJ. Effects of ocular injury and administration of brain-derived neurotrophic factor on survival and regrowth of axotomized retinal ganglion cells. Proceedings of the National Academy of Sciences of the United States of America. 1994;91(5):1632-6.

123. Mey J, Thanos S. Intravitreal injections of neurotrophic factors support the survival of axotomized retinal ganglion cells in adult rats *in vivo*. Brain Research. 1993;602(2):304-17.

124. Nakazawa T, Tamai M, Mori N. Brain-derived neurotrophic factor prevents axotomized retinal ganglion cell death through MAPK and PI3K signaling pathways. Investigative Opthalmology and Visual Science. 2002;43(10):3319-26.

125. Peinado-Ramón P, Salvador M, Villegas-Pérez MP, Vidal-Sanz M. Effects of axotomy and intraocular administration of NT-4, NT-3, and brain-derived neurotrophic factor on the survival of adult rat retinal ganglion cells. A quantitative *in vivo* study. Investigative Opthalmology and Visual Science. 1996;37(4):489-500.

126. Weber AJ, Harman CD. BDNF preserves the dendritic morphology of alpha and beta ganglion cells in the cat retina after optic nerve injury. Investigative Opthalmology and Visual Science. 2008;49(6):2456-63.

127. Weber AJ, Harman CD, Viswanathan S. Effects of optic nerve injury, glaucoma, and neuroprotection on the survival, structure, and function of ganglion cells in the mammalian retina. The Journal of physiology. 2008;586(18):4393-400.

128. Osborne A, Khatib TZ, Songra L, Barber AC, Hall K, Kong GYX, *et al*. Neuroprotection of retinal ganglion cells by a novel gene therapy construct that achieves sustained enhancement of brain-derived neurotrophic factor/tropomyosin-related kinase receptor-B signaling. Cell Death & Disease. 2018;9(10):1007.

129. Harper MM, Grozdanic SD, Blits B, Kuehn MH, Zamzow D, Buss JE, *et al*. Transplantation of BDNF-secreting mesenchymal stem cells provides neuroprotection in chronically hypertensive rat eyes. Investigative Opthalmology and Visual Science. 2011;52(7):4506-15.

130. Kimura A, Namekata K, Guo X, Harada C, Harada T. Neuroprotection, growth factors and BDNF-TrkB signalling in retinal degeneration. International Journal of Molecular Sciences. 2016; 17(9).

131. Pfeifer A, Verma IM. Gene therapy: promises and problems. Annual Review of Genomics and Human Genetics. 2001;2:177-211.

132. Lee CS, Bishop ES, Zhang R, Yu X, Farina EM, Yan S, *et al*. Adenovirus-mediated gene delivery: potential applications for gene and cell-based therapies in the new era of personalized medicine. Genes and Diseases. 2017;4(2):43-63.

133. Maier P, von Kalle C, Laufs S. Retroviral vectors for gene therapy. Future Microbiology. 2010;5(10):1507-23.

134. Vargas JE, Chicaybam L, Stein RT, Tanuri A, Delgado-Cañedo A, Bonamino MH. Retroviral vectors and transposons for stable gene therapy: advances, current challenges and perspectives. Journal of Translational Medicine. 2016;14(1):288.

135. Hardee CL, Arévalo-Soliz LM, Hornstein BD, Zechiedrich L. Advances in non-viral DNA vectors for gene therapy. Genes. 2017;8(2).

136. Hacein-Bey-Abina S, Garrigue A, Wang GP, Soulier J, Lim A, Morillon E, *et al*. Insertional oncogenesis in 4 patients after retrovirus-mediated gene therapy of SCID-X1. The Journal of Clinical Investigation. 2008;118(9):3132-42.

137. Naldini L, Blömer U, Gallay P, Ory D, Mulligan R, Gage FH, *et al*. *In vivo* gene delivery and stable transduction of nondividing cells by a lentiviral vector. Science (New York, NY). 1996;272(5259):263-7.

138. MD.Paul Yang MPJ-AS. Phase I/IIA study of SAR422459 in participants with Stargardt's macular degeneration. 2011 (updated 14.04.2022). Available from: https://clinicaltrials.gov/study/NCT01367444.

139. Palù G, Parolin C, Takeuchi Y, Pizzato M. Progress with retroviral gene vectors. Reviews in Medical Virology. 2000;10(3):185-202.

140. Ghosh S, Brown AM, Jenkins C, Campbell K. Viral vector systems for gene therapy: a comprehensive literature review of progress and biosafety challenges. Applied Biosafety: Journal of the American Biological Safety Association. 2020;25(1):7-18.

141. Nayerossadat N, Maedeh T, Ali PA. Viral and nonviral delivery systems for gene delivery. Advanced Biomedical Research. 2012;1:27.

142. Roth JA, Cristiano RJ. Gene Therapy for Cancer: What have we done and where are we going? Journal of the National Cancer Institute. 1997;89(1):21-39.

143. Johnen S, Izsvak Z, Stocker M, Harmening N, Salz AK, Walter P, *et al*. *Sleeping Beauty* transposon-mediated transfection of retinal and iris pigment epithelial cells. Investigative Opthalmology and Visual Science. 2012;53(8):4787-96.

144. Glover DJ, Lipps HJ, Jans DA. Towards safe, non-viral therapeutic gene expression in humans. Nature reviews Genetics. 2005;6(4):299-310.

145. Sarkis M, Shah N, Papathanasiou MM. Characterization of key manufacturing uncertainties in next generation therapeutics and vaccines across scales. 2023;5(3):e10158.

146. Kim TK, Eberwine JH. Mammalian cell transfection: the present and the future. Analytical and Bioanalytical Chemistry. 2010;397(8):3173-8.

147. Ehrhardt A, Xu H, Kay MA. Episomal persistence of recombinant adenoviral vector genomes during the cell cycle *in vivo*. Journal of Virology. 2003;77(13):7689-95.

148. Ivics Z, Hackett PB, Plasterk RH, Izsvák Z. Molecular reconstruction of *Sleeping Beauty*, a Tc1-like transposon from fish, and its transposition in human cells. Cell. 1997;91(4):501-10.

149. Izsvák Z, Chuah MK, Vandendriessche T, Ivics Z. Efficient stable gene transfer into human cells by the *Sleeping Beauty* transposon vectors. Methods. 2009;49(3):287-97.

150. Zayed H, Izsvák Z, Walisko O, Ivics Z. Development of hyperactive *Sleeping Beauty* transposon vectors by mutational analysis. Molecular therapy : the journal of the American Society of Gene Therapy. 2004;9(2):292-304.

151. Yant SR, Xiaolin W, Yong H, Brian G, M. BS, and Kay MA. High-resolution genome-wide mapping of transposon integration in mammals. Molecular and Cellular Biology. 2005;25(6):2085-94.

152. Izsvák Z, Ivics Z, Hackett PB. Characterization of a Tc1-like transposable element in zebrafish (Danio rerio). Molecular and General Genetics MGG. 1995;247(3):312-22.

153. Voigt K, Gogol-Döring A, Miskey C, Chen W, Cathomen T, Izsvák Z, *et al*. Retargeting *Sleeping Beauty* transposon insertions by engineered zinc finger DNA-binding domains. Molecular Therapy. 2012;20(10):1852-62.

154. Gogol-Döring A, Ammar I, Gupta S, Bunse M, Miskey C, Chen W, *et al*. Genome-wide profiling reveals remarkable parallels between insertion site selection properties of the MLV retrovirus and the *piggyBac* transposon in primary human CD4+ T Cells. Molecular Therapy. 2016;24(3):592-606.

155. Ivics Z, Izsvák Z. Nonviral gene delivery with the *Sleeping Beauty* transposon system. Human gene therapy. 2011;22(9):1043-51.

156. Belur LR, Podetz-Pedersen KM, Sorenson BS, Hsu AH, Parker JB, Carlson CS, *et al*. Inhibition of angiogenesis and suppression of colorectal cancer metastatic to the liver using the *Sleeping Beauty* transposon ystem. Molecular Cancer. 2011;10(1):14.

157. Wu A, Oh S, Ericson K, Demorest ZL, Vengco I, Gharagozlou S, *et al*. Transposon-based interferon gamma gene transfer overcomes limitations of episomal plasmid for immunogene therapy of glioblastoma. Cancer Gene Therapy. 2007;14(6):550-60.

158. Hudecek M, Izsvák Z, Johnen S, Renner M, Thumann G, Ivics Z. Going non-viral: the *Sleeping Beauty* transposon system breaks on through to the clinical side. Critical Reviews in Biochemistry and Molecular Biology. 2017;52(4):355-80.

159. Kotnik T, Rems L, Tarek M, Miklavčič D. Membrane electroporation and electropermeabilization: mechanisms and models. Annual Review of Biophysics. 2019;48:63-91.

160. Rosazza C, Meglic SH, Zumbusch A, Rols MP, Miklavcic D. Gene electrotransfer: a mechanistic perspective. Current Gene Therapy. 2016;16(2):98-129.

161. Young JL, Dean DA. Electroporation-mediated gene delivery. Advances in Genetics. 2015;89:49-88.

162. Shi J, Ma Y, Zhu J, Chen Y, Sun Y, Yao Y, *et al*. A review on electroporation-based intracellular delivery. Molecules. 2018;23(11).

163. Chang L, Li L, Shi J, Sheng Y, Lu W, Gallego-Perez D, *et al*. Micro-/nanoscale electroporation. Lab on a Chip. 2016;16(21):4047-62.

164. Scientific T. Neon Electroporation System user guide - For transfecting mammalian cells, including primary and stem cells, with a high transfection efficiency. Life Technologies Corporation. 2024.

165. Karen Steward P. An introduction to electroporation – A tool for transfection and competent cell generation: Technology Networks - Cell Science. 2022 (updated 16.02.2024). Available from: https://www.technologynetworks.com/cell-science/articles/an-introduction-to-electroporation-a-tool-for-transfection-and-competent-cell-generation-363195.

166. Gene.Co.Ltd N. Comparison of NEPA-21 with Amaxa Nucleofector: Sonidel. Availablefrom:https://articles.sonidel.com/electroporation/nepa21electroporator/comparison_of_nepa21_with_amaxa-nucleofector_neon_and_lipofectamine-2000-pdf/.

167. Nepa Gene Co. L. Cell culture plate electrodes. Available from: https://nepagene.jp/en/products/electroporation-en/cell-culture-plate-electrodes.

168. Williams NP, Voroslakos M, Shi D, Pwint MY, Lanzio V, Mao H, *et al*. *In vivo* microelectrode arrays for neuroscience. Nature Reviews Methods Primers. 2025;5(1):31.

169. Stolwijk JA, Wegener J. Impedance analysis of adherent cells after *in situ* electroporation-mediated delivery of bioactive proteins, DNA and nanoparticles in μL-volumes. Scientific Reports. 2020;10(1):21331.

170. Wegener J, Keese CR, Giaever I. Recovery of adherent cells after *in situ* electroporation monitored electrically. BioTechniques. 2002;33(2):348, 50, 52 passim.

171. Duckert B, Fauvart M, Goos P, Stakenborg T, Lagae L, Braeken D. High-definition electroporation: precise and efficient transfection on a microelectrode array. Journal of Controlled Release : official journal of the Controlled Release Society. 2022;352:61-73.

172. Zeck G, Herrmann T. Electroporation and electrostimulation of blind retina using micro-electrode arrays. 1st World Congress on Electroporation and Pulsed Electric Fields in Biology, Medicine and Food & Environmental Technologies. Springer Singapore. 2016.

173. Zhang Y, Peng T, Ge Y, Li M, Li C, Xi J, *et al*. A flexible electrode array for genetic transfection of different layers of the retina by electroporation. Lab on a Chip. 2024;24(7):1957-64.

174. Kauth A, Mildner A-K, Hegel L, Wegener J, Ingebrandt S. Development of specialized microelectrode arrays with local electroporation functionality. Annals of Biomedical Engineering. 2024;52(1):12-21.

175. Moreno AG. Design and fabrication of enhanced microelectrode array for the electroporation of retinal cells [Master thesis]. IWE-1, Aachen RWTH Aachen University. 2017.

176. Marszalek P, Liu DS, Tsong TY. Schwan equation and transmembrane potential induced by alternating electric field. Biophysical Journal. 1990;58(4):1053-8.

177. Robello M, Gliozzi A. Conductance transition induced by an electric field in lipid bilayers. Biochimica et Biophysica Acta. 1989;982(1):173-6.

178. Teissie J, Rols MP. An experimental evaluation of the critical potential difference inducing cell membrane electropermeabilization. Biophysical Journal. 1993;65(1):409-13.

179. Teissie J, Yow Tsong T. Voltage modulation of Na+/K+ transport in human erythrocytes. Journal of Physiology. 1981;77(9):1043-53.

180. Tomov TC, Tsoneva IC. Changes in the surface charge of cells induced by electrical pulses. Journal of Electroanalytical Chemistry and Interfacial Electrochemistry. 1989;276(2):127-33.

181. Agarwal A, Zudans I, Weber EA, Olofsson J, Orwar O, Weber SG. Effect of cell size and shape on single-cell electroporation. Analytical Chemistry. 2007;79(10):3589-96.

182. Zu Y, Huang S, Lu Y, Liu X, Wang S. Size specific transfection to mammalian cells by micropillar array electroporation. Scientific Reports. 2016;6(1):38661.

183. Towhidi L, Pourmir Firoozabadi SM, Mozdarani H, Kotnik T, Pucihar G, Miklavcic D. Effect of cell size and shape on electric field threshold and critical transmembrane voltage for electroporation. Iranian Journal of Medical Physics. 2008;5(Issue 3,4):1-14.

184. Masoud M, Janoud I, Al-Nahawy A. A measurement study of eccentricity in scientific papers' citation network. Zaytoonah University International Engineering Conference on Design and Innovation in Sustainability. 2014.

185. Seigel GM, Mutchler AL, Imperato EL. Expression of glial markers in a retinal precursor cell line. Molecular Vision. 1996;2:2.

186. Seigel GM. Review: R28 retinal precursor cells: the first 20 years. Molecular Vision. 2014;20:301-6.

187. Percie du Sert N, Ahluwalia A, Alam S, Avey MT, Baker M, Browne WJ, *et al*. Reporting animal research: explanation and elaboration for the ARRIVE guidelines 2.0. PLOS biology. 2020;18(7):e3000411.

188. Pereiro X, Ruzafa N, Acera A, Urcola A, Vecino E. Optimization of a method to isolate and culture adult porcine, rats and mice müller glia in order to study retinal diseases. Frontiers in Cellular Neuroscience. 2020;14:7.

189. Mátés L, Chuah MK, Belay E, Jerchow B, Manoj N, Acosta-Sanchez A, *et al*. Molecular evolution of a novel hyperactive *Sleeping Beauty* transposase enables robust stable gene transfer in vertebrates. Nature Genetics. 2009;41(6):753-61.

190. Stöcker M, Tur MK, Sasse S, Krüßmann A, Barth S, Engert A. Secretion of functional anti-CD30-angiogenin immunotoxins into the supernatant of transfected 293T-cells. Protein Expression and Purification. 2003;28(2):211-9.

191. Mugnaini G, Gelli R, Mori L, Bonini M. How to cross-link gelatin: the effect of glutaraldehyde and glyceraldehyde on the hydrogel properties. ACS Applied Polymer Materials. 2023;5(11):9192-202.

192. Thumann G, Stöcker M, Maltusch C, Salz A-K, Barth S, Walter P, *et al*. High efficiency non-viral transfection of retinal and iris pigment epithelial cells with pigment epithelium-derived factor. Gene Therapy. 2009;17:181-9.

193. Brown CE. Coefficient of Variation. In: Brown CE, editor. Applied multivariate statistics in geohydrology and related sciences. Springer Berlin Heidelberg; 1998. p. 155-7.

194. Boulaiz H, Marchal JA, Prados J, Melguizo C, Aránega A. Non-viral and viral vectors for gene therapy. Cellular and Molecular Biology. 2005;51(1):3-22.

195. Butt MH, Zaman M, Ahmad A, Khan R, Mallhi TH, Hasan MM, *et al*. Appraisal for the potential of viral and nonviral vectors in gene therapy: a review. Genes. 2022;13(8).

196. Raper SE, Chirmule N, Lee FS, Wivel NA, Bagg A, Gao GP, *et al*. Fatal systemic inflammatory response syndrome in a ornithine transcarbamylase deficient patient following adenoviral gene transfer. Molecular Genetics and Metabolism. 2003;80(1-2):148-58.

197. Lyons M, Onion D, Green NK, Aslan K, Rajaratnam R, Bazan-Peregrino M, *et al*. Adenovirus type 5 interactions with human blood cells may compromise systemic delivery. Molecular Therapy : the journal of the American Society of Gene Therapy. 2006;14(1):118-28.

198. Cattoglio C, Pellin D, Rizzi E, Maruggi G, Corti G, Miselli F, *et al*. High-definition mapping of retroviral integration sites identifies active regulatory elements in human multipotent hematopoietic progenitors. Blood. 2010;116(25):5507-17.

199. Cavazzana-Calvo M, Hacein-Bey S, de Saint Basile G, Gross F, Yvon E, Nusbaum P, *et al*. Gene therapy of human severe combined immunodeficiency (SCID)-X1 disease. Science (New York, NY). 2000;288(5466):669-72.

200. Harmening N, Johnen S, Izsvák Z, Ivics Z, Kropp M, Bascuas T, *et al*. Enhanced biosafety of the *Sleeping Beauty* transposon system by using mRNA as source of transposase to efficiently and stably transfect retinal pigment epithelial cells. 2023;13(4):658.

201. Weleber RG, Pennesi ME, Wilson DJ, Kaushal S, Erker LR, Jensen L, *et al*. Results at 2 years after gene therapy for *RPE65*-deficient Leber Congenital Amaurosis and severe early-childhood-onset retinal dystrophy. Ophthalmology. 2016;123(7):1606-20.

202. Mátés L, Chuah MKL, Belay E, Jerchow B, Manoj N, Acosta-Sanchez A, *et al*. Molecular evolution of a novel hyperactive *Sleeping Beauty* transposase enables robust stable gene transfer in vertebrates. Nature Genetics. 2009;41(6):753-61.

203. Kiseleva LN, Kartashev AV, Vartanyan NL, Pinevich AA, Samoilovich MP. A172 and T98G cell lines characteristics. Cell and Tissue Biology. 2016;10(5):341-8.

204. Roesch K, Stadler MB, Cepko CL. Gene expression changes within Müller glial cells in *retinitis pigmentosa*. Molecular vision. 2012;18:1197-214.

205. Vigneswara V, Berry M, Logan A, Ahmed Z. Pigment epithelium-derived factor is retinal ganglion cell neuroprotective and axogenic after optic nerve crush injury. Investigative Opthalmology and Visual Science. 2013;54(4):2624-33.

206. Kenealey J, Subramanian P, Comitato A, Bullock J, Keehan L, Polato F, *et al*. Small retinoprotective peptides reveal a receptor-binding region on pigment epithelium-derived factor. The Journal of Biological Chemistry. 2015;290(42):25241-53.

207. Valiente-Soriano FJ, Di Pierdomenico J, García-Ayuso D, Ortín-Martínez A, Miralles de Imperial-Ollero JA, Gallego-Ortega A, *et al*. Pigment epithelium-derived factor (PEDF) fragments prevent mouse cone photoreceptor cell loss induced by focal phototoxicity *in vivo*. International Journal of Molecular Sciences. 2020;21(19).

208. Michelis G, German OL, Villasmil R, Soto T, Rotstein NP, Politi L, *et al*. Pigment epithelium-derived factor (PEDF) and derived peptides promote survival and differentiation of photoreceptors and induce neurite-outgrowth in amacrine neurons. Journal of Neurochemistry. 2021;159(5):840-56.

209. Bernardo-Colón A, Bighinati A, Parween S, Debnath S, Piano I, Adani E, *et al*. H105A peptide eye drops promote photoreceptor survival in murine and human models of retinal degeneration. Communications Medicine. 2025;5(1):81.

210. Zhang T, Guan M, Xu C, Chen Y, Lu Y. Pigment epithelium-derived factor inhibits glioma cell growth *in vitro* and *in vivo*. Life Sciences. 2007;81(16):1256-63.

211. Okoye G, Zimmer J, Sung J, Gehlbach P, Deering T, Nambu H, *et al*. Increased expression of brain-derived neurotrophic factor preserves retinal function and slows cell death from rhodopsin mutation or oxidative damage. The Journal of Neuroscience : the official journal of the Society for Neuroscience. 2003;23(10):4164-72.

212. Kano T, Abe T, Tomita H, Sakata T, Ishiguro S, Tamai M. Protective effect against ischemia and light damage of iris pigment epithelial cells transfected with the BDNF gene. Investigative Opthalmology and Visual Science. 2002;43(12):3744-53.

213. Liu Y, Tao L, Fu X, Zhao Y, Xu X. BDNF protects retinal neurons from hyperglycemia through the TrkB/ERK/MAPK pathway. Mol Med Rep. 2013;7(6):1773-8.

214. Wójtowicz K, Czarzasta K, Przepiorka L, Kujawski S, Cudnoch-Jedrzejewska A, Marchel A, *et al*. Brain-derived neurotrophic factor (BDNF) concentration levels in cerebrospinal fluid and plasma in patients with glioblastoma: a prospective, observational, controlled study. Cureus. 2023;15(11):e48237.

215. Yin D, Yang WG, Weissberg J, Goff CB, Chen W, Kuwayama Y, *et al*. Cutaneous papilloma and squamous cell carcinoma therapy utilizing nanosecond pulsed electric fields (nsPEF). PLOS ONE. 2012;7(8):e43891.

216. Vernier PT, Aimin L, Marcu L, Craft CM, Gundersen MA. Ultrashort pulsed electric fields induce membrane phospholipid translocation and caspase activation: differential sensitivities of Jurkat T lymphoblasts and rat glioma C6 cells. IEEE Transactions on Dielectrics and Electrical Insulation. 2003;10(5):795-809.

217. Hyder I, Eghbalsaied S, Kues W. Systematic optimization of square-wave electroporation conditions for bovine primary fibroblasts. BMC Molecular and Cell Biology. 2020;21:9.

218. Cao Y, Ma E, Cestellos-Blanco S, Zhang B, Qiu R, Su Y, *et al*. Nontoxic nanopore electroporation for effective intracellular delivery of biological macromolecules. Proceedings of the National Academy of Sciences of the United States of America. 2019;116(16):7899-904.
219. Nathamgari SSP, Mukherjee P, Kessler JA, Espinosa HD. Localized electroporation with track-etched membranes. Proceedings of the National Academy of Sciences of the United States of America. 2019;116(46):22909-10.
220. Barrau C, Teissié J, Gabriel B. Osmotically induced membrane tension facilitates the triggering of living cell electropermeabilization. Bioelectrochemistry. 2004;63(1-2):327-32.
221. Matsuyama C, Seike T, Okahashi N, Niide T, Hara KY, Hirono-Hara Y, *et al*. Metabolome analysis of metabolic burden in *Escherichia coli* caused by overexpression of green fluorescent protein and delta-rhodopsin. Journal of Bioscience and Bioengineering. 2024;137(3):187-94.
222. Walisko O, Izsvák Z, Szabó K, Kaufman CD, Herold S, Ivics Z. *Sleeping Beauty* transposase modulates cell-cycle progression through interaction with Miz-1. Proceedings of the National Academy of Sciences. 2006;103(11):4062-7.
223. Galla M, Schambach A, Falk CS, Maetzig T, Kuehle J, Lange K, *et al*. Avoiding cytotoxicity of transposases by dose-controlled mRNA delivery. Nucleic Acids Research. 2011;39(16):7147-60.
224. Wang CL, Yang DC, Wabl M. Slow, stochastic transgene repression with properties of a timer. Genome Biology. 2006;7(6):R47.
225. Batard P, Jordan M, Wurm F. Transfer of high copy number plasmid into mammalian cells by calcium phosphate transfection. Gene. 2001;270(1-2):61-8.
226. Lesueur LL, Mir LM, André FM. Overcoming the specific toxicity of large plasmids electrotransfer in primary cells *in vitro*. Molecular Therapy Nucleic Acids. 2016;5(3):e291.
227. Peng W, Polajžer T, Yao C, Miklavčič D. Dynamics of cell death due to electroporation using different pulse parameters as revealed by different viability assays. Annals of Biomedical Engineering. 2024;52(1):22-35.
228. Grube S, Freitag D, Kalff R, Ewald C, Walter J. Characterization of adherent primary cell lines from fresh human glioblastoma tissue, defining glial fibrillary acidic protein as a reliable marker in establishment of glioblastoma cell culture. Cancer Reports (Hoboken, NJ). 2021;4(2):e1324.
229. Cellosaurus R28 (CVCL_5I35). 2015 [cited 23.07.2025]. Available from: https://www.cellosaurus.org/CVCL_5I35?

230. Neuhaus B, Tosun B, Rotan O, Frede A, Westendorf AM, Epple M. Nanoparticles as transfection agents: a comprehensive study with ten different cell lines. RSC Advances. 2016;6(22):18102-12.

231. Newton JM, Vlahopoulou J, Zhou Y. Investigating and modelling the effects of cell lysis on the rheological properties of fermentation broths. Biochemical Engineering Journal. 2017;121:38-48.

232. de Souza JG, Starobinas N, Ibañez OCM. Unknown/enigmatic functions of extracellular ASC. Immunology. 2021;163(4):377-88.

233. Ribeiro S, Mairhofer J, Madeira C, Diogo MM, Lobato da Silva C, Monteiro G, *et al*. Plasmid DNA size does affect nonviral gene delivery efficiency in stem cells. Cellular Reprogramming. 2012;14(2):130-7.

234. André FM, Gehl J, Sersa G, Préat V, Hojman P, Eriksen J, *et al*. Efficiency of high- and low-voltage pulse combinations for gene electrotransfer in muscle, liver, tumor, and skin. Human Gene Therapy. 2008;19(11):1261-71.

235. Hayashi H, Mori M, Harashima M, Hashizume T, Furiya M, Mukaigaito C, *et al*. Apolipoprotein E-containing lipoproteins and LRP1 protect from NMDA-induced excitotoxicity associated with reducing alpha2-macroglobulin in Müller glia. Investigative Opthalmology and Visual Science. 2021;62(13):23.

236. Castets P, Rion N, Théodore M, Falcetta D, Lin S, Reischl M, *et al*. mTORC1 and PKB/Akt control the muscle response to denervation by regulating autophagy and HDAC4. Nature Communications. 2019;10(1):3187.

237. Sapir T, Levy T, Sakakibara A, Rabinkov A, Miyata T, Reiner O. Shootin1 acts in concert with KIF20B to promote polarization of migrating neurons. The Journal of Neuroscience : the official journal of the Society for Neuroscience. 2013;33(29):11932-48.

238. Porosk L, Nebogatova J, Härk HH, Vunk B, Arukuusk P, Toots U, *et al*. Predicting transiently expressed protein yields: comparison of transfection methods in CHO and HEK293. Pharmaceutics. 2022;14(9):1949.

239. Yoshimitsu Y, Abe J, Harayama S. Cas9-guide RNA ribonucleoprotein-induced genome editing in the industrial green alga *Coccomyxa sp*. strain KJ. Biotechnology for Biofuels. 2018;11.

240. Satkauskas S, André F, Bureau MF, Scherman D, Miklavcic D, Mir LM. Electrophoretic component of electric pulses determines the efficacy of *in vivo* DNA electrotransfer. Human Gene Therapy. 2005;16(10):1194-201.

241. Guo X, Zhu R. Controllable *in-situ* cell electroporation with cell positioning and impedance monitoring using micro electrode array. Scientific Reports. 2016;6:31392.

242. Zhang Z, Zheng T, Zhu R. Single-cell individualized electroporation with real-time impedance monitoring using a microelectrode array chip. Microsystems and Nanoengineering. 2020;6:81.

243. Patel C, Muthuswamy J. High efficiency, site-specific transfection of adherent cells with siRNA using microelectrode arrays (MEA). Journal of Visualized Experiments. 2012(67):e4415.

244. Browne CJ, Pinyon JL, Housley DM, Crawford EN, Lovell NH, Klugmann M, *et al*. Mapping of bionic array electric field focusing in plasmid DNA-based gene electrotransfer. Gene Therapy. 2016;23(4):369-79.

245. Kung Y, Lihachev A, Šatkauskas S, Lan K-L, Chen W-S. Electroporation by concentric-type needle electrodes and arrays. Bioelectrochemistry. 2017;118:31-7.

246. Lee D-J, Kim DY. Enhanced electrical injury using triangular interdigitated electrodes for catheter-based irreversible electroporation. Applied Sciences. 2023; 13(14).

247. Novickij V, Rembiałkowska N, Szlasa W, Kulbacka J. Does the shape of the electric pulse matter in electroporation? Frontiers in Oncology. 2022;12:958128.

248. García-Sánchez T, Merla C, Fontaine J, Muscat A, Mir LM. Sine wave electropermeabilization reveals the frequency-dependent response of the biological membranes. Biochimica et Biophysica Acta (BBA) - Biomembranes. 2018;1860(5):1022-34.

249. Rems L, Kasimova MA, Testa I, Delemotte L. Pulsed electric fields can create pores in the voltage sensors of voltage-gated ion channels. Biophysical Journal. 2020;119(1):190-205.

250. Sun W, Seigel GM, Salvi RJ. Retinal precursor cells express functional ionotropic glutamate and GABA receptors. Neuroreport. 2002;13(18):2421-4.

251. Ai Y, Zhang X, Hu X, Gao J, Liu J, Ou S, *et al*. Role of the voltage-gated sodium channel Nav1.6 in glioma and candidate drugs screening. International Journal of Molecular Medicine. 2023;51(6).

252. Pehlivanova VN, Tsoneva IH, Tzoneva RD. Multiple effects of electroporation on the adhesive behaviour of breast cancer cells and fibroblasts. Cancer Cell International. 2012;12(1):9.

253. Vassanelli S, Bandiera L, Borgo M, Cellere G, Santoni L, Bersani C, *et al*. Space and time-resolved gene expression experiments on cultured mammalian cells by a single-cell electroporation microarray. New Biotechnology. 2008;25(1):55-67.

254. Jain T, Muthuswamy J. Bio-chip for spatially controlled transfection of nucleic acid payloads into cells in a culture. Lab on a Chip. 2007;7(8):1004-11.

255. Wang X, Li L, Shao Y, Wei J, Song R, Zheng S, *et al*. Effects of the Laplace pressure on the cells during cytokinesis. iScience. 2021;24(9):102945.

256. Drury JL, Dembo M. Hydrodynamics of micropipette aspiration. Biophysical Journal. 1999;76(1):110-28.

257. Hochmuth RM. Micropipette aspiration of living cells. Journal of Biomechanics. 2000;33(1):15-22.

258. Janmey PA, Hinz B, McCulloch CA. Physics and physiology of cell spreading in two and three dimensions. Physiology. 2021;36(6):382-91.

259. Rols MP, Teissie J. Modulation of electrically induced permeabilization and fusion of Chinese hamster ovary cells by osmotic pressure. Biochemistry. 1990;29(19):4561-7.

260. Zhurbitskaya VA, Rovenskii YA, Kaverina IN. Changes in morphology, cytoskeleton, and substrate dependence of proliferation after transfection of immortalized rat embryonic fibroblasts with E7 gene of type 16 human papilloma virus. Bulletin of Experimental Biology and Medicine. 1999;127(1):99-102.

261. Graybill PM, Jana A, Kapania RK, Nain AS, Davalos RV. Single cell forces after electroporation. ACS Nano. 2021;15(2):2554-68.

262. Gross D, Loew LM, Webb WW. Optical imaging of cell membrane potential changes induced by applied electric fields. Biophysical Journal. 1986;50(2):339-48.

263. Hibino M, Itoh H, Kinosita K, Jr. Time courses of cell electroporation as revealed by submicrosecond imaging of transmembrane potential. Biophysical Journal. 1993;64(6):1789-800.

264. Hibino M, Shigemori M, Itoh H, Nagayama K, Kinosita K, Jr. Membrane conductance of an electroporated cell analyzed by submicrosecond imaging of transmembrane potential. Biophysical Journal. 1991;59(1):209-20.

265. Valic B, Golzio M, Pavlin M, Schatz A, Faurie C, Gabriel B, *et al*. Effect of electric field induced transmembrane potential on spheroidal cells: theory and experiment. European Biophysical Journal : EBJ. 2003;32(6):519-28.

266. Müller H. Zur Histologie der Netzhaut.

267. Greenberg KP, Geller SF, Schaffer DV, Flannery JG. Targeted transgene expression in Müller glia of normal and diseased retinas using lentiviral vectors. Investigative Ophthalmology & Visual Science. 2007;48(4):1844-52.

268. Burris C, Klug K, Ngo IT, Sterling P, Schein S. How Müller glial cells in macaque fovea coat and isolate the synaptic terminals of cone photoreceptors. The Journal of Comparative Neurology. 2002;453(1):100-11.

269. Pellissier LP, Quinn PM, Alves CH, Vos RM, Klooster J, Flannery JG, *et al*. Gene therapy into photoreceptors and Müller glial cells restores retinal structure and function in CRB1 *retinitis pigmentosa* mouse models. Human Molecular Genetics. 2015;24(11):3104-18.

270. Peynshaert K, Devoldere J, Philips F, Vergauwe F, De Smedt S, Remaut K. Influence of pathogenic stimuli on Müller cell transfection by lipoplexes. European Journal of Pharmaceutics and Biopharmaceutics : official journal of Arbeitsgemeinschaft fur Pharmazeutische Verfahrenstechnik eV. 2020;150:87-95.

271. Cao W, Knapp RR, Soliman C, Zhou X, Sezate S, Kong L, *et al*. *In vitro* transfection of plasmid DNA encoding pigment epithelum–derived factor (PEDF) into retinal cells protects against hydrogen peroxide–induced cell death. Investigative Ophthalmology & Visual Science. 2005;46(13):153-.

272. Eichler W, Savković-Cvijić H, Bürger S, Beck M, Schmidt M, Wiedemann P, *et al*. Müller cell-derived PEDF mediates neuroprotection via STAT3 activation. Cellular Physiology and Biochemistry : international journal of Experimental Cellular Physiology, Biochemistry, and Pharmacology. 2017;44(4):1411-24.

273. Gauthier R, Joly S, Pernet V, Lachapelle P, Di Polo A. Brain-derived neurotrophic factor gene delivery to Müller glia preserves structure and function of light-damaged photoreceptors. Investigative Ophthalmology & Visual Science. 2005;46(9):3383-92.

274. Liu X, Tang L, Liu Y. Mouse Müller cell isolation and culture. Bio-protocol. 2017;7(15):e2429.

275. Erickson PA, Fisher SK, Guérin CJ, Anderson DH, Kaska DD. Glial fibrillary acidic protein increases in Müller cells after retinal detachment. Experimental Eye Research. 1987;44(1):37-48.

276. Ekström P, Sanyal S, Narfström K, Chader GJ, van Veen T. Accumulation of glial fibrillary acidic protein in Müller radial glia during retinal degeneration. Investigative Opthalmology and Visual Science. 1988;29(9):1363-71.

277. Eisenfeld AJ, Bunt-Milam AH, Sarthy PV. Müller cell expression of glial fibrillary acidic protein after genetic and experimental photoreceptor degeneration in the rat retina. Investigative Ophthalmology & Visual Science. 1984;25(11):1321-8.

278. Lupien C, Brenner M, Guérin SL, Salesse C. Expression of glial fibrillary acidic protein in primary cultures of human Müller cells. Experimental Eye Research. 2004;79(3):423-9.

279. Backstrom JR, Sheng J, Fischer RA, Sappington RM, Rex TS. Phenotypes of primary retinal macroglia: Implications for purification and culture conditions. Experimental Eye Research. 2019;182:85-92.
280. Rodriguez Osuna IA, Cobelli P, Olaiz N. Bubble Formation in Pulsed Electric Field Technology May Pose Limitations. Micromachines [Internet]. 2022; 13(8).
281. Wang S, Zhang X, Wang W, Lee LJ. Semicontinuous flow electroporation chip for high-throughput transfection on mammalian cells. Analytical chemistry. 2009;81(11):4414-21.
282. Srinivasan S, Henry Ho HY. An efficient method for immortalizing mouse embryonic fibroblasts. bioRxiv : the preprint server for biology. 2024.

7. Appendix and Raw Data

Table 11: Flow cytometry analysis of *Venus*-transfected A-172 cell cultures, six days post transfection with the Neon Transfection System (n =4)**.** The numbers indicate the % of *Venus* +ve A-172 cells. (0) -ve control; (1) 1000 V, 30ms, 2 pulses; (2) 1000 V, 30 ms, 3 pulses; (3) 1100 V, 20ms, 2 pulses; (4) 1100 V, 20 ms, 3 pulses; (5) 1100 V, 30 ms, 2 pulses; (6) 1100 V, 30 ms, 3 pulses; (7) 1150 V, 20 ms, 2 pulses; (8) 1150 V, 30 ms, 2 pulses; (9) 1150 V, 30 ms, 3 pulses; (10) 1200 V, 20 ms, 2 pulses; (11) 1200 V, 25 ms, 2 pulses; (12) 1200 V, 30 ms, 3 pulses; (13) 1250 V, 25 ms, 2 pulses, (14) 1250 V, 30 ms, 2 pulses; (15) 1300 V, 20 ms, 2 pulses; (16) 1350 V, 20 ms, 2 pulses

0	**1**	**2**	**3**	**4**	**5**	**6**	**7**	**8**	**9**
0	4.6	31.2	2.8	17.6	29	51	14.9	56.2	33.6
0	4	26.2	3.1	20.4	34.4	51.2	15.7	56.5	32.2
0	10.6	36.8	11.6	34.3	32.6	44.3	8.2	37.2	47.5
0	29.3	56.1	10.5	40.3	62.4	0	3.7	22.9	15
0	20.4	56	8.1	33	45.9	57.4	5.6	25.4	-
0	3.1	30.8	3.1	1.8	26.1	19.5	6.3	34.9	-
0	-	15.2	3.6	-	14.4	-	-	21.3	-
0	-	22.3	2.6	-	19.6	-	-	29.8	-
0	-	11.5	-	-	-	-	-	-	-
0	-	15.7	-	-	-	-	-	-	-

0	10	11	12	13	14	15	16
0	23.5	37.6	29.6	17.9	25.1	14.9	18.3
0	24.9	45.2	37.4	19.5	37.5	8.3	20.1
0	16.8	29.4	14	44.1	11.2	24.7	32.7
0	4.5	19.2	15.3	29.3	20.8	-	-
0	-	16.5	-	22.1	-	-	-
0	-	35.9	-	37.1	-	-	-
0	-	22.3	-	28.8	-	-	-
0	-	22.2	-	9.1	-	-	-
0	-	12.3	-	20.1	-	-	-
0	-	20	-	28	-	-	-
0	-	16.9	-	28.4	-	-	-
0	-	19.3	-	30.4	-	-	-
0	-	27.2	-	-	-	-	-

Table 12: Luciferase-based cell viability analysis of *Venus*-transfected A-172 cell culture, 24 hours post-transfection with the Neon Transfection System (n = 4)**.** The numbers indicate the fluorescence in Relative Light Units (RLU). (0) -ve control; (1) 1000 V, 30ms, 2 pulses; (2) 1000 V, 30 ms, 3 pulses; (3) 1100 V, 20ms, 2 pulses; (4) 1100 V, 20 ms, 3 pulses; (5) 1100 V, 30 ms, 2 pulses; (6) 1100 V, 30 ms, 3 pulses; (7) 1150 V, 20 ms, 2 pulses; (8) 1150 V, 30 ms, 2 pulses; (9) 1150 V, 30 ms, 3 pulses; (10) 1200 V, 20 ms, 2 pulses; (11) 1200 V, 25 ms, 2 pulses; (12) 1200 V, 30 ms, 3 pulses; (13) 1250 V, 25 ms, 2 pulses, (14) 1250 V, 30 ms, 2 pulses; (15) 1300 V, 20 ms, 2 pulses; (16) 1350 V, 20 ms, 2 pulses

0	1	2	3	4	5	6	7	8	9
2559242	1400000	710000	2110396	670000	950000	430000	1027132	748555	114080
2077257	1300000	790000	1944365	870000	620000	39000	1367415	410272	140769
1388025	-	-	1821614	-	-	-	1037314	700312	29216
1297612	-	-	1619627	-	-	-	940547	485610	17910
2055166	-	-	-	-	-	-	1721547	-	-
1807696	-	-	-	-	-	-	1167807	-	-
2470218	-	-	-	-	-	-	1421591	-	-
3229218	-	-	-	-	-	-	1271860	-	-

0	10	11	12	13	14	15	16
2559242	1000000	688970	79000	248116	220000	274968	140268
2077257	740000	486810	33000	233845	200000	293949	144826
1388025	-	470265	-	273821	-	1116663	441277
1297612	-	515277	-	587865	-	871243	411933
2055166	-	1371474	-	111086	-	-	-
1807696	-	628014	-	78879	-	-	-
2470218	-	490001	-	921277	-	-	-
3229218	-	420141	-	732550	-	-	-

Table 13: Long-term transfection analysis of *Venus* transfection of A-172 cells with 1000 V, 30 ms, 3 pulses using the Neon Transfection System (n = 4). The numbers indicate the % of *Venus* +ve A-172 cells.

Month 0	Month 1	Month 2	Month 3	Month 4
45.7	33	21.9	15.4	12
20.9	16.1	18.7	21.1	18.2
42.1	27	14	6.2	1.3
19.4	10	5.8	3.9	2.9

Table 14: Long-term transfection analysis of *Venus* transfection of A-172 cells with 1100 V, 30 ms, 2 pulses using the Neon Transfection System (n = 4). The numbers indicate the % of *Venus* +ve A-172 cells.

Month 0	Month 1	Month 2	Month 3	Month 4
41.4	35.1	23.9	9.6	2.7
36.5	27.1	16	7	2.8
39.1	22.9	19.2	31	-
18.9	10.8	4.1	1.9	0.6

Table 15: Long-term transfection analysis of *Venus* transfection of A-172 cells with 1150 V, 30 ms, 2 pulses using the Neon Transfection System (n = 4). The numbers indicate the % of *Venus* +ve A-172 cells.

Month 0	Month 1	Month 2	Month 3	Month 4
54.9	51.2	36.8	38.3	38.8
48.7	42.3	35.4	24.6	13.3
41.6	26.6	15.4	6.8	2.7
31.5	19.7	15.6	8.6	1.6

Table 16: Long-term transfection analysis of *Venus* transfection of A-172 cells with 1200 V, 25 ms, 2 pulses using the Neon Transfection System (n = 4). The numbers indicate the % of *Venus* +ve A-172 cells.

Month 0	Month 1	Month 2	Month 3	Month 4
37.2	29.2	23	24.9	19.7
33.5	28.8	25.4	8.3	0.6
41.2	34.3	21.5	11.2	5.3
17	11	7.6	3	0.8

Table 17: Western Blot gel-band intensities (pixel^2) of PEDF from A-172 cell line transfected using the Neon Transfection System, six days post-transfection (n = 4). (0) -ve control; (1) 1000 V, 30ms, 3 pulses; (2) 1100 V, 30 ms, 2 pulses; (3) 1150 V, 30ms, 2 pulses; (4) 1200 V, 25 ms, 2 pulses

0	1	2	3	4
1	1.585	1.703	1.583	1.592
1	1.189	1.458	1.196	1.436
1	1.469	1.162	1.216	1.342
1	1.63	1.682	2.068	1.98

Table 18: ELISA OD values, cell number and protein levels (pg/h/10^4 cells) of PEDF from A-172 cells transfected using the Neon Transfection System, six days post-transfection (n = 4) . (0) -ve control; (1) 1000 V, 30ms, 3 pulses; (2) 1100 V, 30 ms, 2 pulses; (3) 1150 V, 30ms, 2 pulses; (4) 1200 V, 25 ms, 2 pulses. Standard curve equation is y = 0.0393x + 0.0369

Sample	Dilution (1:x)	Volume (1/ml)	OD (450 nm)	PEDF [ng/ml]	PEDF [ng/h]	Cells/ml	PEDF [pg/h/10^4 cells]
0 exp 1	50	0.5	0.053	20.483	0.426	320000	13.335
1 exp 1	100	0.5	0,09	135.114	2.814	52500	536.168
2 exp 1	100	0.5	0.091	137.659	2.867	12500	2294.31
3 exp 1	100	0.5	0.114	196.183	4.087	402500	101.544
4 exp 1	100	0.5	0.097	152.926	3.186	400000	79.649
0 exp 2	50	0.5	0.049	15.394	0.320	77500	41.382
1 exp 2	100	0.5	0.139	259.796	5.412	422500	128.104
2 exp 2	100	0.5	0.139	259.796	5.412	165000	328.026
3 exp 2	100	0.5	0.128	231.806	4.829	365000	132.309
4 exp 2	100	0.5	0.128	231.806	4.829	115000	419.939
0 exp 3	50	0.5	0.044	9.033	0.188	12500	150.551
1 exp 3	100	0.5	0.107	178.371	3.716	250000	148.642
2 exp 3	100	0.5	0.113	193.638	4.034	147500	273.50
3 exp 3	100	0.5	0.141	264.885	5.518	227500	242.57
4 exp 3	100	0.5	0.09	135.114	2.814	97500	288.706
0 exp 4	50	0.5	0.043	7.761	0.161	240000	6.736
1 exp 4	100	0.5	0.137	254.707	5.306	15000	3537.6
2 exp 4	100	0.5	0.138	257.252	5.359	350000	153.126
3 exp 4	100	0.5	0.16	313.231	6.525	312500	208.821
4 exp 4	100	0.5	0.135	249.618	5.20	75000	693.384

Table 19: *PEDF* RT qPCR, crossing point (Cp) values and further calculations - experiment 1, runs 1 and 2, six days post-transfection of the A-172 cell line with the Neon Transfection System (n = 4)**.** (0) -ve control; (1) 1000 V, 30ms, 3 pulses; (2) 1100 V, 30 ms, 2 pulses; (3) 1150 V, 30ms, 2 pulses; (4) 1200 V, 25 ms, 2 pulses

Raw Data	Samples	Cp run I	Cp run II
GAPDH	0	18.85	18.75
	1	17.73	18.34
	2	17.57	17.14
	3	17.30	17.75
	4	16.70	17.38
PEDF 1/2	0	26.39	27.08
	1	27.34	27.36
	2	27.48	27.10
	3	27.53	27.66
	4	27.24	27.09
PEDF cod 4	0	28.25	29.15
	1	17.71	17.47
	2	17.92	17.47
	3	16.48	17.44
	4	17.48	17.69
PEDF cod 4	**Samples**	**run I**	**run II**
ΔCt	0	9.40	10.40
	1	-0.02	-0.87
	2	0.35	0.33
	3	-0.82	-0.31
	4	0.78	0.31
ΔΔCt	0	0.00	0.00
	1	-9.42	-11.27
	2	-9.05	-10.07
	3	-10.22	-10.71
	4	-8.62	-10.09
ratio	0	**1.00**	**1.00**
	1	**685.02**	**2469.49**
	2	**530.06**	**1074.91**
	3	**1192.69**	**1675.06**
	4	**393.44**	**1089.92**

Table 20: Experiment 2, runs 1 and 2 (n = 4).

Raw Data	**Samples**	**Cp run I**	**Cp run II**
GAPDH	0	17.08	17.49
	1	17.28	16.96
	2	17.54	18.10
	3	18.00	17.48
	4	19.23	17.88
PEDF 1/2	0	26.52	27.60
	1	27.71	27.17
	2	27.47	28.69
	3	27.43	26.72
	4	28.04	27.19
PEDF cod 4	0	28.66	29.89
	1	17.75	17.54
	2	17.72	17.92
	3	17.18	17.33
	4	17.43	17.47
PEDF cod 4	**Samples**	**run I**	**run II**
ΔCt	0	11.58	12.40
	1	0.47	0.58
	2	0.18	-0.18
	3	-0.82	-0.15
	4	-1.80	-0.41
ΔΔCt	0	0.00	0.00
	1	-11.11	-11.82
	2	-11.40	-12.58
	3	-12.40	-12.55
	4	-13.38	-12.81
ratio	0	**1.00**	**1.00**
	1	**2210.26**	**3615.55**
	2	**2702.35**	**6122.90**
	3	**5404.70**	**5996.90**
	4	**10660.59**	**7181.15**

Table 21: Experiment 3, runs 1 and 2 (n = 4).

Raw Data	Samples	Cp run I	Cp run II
GAPDH	0	17.18	17.67
	1	17.24	17.45
	2	18.19	17.99
	3	17.26	17.07
	4	17.31	18.07
PEDF 1/2	0	26.12	26.31
	1	26.95	26.60
	2	26.66	27.21
	3	27.52	27.04
	4	27.64	27.54
PEDF cod 4	0	28.91	28.95
	1	18.12	17.83
	2	18.00	18.27
	3	17.27	17.04
	4	18.15	17.84
PEDF cod 4	**Samples**	**run I**	**run II**
ΔCt	0	11.73	11.28
	1	0.88	0.38
	2	-0.19	0.28
	3	0.01	-0.03
	4	0.84	-0.23
ΔΔCt	0	0.00	0.00
	1	-10.85	-10.90
	2	-11.92	-11.00
	3	-11.72	-11.31
	4	-10.89	-11.51
ratio	0	**1.00**	**1.00**
	1	**1845.76**	**1910.85**
	2	**3875.05**	**2048.00**
	3	**3373.43**	**2538.92**
	4	**1897.65**	**2916.45**

Table 22: Experiment 4, runs 1 and 2 (n = 4).

Raw Data	**Samples**	**Cp run I**	**Cp run II**
GAPDH	0	17.01	17.33
	1	-	-
	2	16.57	17.23
	3	16.80	17.70
	4	17.09	16.81
PEDF 1/2	0	25.79	27.16
	1	-	-
	2	27.16	27.00
	3	27.56	28.03
	4	27.36	27.27
PEDF cod 4	0	28.47	28.59
	1	-	-
	2	17.05	17.06
	3	16.34	16.15
	4	17,70	17.30
PEDF cod 4	**Samples**	**run I**	**run II**
ΔCt	0	11.46	11.26
	1	0.00	0.00
	2	0.48	-0.17
	3	-0.46	-1.55
	4	0.61	0.49
ΔΔCt	0	0.00	0.00
	1	-	-
	2	-10.98	-11.43
	3	-11.92	-12.81
	4	-10.85	-10.77
ratio	0	**1,00**	**1.00**
	1	**-**	**-**
	2	**2019.80**	**2759.13**
	3	**3875.05**	**7181.15**
	4	**1845.76**	**1746.20**

Table 23: *PEDF* RT qPCR mean $2^{-\Delta\Delta Ct}$ values (n = 4).

0	1	2	3	4
1	1577.26	802.48	1433.88	741.68
1	2912.91	4412.63	5700.8	8920.87
1	1878.31	2961.53	2956.18	2407.05
1	-	2389.47	5528.1	1795.98

Table 24: Western Blot gel-band intensities (pixel^2) of BDNF from A-172 cells transfected using the Neon Transfection System, six days post-transfection (n = 4). (0) -ve control; (1) 1000 V, 30ms, 3 pulses; (2) 1100 V, 30 ms, 2 pulses; (3) 1150 V, 30ms, 2 pulses; (4) 1200 V, 25 ms, 2 pulses

0	1	2	3	4
1	163.12	222.234	180.29	206.076
1	15.991	10.936	3.021	14.407
1	115.56	97.79	142.88	95.89
1	28.92	27.68	30.94	24.9

Table 25: ELISA OD values, cell number and protein levels (pg/h/10^4 cells) of BDNF from A-172 cells transfected using the Neon Transfection System, six days post-transfection (n = 4). (0) -ve control; (1) 1000 V, 30 ms, 3 pulses; (2) 1100 V, 30 ms, 2 pulses; (3) 1150 V, 30ms, 2 pulses; (4) 1200 V, 25 ms, 2 pulses. Standard curve equation is y = 0.4007x - 0.0404

Sample	Dilution (1:x)	Volume (1/ml)	OD (450nm)	BDNF [ng/ml]	BDNF [ng/h]	Cells/ml	BDNF [pg/h/10^4 cells]
0 exp 1	1	0.5	0.193	0.582	0.0121	270000	0.449
1 exp 1	10	0.5	0.449	12.213	0.254	34286	74.214
2 exp 1	10	0.5	0.655	17.354	0.361	57500	62.879
3 exp 1	10	0.5	0.445	12.114	0.252	30000	84.123
4 exp 1	10	0.5	0.592	15.782	0.328	55000	59.781
0 exp 2	1	0.5	0.174	0.535	0.011	412500	0.27
1 exp 2	10	0.5	0.351	9.768	0.203	30000	67.832

2 exp 2	10	0.5	0.198	5.949	0.124	7500	165.266
3 exp 2	10	0.5	0.056	2.405	0.05	0	-
4 exp 2	10	0.5	0.273	7.821	0.163	40000	40.736
0 exp 3	1	0.5	0.163	0.507	0.0105	247500	0.427
1 exp 3	10	0.5	0.615	16.356	0.34	147500	23.102
2 exp 3	10	0.5	0.483	13.062	0.272	167500	16.246
3 exp 3	10	0.5	0.885	23.094	0.481	107500	44.756
4 exp 3	10	0.5	0.464	12.588	0.262	132500	19.792
0 exp 4	1	0.5	0.14	0.45	0.009	300000	0.312
1 exp 4	10	0.5	1.72	43.933	0.915	225000	40.678
2 exp 4	10	0.5	1.525	39.066	0.813	191428	42.516
3 exp 4	10	0.5	1.81	46.179	0.962	240000	40.086
4 exp 4	10	0.5	1.202	31.005	0.646	257500	25.085

Table 26: *BDNF* RT qPCR, crossing point (Cp) values and further calculations - experiment 1, runs 1 and 2, six days post-transfection of the A-172 cell line with the Neon Transfection System (n = 4). (0) -ve control; (1) 1000 V, 30ms, 3 pulses; (2) 1100 V, 30 ms, 2 pulses; (3) 1150 V, 30ms, 2 pulses; (4) 1200 V, 25 ms, 2 pulses

Raw Data	Samples	Cp run I	Cp run II
GAPDH	0	18.58	19.89
	1	17.88	19.14
	2	17.58	18.82
	3	18.34	18.58
	4	17.66	22.05
End. BDNF	0	25.23	25.64
	1	23.34	23.51
	2	22.77	23.92
	3	23.20	24.44
	4	23.84	24.14
Total BDNF	0	25.15	26.09
	1	18.04	19.11
	2	17.38	17.90

	3	17.23	18.35
	4	16.90	18.06
Total BDNF	**Samples**	**run I**	**run II**
ΔCT	0	6.57	6.20
	1	0.16	-0.03
	2	-0.20	-0.92
	3	-1.11	-0.23
	4	-0.76	-3.99
ΔΔCT	0	0.00	0.00
	1	-6.41	-6.23
	2	-6.77	-7.12
	3	-7.68	-6.43
	4	-7.33	-10.19
ratio	0	**1.00**	**1.00**
	1	**85.04**	**75.06**
	2	**109.14**	**139.10**
	3	**205.07**	**86.22**
	4	**160.90**	**1168.14**

Table 27: Experiment 2, runs 1 and 2 (n = 4).

Raw Data	**Samples**	**Cp run I**	**Cp run II**
GAPDH	0	17.17	17.04
	1	17.86	18.35
	2	19.22	20.63
	3	-	-
	4	17.68	18.11
End. BDNF	0	24.61	24.73
	1	24.15	24.41
	2	25.57	24.44
	3	-	-
	4	23.92	24.27

Total BDNF	0	25.11	25.08
	1	18.83	18.64
	2	19.05	19.08
	3	-	-
	4	18.96	19.25
Total BDNF	**Samples**	**run I**	**run II**
ΔCT	0	7.94	8.04
	1	0.97	0.29
	2	-0.17	-1.55
	3	-	-
	4	1.28	1.14
ΔΔCT	0	0.00	0.00
	1	-6.97	-7.75
	2	-8.11	-9.59
	3	-	-
	4	-6.66	-6.90
ratio	0	**1.00**	**1.00**
	1	**125.37**	**215.27**
	2	**276.28**	**770.69**
	3	-	-
	4	**101.13**	**119.43**

Table 28: Experiment 3, runs 1 and 2 (n = 4).

Raw Data	Samples	Cp run I	Cp run II
GAPDH	0	18.93	18.49
	1	18.48	18.64
	2	17.97	18.33
	3	18.15	18.34
	4	18.77	18.74
End BDNF	0	25.20	25.26
	1	24.35	24.75

	2	24.04	24.45
	3	24.18	24.02
	4	25.18	24.84
Total BDNF	0	25.40	25.73
	1	20.66	20.69
	2	20.25	20.43
	3	19.09	19.29
	4	20.89	21.15

Total BDNF	**Samples**	**run I**	**run II**
ΔCT	0	6.47	7.24
	1	2.18	2.05
	2	2.28	2.10
	3	0.94	0.95
	4	2.12	2.41
ΔΔCT	0	0.00	0.00
	1	-4.29	-5.19
	2	-4.19	-5.14
	3	-5.53	-6.29
	4	-4.35	-4.83
ratio	0	**1.00**	**1.00**
	1	**19.56**	**36.50**
	2	**18.25**	**35.26**
	3	**46.21**	**78.25**
	4	**20.39**	**28.44**

Table 29: Experiment 4, runs 1 and 2 (n = 4).

Raw Data	**Samples**	**Cp run I**	**Cp run II**
GAPDH	0	18.41	18.40
	1	18.11	18.37
	2	17.95	18.07
	3	18.44	18.54

	4	18.14	18.81
end BDNF	0	25.02	25.14
	1	24.66	24.66
	2	24.48	24.97
	3	24.76	25.11
	4	25.07	25.32
Total BDNF	0	25.64	25.67
	1	18.70	18.66
	2	18.80	19.19
	3	19.01	19.03
	4	19.36	20.01

BDNF	**Samples**	**run I**	**run II**
ΔCT	0	7.23	7.27
	1	0.59	0.29
	2	0.85	1.12
	3	0.57	0.49
	4	1.22	1.20
ΔΔCT	0	0.00	0.00
	1	-6.64	-6.98
	2	-6.38	-6.15
	3	-6.66	-6.78
	4	-6.01	-6.07
ratio	0	**1.00**	**1.00**
	1	**99.73**	**126.24**
	2	**83.29**	**71.01**
	3	**101.13**	**109.90**
	4	**64.45**	**67.18**

Table 30: *BDNF* RT qPCR mean $2^{-\Delta\Delta Ct}$ values (n = 4).

0	**1**	**2**	**3**	**4**
1	80.05	124.12	145.65	664.52

1	170.32	523.48	-	110.28
1	28.03	26.76	62.23	24.42
1	112.99	77.15	105.51	65.81

Table 31: Cell viability assay of *PEDF* and *BDNF*-transfected A-172 cells, measured 24 hours post-transfection using the Neon Transfection System, (Relative Light Units (RLU)) (n = 10)**.** (0) -ve control; (1) 1000 V, 30ms, 3 pulses; (2) 1100 V, 30 ms, 2 pulses; (3) 1150 V, 30ms, 2 pulses; (4) 1200 V, 25 ms, 2 pulses

0		**1**		**2**		**3**		**4**	
PEDF	**BDNF**	**PEDF**	**BDNF**	**PEDF**	**BDNF**	**PEDF**	**BDNF**	**PEDF**	**BDNF**
2300000	2300000	1500000	1300000	1300000	970000	920000	1100000	1000000	1300000
2000000	2000000	1400000	1100000	950000	1000000	760000	650000	490000	450000
1600000	1600000	990000	490000	650000	400000	160000	140000	520000	370000
1600000	1600000	790000	640000	610000	430000	490000	300000	500000	270000
2100000	2100000	550000	390000	550000	160000	540000	16000	410000	270000
1900000	1900000	400000	250000	550000	110000	400000	36000	390000	400000
1800000	1800000	1500000	1000000	1200000	910000	840000	560000	1100000	310000
1600000	1600000	1300000	1100000	1100000	760000	730000	470000	800000	370000
2000000	2000000	1200000	1200000	710000	720000	740000	1000000	610000	950000
2000000	2000000	1100000	1100000	1900000	540000	730000	980000	730000	1000000

Table 32: Transfection efficiency of the *Venus*-transfected A-172 cells, seven days post transfection with the NEPA-21 device using the electrode in one direction, with both PP and TP set with polarity exchange (n = 4)**.** The numbers shown the % of *Venus* +ve A-172 cells. (0) -ve control; (1) 125 V, 2.5 ms PP; (2) 150 V, 2.5 ms PP; (3) 175 V, 2.5 ms PP; (4) 200 V, 1 ms PP; (5) 200 V, 2.5 ms PP; (6) 200 V, 5 ms PP; (7) 225 V, 2.5 ms PP; (8) 250 V, 2.5 ms PP; (9) 275 V, 2.5 ms PP

0	**1**	**2**	**3**	**4**	**5**	**6**	**7**	**8**	**9**
-	-	-	-	-	-	-	-	-	-
0	0.5	0.8	0.9	0.7	0.8	1.9	0.9	1.4	1.2
0	0.2	0.4	0.6	0.2	0.4	0.9	0.5	0.6	0.4
0	0.3	0.5	0.5	0.4	0.4	1.1	0.3	0.4	0.2

Table 33: Transfection efficiency of the *Venus*-transfected A-172 cells, seven days post transfection with the NEPA-21 device using the electrode in two directions, with both PP and TP set with polarity exchange (n = 4)**.** The numbers indicate the % of *Venus* +ve A-172 cells**.** (0) -ve control; (1) 125 V, 2.5 ms PP; (2) 150 V, 2.5 ms PP; (3) 175 V, 2.5 ms PP; (4) 200 V, 1 ms PP; (5) 200 V, 2.5 ms PP; (6) 200 V, 5 ms PP.

0	1	2	3	4	5	6
-	-	-	-	-	-	-
-	-	-	-	-	-	-
0	0.4	0.6	0.5	0.1	0	0
-	-	-	-	-	-	-

Table 34: Transfection efficiency of the *Venus*-transfected A-172 cells, seven days post transfection with the NEPA-21 device using the electrode in two directions, with PP set with polarity exchange and TP without (n = 4)**.** The numbers indicate the % of *Venus* +ve A-172 cells. (0) -ve control; (1) 125 V, 2.5 ms PP; (2) 150 V, 2.5 ms PP; (3) 175 V, 2.5 ms PP; (4) 200 V, 1 ms PP; (5) 200 V, 2.5 ms PP; (6) 200 V, 5 ms PP; (7) 225 V, 2.5 ms PP; (8) 250 V, 2.5 ms PP; (9) 275 V, 2.5 ms PP

0	1	2	3	4	5	6	7	8	9
0	0.8	1.1	0.9	0.9	1.6	1	1.5	1.8	2.3
0	0.6	0.8	1.6	0.2	0.8	-	0.6	0.4	-
0	0.7	1	1.1	0.3	1.3	-	1.4	2.6	-
0	0.7	1.2	1.6	0.3	1.1	2	1	0.9	-

Table 35: Transfection efficiency of the *Venus*-transfected A-172 cells, seven days post transfection with the NEPA-21 device using the electrode in two directions, with TP set with polarity exchange and PP without (n = 4)**.** The numbers indicate the % of *Venus* +ve A-172 cells. (0) -ve control; (1) 125 V, 2.5 ms PP; (2) 150 V, 2.5 ms PP; (3) 175 V, 2.5 ms PP; (4) 200 V, 1 ms PP; (5) 200 V, 2.5 ms PP; (6) 200 V, 5 ms PP; (7) 225 V, 2.5 ms PP; (8) 250 V, 2.5 ms PP; (9) 275 V, 2.5 ms PP

0	1	2	3	4	5	6	7	8	9
0	0.7	0.7	1	1	1.7	3.6	-	-	-
0	0.5	0.5	1.5	0.6	2.1	3	2.7	-	-
0	0.1	0.7	1	0.6	1.2	1.9	0.9	1.1	-
0	0.3	0.5	0.5	0.4	1.4	1.8	2.2	2.5	2.6

Table 36: Western Blot gel-band intensities (pixel^2) of PEDF secreted from A-172 cells transfected using the NEPA-21 device, seven days post-transfection. (n = 4) (0) -ve control; (1) 125 V, 2.5 ms PP; (2) 150 V, 2.5 ms PP; (3) 175 V, 2.5 ms PP; (4) 200 V, 1 ms PP; (5) 200 V, 2.5 ms PP; (6) 200 V, 5 ms PP; (7) 225 V, 2.5 ms PP; (8) 250 V, 2.5 ms PP; (9) 275 V, 2.5 ms PP

0	1	2	3	4	5	6	7	8	9
1	0.858181	0.571671	0.77425	0.664913	0.563031	0.723464	0.851354	0.955893	0.885835
1	1.135051	1.003576	0.70483	0.859655	0.975103	1.010191	0.862561	0.916027	1.101121
1	0.9508	0.885201	0.89864	0.765536	0.851435	0.839181	1.063009	0.918464	0.809984
1	0.970275	0.977536	0.936297	0.917529	0.863985	0.852542	0.797945	0.902011	0.929732

Table 37: ELISA OD values, cell number and protein levels (pg/h/10^4 cells) of PEDF from A-172 cells transfected using the NEPA-21 device, seven days post-transfection (n = 4)**.** (0) Control; (1) 125 V, 2.5 ms PP; (2) 150 V, 2.5 ms PP; (3) 175 V, 2.5 ms PP; (4) 200 V, 1 ms PP; (5) 200 V, 2.5 ms PP; (6) 200 V, 5 ms PP; (7) 225 V, 2.5 ms PP; (8) 250 V, 2.5 ms PP; Standard curve equation is y = 2.6475x + 0.2579.

Sample	Dilution (1:x)	Volume (1/ml)	OD (450 nm)	PEDF [ng/ml]	PEDF [ng/h]	Cells/ml	PEDF [pg/h/10^4 cells]
0 exp 1	50	0.5	0.469	3.986	0,083	215000	3.863
1 exp 1	50	0.5	0.502	4.61	0,096	150000	6.402
2 exp 1	50	0.5	0.554	5.592	0.116	222500	5.236
3 exp 1	50	0.5	0.475	4.1	0,085	12500	68.334
4 exp 1	50	0.5	0.538	5.289	0.110	0	-
5 exp 1	50	0.5	0.65	7.405	0.154	340000	4.537
6 exp 1	50	0.5	0.595	6.366	0.132	150000	8.842
7 exp 1	50	0.5	0.578	6.045	0.126	72000	17.492
8 exp 1	50	0.5	0.487	4.326	0.09	17500	51.508
9 exp 1	50	0.5	0.453	3.684	0.076	0	-
0 exp 2	50	0.5	0.449	3.609	0.075	370000	2.032
1 exp 2	50	0.5	0.454	3.703	0.077	27500	28.056
2 exp 2	50	0.5	0.455	3.722	0.077	30000	25.849
3 exp 2	50	0.5	0.495	4.477	0.093	52500	17.769
4 exp 2	50	0.5	0.469	3.986	0.083	20000	41.528
5 exp 2	50	0.5	0.464	3.892	0.081	20000	40.545

6 exp 2	50	0.5	0.508	4.723	0.098	75000	13.120
7 exp 2	50	0.5	0.423	3.118	0.065	0	-
8 exp 2	50	0.5	0.474	4.081	0.085	0	-
9 exp 2	50	0.5	0.459	3.798	0.079	0	-
0 exp 3	50	0.5	0.481	4.213	0.087	235000	3.735
1 exp 3	50	0.5	0.446	3.552	0.074	7500	98.677
2 exp 3	50	0.5	0.43	3.25	0.067	5000	135.426
3 exp 3	50	0.5	0.432	3.288	0.068	5000	137.0
4 exp 3	50	0.5	0.393	2.551	0.053	17500	30.374
5 exp 3	50	0.5	0.48	4.194	0.087	147500	5.924
6 exp 3	50	0.5	0.491	4.402	0.091	0	-
7 exp 3	50	0.5	0.427	3.193	0.066	47500	14.006
8 exp 3	50	0.5	0.506	4.685	0.097	20000	48.807
9 exp 3	50	0.5	0.485	4.288	0.089	0	-
0 exp 4	50	0.5	0.528	5.101	0.106	302500	3.513
1 exp 4	50	0.5	0.452	3.665	0.076	30000	25.456
2 exp 4	50	0.5	0.422	3.099	0.064	22500	28.695
3 exp 4	50	0.5	0.486	4.307	0.089	22500	39.887
4 exp 4	50	0.5	0.558	5.667	0.118	17500	67.471
5 exp 4	50	0.5	0.507	4.704	0.098	85000	11.53
6 exp 4	50	0.5	0.529	5.119	0.106	12500	85.332
7 exp 4	50	0.5	0.523	5.006	0.104	10000	104.304
8 exp 4	50	0.5	0.461	3.836	0.079	7500	106.547
9 exp 4	50	0.5	0.491	4.402	0.091	0	-

Table 38: *PEDF* RT qPCR, crossing point (Cp) values and further calculations - experiment 1, runs 1 and 2, a week post-transfection of the A-172 cell line with the NEPA-21 device (n = 4)**.** (0) Control; (1) 125 V, 2.5 ms PP; (2) 150 V, 2.5 ms PP; (3) 175 V, 2.5 ms PP; (4) 200 V, 1 ms PP; (5) 200 V, 2.5 ms PP; (6) 200 V, 5 ms PP; (7) 225 V, 2.5 ms PP; (8) 250 V, 2.5 ms PP

Raw Data	Samples	Cp run I	Cp run II
GAPDH	0	16.77	17.14
	1	18.31	17.98
	2	18.32	17.88

	3	17.81	17.44
	4	17.81	17.23
	5	17.56	17.41
	6	17.31	17.25
	7	-	-
	8	-	-
PEDF cod 4	0	29.94	29.62
	1	29.34	29.29
	2	28.34	28.00
	3	27.53	27.57
	4	27.52	27.68
	5	27.12	26.94
	6	25.85	26.18
	7	-	-
	8	-	-

PEDF cod4	**Samples**	**run I**	**run II**
ΔCT	0	13.17	12.48
	1	11.03	11.31
	2	10.02	10.12
	3	9.72	10.13
	4	9.71	10.45
	5	9.56	9.53
	6	8.54	8.93
	7	-	-
	8	-	-
ΔΔCT	0	0.00	0.00
	1	-2.14	-1.17
	2	-1.68	-2.30
	3	-1.71	-1.50
	4	-2.01	-0.31
	5	-3.45	-3.02
	6	-3.41	-2.73
	7	-	-

	8	-	-
ratio	0	**1.00**	**1.00**
	1	**4.41**	**2.25**
	2	**3.20**	**4.92**
	3	**3.27**	**2.83**
	4	**4.03**	**1.24**
	5	**10.93**	**8.11**
	6	**10.63**	**6.63**
	7	**-**	**-**
	8	**-**	**-**

Table 39: Experiment 2, runs 1 and 2 (n = 4)

Raw Data	Samples	Cp run I	Cp run II
GAPDH	0	18.52	18.26
	1	20.13	19.87
	2	19.42	19.34
	3	17.61	17.59
	4	17.24	18.43
	5	18.48	17.56
	6	18.50	18.15
	7	18.01	17.18
	8	18.47	18.19
PEDF cod 4	0	30.08	29.51
	1	30.51	29.97
	2	29.30	29.53
	3	28.33	27.41
	4	28.60	28.85
	5	26.40	27.03
	6	27.65	27.72
	7	27.82	27.40
	8	25.95	25.90

PEDF cod4	Samples	run I	run II
ΔCT	0	11.56	11.25
	1	10.38	10.10
	2	9.88	10.19
	3	10.72	9.82
	4	11.36	10.42
	5	7.92	9.47
	6	9.15	9.57
	7	9.81	10.22
	8	7.48	7.71
ΔΔCT	0	0.00	0.00
	1	-1.18	-1.15
	2	-1.71	-1.77
	3	-0.85	-1.87
	4	0.53	-1.33
	5	-3.95	-1.73
	6	-2.10	-1.10
	7	-2.51	-1.53
	8	-4.88	-4.15
ratio	0	**1.00**	**1.00**
	1	**2.27**	**2.22**
	2	**3.27**	**3.41**
	3	**1.80**	**3.66**
	4	**0.69**	**2.51**
	5	**15.45**	**3.32**
	6	**4.29**	**2.14**
	7	**5.70**	**2.89**
	8	**29.45**	**17.75**

Table 40: Experiment 3, runs 1 and 2 (n = 4)

Raw Data	Samples	Cp run I	Cp run II
GAPDH	0	17.50	18.05
	1	17.62	18.13
	2	18.42	18.41
	3	21.16	21.87
	4	23.67	23.96
	5	17.21	17.33
	6	20.21	20.41
	7	25.13	25.34
	8	-	-
PEDF cod 4	0	29.10	29.59
	1	27.78	28.41
	2	26.81	27.33
	3	27.99	28.69
	4	30.18	30.09
	5	26.47	27.01
	6	27.25	26.87
	7	27.73	30.20
	8	-	-
PEDF cod4	**Samples**	**run I**	**run II**
ΔCT	0	11.60	11.54
	1	10.16	10.28
	2	8.39	8.92
	3	6.83	6.82
	4	6.51	6.13
	5	9.26	9.68
	6	7.04	6.46
	7	2.60	4.86
	8	-	-
ΔΔCT	0	0.00	0.00
	1	-1.44	-1.26
	2	-3.39	-2.14

	3	-5.08	-4.83
	4	-4.39	-4.11
	5	-1.33	-1.38
	6	-4.12	-5.02
	7	-9.27	-6.36
	8	-	-
ratio	0	**1.00**	**1.00**
	1	**2.71**	**2.39**
	2	**10.48**	**4.41**
	3	**33.82**	**28.44**
	4	**20.97**	**17.27**
	5	**2.51**	**2.60**
	6	**17.39**	**32.45**
	7	**617.37**	**82.14**
	8	**-**	**-**

Table 41: Experiment 4, runs 1 and 2 (n = 4).

Raw Data	Samples	Cp run I	Cp run II
GAPDH	0	17.21	17.77
	1	17.61	17.65
	2	17.23	17.15
	3	18.16	18.50
	4	17.11	17.46
	5	17.33	17.24
	6	16.77	17.40
	7	17.92	18.35
	8	-	-
PEDF cod 4	0	29.58	29.10
	1	28.55	28.79
	2	27.34	28.02
	3	28.29	28.35

	4	27.51	27.71
	5	27.05	27.29
	6	26.43	26.55
	7	27.34	27.51
	8		

PEDF cod4	**Samples**	**run I**	**run II**
ΔCT	0	12.37	11.33
	1	10.94	11.14
	2	10.11	10.87
	3	10.13	9.85
	4	10.40	10.25
	5	9.72	10.05
	6	9.66	9.15
	7	9.42	9.16
	8	0.00	0.00
ΔΔCT	0	0.00	0.00
	1	-1.43	-0.19
	2	-1.10	-0.06
	3	-0.59	-1.46
	4	-0.88	-1.23
	5	-1.51	-1.22
	6	-2.42	-2.19
	7	-2.17	-2.40
	8	0.00	0.00
ratio	0	**1.00**	**1.00**
	1	**2.69**	**1.14**
	2	**2.14**	**1.04**
	3	**1.51**	**2.75**
	4	**1.84**	**2.35**
	5	**2.85**	**2.33**
	6	**5.35**	**4.56**
	7	**4.50**	**5.28**
	8	**1.00**	**1.00**

Table 42: *PEDF* RT qPCR mean $2^{-\Delta\Delta Ct}$ values (n = 4).

0	1	2	3	4	5	6	7	8
1	3.33	4.06	3.05	2.63	9.52	8.63	-	-
1	2.24	3.34	2.73	1.6	9.39	3.22	4.29	23.6
1	2.55	7.45	31.13	19.12	2.56	24.92	-	-
1	1.92	1.59	2.13	2.09	2.59	4.96	4.89	-

Table 43: ELISA OD values, cell number and protein levels (pg/h/10^4 cells) of BDNF from A-172 cells transfected using the NEPA device, seven days post-transfection, (0) -ve control; (1) 125 V, 2.5 ms PP; (2) 150 V, 2.5 ms PP; (3) 175 V, 2.5 ms PP; (4) 200 V, 2.5 ms PP; Standard curve equation is y = 0.0479x - 1.3493.

Sample	Dilution (1:x)	Volume (1/ml)	OD (450nm)	BDNF [ng/ml]	BDNF [ng/h]	Cells/ml	BDNF [pg/h/10^4 cells]
0 exp 1	1	0.5	0.038	28.962	0.603	175000	34.479
1 exp 1	10	0.5	0.031	288.162	6.003	102500	585.696
2 exp 1	10	0.5	0.033	288.58	6.012	40000	1503.022
3 exp 1	10	0.5	0.034	288.789	6.016	10000	6016.44
4 exp 1	10	0.5	0.034	288.789	6.016	22500	2673.973
0 exp 2	1	0.5	0.033	28.858	0.601	40000	150.302
1 exp 2	10	0.5	0.033	288.58	6.012	15000	4008.06
2 exp 2	10	0.5	0.033	288.58	6.012	17500	3435.48
3 exp 2	10	0.5	0.04	290.041	6.042	7500	8056.715
4 exp 2	10	0.5	0.036	289.206	6.025	25000	2410.055
0 exp 3	1	0.5	0.034	28.878	0.601	100000	60.164
1 exp 3	10	0.5	0.033	288.58	6.012	37500	1603.224
2 exp 3	10	0.5	0.034	288.789	6.016	72500	829.853
3 exp 3	10	0.5	0.035	288.997	6.02	2500	24083.159
4 exp 3	10	0.5	-	281.691	5.868	0	-

Table 44: *BDNF* RT qPCR, crossing point (Cp) values and further calculations - experiment 1-3, runs 1 and 2, seven days post-transfection of the A-172 cell line with the NEPA-21 device (n = 3)**.** (0) Control; (1) 125 V, 2.5 ms PP; (2) 150 V, 2.5 ms PP; (3) 175 V, 2.5 ms PP; (4) 200 V, 2.5 ms PP

Raw Data	Samples	Cp run I	Cp run II
GAPDH	0 exp 1	**18.71**	**19.23**
	1 exp 1	**19.02**	**19.13**
	2 exp 1	**18.57**	**18.81**
	3 exp 1	**20.85**	**20.91**
	4 exp 1	**19.08**	**18.95**
	0 exp 2	19.01	18.68
	1 exp 2	19.53	19.47
	2 exp 2	19.12	18.71
	3 exp 2	19.88	19.95
	4 exp 2	18.69	19.32
	0 exp 3	19.01	19.27
	1 exp 3	20.09	20.42
	2 exp 3	18.27	18.97
	3 exp 3	-	-
	4 exp 3	18.73	18.88
Total BDNF	0 exp 1	26.79	26.72
	1 exp 1	26.06	26.31
	2 exp 1	24.14	25.06
	3 exp 1	26.20	26.52
	4 exp 1	23.65	24.99
	0 exp 2	25.44	25.90
	1 exp 2	26.03	26.13
	2 exp 2	24.84	25.59
	3 exp 2	26.03	26.29
	4 exp 2	25.04	25.61
	0 exp 3	25.43	25.60
	1 exp 3	26.60	27.01
	2 exp 3	24.90	25.34
	3 exp 3	-	-

	4 exp 3	25.14	25.68
Total BDNF	**Samples**	**run I**	**run II**
ΔCT	0 exp 1	8.08	7.49
	1 exp 1	7.04	7.18
	2 exp 1	5.57	6.25
	3 exp 1	5.35	5.61
	4 exp 1	4.57	6.04
	0 exp 2	6.43	7.22
	1 exp 2	6.50	6.66
	2 exp 2	5.72	6.88
	3 exp 2	6.15	6.34
	4 exp 2	6.35	6.29
	0 exp 3	6.42	6.33
	1 exp 3	6.51	6.59
	2 exp 3	6.63	6.37
	3 exp 3	-	-
	4 exp 3	6.41	6.80
ΔΔCT	0 exp 1	0.00	0.00
	1 exp 1	0.00	0.00
	2 exp 1	0.00	0.00
	3 exp 1	0.00	0.00
	4 exp 1	0.00	0.00
	0 exp 2	0.00	0.00
	1 exp 2	0.00	0.00
	2 exp 2	-2.36	-0.61
	3 exp 2	-1.11	-0.97
	4 exp 2	-0.69	-0.89
	0 exp 3	0.85	0.08
	1 exp 3	1.16	0.98
	2 exp 3	2.06	0.33
	3 exp 3	-	-
	4 exp 3	-0.02	-0.42
ratio	0 exp 1	**1.00**	**1.00**

1 exp 1	**1.00**	**1.00**
2 exp 1	**1.00**	**1.00**
3 exp 1	**1.00**	**1.00**
4 exp 1	**1.00**	**1.00**
0 exp 2	**1.00**	**1.00**
1 exp 2	**1.00**	**1.00**
2 exp 2	**5.13**	**1.53**
3 exp 2	**2.16**	**1.96**
4 exp 2	**1.61**	**1.85**
0 exp 3	**0.55**	**0.95**
1 exp 3	**0.45**	**0.51**
2 exp 3	**0.24**	**0.80**
3 exp 3	-	-
4 exp 3	**1.01**	**1.34**

Table 45: *BDNF* RT qPCR mean $2^{-\Delta\Delta Ct}$ values (n = 3)

0	**1**	**2**	**3**	**4**
1	1	1	1	1
1	1	3.33	2.06	1.73
1	0.64	0.69	-	1.57

Table 46: Flow cytometry analysis of *Venus*-transfected R28 cell cultures, 48 hours post transfection with the Neon Transfection System (n = 4). The numbers shown the % of *Venus* +ve R28 cells. (0) -ve control; (1) 1100 V, 30 ms, 2 pulses; (2) 1150 V, 30 ms, 2 pulses; (3) 1200 V, 25 ms, 2 pulses; (4) 1300 V, 30 ms, 1 pulse

0	**1**	**2**	**3**	**4**
0	5.1	7.7	10.1	9.1
0	6.7	17.7	17.9	15.3
0	12.8	17.9	27.5	23.5
0	4.2	9.5	9.2	8.8

Table 47: Area, CVa and mean *e* values of different cell lines measured using the Cell Profiler 4.2.6 software

	Area mean (pixel²)	Area mean (µm²)	Area std (pixel²)	Area CV	*e* mean
A172 in suspension before transfection (same flask)					
Image 1	1104.53	22766.13055	381.22	0.34514228	0.56
Image 2	1007.84	20773.19494	307.31	0.30491943	0.58
Image 3	1059.69	21841.9064	286	0.26989025	0.54
Image 4	1001.79	20648.49476	229.36	0.22895018	0.53
A172 on a surface, one week before transfection					
Image 1	5477.86	112907.4592	2852.75	0.52077819	0.95
Image 2	2858.09	58909.80784	1479.46	0.5176394	0.94
Image 3	5063.16	104359.8287	3465.86	0.68452508	0.89
Image 4	5764.72	118820.1028	3035.58	0.52657891	0.9
A172 24 hours post-transfection (Neon)					
Image 1 fluo	4122.83	84978.12283	3055.81	0.74119234	0.89
Image 2 fluo	6689.27	137876.5575	2450.92	0.36639574	0.82
Image 3 fluo	4846.67	99897.62337	2828.15	0.58352436	0.85
Image 4 fluo	4909.62	101195.1236	2329.08	0.47439109	0.85
A172 six days post-transfection (Neon, 1200 V, 25 ms, 2 p)					
Image 1 fluo	4049.59	83468.52924	1544.57	0.38141392	0.95
Image 2 fluo	6388.1	131668.962	2679.81	0.41950032	0.9
Image 3 fluo	4819.11	99329.56768	2064.69	0.42843803	0.91
Image 4 fluo	3735.96	77004.11314	1854.23	0.49631955	0.91
A172 (NEPA, 24 well plate, 24 hours post-plating), immediately before transfection					
Image 1	8376.83	172659.8692	4516.29	0.5391407	0.88
Image 2	8525.65	175727.2875	5097.4	0.5978899	0.88
Image 3	5756.08	118642.0185	3084.14	0.53580562	0.87
Image 4	5430.96	111940.7751	3086.11	0.56824392	0.92

A172 a week post-transfection (NEPA, PP+ TP±, 200 V, 2.5 ms, electrode 2 directions)					
Image 1 fluo	3491.55	71966.43198	2798.42	0.80148358	0.88
Image 2 fluo	6145.6	126670.649	4518.8	0.73529029	0.89
Image 3 fluo	4570.09	94196.86704	3930.63	0.86007715	0.89
Image 4 fluo	2616.45	53929.22082	1274.3	0.48703396	0.93
A172, a week post-transfection (NEPA, PP± TP±, 200 V, 2.5 ms, electrode 1 direction)					
Image 1 fluo	2823.49	58196.64648	1465.43	0.5190137	0.9
Image 2 fluo	2411.83	49711.67523	1044.29	0.43298657	0.93
Image 3 fluo	2656.52	54755.12763	1037.47	0.39053724	0.91
ARPE-19 in suspension before MP (same flask)					
Image 1	815.04	16799.27846	145.53	0.17855565	0.56
Image 2	896.93	18487.16239	247.09	0.27548415	0.36
Image 3	891.34	18371.94354	168.99	0.18959095	0.4
Image 4	800.2	16493.40232	133.3	0.16658335	0.41
ARPE-19 on a surface, one week before MP					
Image 1	3443.72	70980.57915	1507.4	0.43772432	0.9
Image 2	3599.91	74199.90496	1486.12	0.41282143	0.89
Image 3	4219.12	86962.81379	1200.91	0.28463518	0.76
Image 4	3599.93	74200.31719	1709.4	0.47484257	0.84
ARPE-19 24 hours post-transfection (Neon)					
Image 1 fluo	3050.01	62865.58612	1158.48	0.37982826	0.69
Image 2 fluo	2929.05	60372.40698	1492.24	0.50946211	0.73
Image 3 fluo	2996.59	61764.51444	1504.99	0.50223421	0.82
R28, MEA (Neg C, 24 hours post-passage) (no uniformity in electrode shape)					
Image 1	1531.77	18231.89243	739.22	0.48259203	0.71
Image 2	1814.45	21596.49113	825.97	0.45521783	0.74
Image 3	3584.58	42665.46345	1578.04	0.4402301	0.8
Image 4	6358.27	75679.30868	3287.56	0.51705259	0.94

R28, MEA (24 hours post-transfection) (triangle electrodes, 6500 cycles, 14 V Vpp)					
Image 1 fluo	512.11	6095.389275	205.28	0.40085138	0.77
Image 2 fluo	2163.55	25751.65388	856.27	0.39577084	0.81
Image 3 fluo	4807.5	57221.26875	1591.99	0.33114717	0.82
Image 4 fluo	1463.5	17419.30875	513,63	0.35096003	0.75

Table 48: Different parameters tested for transfections of the A-172 cell line using the MEA device. Frequency was maintained at 40 kHz and number of pulses was maintained at one. A square wave pulse was applied. G - gelatin, C - circle, T - triangle, SCT - semi-circular triangle, B - butterfly, Ch - checkerboard, Con - concentric, DAR - double alternating rows, H - half, LCh - long checkerboard, MAR - multiple alternating rows, Rcon - repeated ceoncentric, SAR - single alternating rows. The voltage here refers to the V_{pp}. The time here refers to the time post-transfection, when the samples were analysed.

Time (h)	Seeding time	Coating	Pattern	V	Width (ms)	Shapes	Plasmid/ dye	Plasmid con
48	15 min RT	-	Ch	12	100	SCT	FITC	2µg/µl
48	15 min RT	-	Ch	14	100	SCT	FITC	2µg/µl
48	15 min RT	-	H	12	100	SCT	FITC	2µg/µl
48	15 min RT	-	H	14	100	SCT	FITC	2µg/µl
48	15 min RT	-	LCh	12	100	SCT	FITC	2µg/µl
48	15 min RT	-	LCh	14	100	SCT	FITC	2µg/µl
72	15 min RT	-	H	12	100	SCT	pmaxGFP	750 ng
72	15 min RT	-	H	14	100	SCT	pmaxGFP	750 ng
72	15 min RT	-	H	16	100	SCT	pmaxGFP	750 ng
96	15 min RT	-	H	12	100	SCT	pmaxGFP	750 ng
96	15 min RT	-	H	14	75	SCT	pmaxGFP	750 ng
96	15 min RT	-	H	14	100	SCT	pmaxGFP	750 ng
24	15 min RT	-	Ch	8	200	SCT	pmaxGFP	750 ng
24	15 min RT	-	Ch	10	200	SCT	pmaxGFP	750 ng
24	15 min RT	-	Ch	12	100	SCT	pmaxGFP	750 ng
24	15 min RT	-	Ch	12	200	SCT	pmaxGFP	750 ng
24	15 min RT	-	Ch	14	100	SCT	pmaxGFP	750 ng

24	15 min RT	-	Ch	16	100	SCT	pmaxGFP	750 ng
24	15 min RT	-	Con	8	200	SCT	pmaxGFP	750 ng
24	15 min RT	-	Con	10	200	SCT	pmaxGFP	750 ng
24	15 min RT	-	Con	12	200	SCT	pmaxGFP	750 ng
24	15 min RT	-	DAR	12	100	SCT	pmaxGFP	750 ng
24	15 min RT	-	DAR	14	100	SCT	pmaxGFP	750 ng
24	15 min RT	-	DAR	16	100	SCT	pmaxGFP	750 ng
24	15 min RT	-	H	8	200	SCT	pmaxGFP	750 ng
24	15 min RT	-	H	10	200	SCT	pmaxGFP	750 ng
24	15 min RT	-	H	12	100	T	pmaxGFP	750 ng
24	15 min RT	0.5% G	H	12	100	SCT	pmaxGFP	750 ng
24	15 min RT	-	H	12	200	SCT	pmaxGFP	750 ng
24	15 min RT	0.5% G	H	12	200	C	pmaxGFP	750 ng
24	15 min RT	-	H	14	100	C	pmaxGFP	750 ng
24	15 min RT	0.5% G	H	14	100	SCT	pmaxGFP	750 ng
24	15 min RT	0.5% G	H	14	100	T	pmaxGFP	750 ng
24	15 min RT	0.5% G	H	14	100	C	pmaxGFP	750 ng
24	15 min RT	0.5% G	H	14	200	T	pmaxGFP	750 ng
24	15 min RT	0.5% G	H	14	200	C	pmaxGFP	750 ng
24	15 min RT	0.5% G	H	14	200	SCT	pmaxGFP	750 ng
24	15 min RT	-	LCh	12	100	SCT	pmaxGFP	750 ng
24	15 min RT	-	LCh	14	100	SCT	pmaxGFP	750 ng
24	15 min RT	-	LCh	16	100	SCT	pmaxGFP	750 ng
24	15 min RT	-	SAR	8	200	SCT	pmaxGFP	750 ng
24	15 min RT	-	SAR	10	200	SCT	pmaxGFP	750 ng
24	15 min RT	-	SAR	12	100	SCT	pmaxGFP	750 ng
24	15 min RT	-	SAR	12	200	SCT	pmaxGFP	750 ng
24	15 min RT	-	SAR	14	100	SCT	pmaxGFP	750 ng
24	15 min RT	-	SAR	16	100	SCT	pmaxGFP	750 ng
48	20 min RT, 30 min 37°C	0.5% G	MAR	12	100	SCT	pmaxGFP	750 ng
48	20 min RT, 30 min 37°C	0.5% G	MAR	12	100	T	pmaxGFP	750 ng

48	20 min RT, 30 min 37°C	0.5% G	MAR	12	100	C	pmaxGFP	750 ng
48	20 min RT, 30 min 37°C	0.5% G	MAR	14	100	SCT	pmaxGFP	750 ng
48	20 min RT, 30 min 37°C	0.5% G	MAR	14	100	T	pmaxGFP	750 ng
48	20 min RT, 30 min 37°C	0.5% G	MAR	14	100	C	pmaxGFP	750 ng
24	30 min RT, 37°C	1% PDL	MAR	12	100	SCT	pmaxGFP	750 ng
24	30 min RT, 37°C	1% PDL	MAR	12	100	T	pmaxGFP	750 ng
24	30 min RT, 37°C	1% PDL	MAR	12	100	C	pmaxGFP	750 ng
24	30 min RT, 37°C	1% PDL	MAR	14	100	SCT	pmaxGFP	750 ng
24	30 min RT, 37°C	1% PDL	MAR	14	100	T	pmaxGFP	750 ng
24	30 min RT, 37°C	1% PDL	MAR	14	100	C	pmaxGFP	750 ng
48	30 min RT, 37°C	0.5% G	B	12	100	SCT	pmaxGFP	750 ng
48	30 min RT, 37°C	0.5% G	B	12	100	T	pmaxGFP	750 ng
48	30 min RT, 37°C	0.5% G	B	12	100	C	pmaxGFP	750 ng
48	30 min RT, 37°C	0.5% G	B	14	100	SCT	pmaxGFP	750 ng
48	30 min RT, 37°C	0.5% G	B	14	100	T	pmaxGFP	750 ng
48	30 min RT, 37°C	0.5% G	B	14	100	C	pmaxGFP	750 ng
24	30 min RT, 37°C	0.5% G	Rcon	12	100	SCT	pmaxGFP	750 ng
24	30 min RT, 37°C	0.5% G	Rcon	12	100	T	pmaxGFP	750 ng
24	30 min RT, 37°C	0.5% G	Rcon	12	100	C	pmaxGFP	750 ng
24	30 min RT, 37°C	0.5% G	Rcon	12	150	T	pmaxGFP	750 ng
24	30 min RT, 37°C	0.5% G	Rcon	12	150	C	pmaxGFP	750 ng
24	30 min RT, 37°C	0.5% G	Rcon	12	150	SCT	pmaxGFP	750 ng
24	30 min RT, 37°C	0.2% G	Rcon	12	150	T	pmaxGFP	750 ng
24	30 min RT, 37°C	0.2% G	Rcon	12	150	C	pmaxGFP	750 ng
24	30 min RT, 37°C	0.2% G	Rcon	12	150	SCT	pmaxGFP	750 ng
24	30 min RT, 37°C	0.1% G	Rcon	12	162.5	T	pmaxGFP	750 ng
24	30 min RT, 37°C	0.1% G	Rcon	12	162.5	C	pmaxGFP	750 ng
24	30 min RT, 37°C	0.1% G	Rcon	12	162.5	SCT	pmaxGFP	750 ng
24	30 min RT, 37°C	0.1% G	Rcon	12	175	T	pmaxGFP	750 ng

24	30 min RT, 37°C	0.1% G	Rcon	12	175	C	pmaxGFP	750 ng
24	30 min RT, 37°C	0.1% G	Rcon	12	175	SCT	pmaxGFP	750 ng
24	30 min RT, 37°C	0.5% G	Rcon	14	100	SCT	pmaxGFP	750 ng
24	30 min RT, 37°C	0.5% G	Rcon	14	100	T	pmaxGFP	750 ng
24	30 min RT, 37°C	0.5% G	Rcon	14	100	C	pmaxGFP	750 ng
24	30 min RT, 37°C	-	Rcon	14	100	SCT	pmaxGFP	750 ng
24	30 min RT, 37°C	-	Rcon	14	100	T	pmaxGFP	750 ng
24	30 min RT, 37°C	-	Rcon	14	100	C	pmaxGFP	750 ng
24	30 min RT, 37°C	0.5% G	Rcon	14	150	T	pmaxGFP	750 ng
24	30 min RT, 37°C	0.5% G	Rcon	14	150	C	pmaxGFP	750 ng
24	30 min RT, 37°C	0.5% G	Rcon	14	150	SCT	pmaxGFP	750 ng
24	30 min RT, 37°C	0.2% G	Rcon	14	150	T	pmaxGFP	750 ng
24	30 min RT, 37°C	0.2% G	Rcon	14	150	C	pmaxGFP	750 ng
24	30 min RT, 37°C	0.2% G	Rcon	14	150	SCT	pmaxGFP	750 ng
24	30 min RT, 37°C	0.1% G	Rcon	14	162.5	T	pmaxGFP	750 ng
24	30 min RT, 37°C	0.1% G	Rcon	14	162.5	C	pmaxGFP	750 ng
24	30 min RT, 37°C	0.1% G	Rcon	14	1625	SCT	pmaxGFP	750 ng
24	30 min RT, 37°C	0.1% G	Rcon	14	175	T	pmaxGFP	750 ng
24	30 min RT, 37°C	0.1% G	Rcon	14	175	C	pmaxGFP	750 ng
24	30 min RT, 37°C	0.1% G	Rcon	14	175	SCT	pmaxGFP	750 ng

Table 49: Different parameters attempted for transfections of the R28 cell line using the MEA device.

Time (h)	Seeding	Coating	Pattern	V	Width (ms)	Shapes	Plasmid	Plasmid con
24	30 min RT, 37°C	0.1% G	Ch	14	162.5	T	pmaxGFP	750 ng
24	30 min RT, 37°C	0.1% G	Ch	14	162.5	C	pmaxGFP	750 ng
24	30 min RT, 37°C	0.1% G	Ch	14	162.5	SCT	pmaxGFP	750 ng
24	30 min RT, 37°C	0.1% G	H	14	162.5	T	pmaxGFP	750 ng
24	30 min RT, 37°C	0.1% G	H	14	162.5	C	pmaxGFP	750 ng
24	30 min RT, 37°C	0.1% G	H	14	162.5	SCT	pmaxGFP	750 ng
24	30 min RT, 37°C	0.1% G	Rcon	12	150	T	pmaxGFP	750 ng

24	30 min RT, 37°C	0.1% G	Rcon	12	150	C	pmaxGFP	750 ng
24	30 min RT, 37°C	0.1% G	Rcon	12	150	SCT	pmaxGFP	750 ng
24	30 min RT, 37°C	0.1% G	Rcon	14	150	T	pmaxGFP	750 ng
24	30 min RT, 37°C	0.1% G	Rcon	14	150	C	pmaxGFP	750 ng
24	30 min RT, 37°C	0.1% G	Rcon	14	150	SCT	pmaxGFP	750 ng
24	30 min RT, 37°C	0.1% G	Rcon	14	162.5	T	pmaxGFP	750 ng
24	30 min RT, 37°C	0.1% G	Rcon	14	162.5	C	pmaxGFP	750 ng
24	30 min RT, 37°C	0.1% G	Rcon	14	162.5	SCT	pmaxGFP	750 ng

6.1. Cell Profiler pipeline : Cells in suspension

1. Main pipeline

Images -

Filter image? - image only

Apply filters to file list - yes

Metadata -

Extract metadata? - no

Names and types -

Assign a name to - all images

Process as 3D? - no

Select the image type - grayscale image

Name to assign to these images - ARPE-19_suspension

Set the intensity range from - image metadata

2. Modules

IdentifyPrimaryObjects

Use advanced settings - no

Set the input image - ARPE19_suspension

Name the primary objects to be identified - IdentifyPrimaryObjects

Typical diameter of objects in pixel units - 30 (min) 60 (max)

Discard objects outside diameter range? - yes

Discard objects touching the border of the image? - yes

Edit Objects Manually

Select the objects to be edited - IdentifyPrimaryObjects

Name the edited objects - EditedObjects

Allow overlapping objects? - no

Numbering of edited objects - renumber

Display a guiding image? - yes

Select the guiding image - ARPE19_suspension

Measure Object Size Shape

Select objects to measure - EditedObjects

Calculate the Zernike features? - yes

Calculate the advanced features? - no

When running the program, it paused to request object editing for every image. The cells were individually and manually edited to be selected as objects for further processing.

6.2. Cell Profiler pipeline : Cells on a surface

1. Main pipeline

Images -

Filter image? - image only

Apply filters to file list - yes

Metadata -

Extract metadata? - no

Names and types -

Assign a name to - all images

Process as 3D? - no

Select the image type - grayscale image

Name to assign to these images - ARPE-19

Set the intensity range from - image metadata

2. Modules

Image Math

Operation - invert

Name the output image - ImageAfterMath

Select the first image - ‘A-172’ from Names and types

Multiply the first image by - 1.0

Raise the power of the result by - 1.0

Multiply the result by - 1.0

Add to result - 0.0

Set values less than 0 as equal to 0? - yes

Set values greater than 1 as equal to 1? - yes

Replace invalid values with 0? - yes

Ignore the image masks - no

Image Math 2

Operation - log transform (base 2)

Name the output image - ImageAfterMath2

Select the first image - ImageAfterMath

Multiply the first image by - 1.0

Raise the power of the result by - 2.0

Multiply the result by - 1.0

Add to result - 0.0

Set values less than 0 as equal to 0? - yes

Set values greater than 1 as equal to 1? - yes

Replace invalid values with 0? - yes

Ignore the image masks - no

Enhanced Edges

Select the input image - ImageAfterMath2

Name the output image - EdgedImage

Select an edge finding method - Prewitt

Select edge direction to enhance - all

Identify Primary Objects

Use advanced settings - yes

Set the input image - EdgedImage (output from EnhancedEdges)

Name the primary objects to be identified - IdentifyPrimaryObjects

Typical diameter of objects in pixel units - 20 (min) 1000 (max)

Discard objects outside diameter range? - yes

Discard objects touching the border of the image? - yes

Threshold strategy - global

Thresholding method - Robust Background

Lower outlier fraction - 0.15

Upper outlier fraction - 0.39

Averaging method - mean

Variance method - median absolute deviation

# of deviations - 3.3

Threshold smoothing scale - 1.5488

Threshold correction factor - 1.0

Lower and upper bounds on threshold - 0.0 - 1.0

Method to distinguish clumped objects - shape

Method to draw dividing line between clumped objects - intensity

Automatically calculate size of smoothing filter for declumping? - yes

Automatically calculate minimum allowed distance between local maxima - no

Supress local maxima that are closer than this minimum allowed distance - 100.0

Speed up by using lower resolution image to find local maxima? - yes

Display accepted local maxima? - no

Fill holes in identified objects? - never

Handling of objects if excess number of objects identified - continue

Edit Objects Manually

Select the objects to be edited - IdentifyPrimaryObjects

Name the edited objects - EditedObjects

Allow overlapping objects? - no

Numbering of edited objects - renumber

Display a guiding image? - yes

Select the guiding image - ImageAfterMath2

Measure Object Size Shape

Select objects to measure - EditedObjects

Calculate the Zernike features? - yes

Calculate the advanced features? - yes

When running the program, it paused to request object editing for every image. The cells were individually and manually edited and selected as objects for further processing.

Table 50: Different culture conditions tested for the Müller cell isolation. The number of mice here refers to the mice used in one isolation. G - gelatin; laminin was diluted in DPBS

No of mice	Coating	Coating time	FBS	Dissociation time	Cultured on	medium change after isolation
3	0.1% G	30 min	10%	1 h	6 well	5 days
3	0.1% G	30 min	10%	1 h	24 well	5 days
3	0.1% G	30 min	10%	1 h	LabTek, 4 well	5 days
3	0.1% G	30 min	20%	1 h	LabTek, 4 well	72 h
3	0.1% G	30 min	20%	1 h	LabTek, 4 well	24 h
3	0.15% G	30 min	20%	1 h	LabTek, 16 well	24 h
4	0.1% G	30 min	20%	1 h	LabTek, 16 well	24 h
4	0.1% G	30 min	20%	45 min	LabTek, 16 well	24 h
4	0.1% G	30 min	20%	40 min	LabTek, 16 well	24 h
4	0.1% G	30 min	20%	35 min	Lab-Tek 16 well	24 h
2	0.15% G	30 min	20%	40 min	Lab-Tek 16 well	24 h
4	0.15% G	30 min	20%	40 min	Lab-Tek 4 well	24 h
4	0.15% G	1 h	20%	40 min	Lab-Tek 4 well	24 h

4	10% laminin	overnight	20%	40 min	Lab-Tek 4 well	24 h
4	0.2% G	1 h	20%	40 min	Lab-Tek 4 well	24 h
4	0.2% G	1 h	20%	40 min	24 well	24 h
4	0.2% G	2.5 h	20%	40 min	Lab-Tek 4 well	24 h
4	0.2% G	1.25 h	20%	40 min	Lab-Tek 4 well	24 h

8. List of Figures

Figure 1: Schematic illustration of the mammalian retina. 2
Figure 2: Remodelling of the mammalian retina in retinal degeneration. 5
Figure 3: Anatomical locations for the different types of retinal prostheses 8
Figure 4: The *Sleeping Beauty* transposon system 14
Figure 5: Mechanism of electropermeabilization and electroporation 15
Figure 6: Cuvette-based and pipette tip-based electroporation 16
Figure 7: The CUY900-13-3-5 cell culture plate electrode used for transfection with the NEPA-21 device 17
Figure 8: The MEA design used for transfection experiments 18
Figure 9: Individual steps of the Müller cell isolation from WT mouse retinas 31
Figure 10: Illustration of the *SB* transposase and transposon plasmids used in this study. 33
Figure 11: The CUY900-13-3-5 electrode placed inside a 24 well, ready for electroporation 36
Figure 12: Installation of the MEA setup used for electroporation 37
Figure 13: The different arrangements of active electrodes and ground electrodes 38
Figure 14: The basic pipeline for measuring cell properties from images of cells cultured on a surface with the aid of the Cell Profiler 4.2.6 software 44
Figure 15: The *Venus*-positive A-172 cells, transfected in suspension using the Neon Transfection System, as observed 24 hours post-transfection. 47
Figure 16: Flow cytometry analysis of *Venus*-transfected A-172 cell cultures, six days post-transfection. 48
Figure 17: Luciferase-based cell viability analysis of *Venus*-transfected A-172 cell culture, 24 hours post-transfection 49
Figure 18: Fluorescence images of *Venus*-expressing A-172 cells, transfected with the four optimal settings and recorded over four months (10x). 50
Figure 19: Long term analysis of *Venus* transfected A-172 cells, studied over a period of four months 51

Figure 20: SDS PAGE and western blot of supernatant from A-172 cells transfected with *PEDF* using the Neon Transfection System six days post-transfection 52
Figure 21: ELISA based analysis of PEDF protein secretion from A-172 cells transfected using the Neon Transfection System, six days post-transfection 53
Figure 22: Expression analysis of *PEDF* gene measured by real-time quantitative PCR, six days post transfection of the A-172 cells with the Neon Transfection System 54
Figure 23: SDS PAGE and western blot of supernatant from A-172 cells transfected with *BDNF* using the Neon Transfection System, six days post-transfection. 55
Figure 24: ELISA based analysis of BDNF protein secretion from A-172 cells transfected using the Neon Transfection System, six days post-transfection. 56
Figure 25: Expression analysis of *BDNF* gene measured by real-time quantitative PCR, six days post-transfection of the A-172 cells with the Neon Transfection System. 56
Figure 26: Comparison of cell viability of cells transfected with *PEDF* and *BDNF*, 24 hours post-transfection of the A-172 cells with the Neon Transfection System 57
Figure 27: Flow cytometry analysis of A-172 cells transfected on a surface with *Venus* using the NEPA-21 electroporation device, seven days post-transfection 59
Figure 28: SDS PAGE and western blot of supernatants from A-172 cells transfected with *PEDF* using the NEPA-21 electroporation device, seven days post-transfection. 61
Figure 29: ELISA-based analysis of PEDF protein secretion by A-172 cells transfected with *PEDF* using the NEPA-21 electroporation device, seven days post-transfection. 61
Figure 30: Expression analysis of the *PEDF* gene measured by quantitative real-time PCR performed for A-172 cells transfected with *PEDF* using the NEPA-21 electroporation device, seven days post-transfection.. 62
Figure 31: SDS PAGE and western blot supernatants from A-172 cells transfected with *BDNF* using the NEPA-21 electroporation device, seven days post-transfection 63
Figure 32: ELISA-based analysis of BDNF protein secretion by A-172 cells transfected with *BDNF* using the NEPA-21 electroporation device, seven days post-transfection. 63
Figure 33: Expression analysis of the *BDNF* gene measured by real-time quantitative PCR performed for A-172 cells transfected with *BDNF* using the NEPA-21 electroporation device, seven days post-transfection 64
Figure 34: Results of MEA-based transfection of A-172 cells with pmaxGFP, 24 hours post-transfection (10x) 65
Figure 35: Fluorescence images of *Venus*-transfected R28 cell line at different time points (10x) 66

Figure 36: Flow cytometry analysis of R28 cells transfected with *Venus* using the Neon Transfection System, 48 hours post-transfection. 66
Figure 37: Results of MEA-based electroporation of R28 cells, transfected with pmaxGFP, 24 hours post-transfection (10x) 69
Figure 38: Results of MEA-based electroporation of R28 cells, transfected with pmaxGFP, 24 hours post-transfection (10x) 69
Figure 39: Cell mean area measurement using Cell Profiler 4.2.6 software 71
Figure 40: Comparison of different cell properties, before and post-transfection 75
Figure 41: Primary Müller cells, as observed at different time points after isolation (10x). 76
Figure 42: Primary Müller cell culture 76
Figure 43: Immunocytochemical analysis of primary Müller cell cultures isolated from four-week-old C57BL/6J WT mice (20x), four weeks post-isolation. 77
Figure 44: Fluorescent images of the primary Müller cells transfected with *Venus*, using the Neon Transfection System (10x) 78
Figure 45: Immunocytochemical analysis of transfected primary Müller cell cultures, seven days post-transfection with *Venus*, using the Neon Transfection System (20x) 80
Figure 46: Immunocytochemical analysis of primary Müller cell cultures transfected with *Venus*, 14 days post-transfection with the NEPA-21 device (20x) 81

9. List of tables

Table 1: Overview of general devices and the corresponding companies. 21
Table 2: Overview of electroporation devices and the corresponding companies. 22
Table 3: Overview of consumables and the corresponding companies 23
Table 4: Overview of chemicals and the corresponding companies. 24
Table 5: Overview of kits and the corresponding companies. 26
Table 6: Overview of primary antibodies and the corresponding companies. 27
Table 7: Overview of secondary antibodies and the corresponding companies 27
Table 8: Overview of software and the corresponding companies. 28
Table 9: Primers utilized in RT qPCR 42
Table 10: Thermal cycler conditions applied for RT qPCR 42
Table 11: Flow cytometry analysis of *Venus*-transfected A-172 cell cultures, six days post transfection with the Neon Transfection System 123
Table 12: Luciferase-based cell viability analysis of *Venus*-transfected A-172 cell culture, 24 hours post-transfection with the Neon Transfection System 124
Table 13: Long-term transfection analysis of *Venus* transfection of A-172 cells with 1000 V, 30 ms, 3 pulses using the Neon Transfection System 125
Table 14: Long-term transfection analysis of *Venus* transfection of A-172 cells with 1100 V, 30 ms, 2 pulses using the Neon Transfection System 125
Table 15: Long-term transfection analysis of *Venus* transfection of A-172 cells with 1150 V, 30 ms, 2 pulses using the Neon Transfection System 126
Table 16: Long-term transfection analysis of *Venus* transfection of A-172 cells with 1200 V, 25 ms, 2 pulses using the Neon Transfection System 126
Table 17: Western Blot gel-band intensities (pixel^2) of PEDF from A-172 cell line transfected using the Neon Transfection System, six days post-transfection 126
Table 18: ELISA OD values, cell number and protein levels (pg/h/10^4 cells) of PEDF from A-172 cells transfected using the Neon Transfection System, six days post-transfection 127

Table 19: *PEDF* RT qPCR, crossing point (Cp) values and further calculations - experiment 1, runs 1 and 2, six days post-transfection of the A-172 cell line with the Neon Transfection System....127
Table 20: Experiment 2, runs 1 and 2 (n = 4). 129
Table 21: Experiment 3, runs 1 and 2 (n = 4). 130
Table 22: Experiment 4, runs 1 and 2 (n = 4). 131
Table 23: *PEDF* RT qPCR mean $2^{-\Delta\Delta Ct}$ values (n = 4). 132
Table 24: Western Blot gel-band intensities (pixel^2) of BDNF from A-172 cells transfected using the Neon Transfection System, six days post-transfection 132
Table 25: ELISA OD values, cell number and protein levels (pg/h/10^4 cells) of BDNF from A-172 cells transfected using the Neon Transfection System, six days post-transfection 132
Table 26: *BDNF* RT qPCR, crossing point (Cp) values and further calculations - experiment 1, runs 1 and 2, six days post-transfection of the A-172 cell line with the Neon Transfection System....133
Table 27: Experiment 2, runs 1 and 2 (n = 4). 134
Table 28: Experiment 3, runs 1 and 2 (n = 4). 135
Table 29: Experiment 4, runs 1 and 2 (n = 4). 136
Table 30: *BDNF* RT qPCR mean $2^{-\Delta\Delta Ct}$ values (n = 4)....137
Table 31: Cell viability assay of *PEDF* and *BDNF*-transfected A-172 cells, measured 24 hours post-transfection using the Neon Transfection System, (Relative Light Units (RLU)) 138
Table 32: Transfection efficiency of the *Venus*-transfected A-172 cells, seven days post transfection with the NEPA-21 device using the electrode in one direction, with both PP and TP set with polarity exchange....138
Table 33: Transfection efficiency of the *Venus*-transfected A-172 cells, seven days post transfection with the NEPA-21 device using the electrode in two directions, with both PP and TP set with polarity exchange....139
Table 34: Transfection efficiency of the *Venus*-transfected A-172 cells, seven days post transfection with the NEPA-21 device using the electrode in two directions, with PP set with polarity exchange and TP without 139
Table 35: Transfection efficiency of the *Venus*-transfected A-172 cells, seven days post transfection with the NEPA-21 device using the electrode in two directions, with TP set with polarity exchange and PP without....139
Table 36: Western Blot gel-band intensities (pixel^2) of PEDF secreted from A-172 cells transfected using the NEPA-21 device, seven days post-transfection....140

Table 37: ELISA OD values, cell number and protein levels (pg/h/10^4 cells) of PEDF from A-172 cells transfected using the NEPA-21 device, seven days post-transfection 140
Table 38: *PEDF* RT qPCR, crossing point (Cp) values and further calculations - experiment 1, runs 1 and 2, a week post-transfection of the A-172 cell line with the NEPA-21 device 141
Table 39: Experiment 2, runs 1 and 2 (n = 4) 143
Table 40: Experiment 3, runs 1 and 2 (n = 4) 145
Table 41: Experiment 4, runs 1 and 2 (n = 4). 146
Table 42: *PEDF* RT qPCR mean $2^{-\Delta\Delta Ct}$ values (n = 4). 148
Table 43: ELISA OD values, cell number and protein levels (pg/h/10^4 cells) of BDNF from A-172 cells transfected using the NEPA device, seven days post-transfection.....148
Table 44: *BDNF* RT qPCR, crossing point (Cp) values and further calculations - experiment 1-3, runs 1 and 2, seven days post-transfection of the A-172 cell line with the NEPA-21 device 149
Table 45: *BDNF* RT qPCR mean $2^{-\Delta\Delta Ct}$ values (n = 3).....151
Table 46: Flow cytometry analysis of *Venus*-transfected R28 cell cultures, 48 hours post transfection with the Neon Transfection System 151
Table 47: Area, CVa and mean *e* values of different cell lines measured using the Cell Profiler 4.2.6 software.....152
Table 48: Different parameters tested for transfections of the A-172 cell line using the MEA device.. 154
Table 49: Different parameters attempted for transfections of the R28 cell line using the MEA device. 157
Table 50: Different culture conditions tested for the Müller cell isolation.....163

10. List of pipelines

6.1 Cells in suspension…….. 152

6.2 Cells on a surface…… 153

11. Data availability

All original data are stored at AG Johnen, Department of Ophthalmology, University Hospital RWTH Aachen, and can be acquired upon request.

12. Publications

Part of this doctoral thesis will be published shortly.

10.1. Journal articles with contents of the present study (in preparation)

Iyer.S, Ingebrandt.S, Walter.P, Johnen.S, Effects of culturing conditions on non-viral transfection efficiency in glial cells

10.2. Conference contributions

04/2023	**ARVO** New Orleans, USA	Poster	Non-viral transfection of glial cells in suspension and in the adherent state using different electroporation devices
09/2023	**Artificial Vision** Duisburg	Talk	Differences in the non-viral electroporation-based transfection of glial cells in suspension or adherent state
09-10/2023	**DOG** Berlin	Poster	Electroporation-based non-viral genetic modification of glial cells in suspension or adherent state

13. Curriculum vitae

04/2021 - 06/2024	**Wissenschaftliche Angestellte** *Uniklinik der RWTH Aachen* Biologische Doktorand in der experimentellen Ophthalmologie
10/2017 - 05/2020	**Master of Science Molecular Biology and Biotechnology** *Rheinische Freidrich Wilhelms Universität Bonn* Vertiefungsrichtung: Molecular Biology, Biotechnology, Cell biology Masterarbeit: IRES blocker variations for efficient translation of selectively expressed RNA
09/2013 - 05/2017	**Bachelor of Technology Biotechnology** *Sri Venkateswara College of Engineering, Anna University* Vertiefungsrichtung: Biotechnology Bachelorarbeit: Construction and expression of synthetic antimicrobial peptides in *E.coli*
05/2013	**Abitur** Sri Sankara Vidhyashramam.Mat. Hr. Sec. School

14. Eidesstattliche Erklärung

Saishreyas Iyer

erklärt hiermit, dass diese Dissertation und die darin dargelegten Inhalte die eigenen sind und selbstständig, als Ergebnis der eigenen originären Forschung, generiert wurden.

Hiermit erkläre ich an Eides statt

1. Diese Arbeit wurde vollständig oder größtenteils in der Phase als Doktorand dieser Fakultät und Universität angefertigt;

2. Sofern irgendein Bestandteil dieser Dissertation zuvor für einen akademischen Abschluss oder eine andere Qualifikation an dieser oder einer anderen Institution verwendet wurde, wurde dies klar angezeigt;

3. Wenn immer andere eigene- oder Veröffentlichungen Dritter herangezogen wurden, wurden diese klar benannt;

4. Wenn aus anderen eigenen- oder Veröffentlichungen Dritter zitiert wurde, wurde stets die Quelle hierfür angegeben. Diese Dissertation ist vollständig meine eigene Arbeit, mit der Ausnahme solcher Zitate;

5. Alle wesentlichen Quellen von Unterstützung wurden benannt; (siehe auch Kapitel 15 Hiflestellungen);

6. Wenn immer ein Teil dieser Dissertation auf der Zusammenarbeit mit anderen basiert,wurde von mir klar gekennzeichnet, was von anderen und was von mir selbst erarbeitetwurde;

7. Kein Teil dieser Arbeit wurde vor deren Einreichung veröffentlicht.

_____

Datum

_____

Unterschrift

15. Hilfestellungen

Prof. Dr. med. Peter Walter Klinik für Augenheilkunde Uniklinik RWTH Aachen Pauwelsstraße 30 52074 Aachen	Fachliche Beratung, Unterstützung, Betreuung als Sprecher des Graduiertenkollegs 2610 InnoRetVision und Einwerbung von Forschungsmitteln
Priv.-Doz. Dr. rer. nat. Sandra Johnen Klinik für Augenheilkunde Uniklinik RWTH Aachen Pauwelsstraße 30 52074 Aachen	Fachliche Anleitung, Akquirierung von Forschungsmitteln, Projektplanung und Korrekturlesen
Prof. Dr. rer. nat. Sven Ingebrandt Institut für Werkstoff und Elektrotechnik I Sommerfeldstraße 24 52074 Aachen	Technische Beratung, Beschaffung des MEA-Geräts, Projektplanung und Korrekturlesen
Prof. Dr. rer. nat. Frank Müller Institut für Biologische Informationsprozesse Forschungszentrum Jülich Wilhelm-Johnen-Straße 52428 Jülich	Fachliche Anleitung, Projektplanung und Korrekturlesen
Prof. Dr. rer. nat. Björn Kampa Institut für Biologie II RWTH Aachen Worringerweg 3 52074 Aachen	Fachliche Anleitung, Projektplanung und Korrekturlesen
Senior Prof. Dr. rer. nat, Martin Zenke Uniklinik RWTH Aachen Pauwelsstraße 30 52074 Aachen	Fachliche Anleitung, Korrekturlesen
Dr. rer. nat. Sabrina Ernst Institut für Biochemie und Molekularbiologie Uniklinik RWTH Aachen	Technischer und Wissenschaftlicher Hilfe

Pauwelsstraße 30
52074 Aachen

Anne Rohn — Einarbeitung im Labor
Klinik für Augenheilkunde
Uniklinik RWTH Aachen
Pauwelsstraße 30
52074 Aachen

Alicia Hühnlein — Einarbeitung im Labor
Klinik für Augenheilkunde
Uniklinik RWTH Aachen
Pauwelsstraße 30
52074 Aachen

Antje Schiefer — Einarbeitung im Labor
Klinik für Augenheilkunde
Uniklinik RWTH Aachen
Pauwelsstraße 30
52074 Aachen

Lea Jiang — Zellaussaat und MEA-Verwaltung
Institut für Werkstoffe und Elektrotechnik I
Sommerfeldstraße 24
52074 Aachen

Sarah Göbbels — Zellaussaat und MEA-Verwaltung
Institut für Werkstoffe und Elektrotechnik I
Sommerfeldstraße 24
52074 Aachen

Johannes Wüffel — Technischer service
Interdisziplinäres Zentrum für Klinische Forschung (IZKF)
Uniklinik RWTH Aachen
Pauwelsstraße 30
52074 Aachen

Sikle Vaßen — Technischer service
Interdisziplinäres Zentrum für Klinische Forschung (IZKF) - FCF
Uniklinik RWTH Aachen
Pauwelsstraße 30
52074 Aachen

16. Danksagung

Zuallererst möchte ich mich bei Prof. Dr. Med. Peter Walter bedanken. Ich möchte ihm herzlich dafür danken, dass er die Rolle des Sprechers des GRK 2610 InnoRetVision übernommen und mein Projekt im Rahmen dieses GRK ermöglicht hat. Ich möchte mich auch für seinen fachkundigen Rat, seine ansteckende Begeisterung für die experimentelle Ophthalmologie und seinen Optimismus in der Forschung bedanken.

Mein Dank an Priv.-Doz. Dr. rer. nat Sandra Johnen für die Bereitstellung des Forschungsthemas, die Betreuung der Arbeit, die ständige Erreichbarkeit bei Fragen, die tatkräftige Unterstützung während meiner Zeit in der Arbeitsgruppe, das Vertrauen in meine Forschungsfähigkeit und die Übernahme des Zweitgutachtens ist mit Worten nicht auszudrücken.

Prof. Dr. rer. nat. Sven Ingebrandt möchte ich dafür danken, dass er mir den Zugang zum MEA-Gerät ermöglicht hat, der für meine Forschung unerlässlich war. Ich danke ihm auch für seine fachkundige Beratung und für die Übernahme der Rolle meines Zweitbetreuers.

Prof. Dr. rer. nat. Björn Kampa danke ich für seinen hilfreichen technischen Input und seine freundliche und unkomplizierte Übernahme des Erstgutachtens.

Prof. Dr. rer. nat. Frank Müller danke ich für die freundliche fachliche Unterstützung und die schnelle Beantwortung von aufkommenden Fragen zu Müllerzellen sowie für die freundliche Übernahme des Drittgutachtens.

Außerdem möchte ich mich bei Senior Prof. Dr. rer. nat, Martin Zenke afür bedanken, dass er sich die Zeit genommen hat, an allen meinen Fortschrittsberichten teilzunehmen und die Rolle des externen Betreuers meines Graduiertenkollegs übernommen hat.

Samantha Nqoko bin ich sehr dankbar für ihre Hilfe als Koordinatorin des Graduiertenkollegs. Sie hat das Graduiertenkolleg durch ihre fachkundige Organisation von Personen, Treffen und

Geldern erst möglich gemacht. Außerdem ist sie eine wirklich gute Freundin, mit der man in Zeiten der Not reden kann.

Ich möchte mich bei Andrea Kauth und Roman Deubel vom Institut für Werkstoffe und Elektrotechnik I (IWE-I) bedanken, die mir das MEA-Gerät zur Verfügung gestellt haben und immer als kompetente technische Berater für alle Fragen rund um das MEA-Gerät zur Verfügung standen.

Ein herzliches Dankeschön geht an Lea Baumann vom IWE-I, die die MEA-Experimente ermöglichte, indem sie die Zellaussaat und die MEA-Wartung durchführte, wenn ich keine Zeit dafür fand. Ich möchte ihr auch dafür danken, dass sie meine Freundin ist, an die ich mich in Zeiten der Not immer wenden kann.

Ein herzliches Dankeschön geht auch an Anne Freialdenhoven für ihre immense Hilfe bei der Ausbildung für die Netzhautisolation aus Mäusen und ihre Unterstützung bei der Durchführung derselben.

Vielen Dank an Antje Schiefer und Alicia Hühnlein für ihre Hilfe bei der Ausbildung und für ihr technisches Fachwissen in Bezug auf die Zellkultur und die anschließende Verarbeitung der transfizierten Proben.

Ich möchte mich bei allen Mitgliedern des GRK 2610 InnoRetVision, sowohl bei den Studenten als auch bei den Betreuern, für ihren Enthusiasmus für die Wissenschaft und dafür bedanken, dass sie meine ständige Quelle des Optimismus und der Neugierde sind.

Ich möchte meinen Eltern meinen tiefsten Dank dafür aussprechen, dass sie für mich Liebe und Verständnis aufbrachten, als ich meiner Leidenschaft für die Wissenschaft nachging. Viel von meiner Stärke kommt daher, dass ich weiß, dass sie immer an meiner Seite sind.

Ich möchte Jiao Zhang danken, ohne die meine Zeit als Doktorand nicht dieselbe gewesen wäre. Die Zusammenarbeit mit ihr und ihre ständige Inspiration haben mich zu einem besseren Forscher und Menschen gemacht. Vielen Dank.

Und schließlich bin ich meinem besten Freund und Mentor, Bhagavan Sri Sathya Sai Baba, äußerst dankbar, ohne den all dies nicht möglich gewesen wäre. Ich habe nie einen besseren Freund oder stärkeren Verbündeten gekannt. Ich widme ihm all diese Arbeit.